On the investigation of experimental and numerical methods to characterise the fracture behaviour of epoxy resins : an approach to prevent failure in electronic component

Julien Roger

HAL Id: tel-02998333
https://uphf.hal.science/tel-02998333

Submitted on 10 Nov 2020

THESE
PRESENTEE A
L'UNIVERSITE DE VALENCIENNES
ET DU HAINAUT-CAMBRESIS

EN VUE DE L'OBTENTION D'UN
DOCTORAT EN GENIE MECANIQUE

PAR
JULIEN ROGER

On the investigation of experimental and numerical methods to characterise the fracture behaviour of epoxy resins: an approach to prevent failure in electronic component

Sur la mise en œuvre de méthodes expérimentale et numérique pour caractériser le comportement en rupture des résines époxy : une approche pour prévenir la défaillance de composants électroniques

Le mercredi 5 Décembre 2007, devant le jury composé de:

Rapporteur	Pierre-Alain Boucard, Professeur, ENS, Cachan, France
Rapporteur	Laurent Gornet, MCF HDR, Ecole Centrale, Nantes, France
Examinateur	Daniel Brissaud, Professeur, INP, Grenoble, France
Examinateur	Daniel Coutellier, Professeur, ENSIAME, Valenciennes, France
Examinateur	Marc Dressler, Docteur, Robert Bosch GmbH, Stuttgart, Allemagne
Examinateur	

LAMIH

**LABORATOIRE
D'AUTOMATIQUE
DE MECANIQUE ET
D'INFORMATIQUE
INDUSTRIELLES
ET HUMAINES**

On the investigation of experimental and numerical methods to characterise the fracture behaviour of epoxy resins: an approach to prevent failure in electronic component

BOSCH

Invented for life

Acknowledgements

Abstract

Prediction of crack growth in encapsulating material has a critical issue on the reliability of electronic components. To prevent the risk of material rupture or to extend the lifetime of these structures, experimental and numerical methods are developed within the context of linear elastic fracture mechanics. The present study proposes to extend techniques, which were previously established for metals, to epoxy resins. First, an experimental procedure using compact tension (CT) specimens is applied to characterise the fracture toughness of epoxy resins. The test dispersion is estimated with a statistical method based on a Weibull distribution. This technique is then used to compare different epoxy resins and to quantify effects due to presence of filler particles. The influence of the temperature is also described. Then, a method is proposed to determine a fracture criterion for cracks under mixed mode loading. Experiments are performed on centre cracked tension (CCT) specimens. This geometry additionally enable to extract the direction of crack propagation for given proportions of tensile and shear loading. Based on finite element methods, a numerical analysis is used to calculate the direction of crack propagation. A comparison between experimental and numerical results confirms the capability of FE codes to predict curved crack path. As well, fatigue crack growth is investigated with CT specimens under cyclic loading. Material parameters are identified in accordance with the Paris law. With the help of the commercial software Zencrack, a crack propagation can be simulated by a sequential approach, in which the crack length is updated step by step. 2D and 3D models are generated. The influence of the crack curvature through the thickness is described. On that purpose, a modified Paris law is proposed. The simulated crack propagation provides excellent agreements with experimental measurements.

Keywords: epoxy resin, fracture toughness, mixed mode fracture criteria, fatigue analysis, finite element method, numerical crack growth

Zusammenfassung

Bezüglich der Zuverlässigkeit von elektronischen Bauteilen ist die Vorhersage von Rissausbreitung in Vergussmassen eine entscheidende Methode. Im Rahmen der linearen elastischen Bruchmechanik, experimentelle und numerische Verfahren erlauben das Versagen von Materialien zu vermeiden oder die Lebensdauer zu verlängern. Diese Methoden, die für Metalle entwickelt wurden, sind in dieser Studie für Epoxidharze erweitert. Zuerst, eine dito experimentelle Vorgehensweise ist vorgeschlagen, um die Bruchzähigkeit von Epoxidharzen mit CT-Proben zu charakterisieren. Die Streuung der Versuche ist mittels einer statistischen Methode basiert auf eine Weibull Verteilung bewertet. Diese Technik ermöglicht den Vergleich von verschiedenen Epoxidharzen (mit oder ohne Füllstoffen). Der Einfluss von Temperatur auf die Bruchzähigkeit ist zusätzlich beschrieben. Außerdem ist eine Methode dargestellt, um ein Bruchkriterium für Risse unter mixed-mode Belastung zu bewerten. Die Geometrie der CCT-Proben, mit denen die Versuche durchgeführt sind, ermöglicht auch die Richtung der Rissausbreitung für eine gegebene Zug/Scher Spannung zu beobachten. Die Richtung der Ausbreitung kann auch mittels einer Finiten-Elemente Analyse berechnet werden. Der Vergleich zwischen experimentellen und numerischen Ergebnissen bestätigt die Fähigkeit von FE Analysen gekrümmte Risspfade vorherzusagen. Schließlich wird die Untersuchung von Ermüdungs-risswachstum mit zyklischen Versuchen an CT-Proben durchgeführt. Nach der Bearbeitung, werden die gemessenen Daten mit einer Paris-Gleichung angepasst. Zusätzlich ermöglicht die Software Zencrack eine Rissfortschrittsberechnung, während der die Rissfront schrittweise generiert wird. 2D sowie 3D Modellen sind untersucht. Insbesondere in 3D zeigt die Verteilung des Spannungsintensitätsfaktors entlang der Rissfront einen Dickeneffekt auf. Aus diesem Grund wird eine modifizierte Paris-Gleichung eingesetzt.

Stichwörter: Epoxidharz, Bruchzähigkeit, mixed-mode Bruchkriterium, Ermüdungs-risswachstum, Finite Elemente Methode, numerische Rissausbreitung

Résumé

La fiabilité des composants électroniques est parfois détériorée à cause de la propagation de fissures dans les matériaux de protection. Pour anticiper les risques de rupture et améliorer la durée de vie de ces structures, des méthodes expérimentales et numériques sont développées dans le cadre de la mécanique de la rupture linéaire élastique. Préalablement établies pour des matériaux métalliques, la présente étude propose d'étendre ces techniques aux résines époxy. Une procédure expérimentale est mise en place afin de caractériser la ténacité de résines époxy. La dispersion du test est évaluée avec une méthode statistique basée sur une distribution de Weibull. Cette technique permet une comparaison entre différents types de résines (chargées ou non chargées). L'influence de la température sur la ténacité est aussi décrite. Une méthode est ensuite proposée pour déterminer un critère de rupture pour les fissures sous chargement de mode mixte. Les essais sont réalisés avec des éprouvettes de type Centre Crack Tension (CCT), dont la géométrie permet également d'observer la direction de propagation de la fissure. Une analyse numérique, basée sur un code éléments finis, est parallèlement utilisée pour calculer la direction de propagation. Une comparaison entre résultats numériques et expérimentaux confirme la capacité du code EF à prédire un chemin de fissuration incurvé. En outre, l'analyse de propagation de fissure en fatigue découle de résultats expérimentaux réalisés sur des éprouvettes Compact Tension (CT) soumises à un chargement cyclique en traction. Les paramètres matériaux sont extraits suivant une loi de type Paris. A l'aide du logiciel Zencrack, une propagation de fissure en 3D peut être simulée via une approche séquentielle, durant laquelle la fissure est propagée pas-à-pas. L'influence de la géométrie du front de fissure sur les prédictions numériques est mise en évidence. Les résultats numériques présentés sont en bon accord avec les résultats expérimentaux.

Mots clés: résine époxy, ténacité, critère de rupture en mode mixte, fatigue, méthode éléments finis, modèle numérique de propagation

Table of contents

8 DISCUSSION: "FRACTURE MECHANICS IN CONCEPTION" .... - 164 -

9 CONCLUSION .... - 170 -

List of symbols

Latin symbols

a	crack length
a_d	minimal detectable crack length
a_c	critical crack length
$\bar{a}$	average crack length
A	crack surface
b	ligament depth
B	thickness of the body or specimen or sample
c	effective crack length in the Dugdale's model
C	elastic compliance
	or Paris law parameter
C_{eff}	effective Paris law parameter
C_i	parameters of the Airy stress function
da	crack extension increment
da/dN	crack growth rate
dA	surface extension increment
du	displacement increment
dP	load increment
ds	element of arc length
dV	volume increment
E	modulus of elasticity or Young's modulus
E'	effective Young's modulus
f_j	body forces per unit volume
f_{ij}^k	dimensionless function between σ_{ij} and K_k
f_{CT}	dimensionless function specific to CT specimen
f_{SEN}	dimensionless function specific to SEN specimen
F_{ASTM}	dimensionless function specific to CT specimen
F_{eff}	effective dimensionless function
F	two-parametric Weibull's function
F_{Xc}	nodal forces in the X-direction on node C
G	mechanical energy release rate (ERR)
G_c	critical energy release rate
G_i	energy release rate for mode i
G_{max}	maximum potential energy release rate
G_P	energy release rate associated to the applied load P
H	dimension of a beam
I_Γ	integral on the closed contour Γ
J	Rice contour integral - J-integral
J^T	J-integral vector
J_k	component of the J-integral vector
K	elastic stiffness
$\boldsymbol{K}$	stiffness matrix
K	stress intensity factor (for mode I)
K_{avg}	average value of K_{Ic}
K_{ASTM}	stress intensity factor evaluated from the ASTM solution for CT specimen
K_{FEM}	stress intensity factor computed with the FE model for CT specimen
K_k	stress intensity factor for mode k
K_{Ic}	fracture toughness
K_{IIc}	critical stress intensity factor in mode II

(K_I^c, K_{II}^c)	critical stress intensity factor couple for mixed mode loading
K_I^n	normalised stress intensity factor in mode I
K_{eff}	effective stress intensity factor
K_ρ	stress intensity factor over the length ρ in the Dugdale's model
K_P	stress intensity factor associated to the applied load P
K_0	Weibull scaling parameter
L	reference length of FE element
m	Paris law exponent
m_{eff}	effective Paris law exponent
m_0	Weibull modulus
N_c	lifetime or critical number of elapsed cycles
$\boldsymbol{n}$	normal vector to a surface
p	wedge forces in the Dugdale's model
P	applied force or measured force
P_c	critical load
$\boldsymbol{P}$	vector of external forces applied to the nodes
$\boldsymbol{q}$	weighting vector
r	distance of a point to the origin in cylindrical system
r_k	Radius of the K-annulus
r_y	radius of the process zone at crack tip
r_0	critical distance at which the SIFs are evaluated
R	crack resistance energy
	or stress ratio
S	surface
	or energy density factor
S_{min}	minimum strain energy density
T_g	glass transition temperature
$\boldsymbol{T}$	traction vector
u	applied displacement or measured displacement
$\boldsymbol{u}$	vector of nodal displacements
U	total energy of the system
U_E	potential strain energy stored in the elastic system
U_A	potential energy of the outer applied loading
U_M	mechanical energy of the system
U_S	surface energy of the system
V_i	opening displacements along the direction i
W	width of the body or specimen
	or strain energy density

Greek symbols

α	ratio a / W
γ_s	specific surface energy
Γ	closed contour
δ_{ik}	Kronecker's delta
Δa	crack extension increment
ΔE	released energy during the crack extension Δa
ΔK	crack growth rate
ΔK_{th}	fatigue threshold
ΔK_∞	asymptotic value in the domain III of the curve da/dN - ΔK
ΔP	load range
Δu	displacement increment
ε	strain
$[\varepsilon_{ij}]$	strain tensor

ε_{ij}^{m}	mechanical strain component
ε_{ij}^{th}	thermal strain component
η	arc length
θ	angle in a cylindrical coordinate system or direction of crack propagation
θ_0	kinking angle
μ	shear modulus
v	Poisson's ratio
V	unit vector in the direction of crack advance
σ	stress
σ_y	yield stress
$[\sigma_{ij}]$	stress tensor
σ_∞	stress applied for infinite plates
$\sigma_{\theta max}$	maximum tangential stress
τ	shear stress
φ	crack orientation
ψ_0	twisting angle

Abbreviations

ASTM	American Society for Testing and Materials
CCT	Center cracked Tension (specimen)
CT	Compact Tension (specimen)
CTS	Compact Tension Shear (specimen)
CTOD	Crack Tip Opening Displacement
DMA	Dynamic Mechanical Analysis
EPFM	Elastic-Plastic Fracture Mechanics
ERR	Energy Release Rate
ESIS	European Structural Integrity Society
FEM	Finite Element Method
LEFM	Linear Elastic Fracture Mechanics
MERR	Maximum Energy Release Rate
MSED	Minimum Strain Energy Density
MTS	Maximum Tangential Stress
OCT	Optical Crack Tracing equipment
PMMA	Polymethyl methacrylate
SEN	Single Edge Notched
SIFs	Stress Intensity Factor
SSY	Small Scale Yielding
VCCT	Virtual Crack Closure Technique
VCE	Virtual Crack Extension

1 Introduction

Reliability is one of the main objectives during the conception of industrial products. In fact, the ability of a system to perform its required functions under operating conditions has to be ensured for a specified time. This notion is essential at each system level. For example, the reliability of an engine is equivalent to the reliability of each engine component, which directly depends on the reliability of each component module. Consequently, manufacturing process are continuously controlled and improved to offer a high product quality. Especially for automotive engineers, the minimisation of failure and the enhancement of lifetime constitute a daily challenge. Components have also to fulfil additional specifications. Amongst others, downsizing or weight reduction are requested to decrease the fuel consumption, whose effects are not always compatible with the conception of robust and reliable products. For this reason, effective experimental and numerical methods are required to improve the development of complex structures.

The present work focuses on materials used in electronic packaging for automotive applications. The exposition of electronic devices to external environnements like humidity, aggressive media or dust particles annihilates their functionnality or limits their efficiency. Techniques of encapsulation enable to protect an electronic part by moulding a compound material around it. In most cases, a thermal and electrical isolation is also combined. Epoxy resins are particularly appropriate to encapsulation techniques with respect to their material properties and their price/performance ratio. As the manufactured assembly is composed by several materials, mechanical stress concentrations may locally appear on edge or corner of the structure. As well, the curing process of polymers generates residual stresses. Defects like micro-cracks or material flaws may be introduced during the manufacturing. Reinforced epoxy resins are also sensitive to damage mechanism. All these phenomena induce mechanical stress concentrations, which causes the initiation of cracks. However, crack propagation may lead to the complete failure of the component. Therefore, it is essential to evaluate if the crack propagation will have a critical issue on the functionality of the component during the conception phase.

Epoxy resins are brittle materials, in which the extension of crack may be described using the linear elastic fracture mechanics (LEFM). The LEFM was first developed to analyse the failure of naval constructions made of metallic materials. Applications were recently extended to plastics materials as they are intensively used in aircraft, automotive and communication industries. The LEFM helps to describe the stress state at the crack tip by introducing fracture mechanics parameters, like stress intensity factors or energy release rate. Based on these parameters, fracture criteria enable to predict if a crack will grow or not. Similar to the yield stress for plasticity, the fracture toughness is defined as the resistance to fracture for a crack under an opening loading condition. Standardised procedures describe the experimental measurement of fracture toughness. Evaluated parameters complete the material database, which is used during the conception phase to determine the material offering the best combination between stiffness, resistance to fracture and temperature behaviour.

Not only the material, but also the design of products is optimised during the development. Numerical methods enable a flexible variation of geometries or of material data. Moreover, the reduction of costs and time development incites to the integration of numerical solutions. Several simulation methods are available to predict the growth of cracks, like meshless or boundary element methods. As the Finite Element Method (FEM) is largely used in industry,

this method is applied in this work. From the stress distributions, it is possible to determine critical zones inside the component. Till now, FEM is principally used after failure to understand the cause of crack propagation. The systematic use of numerical methods with regard to fracture mechanics may contribute to the reduction of failure occurrence. The material which minimises the risk of crack propagation can be determined. As well, the geometry may be optimised to limit stress gradients.

Numerical and experimental methods are principally based on the propagation of a crack subjected to an opening loading. However, material flaws or precrack are arbitrarily oriented in the structure. In the case of a mixed mode loading, a combination of shear and tensile stresses occurs at the crack tip. A variation of the shear/tensile stress at the crack tip may be used to experimentally determine a mixed mode fracture criteria for epoxy resins. Furthermore, the numerical analysis of a structure containing a crack returns the stress distribution near the crack tip. If the shear/tensile stress proportion reaches a critical value, the crack is assumed to propagate in the structure. Under mixed mode loading condition, crack propagation leads to a deviation of the crack. Based on the LEFM theory, models of crack propagation are implemented in software packages to predict the direction of crack extension. Experiments may have to be performed to validate these analytical models for filled epoxy resins. More than stress fields at the crack tip and direction of crack propagation, numerical tools are also able to predict the entire crack path generated during the propagation. So, simulations are powerful tools to examine crack growth, the precision of which has to be confirmed.

Products can be dimensioned to resist fracture under critical static loading combining experimental and numerical techniques. Nevertheless, progressive crack propagation can appear under repeated loading. This second mode of fracture is named fatigue crack growth. As well, material parameters can be experimentally extracted to characterise the fatigue behaviour of cracks in epoxy resins. In this case, basic specimens are subjected to cyclic loading. The relation between crack growth rate and applied load is extracted from the tests. Thus, material parameters constitute a useful input data for numerical simulations. Fatigue crack growth is numerically analysed using a sequential approach, in which the crack extension and direction of propagation are updated step by step. Such FE simulations enable the evaluation of component lifetime. Complex structures are not always symmetric and require the use of 3D models. As the majority of works in LEFM concentrates on 2D models, the extension to three-dimensions requires the investigation of some parameters. For example, the curved nature of the crack front through the thickness may be investigated.

This work proposes an overview of experimental and numerical methods to characterise the crack propagation in epoxy resins. Fractures obtained under static or cyclic loading are investigated. The accuracy of the proposed methods is also discussed, as the integration of such methods in the development of electronic components.

2 About fracture mechanics

The notion of *fracture* is generally understood as the limited or complete partition of an originally solid body. The description of these phenomena is the object of fracture mechanics. Historically developed to analyse the failure of naval and aircraft constructions, the fracture mechanics is now present in all engineering domains. In fact, standardised tests, numerical tools and statistical methods are available to investigate the problem of crack propagation. Thus, these techniques contribute to improve the reliability of components. The most studies concentrate on metallic materials, but similar methods exist for plastics and polymers since they began to be widely used in engineering applications.

2.1 Concepts of fracture mechanics

2.1.1 Crack initiation and crack propagation

A crack evolution can be divided into two parts: *initiation* and *propagation*. In terms of initiation, no fracture events occur, until a critical internal load criterion is reached. The microcrack nucleation occurs easily at micro-defects such as impurities, cavities or oxidation. With an increase of load, we can observe microcrack propagation. In the case of polycrystalline materials, the grid geometry and grain topology involves trans- or inter-crystalline crack propagation. However, the crack propagation in solids is generally described with the help of macroscopic continuum mechanics, where the crack is regarded as a shape in a body. During crack propagation, the crack front progressively advances into the body. The sides opposite to each other are the crack surfaces. In most cases, crack surfaces can be assumed to be free of load.

Crack surface

Crack front
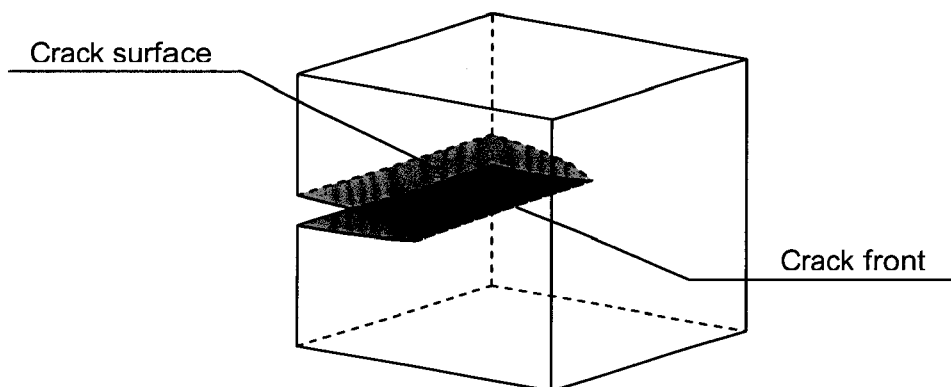
Fig. 1: Description of a crack tip

2.1.2 Linear elastic and elastic-plastic fracture mechanics

The fracture mechanics was developed to predict conditions under which a material fails for a preset crack. To characterise material behaviours within the context of fracture, experimental techniques are based on simple loading conditions. The most well-known is a basic uniaxial tensile test, which can be represented through a stress-strain diagram:

σ | fracture ✗

(a) brittle material

σ | σ_y | fracture ✗ yielding
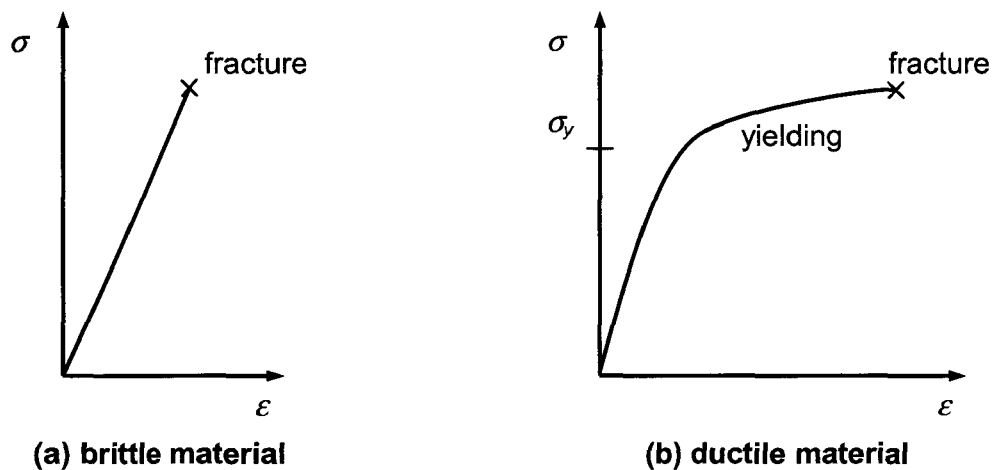
(b) ductile material

Fig. 2: Brittle and ductile material behaviour

Generally, a reversible deformation, which is characterised by a linear relation between stress and strain, is first observed. Brittle materials follow this linear elastic behaviour till the crack propagates, as represented in Fig. 2a. The yielding strength limit corresponds to the fracture point of the material. On the contrary, ductile materials undergo a larger deformation without fracture, as seen in Fig. 2b. As soon as the stress reaches the yield stress σ_y, an irreversible or plastic deformation occurs. For ductile materials, the plastic deformation precedes the fracture phenomenon. Brittle or ductile behaviours are theoretical models, which constitute an accurate representation for the majority of materials. For that purpose, the fracture mechanics theory is divided into two parts:

- the Linear Elastic Fracture Mechanics (LEFM)
- the Elastic-Plastic Fracture Mechanics (EPFM)

On the one hand, for ductile materials, failure can be defined regarding the yield strength or the fracture limit. In fact, if plastic deformations are inappropriate for the reliability of the system, the yield stress should not be exceeded. If plastic deformations are tolerated, the fracture limit has to be considered. For brittle material, yield strength and fracture threshold are equivalent. On the other hand, a given material can follow a brittle behaviour under a defined loading condition and a ductile behaviour under another loading condition. That is why the LEFM or EPFM techniques shall be applied carefully and with respect to the loading conditions of the material.

LEFM and EPFM propose different concepts to describe the behaviour of a crack [Gro96]. The LEFM introduces two crack growth criteria, based on the evaluation of the energy release rate or of the stress intensity factors. In the same way, the EPFM establishes a global and a local fracture criterion: the J-integral and the crack tip opening displacement (CTOD). Those two further fracture criteria are also valid within the context of LEFM, since the EPFM can be considered as an extension of the LEFM theory for ductile materials. In this study, materials are considered has brittle materials. Thus the LEFM theory will be assumed.

2.1.3 Small scale yielding condition

The continuum mechanics considers a crack as a shape in a body, such that a singularity in the stress and strain fields exists in the vicinity of the crack tip. Particularly, the stress concentration near the crack tip is determined by the load applied and the geometry of the body. The material behaviour is consequently the central parameter for the definition of the fracture criterion.

Consider an isotropic linear elastic body containing a crack, which is subjected to a tensile opening. The stress tends to infinity near the crack tip, due to the singularity in the stress distribution, as shown in Fig. 3a. However, this infinite value has no physical meaning. This phenomenon directly derives from the application of an idealised elastic behaviour of the material. In reality, such stresses are limited by local crack tip yielding, which occurs over a small region in front of the crack tip known as the plastic zone size r_y [Rit83]. Irwin proposed this simple model of plasticity at the crack tip, as presented in Fig. 3b.
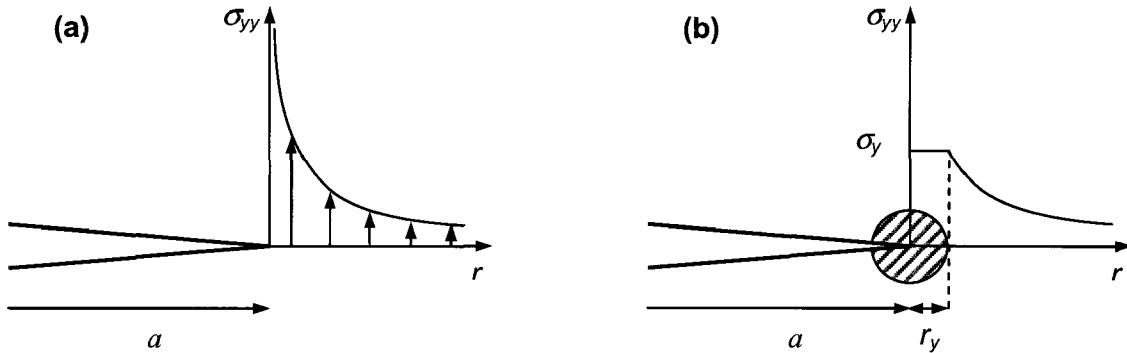
Fig. 3: a) Shear stress distribution at the crack tip for ideal elastic material behaviour; b) Irwin's plastic zone [Gro96]

The application of the LEFM theory is restricted to a zone outside of the plastic zone. But near crack tip ($r \to 0$), the asymptotic solutions give an accurate representation of the stress distribution in the vicinity of the crack tip. Consequently, the domain where inelastic deformations occur has to be confined inside a small region. In this case, the plastic deformation is only considered as a slight perturbation in the linear elastic solutions. These conditions are called the small scale yielding (SSY) condition. Physically, the process zone shall be clearly smaller than other dimensions of the geometry, like the crack length a or the thickness B.

$$r_y \ll B, a \qquad \text{Eq. 1}$$

Due to the restriction of small scale yielding, the LEFM is only valid for brittle material and high strength materials. For the description of failure in lower strength ductile materials, where large inelasticity precedes and accompanies fracture, the ductile or elastic-plastic fracture mechanics EPFM theory is required.

2.2 Linear elastic fracture mechanics LEFM

As a part of the macroscopic continuum mechanics, the linear elastic fracture mechanics LEFM describes the behaviour of cracked body, whose material properties are considered linear elastic. This concept is suitable for brittle materials and also for high strength materials. In the case of high strength materials, the plastic zone in front of the crack tip is small compared to other dimensions, so that a linear elastic behaviour is assumed outside this process zone. This specification is named the small scale yielding condition and was defined in the chapter 2.1.3.

2.2.1 Modes of crack propagation

For the continuum mechanics analysis of a crack, it is useful to distinguish three basic *modes* of fracture (see Fig. 4). Mode I, the *opening mode*, corresponds to normal separation of the crack surfaces under the action of tensile stresses. Mode II, the *sliding mode*, corresponds to longitudinal shearing of the crack surfaces in a direction normal to the crack front. Mode III, the *tearing mode*, corresponds to lateral shearing parallel to the crack front.
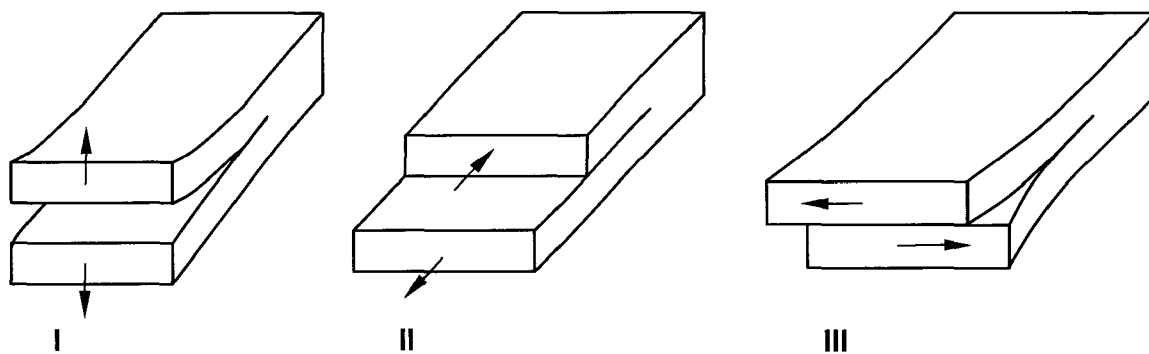
Fig. 4: Three modes of fracture: I, opening mode; II, sliding mode; III, tearing mode

The crack propagation results primarily from the stress distribution in the vicinity of the crack tip. Considering a linear elastic stress analysis, the stress distribution near the crack tip can be decomposed into a combination of mode I, II and III, such that each mode of fracture is characterised by a stress state in each plane. For this reason, a local coordinate system (I, II, III) at the crack tip is defined at each position along the crack front, as depicted in Fig. 5. Of the three modes, the first is by far the most pertinent to crack propagation in highly brittle solids. This is documented by the tendency for a brittle crack to seek an orientation that minimises the shear loading [Bit96].

Mode I or opening mode:
perpendicular to crack plane

Mode II or sliding mode:
normal to crack front

Mode III or tearing mode:
tangent to crack front
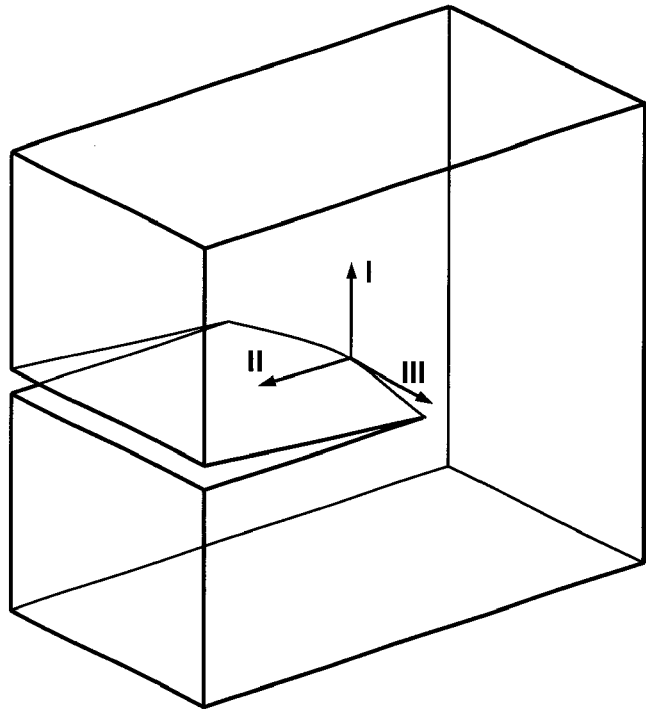
Fig. 5: Local coordinate system at an opened crack front

2.2.2   Energy release rate

Energy balance concept

In the twentieth century, A. A. Griffith [Gri21-24] proposed to model a static crack as a reversible thermodynamic system. The system was described as follows (Fig. 6): an elastic body containing a plane-crack surface S of length a is subjected to loads P applied at the outer boundary.

System boundary
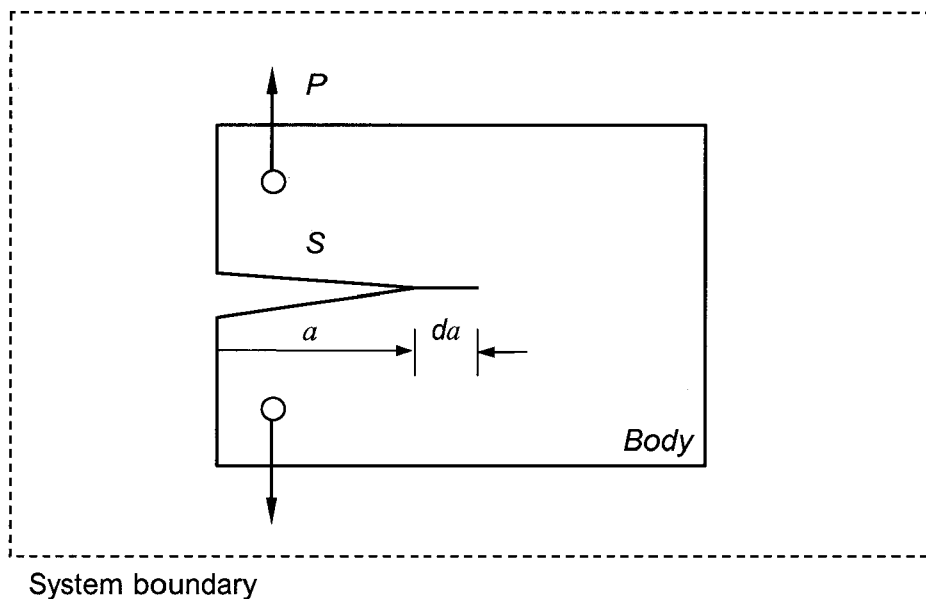
Fig. 6: Reversible thermodynamic system for energy balance concept [Gri21-24]

Griffith sought the configuration that minimised the total free energy of the system; the crack would be in a state of equilibrium, and thus on the limit of extension. The total energy U of the system can be partitioned into the mechanical and surface energy, called U_M and U_S.

$$U = U_M + U_S$$ Eq. 2

The mechanical energy U_M itself consists of two terms:
- U_E, which is the potential strain energy stored in the elastic body.
- U_A, which is the potential energy of the outer applied loading, expressible as the negative work associated with any displacements of the loading points.

$$U_M = U_E + U_A$$ Eq. 3

The surface energy U_S is the free energy expended in creating the new crack surfaces, which corresponds to an irreversible dissipation of energy during crack growth.

Thermodynamic equilibrium is then attained by balancing the mechanical and surface energy terms over a virtual crack extension da. It is obvious to see that the mechanical energy will generally decrease, as the crack extends ($dU_M/da < 0$). On the other hand, the surface energy term will generally increase ($dU_S/da > 0$).Thus U_M favours crack extension, while U_S opposes it. This is the Griffith energy-balance concept, a formal statement of which is given by the equilibrium requirement.

$$dU/da = 0 \quad \text{or} \quad dU_S/da = -dU_M/da$$ Eq. 4

This relation yields a criterion for predicting the fracture behaviour of a body. A crack extends by small displacements from the equilibrium length. Crack propagation can be regarded as the creation of a surface inside the structure. For this reason, the interfacial crack area dA is preferred to the crack length increment da for the definition of the mechanical energy release rate. G has the dimension of energy per unit area:

$$G = -\frac{dU_M}{dA}$$ Eq. 5

The surface energy U_S is defined as the crack resistance energy R, which can be interpreted as the resistance that the material opposes to the crack propagation. In the case of a brittle material behaviour, the crack resistance energy is associated to the specific surface energy γ_S of the material, which has the dimensions of energy per unit area and is independent of the crack length:

$$R = \frac{dU_S}{dA} = 2\gamma_S$$ Eq. 6

From Eq. 5 and Eq. 6, an equivalent formulation of the energy balance concept results:

$$R = G$$ Eq. 7

The energy release rate grows continually with the increase of the external loading. As the energy release rate reaches the value of the crack resistance energy, the crack propagates. The stability of crack propagation is dependent on the relative evolution of R and G with crack length:

$$R = G \quad and \quad \begin{cases} \dfrac{dG}{dA} < \dfrac{dR}{dA} & stable\ crack\ propagation \\[2ex] \dfrac{dG}{dA} = \dfrac{dR}{dA} & critical\ point \\[2ex] \dfrac{dG}{dA} > \dfrac{dR}{dA} & unstable\ crack\ propagation \end{cases}$$

Eq. 8

Energy release rate definition

The basic cracked plate described in Fig. 7 has a thickness B. The crack has a length a and the crack surfaces are free of loading.
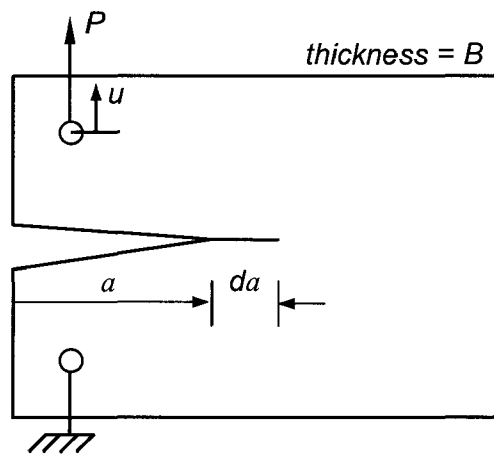
Fig. 7: Cracked plate subjected to an external load P

The specimen is fixed on its lower region and a tensile load P is applied on the upper region. Consider the plate before the crack extends. An elastic behaviour is assumed, i.e. the resulted displacement u on the upper bound is related to the applied load P via the elastic compliance C. The term C is a global value for the all specimen and consequently is dependent on the crack length $C = C(a)$.

$$u = CP$$

Eq. 9

The potential strain energy stored in the elastic body is equal to the work of the elastic loading:

$$U_E = \frac{1}{2} Pu = \frac{1}{2} \frac{u^2}{C} = \frac{1}{2} CP^2$$

Eq. 10

Consider now the load P to be maintained at a level which enables an extension of the crack length from a to $a+da$. Since the crack propagates of a length da, the displacement increases of an increment du. The work generated by the external force is then:

$$dU_A = -Pdu$$

Eq. 11

To characterise the energy release rate under a mathematical form, the mechanical definition dU_M/dA of Eq. 5 is required and leads to:

$$dU_M = d(U_E + U_A) = \left(\frac{1}{2}dPu + \frac{1}{2}Pdu\right) - Pdu = \frac{1}{2}dPu - \frac{1}{2}Pdu \qquad \text{Eq. 12}$$

The differentiation of Eq. 9 yields:

$$du = PdC + CdP \qquad \text{Eq. 13}$$

With the help of Eq. 9 and Eq. 13, the total mechanical energy change is then reduced to:

$$dU_M = -\frac{1}{2}P^2 dC \qquad \text{Eq. 14}$$

Finally, from Eq. 5 with the interfacial crack area $dA = Bda$, the energy release rate is:

$$G = -\frac{dU_M}{Bda} = \frac{1}{2}\frac{P^2}{B}\frac{dC}{da} \qquad \text{Eq. 15}$$

Another way to describe the relation between force and displacement is to introduce the stiffness K, which is the inverse of the compliance C. In the same way, the stiffness depends on the crack length $K = K(a)$.

$$P = Ku \qquad \text{Eq. 16}$$

By analogy, the energy release rate can be expressed as a function of displacement and stiffness:

$$G = -\frac{dU_M}{Bda} = -\frac{1}{2}\frac{u^2}{B}\frac{dK}{da} \qquad \text{Eq. 17}$$

To illustrate graphically these results, two extreme loading configurations can be considered during the crack extension: constant force or constant displacement.

Crack extension under constant force

If crack extension takes place at constant load, the displacement increases of an amount du ($du \neq 0$). The load stays constant, so that $dP = 0$. The work done by the external load and the elastic strain energy change are:

$$\begin{cases} dU_A = -Pdu = -P^2 dC \\ dU_E = d\left(\frac{1}{2}CP^2\right) = \frac{1}{2}P^2 dC \end{cases} \qquad \text{Eq. 18}$$

From Eq. 3, the total mechanical energy change is:

$$dU_M = -\frac{1}{2}P^2 dC \qquad \text{Eq. 19}$$

As well, the energy release rate G can be described graphically. For a crack length a, the load-displacement is represented by the line OA in Fig. 8a. For a crack length $a+da$, the load-displacement is represented by the line OE. The stiffness of the specimen will decrease after crack propagation and consequently the compliance will increase.
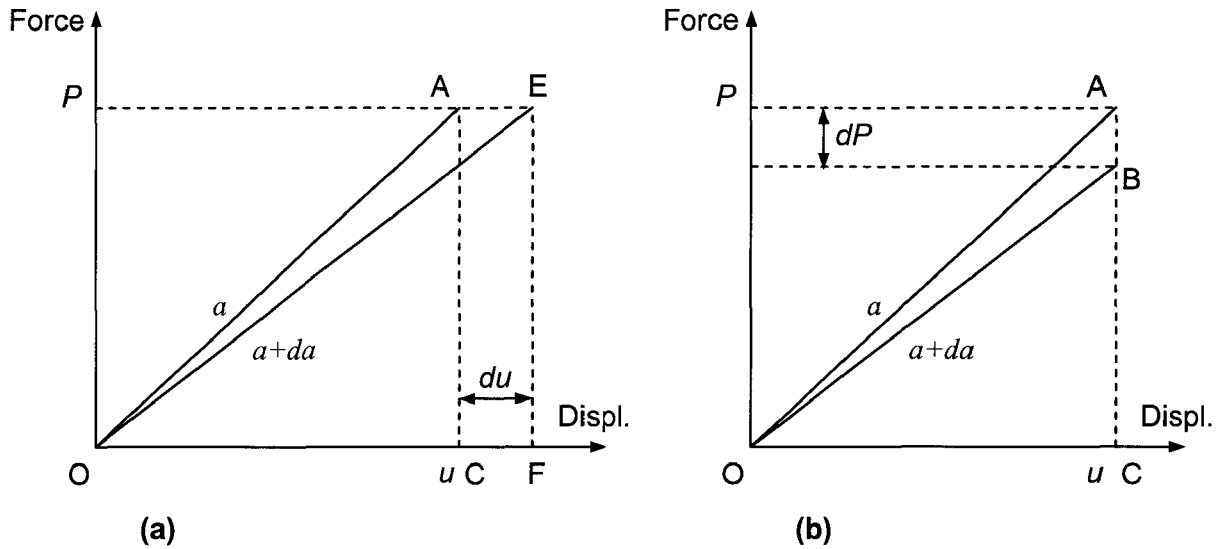
Fig. 8: Graphical representation of the energy release rate - Crack extension (a) under constant force; (b) under constant displacement

Considering the load-displacement diagram (Fig. 8a), the potential strain energy stored in the elastic body for a crack length a is equal to area of the triangle OAC, and to area OEF for a crack length $a+da$ respectively. During crack growth from a to $a+da$, U_E evolves from OAC to OEF and the elastic energy change dU_E is equal to area OAE. Besides, the work done by the external load is equivalent to area AEFC. Since area AEFC is twice OAE, the total mechanical energy change is equal to the area OAE.

Crack extension under constant displacement

The displacement stays constant, so that $du = 0$. The work done by the external load and the elastic strain energy change are:

$$\begin{cases} dU_A = -Pdu = 0 \\ dU_E = d\left(\frac{1}{2}\frac{u^2}{C}\right) = \frac{1}{2}u^2 d\left(\frac{1}{C}\right) = -\frac{1}{2}P^2 dC \end{cases}$$

Eq. 20

As evaluated for constant force in Eq. 19, the total mechanical energy change is:

$$dU_M = -\frac{1}{2}P^2 dC$$

Eq. 21

Graphically, the same procedure is following. The potential strain energy stored in the elastic body for a crack length a is unchanged and equal to area of the triangle OAC. However, in the case of a constant displacement, the load-displacement is represented by the line OB for a crack length $a+da$ and area OBC represents the elastic energy for a crack length $a+da$. The elastic energy variation dU_E is then equivalent to the surface OAB. The work of external

forces is here equal to zero as the displacement du = 0. Finally, the mechanical energy change is represented by surface OAB.

The assumption of constant loading (force or displacement) during crack extension is only a theoretical point of view and is only valid for short crack increment da. In this case, the surface OAB and OAE tends to have the same area, i.e. the total mechanical energy change is equal for both loading configurations.

2.2.3 Stress intensity factors

Field near the crack tip

As previously reported, the energy release rate approach consists in a global energetic description of a system. Based on stress and strain fields near the crack tip, the concept of stress intensity factors considers contrariwise the crack with a local approach within the context of LEFM.

Irwin [Irw54-57] examined in the 1950's the analytical solutions for stress and displacement fields around the tip of a slit-like plane crack in an ideal elastic continuum solid. The presence of a crack tip induces a singularity in the stress field near the crack tip. The solution suggested by Inglis [Ing13] for elastic material show that a theoretical infinite stress occurs at the crack tip. In order to properly describe the strain and stress fields, Irwin introduces the stress intensity factor K.

Consider an infinite plate containing a crack of length $2a$ through the thickness. Plane strain or plane stress conditions are observed. Stresses σ_∞ are applied in the y-direction on both extremities of the plate, as shown in Fig. 9, which consists in a pure opening mode of loading.
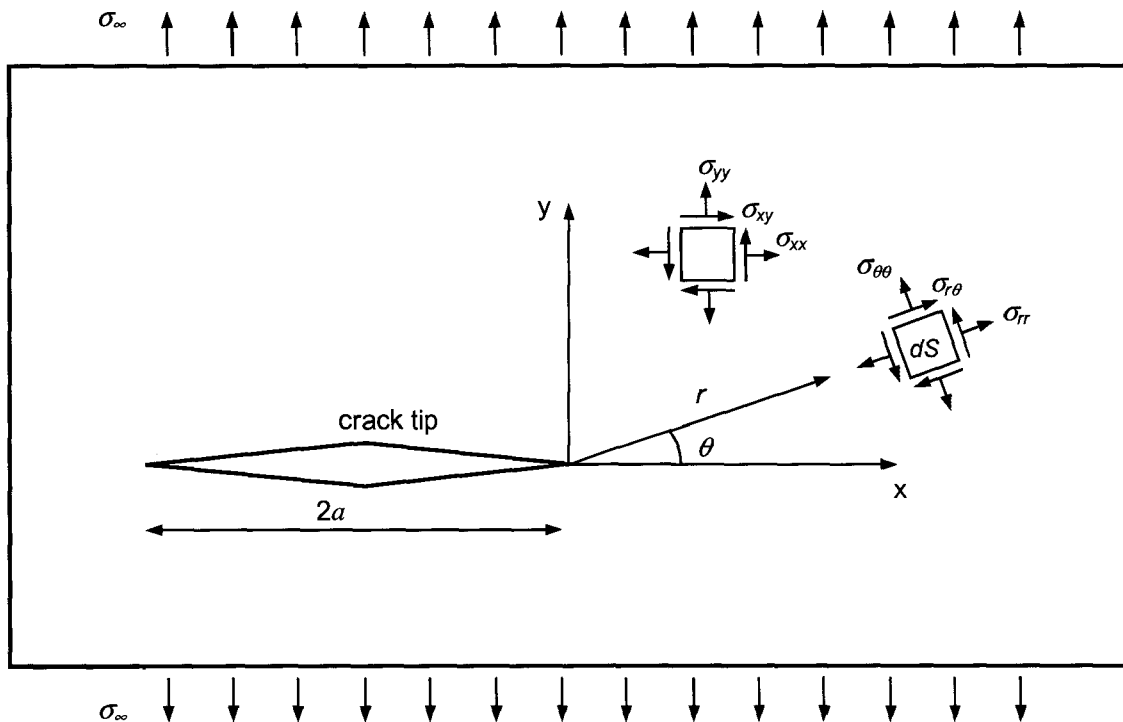
Fig. 9: Coordinate system and stresses in the near-tip region of a crack

Far from crack tip:

$$\begin{cases} \sigma_{xx}(r \to \infty) = 0 \\ \sigma_{yy}(r \to \infty) = \sigma_\infty \\ \sigma_{xy}(r \to \infty) = 0 \end{cases}$$ **Eq. 22**

However, near the crack tip, these conditions are not more valid. The stresses in the basic element dS, which has the dimensions dx and dy, can be expressed in the local cartesian (x, y), as in a local cylindrical (r, θ) coordinate system [Irw57]:

$$\begin{Bmatrix} \sigma_{xx} \\ \sigma_{yy} \\ \sigma_{xy} \end{Bmatrix} = \frac{K_I}{\sqrt{2\pi r}} \begin{Bmatrix} \cos(\theta/2)[1 - \sin(\theta/2)\sin(3\theta/2)] \\ \cos(\theta/2)[1 + \sin(\theta/2)\sin(3\theta/2)] \\ \sin(\theta/2)\cos(\theta/2)\cos(3\theta/2) \end{Bmatrix}$$

$$\begin{Bmatrix} \sigma_{rr} \\ \sigma_{\theta\theta} \\ \sigma_{r\theta} \end{Bmatrix} = \frac{K_I}{\sqrt{2\pi r}} \begin{Bmatrix} \cos(\theta/2)[1 + \sin^2(\theta/2)] \\ \cos(\theta/2)[1 - \sin^2(\theta/2)] \\ \sin(\theta/2)\cos^2(\theta/2) \end{Bmatrix}$$ **Eq. 23**

$$\sigma_{zz} = v'(\sigma_{xx} + \sigma_{yy}) = v'(\sigma_{rr} + \sigma_{\theta\theta})$$

$$\sigma_{xz} = \sigma_{yz} = \sigma_{rz} = \sigma_{\theta z} = 0$$

where $K_I = \sigma_\infty \sqrt{\pi a}$. The corresponding displacements are:

$$\begin{Bmatrix} u_x \\ u_y \end{Bmatrix} = \frac{K_I}{2E}\sqrt{\frac{r}{2\pi}} \begin{Bmatrix} (1+v)[(2\kappa-1)\cos(\theta/2) - \cos(3\theta/2)] \\ (1+v)[(2\kappa+1)\sin(\theta/2) - \sin(3\theta/2)] \end{Bmatrix}$$

$$\begin{Bmatrix} u_r \\ u_\theta \end{Bmatrix} = \frac{K_I}{2E}\sqrt{\frac{r}{2\pi}} \begin{Bmatrix} (1+v)[(2\kappa-1)\cos(\theta/2) - \cos(3\theta/2)] \\ (1+v)[-(2\kappa+1)\sin(\theta/2) + \sin(3\theta/2)] \end{Bmatrix}$$ **Eq. 24**

$$u_z = -v''z\frac{(\sigma_{xx} + \sigma_{yy})}{E} = -v''z\frac{(\sigma_{rr} + \sigma_{\theta\theta})}{E}$$

where $\kappa = 3 - 4v$, $\quad v'' = 0$ and $v' = v$ for plane strain

$\kappa = (3-v)/(1+v)$, $\quad v'' = v$ and $v' = 0$ for plane stress

In the real case of a finite plate, with a width W, Irwin shows that K_I can be explained as [Gro96]:

$$K_I = \sigma_\infty \sqrt{\pi a}\, f\!\left(\frac{a}{W}\right)$$ **Eq. 25**

The factor K_I is not dependent from localisation variables, such as r and θ, but only from the crack length a, from the plate width W and from the applied load σ_∞. A variation of the applied load direction returns similar results for pure mode II and III [Law93].

Westergaard [Wes39] and Williams [Wil52-57] propose to determine the stress field in the body with the help of the Airy stress function method, which gives an exact representation of the stress field for linear elastic material. The general solution is:

$$\sigma_{ij}(r,\theta) = \frac{C_I}{\sqrt{r}} f_{ij}^{I}(\theta) + \sum_{n=1}^{\infty} C_n \, r^{(n+1)/2} f_{ij}^{n}(\theta) \qquad \text{Eq. 26}$$

Far away from the crack tip ($r \to \infty$), the first term vanishes and the term with r^0 is equivalent to the applied stress σ_∞. In the vicinity of the crack tip ($r \to 0$), the higher order terms are negligible. Only the first term subsists, which is analogous to Eq. 23:

$$\sigma_{ij}(r,\theta) = \frac{C_I}{\sqrt{r}} f_{ij}^{I}(\theta) \quad \text{with} \quad C_I = \frac{K_I}{\sqrt{2\pi}} \qquad \text{Eq. 27}$$

From the exact expressions of stress field, a more general form of the stress intensity factors is:

$$\begin{Bmatrix} K_I \\ K_{II} \\ K_{III} \end{Bmatrix} = \lim_{r \to 0} \sqrt{2\pi r} \begin{Bmatrix} \sigma_{yy} \\ \sigma_{xy} \\ \sigma_{yz} \end{Bmatrix}_{\theta=0} \qquad \text{Eq. 28}$$

Stresses follow a power law at the distance r from the crack tip. A general formulation derives from a linear combination of the three modes. Stresses at a point in the vicinity of the crack tip and subjected to an arbitrary load are given by:

$$\sigma_{ij}(r,\theta) = \frac{1}{\sqrt{2\pi r}} \left(K_I f_{ij}^{I}(\theta) + K_{II} f_{ij}^{II}(\theta) + K_{III} f_{ij}^{III}(\theta) \right) \qquad \text{Eq. 29}$$

where f_{ij}^{k} is a dimensionless function, which is only dependent upon the angle θ, and which is related to each pure mode of loading and its stress intensity factor K_k. Eq. 29 shows that the relevant information from the elastic field is reduced to three parameters, the three K_k. As well, the expression for displacements takes a similar form.

Fracture toughness concept

Stress intensity factors are fracture mechanics parameters, which precisely describe the loading state near the crack tip. Moreover, stress intensity factors describe the singularity at the crack tip, unlike the classical stress distribution. Thus, this quantity is appropriate to be used as fracture criteria. Consider the case of a pure opening mode: a crack extension occurs, only if the stress intensity factor K_I reaches a specific material critical value K_{Ic}, whose name is fracture toughness K_{Ic}:

$$K_I = K_{Ic} \qquad \text{Eq. 30}$$

The energy balance concept, especially Eq. 7, consists in the formulation of a fracture criterion within a global approach of the system. Here, the fracture toughness concept furnishes an analogous expression, using a local fracture parameter K_I.

The fracture toughness K_{Ic} is a material parameter, as the Young's modulus or the Poisson's ratio. Established standards describe precisely the experimental process to evaluate the fracture toughness for different types of materials, like metals [A-399] or for polymers [A-5045, Esi01]. Generally, tests are performed on Compact Tension (CT) or on Single Edge Notched (SEN) specimens, as described later in section 4. As defined in Eq. 28, the fracture toughness has the dimensions of [stress].[length]$^{1/2}$. The usual units are MPa.m$^{1/2}$, but units like N.m$^{-3/2}$ or MPa.mm$^{1/2}$ are also suitable.

The fracture toughness concept was introduced for a pure Mode I, as the opening mode is the critical mode of crack propagation. Analogous formulations for pure mode II, respectively mode III of loading are available:

$$K_{II} = K_{IIc} \quad \text{or} \quad K_{III} = K_{IIIc} \qquad \text{Eq. 31}$$

The critical stress intensity factors K_{IIc} and K_{IIIc} can also be experimentally determined. With the help of adapted specimen geometries or modified applied loading [Rid83, Rich81, Erd63], pure sliding or tearing modes of loading are generated at the crack tip.

It should be noted that each K_i gives information on load conditions for the respective mode, but the total loading condition is not represented by a one-parameter variable, like a global stress intensity factor. However, an expression between the three modes can be formulated as fracture criterion, in the case of a mixed mode loading [Gro96]:

$$f(K_I, K_{II}, K_{III}) = 0 \qquad \text{Eq. 32}$$

K-dominance region

The region of application of LEFM is generally assimilated to the region of K-dominance, which is delimited by the annular region between the radii r_k and r_y. In fact, the radius r_k defines the zone for which the stress intensity factor K can be used to precisely determine the stress distribution near the crack tip. As seen in Eq. 28, the definition of the stress intensity factor is only valid in the vicinity of the crack tip ($r \to 0$).
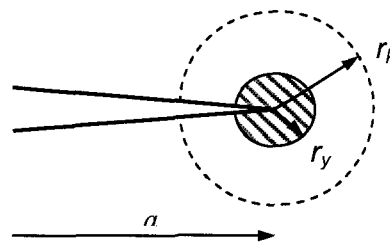
Fig. 10: K-dominance region

As previously explained, the radius r_y sets the limit of the small domain where inelastic deformations occur. An estimation of the radius r_y can be established using the definition of the stress intensity factor. For a crack under an opening loading condition, in the crack plane ($\theta = \pm \pi$), the stress field near the crack tip is:

$$\sigma_{yy} = \frac{K_I}{\sqrt{2\pi r}} \qquad \text{Eq. 33}$$

At the distance $r = r_y$, the stress σ_{yy} is approximated by the yield stress σ_y (see Fig. 3), and yields to an estimation of the process zone size:

$$r_y \approx \frac{1}{2\pi}\left(\frac{K_I}{\sigma_y}\right)^2$$

Eq. 34

In order to accurately determine the fracture toughness K_{Ic}, standards like the ASTM E399 [A-399] recommend that the plastic zone has to be 15 times smaller than the sample dimensions like the crack length a, ligament depth b or the thickness B.

$$a, b, B \geq 2.5\left(\frac{K_{Ic}}{\sigma_y}\right)^2$$

Eq. 35

This evaluation fixes the size requirements of the sample used during the test and delivers a condition for the test validity after measurement of K_{Ic}. For most brittle and high strength materials, this condition is easily satisfied and enables the use of the LEFM. However, in the case of low strength materials, this condition returns extreme large size for the specimen. In fact, the ratio fracture toughness-yield stress takes a higher value. All applications, where the size of the process zone is comparable with the crack length or other geometric dimensions, have to be investigated with the linear-plastic fracture mechanics.

Plane strain versus plane stress

Most of the classical solutions in fracture mechanics reduce the problem to two dimensions [And95], in which plane stress ($\sigma_{zz} = 0$) or plane strain ($\varepsilon_{zz} = 0$) state are assumed. In general, neither plane stress nor plane strain conditions describe the real loading in the vicinity of the crack tip: a three-dimensional stress/strain distribution has to be considered. Actually, stresses σ_{zz} are perpendicular to the outer surface and equal to zero, which corresponds to a plane stress condition at the free surface. On the other hands, plane strain conditions prevail in the inner part of the plate, so that stresses σ_{zz} evolve continuously from zero to the relative plane strain value in the centre of the plate, as seen in Fig. 11.
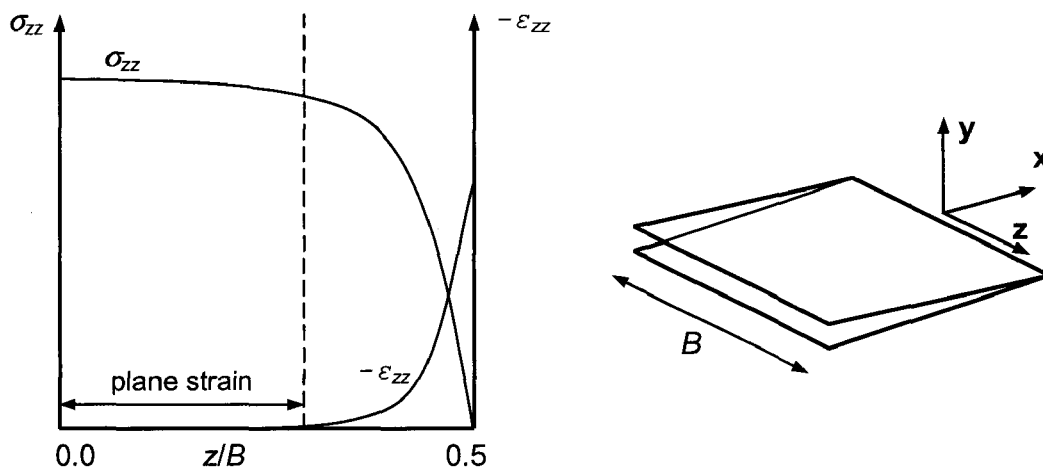
Fig. 11: Variation of transverse stress and strain through the thickness

The material in the interior is constrained, resulting in a triaxial stress state. Consequently, even if the plastic zone is very small ($r \gg r_y$), the size of the plastic zone gradually decreases from the free surface to the interior of the plate [Bro82], as described in Fig. 12:
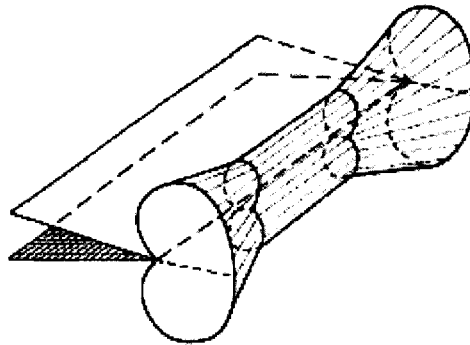
Fig. 12: Three-dimensional plastic zone [Bro82]

For $r_y \ll r \ll B$, the variation between plane strain and plane stress through the thickness may introduce an uncertainty in the determination of the critical stress intensity factor since it is related to the principal stresses. Fig. 13 shows that the fracture toughness value obtained in the case of a dominant plane strain condition is smaller than in the case of prevailing plane stress state. In general, the fracture mechanics is used as method to estimate the critical point at which the material will fail or to predict the lifetime of product. A conservative approach has the advantage to consider the worst case for the structure, so that the evaluation of the fracture toughness is performed on specimens, whose geometry optimally reproduces a plane strain condition along the crack front. In fact, the term fracture toughness K_{lc} is commonly employed in place of plane strain fracture toughness.
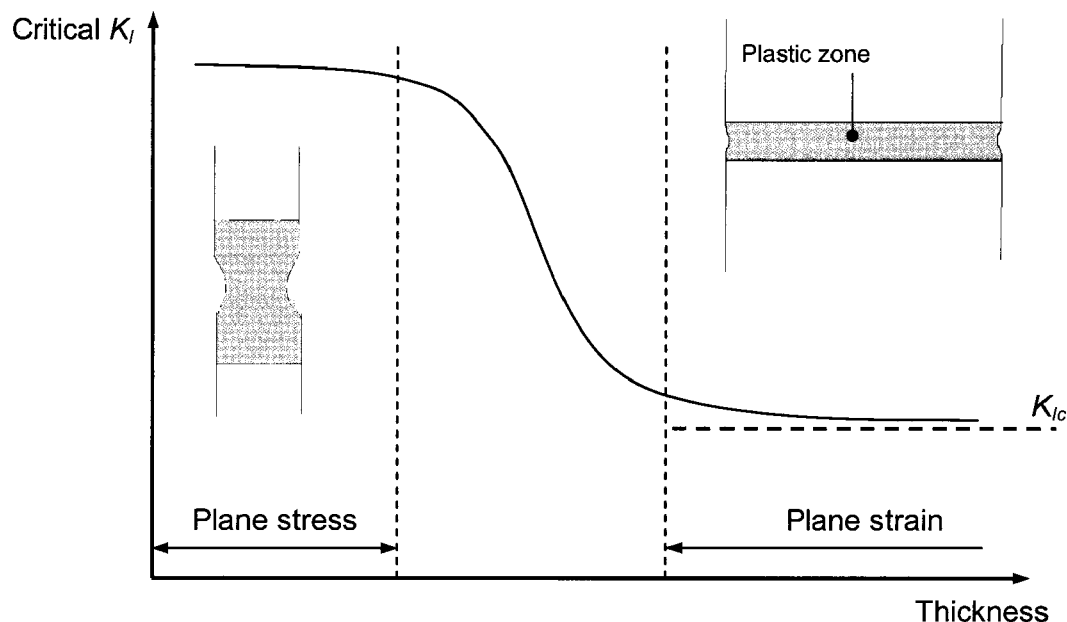
Fig. 13: Effect of specimen thickness on K_{lc}

Although a three-dimensional stress distribution exists in the vicinity of the crack tip, the reduction to a two-dimensional model provides a good approximation. In most cases, plane strain conditions are specified in numerical analysis in order to generate a conservative prediction. In the same way, large samples experimentally induce a plane strain dominancy, as the plane stress state is limited to the outer surfaces.

2.2.4 Relation between ERR and SIF

Within the context of LEFM, the energy release rate and the stress intensity factor are defined as crack propagation criteria. Although the first one is considered as a global and the second one as a local parameter, a relation between ERR and SIF exists.

Consider an infinite plate submitted to a pure opening mode of loading or mode I. The energy release rate G is defined as the amount of mechanical energy dU_M released for a virtual crack extension da, as described in Eq. 5. A crack propagation from a to $a+\Delta a$ is represented in Fig. 14.
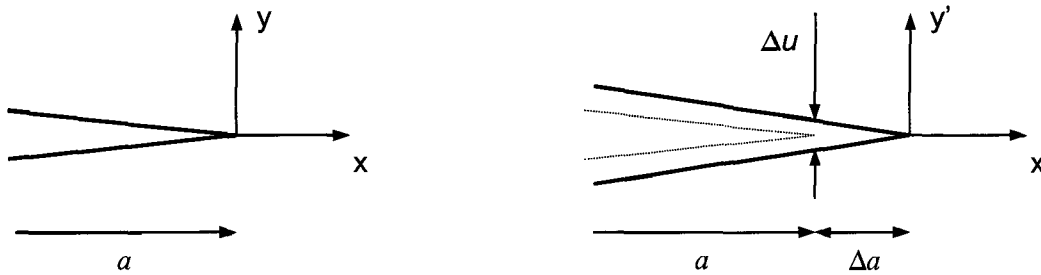
Fig. 14: Crack extension from a to $a+\Delta a$

During the crack extension, the stress at the crack tip σ_{yy} decreases from $\sigma_{yy}(x)$ to 0, while the crack tip opening displacement increases from 0 to $\Delta u(x')$. The amount of mechanical energy dU_M released is:

$$dU_M = -\int_0^B \int_0^{\Delta a} \frac{1}{2}\sigma_{yy}(x)\Delta u(x)\,dx\,dy \qquad \text{Eq. 36}$$

For mode I, Eq. 28 yields:

$$\sigma_{yy}(x) = \frac{K(a)}{\sqrt{2\pi x}} \qquad \text{at } \theta = 0 \qquad \text{Eq. 37}$$

As well for $\theta = \pm\pi$, displacements behind the crack tip are given by Eq. 24 and the opening displacement $\Delta u(x')$ is reduced to:

$$\Delta u(x') = \frac{8K(a+\Delta a)}{E'}\sqrt{\frac{-x'}{2\pi}} \qquad \text{with } x' < 0 \qquad \text{Eq. 38}$$

where E' is the effective Young's modulus with $E' = E/(1-v^2)$ for plane strain and $E' = E$ for plane stress state. Details about Δu can be found in chapter 2.2.6. The transposition from the coordinates (x', y') to the coordinates (x, y), yields:

$$\Delta u(x) = \frac{8K(a+\Delta a)}{E'}\sqrt{\frac{\Delta a - x}{2\pi}} \qquad \text{Eq. 39}$$

Substituting in the above equation, it leads to:

$$dU_M = -2B \frac{K(a)K(a+\Delta a)}{\pi E'} \int_0^{\Delta a} \sqrt{\frac{\Delta a - x}{x}} \, dx \qquad \text{Eq. 40}$$

The integral is equal to $\pi/2$, so that:

$$dU_M = -\frac{K(a)K(a+\Delta a)}{E'} B\Delta a \qquad \text{Eq. 41}$$

For a vanishing Δa, $K(a) \rightarrow K(a+\Delta a)$, yielding to the energy release rate:

$$G = -\frac{dU_M}{B\Delta a} = \frac{K^2}{E'} \qquad \text{Eq. 42}$$

The above expression is valid in the case of an opening mode of loading. The notation G_I is introduced as the component of the global energy release rate G due to a tensile loading (Mode I).

$$G_I = \frac{K_I^2}{E'} \qquad \text{Eq. 43}$$

As well, G_{II} is the component due to a sliding shear (Mode II) and G_{III} is due to a scissoring shear (Mode III). Due to the principle of superposition in LEFM, the global strain energy release rate G can be decomposed into the energy release rates for pure modes of loading (cf. Fig. 5):

$$G = G_I + G_{II} + G_{III} \qquad \text{Eq. 44}$$

In addition, the expression of the relation between stress intensity factors K_i and energy release rate G for linear elastic isotropic materials is suitable and yields:

$$G = \frac{\left(K_I^2 + K_{II}^2\right)}{E'} + \frac{1}{2\mu}K_{III}^2 \qquad \text{Eq. 45}$$

2.2.5   J-integral

Path-independency

The J-integral was introduced by Rice [Ric68] as supplementary global fracture criterion. Although the J-integral is equivalent to the energy release rate within the context of LEFM, it can also be used in EPFM as energetic fracture criterion [Gro96]. In fact, Rice extends the definition of the energy released during crack propagation to non-linear elastic material. With a non-linear elastic material behaviour, the strain-stress relation is not more linear and the relation $u = CP$ (Eq. 9) is also not more valid. The plastic behaviour of a material can sometimes be treated as a non-linear elastic behaviour. This representation is limited to problems in which unloading doesn't occur. Contrary to the stress-strain behaviour of a non-linear elastic material, plasticity corresponds to a non-reversible phenomenon and permanent deformations appear during unloading phases. Regarding this limitation, the J-integral is assimilated as a fracture criterion applicable to plastic fracture. The J-integral approach is valid for cracks in linear as in non-linear elastic material. In this work, the J-integral is considered as an energy-based parameter for LEFM.

Consider a homogeneous body of linear elastic material free of body forces and subjected to a two-dimensional deformation field. As seen in Fig. 15, Γ is a closed contour enclosing the area A. The traction vector T is defined according to the outward normal n along Γ and represents the average force per unit area exerted by the rest of the body on the closed contour Γ, with $T = \sigma_{ij}n$. The displacement vector is noted u and ds is an element of arc length along Γ.
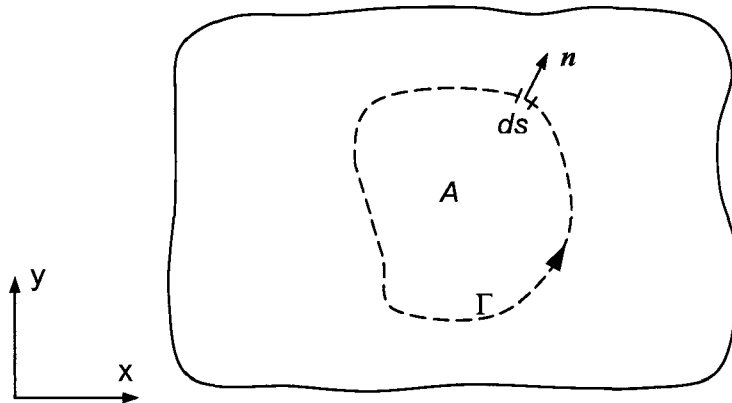
Fig. 15: Definition of the closed contour Γ

The outward normal n and the arc length ds along Γ are related by:

$$ds = \sqrt{dx^2 + dy^2} \quad \text{and} \quad n = \begin{Bmatrix} n_1 \\ n_2 \end{Bmatrix} = \begin{Bmatrix} \dfrac{dy}{ds} \\ -\dfrac{dx}{ds} \end{Bmatrix} \qquad \text{Eq. 46}$$

The strain energy per unit volume or strain energy density W is given by:

$$W = \frac{dU_E}{dV} = W(x,y) = W(\varepsilon) = \int_0^\varepsilon \sigma_{ij} d\varepsilon_{ij} \qquad \text{Eq. 47}$$

where $\varepsilon = [\varepsilon_{ij}]$ is the infinitesimal strain tensor. The integral I_Γ is integrated in a contraclockwise sense along the closed path Γ:

$$I_\Gamma = \int_\Gamma \left(W dy - T \frac{\partial u}{\partial x} ds \right) \qquad \text{Eq. 48}$$

It can be shown with the help of the divergence theorem that the integral I_Γ is equal to zero along any closed contour [Ric68].

Rice's J-integral

Now, consider a similar homogeneous body of linear elastic material. As shown in Fig. 16, a notch with a rounded tip is introduced in the current body. The global solution proposed by Rice [Ric68] for a notch is valid for a slit too, since a straight crack can be considered as a notch with a radius equal to zero.
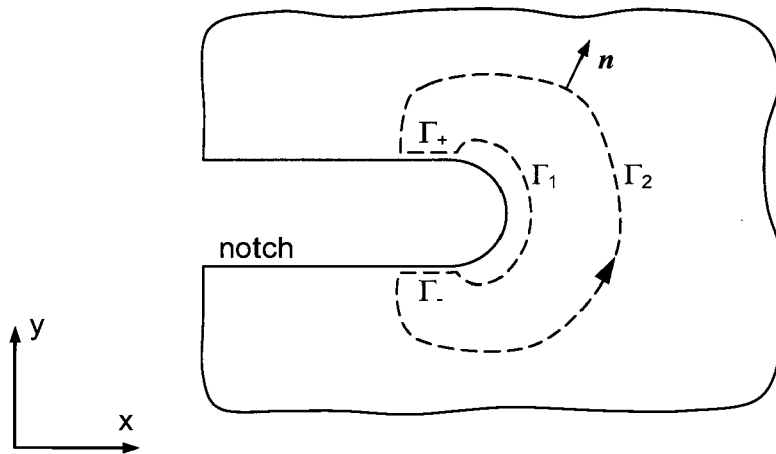
Fig. 16: Two-dimensional body containing a notch

The contour Γ is here split into Γ_1, Γ_-, Γ_2 and Γ_+. The paths Γ_- and Γ_+ are parallel to the upper and lower faces of the crack tip, when Γ_1 and Γ_2 surround the notch extremity. The region enclosed by Γ contains no singularity, so that:

$$I_\Gamma = \int_{\Gamma_1 + \Gamma_- + \Gamma_2 + \Gamma_+} \left(W dy - T \frac{\partial u}{\partial x} ds \right) = 0 \qquad \text{Eq. 49}$$

The crack surfaces are traction free, so that $T = 0$ and $dy = 0$ along the paths Γ_- and Γ_+. Consequently, the related integral $I_{\Gamma+}$ and $I_{\Gamma-}$ vanishes. From the equation Eq. 49 yields:

$$\int_{\Gamma_2} \left(W dy - T \frac{\partial u}{\partial x} ds \right) = - \int_{\Gamma_1} (...) = \int_{\Gamma_1 -} (...) \qquad \text{Eq. 50}$$

Γ_1- follows the same pathway as Γ_1, but the direction of integration is reversed for Γ_1-. The paths Γ_1- and Γ_2 are contraclockwise oriented. The J-integral is defined by:

$$J = \int_\Gamma \left(W dy - T \frac{\partial u}{\partial x} ds \right) \qquad \text{Eq. 51}$$

where Γ is any path starting on the lower side of the notch face and finishing at the upper side, like Γ_1- and Γ_2. As demonstrated by Eq. 50, the J-integral is path-independent.
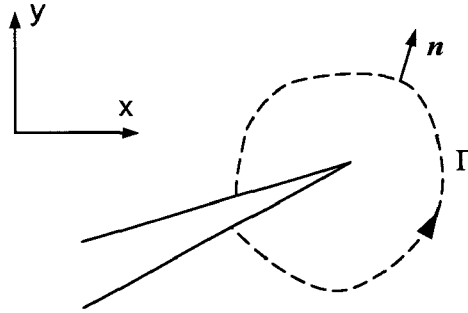
Fig. 17: J-integral contour for a straight crack

Rice [Ric68] noticed that J-integral is the rate of change of potential energy and is equivalent to the energy release rate G for a linear elastic body.

$$\text{in LEFM,} \quad J = G \qquad \qquad \textbf{Eq. 52}$$

J-integral vector

The previous conventional definition of the J-integral can be considered as the first component of a vector $J^T = \{J_1, J_2\}$. Knowles and Sternberg [KnS72] proved that both coordinates are also path-independent. For two dimensional cases, in the coordinate system (x_1, x_2) at the crack tip (see Fig. 18), integrals J_1 and J_2 are:

$$J_1 = \int_\Gamma \left(W\,dx_2 - T\frac{\partial u}{\partial x_1}\,ds \right)$$

$$J_2 = \int_\Gamma \left(W\,dx_1 - T\frac{\partial u}{\partial x_2}\,ds \right) \qquad \textbf{Eq. 53}$$

From the definition of n derives a general formulation of the components J_k:

$$J_k = \int_\Gamma \left(W\,n_k - n_i\sigma_{ij}\frac{\partial u_j}{\partial x_k} \right)ds \qquad \textbf{Eq. 54}$$

Within the context of LEFM, the parity between J-integral and energy release rate G was demonstrated by Rice [Ric68], as presented in Eq. 52. It leads to a relation between the J-integral components and the stress intensity factors:

$$J_1 = \frac{\left(K_I^2 + K_{II}^2\right)}{E'}$$

$$J_2 = -\frac{2K_I\,K_{II}}{E'} \qquad \textbf{Eq. 55}$$

with E' is the effective Young's modulus with $E'=E/(1-v^2)$ for plane strain and $E'=E$ for plane stress state. The values J_1 and J_2 correspond to the energy release rates for crack extensions parallel and perpendicular to the crack, respectively.

Domain integral method

In the context of quasi-static analysis, an alternative form of the J-integral components [And95] is defined in two dimensions as:

$$J_k = \lim_{\Gamma_1 \to 0} \int_{\Gamma_1} \left(W\, n_k - n_i \sigma_{ij} \frac{\partial u_j}{\partial x_k} \right) ds \qquad\qquad \textbf{Eq. 56}$$

This equation is available for all types of materials, as it comes from an energy balance approach. If the path Γ_1 passes through an elastic zone, then the J-integral is defined as path-independent. However, if the path Γ_1 is within the plastic zone at the crack tip, the J-integral will be path-dependent.

This mathematical definition is not appropriate for an experimental or numerical evaluation of the J-integral, since the stresses and strains inside a vanishing path Γ_1 can not be accurately determined. From this remark, Shih et al. [Shi86] extend the contour along the crack surfaces and around the crack tip to form a closed contour $\Gamma_0 = \Gamma_1 + \Gamma_- + \Gamma_2 + \Gamma_+$ around the area A with outward normal m, as shown in Fig. 18.

The vector n is the normal to the relative contour, pointing away from the crack tip, so that the vector $m^T = \{m_1, m_2\}$ is defined by: $m = n$ on Γ_2 and $m = -n$ on Γ_1. On Γ_- and Γ_+, the components of m are $m_1 = 0$ and $m_2 = \pm 1$.
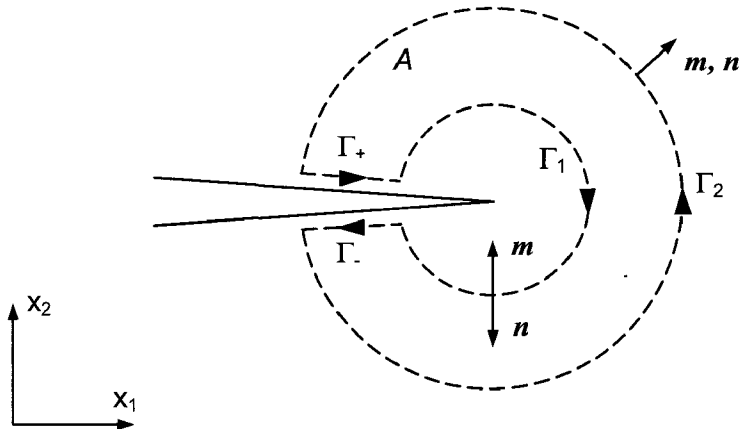
Fig. 18: Closed contour Γ_0 around the crack tip

Let v be a unit vector in the direction of crack advance and let q be a weighting vector, which is continuous within A. The vector $q^T = \{q_1, q_2\}$ is defined by $q = v$ on Γ_1 and has the magnitude $\sqrt{qq} = 0$ on Γ_2. On Γ_- and Γ_+, the norm $\sqrt{qq}$ varies continuously from 0 to 1.

It yields:

$$J_k = \oint_{\Gamma_0} m_i \left(\sigma_{ij} \frac{\partial u_j}{\partial x_k} - W \delta_{ik} \right) q_k \, ds - \int_{\Gamma_+ + \Gamma_-} \left(t_i \frac{\partial u_j}{\partial x_1} \right) q_k \, ds \qquad \text{Eq. 57}$$

where $t_i = m_i \sigma_{ij}$ represents the surface traction on the crack faces Γ_- and Γ_+ and δ_{ik} is the Kronecker's delta. The divergence theorem enables to convert the closed line integral into a domain integral:

$$J_k = \int_A \frac{\partial}{\partial x_i} \left[\left(\sigma_{ij} \frac{\partial u_j}{\partial x_k} - W \delta_{ik} \right) q_k \right] dA - \int_{\Gamma_+ + \Gamma_-} \left(t_i \frac{\partial u_j}{\partial x_1} \right) q_k \, ds \qquad \text{Eq. 58}$$

The integrand I of the domain integral can be written [Aba05]:

$$
\begin{aligned}
I &= \frac{\partial}{\partial x_i} \left(\sigma_{ij} \frac{\partial u_j}{\partial x_k} q_k - W q_i \right) \\
&= \frac{\partial \sigma_{ij}}{\partial x_i} \frac{\partial u_j}{\partial x_k} q_k + \sigma_{ij} \frac{\partial^2 u_j}{\partial x_i \partial x_k} q_k + \sigma_{ij} \frac{\partial u_j}{\partial x_k} \frac{\partial q_k}{\partial x_i} - \frac{\partial W}{\partial x_i} q_i - W \frac{\partial q_i}{\partial x_i} \qquad \text{Eq. 59} \\
&= -f_j \frac{\partial u_j}{\partial x_k} q_k + \sigma_{ij} \frac{\partial \varepsilon_{ij}}{\partial x_k} q_k + \sigma_{ij} \frac{\partial u_j}{\partial x_k} \frac{\partial q_k}{\partial x_i} - \frac{\partial W}{\partial x_i} q_i - W \frac{\partial q_i}{\partial x_i}
\end{aligned}
$$

where $f_j = \partial \sigma_{ij} / \partial x_i$ are the body forces per unit volume.

If the concept of the equivalent elastic material is adopted, the strain energy density can be expressed as a function of the mechanical strain. In fact, the global strain $\varepsilon_{ij} = \varepsilon_{ij}^m + \varepsilon_{ij}^{th}$ is divided into thermal and mechanical strain, so that:

$$\frac{\partial W}{\partial x_i} = \frac{\partial W}{\partial \varepsilon_{ij}^m} \frac{\partial \varepsilon_{ij}^m}{\partial x_i} = \sigma_{ij} \left(\frac{\partial \varepsilon_{ij}}{\partial x_i} - \frac{\partial \varepsilon_{ij}^{th}}{\partial x_i} \right) \qquad \text{Eq. 60}$$

Finally, the J-integral is defined by:

$$J_k = \int_A \left[\sigma_{ij} \frac{\partial u_j}{\partial x_k} \frac{\partial q_k}{\partial x_i} - f_j \frac{\partial u_j}{\partial x_k} q_k - W \frac{\partial q_i}{\partial x_i} + \sigma_{ij} \frac{\partial \varepsilon_{ij}^{th}}{\partial x_i} q_k \right] dA - \int_{\Gamma_+ + \Gamma_-} \left(t_i \frac{\partial u_j}{\partial x_1} \right) q_k \, ds \qquad \text{Eq. 61}$$

The second term of the equation represents the effect of the surface traction on the crack faces Γ_- and Γ_+. In the case of crack surfaces free of traction, the second term vanishes. Moreover, if the system considered is free of body forces and free of temperature field, the terms with f_j and ε_{ij}^{th} are equal to zero. An equivalent formulation of Eq. 51 follows for $k = 1$:

$$J = J_1 = \int_A \left[\left(\sigma_{ij} \frac{\partial u_j}{\partial x_1} - W \delta_{1i} \right) \frac{\partial q}{\partial x_i} \right] dA \qquad \text{Eq. 62}$$

3D generalisation

The J-integral concept can be generalised to three dimensions by considering a tubular surface S enclosing the crack front (see Fig. 19).
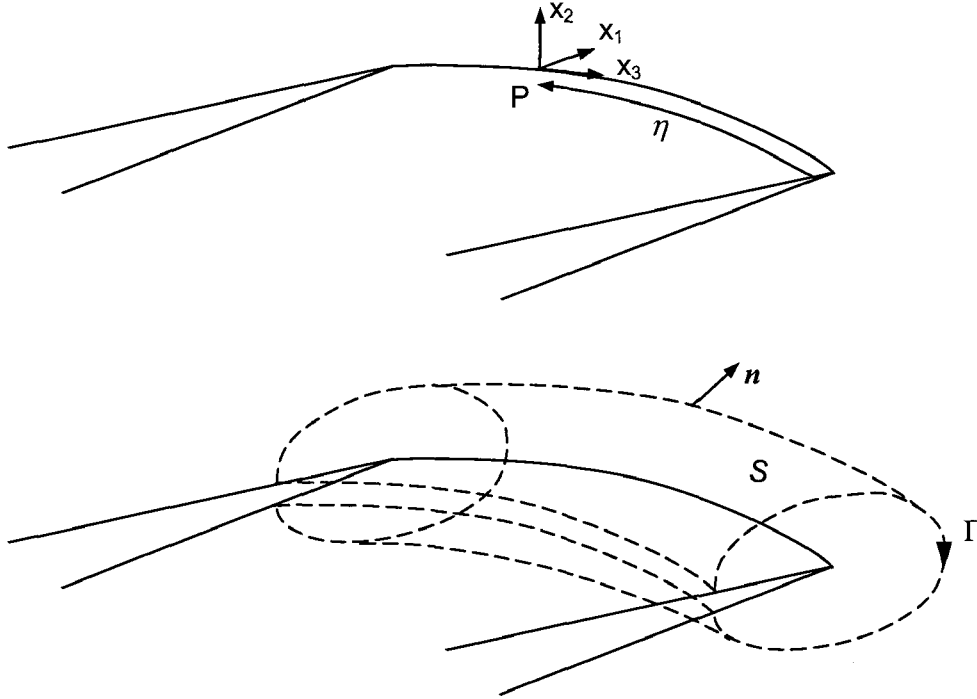
Fig. 19: J-integral in 3D: local coordinate system and closed surface

The local plane of crack propagation (x_1, x_3) and the local normal to the plane of crack x_2 are defined at the point P, whose position along the crack front is referred by the arc length η. The crack has a length L, such that η varies between 0 and L. At the point P, a local two-dimensional J-integral can be evaluated, which is path-independent on any contour in the plane (x_1, x_2). This integral is named point-wise J-integral $J(\eta)$:

$$J_k(\eta) = \lim_{\Gamma \to 0} \int_\Gamma \left(W\, n_k - n_i \sigma_{ij} \frac{\partial u_j}{\partial x_k} \right) ds \qquad \textbf{Eq. 63}$$

For a virtual crack advance $\lambda(\eta)$ in the plane of a three-dimensional crack [Aba05], the J-integral is given by:

$$J_k^{3D} = \int_L J_k(\eta)\lambda(\eta)d\eta = \lim_{\Gamma \to 0} \int_S \left(W\, n_k - n_i \sigma_{ij} \frac{\partial u_j}{\partial x_k} \right)\lambda(\eta)dS \qquad \textbf{Eq. 64}$$

where the surface of integration is $dS = d\eta ds$. The virtual crack advance $\lambda(\eta)$ is the three-dimensional equivalent of the two-dimensional amplitude of the vector v. As well, the divergence theorem enables the conversion of a closed surface integral into a volume integral.

Let consider a system free of body forces and free of temperature fields and in which crack surfaces are free of traction. Within the context of LEFM, the parity between J-integral and

energy release rate G was demonstrated by Rice [Ric68], as presented in Eq. 52. It leads to a relation between the J-integral components and the stress intensity factors:

$$\begin{cases} K_I = \dfrac{1}{2}\sqrt{E'}\left(\sqrt{J_1 - J_2 - J_3} + \sqrt{J_1 + J_2 - J_3}\right) \\[2mm] K_{II} = \dfrac{1}{2}\sqrt{E'}\left(\sqrt{J_1 - J_2 - J_3} - \sqrt{J_1 + J_2 - J_3}\right) \\[2mm] K_{III} = \sqrt{2\mu J_3} \end{cases}$$

Eq. 65

$$\text{with } E' = E\left[\frac{1}{1-v^2} + \frac{v}{1+v}\frac{\varepsilon_{33}}{\varepsilon_{11} + \varepsilon_{22}}\right]$$

In the case of $\varepsilon_{33} = 0$, then J_3 vanishes and these expressions are reduced to the previous equations find for a two-dimensional body (see Eq. 55).

2.2.6 Crack tip opening displacement

An experimental concept

The development of the crack tip opening displacement (CTOD) was motivated by concrete and experimental applications. Wells [Wel65] considers that the crack propagation occurs for ductile materials, when the material at the crack tip exceeds a maximum permissible plastic strain. Wells proposes to quantify this value by measuring the crack tip opening displacement, which is directly related to the strain distribution behind the crack tip. The crack will propagate, if the critical value of crack opening displacement is reached. In the case of small scale yielding (SSY) conditions, the plastic zone is small and the plastic deformation can be considered as a perturbation in the linear elastic solutions (cf. chapter 2.1.3). Consequently, the CTOD is here considered as a local criterion in the context of LEFM.

Irwin's model

As described in the Fig. 3, Irwin introduced a simple model to describe the strain/stress distribution [Irw58], where yielding limits the stresses over a small region at the crack tip. The plastic zone is defined by the radius r_y. Outside the plastic zone, the material has an elastic behaviour.
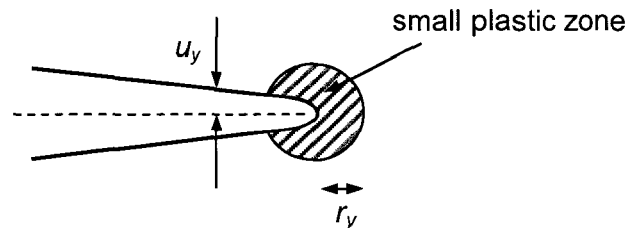
Fig. 20: CTOD definition using Irwin's plastic zone model

In the case of SSY conditions, displacements are approximated by the elastic solutions. In the case of a pure mode I loading:

$$u_y = \frac{K_I}{2E}\sqrt{\frac{r}{2\pi}}(1+v)[(2\kappa+1)\sin(\theta/2)-\sin(3\theta/2)] \qquad \text{Eq. 66}$$

where $\kappa = 3 - 4v$ for plane strain

$\kappa = (3-v)/(1+v)$ for plane stress

For $\theta = \pm \pi$ on the crack surfaces, displacements behind the crack tip are reduced to:

$$CTOD = 2u_y = 2\frac{K_I}{E}\sqrt{\frac{r}{2\pi}}(1+v)(\kappa+1) \qquad \text{Eq. 67}$$

$$CTOD = 8\frac{K_I}{E'}\sqrt{\frac{r}{2\pi}} \qquad \text{Eq. 68}$$

The Irwin's plastic zone correction gives an approximation of the radius r_y (see Eq. 34):

$$r_y \approx \frac{1}{2\pi}\left(\frac{K_I}{\sigma_y}\right)^2 \qquad\qquad \textbf{Eq. 69}$$

So that, at the distance r_y, the crack tip opening displacement can be approximated by:

$$CTOD \approx \frac{4}{\pi}\frac{K_I^2}{E'\sigma_y} \qquad\qquad \textbf{Eq. 70}$$

It can easily be demonstrated that this criterion is equivalent to the K_{Ic} and R criteria in the case of LEFM [Gro96].

Dugdale's Model

Dugdale [Dug60] proposes a different model, which integrates the plasticity phenomenon in the crack definition. The plasticity is interpreted as a force, which maintains the crack closed. For this, an effective crack length is introduced, which is longer than the physical crack. The following definition is valid for LEFM, only if the small scale yielding condition is verified, i.e. only if a small plastic zone exists at the crack tip.

Let consider a crack in an infinite plate under a mode I loading. The physical crack has a length $2a$, whereas the effective crack length is $2c$, where $c = a + p$. As presented in Fig. 45, a constant yielding stress σ_y is applied over p.
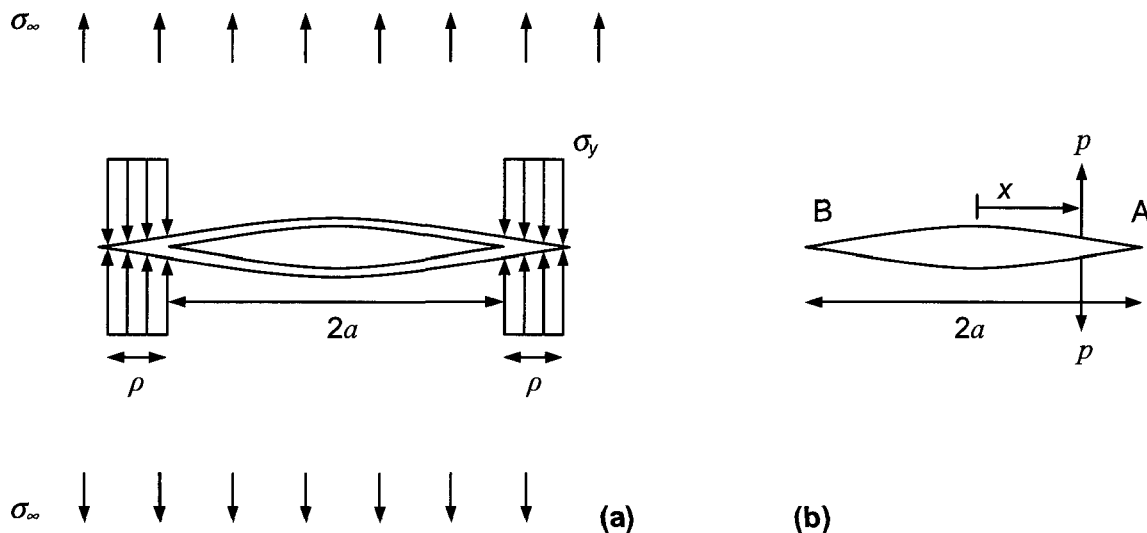
Fig. 21: a) Dugdale's plastic zone model b) Wedge forces

The yield stress over p on the crack surfaces tends to close the crack. Consequently, a negative stress intensity factor K_p results from this effect. The size of p is chosen, so that the singularity disappears: the sum of stress intensity factors is equal to zero.

$$K_\sigma = K_p \qquad\qquad \textbf{Eq. 71}$$

The stress intensity due to wedge forces p at the position x, as represented in Fig. 21, is given:

$$K_A = \frac{p}{\sqrt{\pi a}} \sqrt{\frac{a+x}{a-x}} \quad \text{and} \quad K_B = \frac{p}{\sqrt{\pi a}} \sqrt{\frac{a-x}{a+x}} \qquad \text{Eq. 72}$$

Assuming $dp = \sigma_y \, dx$, the stress intensity factor K_p is

$$K_p = \frac{\sigma_y}{\sqrt{\pi a}} \int_a^{a+\rho} \left(\sqrt{\frac{a+x}{a-x}} + \sqrt{\frac{a-x}{a+x}} \right) dx \qquad \text{Eq. 73}$$

$$K_p = 2\sigma_y \sqrt{\frac{a+\rho}{\pi}} \arccos\left(\frac{a}{a+\rho} \right) \qquad \text{Eq. 74}$$

As defined previously, $K_\sigma = \sigma_\infty \sqrt{\pi}\sqrt{a+\rho}$. Eq. 71 yields an expression of ρ:

$$\frac{a}{a+\rho} = \cos\left(\frac{\pi}{2} \frac{\sigma_\infty}{\sigma_y} \right) \qquad \text{Eq. 75}$$

Using Taylor's expression, the length ρ can be approximated by:

$$\rho \approx \frac{\pi^2}{8} \left(\frac{\sigma_\infty}{\sigma_y} \right)^2 a \qquad \text{Eq. 76}$$

A solution for the crack opening behind crack tip derives from the Dugdale's model [Dug60]:

$$u_y(x) = \frac{2}{\pi} \frac{\sigma_y}{E'} a \left\{ \ln\left(\frac{\sqrt{c^2 - a^2} + \sqrt{c^2 - x^2}}{\sqrt{c^2 - a^2} - \sqrt{c^2 - x^2}} \right) + \frac{x}{a} \ln\left(\frac{x\sqrt{c^2 - a^2} + a\sqrt{c^2 - x^2}}{x\sqrt{c^2 - a^2} - a\sqrt{c^2 - x^2}} \right) \right\} \qquad \text{Eq. 77}$$

For $x = a$, the expression is reduced to:

$$u_y(a) = \frac{4}{\pi} \frac{\sigma_y}{E'} a \ln\left(\frac{c}{a} \right) \qquad \text{Eq. 78}$$

Combined with Eq. 75, the CTOD is expressed by:

$$CTOD = 2u_y = \frac{8}{\pi} \frac{\sigma_y}{E'} a \ln\left(\sec \frac{\pi}{2} \frac{\sigma_\infty}{\sigma_y} \right) \qquad \text{Eq. 79}$$

And asymptotically, when $\sigma_\infty \ll \sigma_y$

$$CTOD \approx \frac{K_I^2}{E'\sigma_y} \qquad \text{Eq. 80}$$

The Irwin's and Dugdale's plastic zone model return the same approximation for the crack tip opening displacement.

2.3 Mixed-mode loading

2.3.1 Direction of crack propagation

Within the context of LEFM, the evaluation of stress intensity factors and/or of energy release rate is first used to determine if a crack will propagate. More than fracture criteria, they establish the basis for the computation of the crack growth direction. In the case of mixed mode loading, a crack will attempt to seek an orientation that minimises the shear loading [Bit96]. Resultant crack paths are generally curved.

From an experimental point of view, the material data for fracture mechanics are generally limited to fracture toughness K_{Ic}. In most studies, the material resistance to crack growth under mode I loading conditions is compared to the local maximum stress. Thus, mode II with the critical stress intensity factor K_{IIc} (and resp. mode III with K_{IIIc}) is seldom investigated. However, parameters to predict the direction of crack growth are required to perform numerical crack propagation analysis.

Schöllmann [Sch01] recently propose a three-dimensional approach to evaluate the direction of crack propagation. Nevertheless, mode III is rarely preponderant and therefore not taken into account in most cases [Erd63, Bro82, Gro96]. For planar problems, Richard outlines in [Rich85] an overview of criteria to predict the direction of crack propagation. This study concentrates on three criteria:

- the maximum tangential stress ($\sigma_{\theta max}$) [Erd63]
- the maximum potential energy release rate (G_{max}) [Hus74]
- the minimum strain energy density (S_{min}) [Sih74]

The next sections give an overview of all these criteria. Other criteria, which are based either on the J-integral [Yu82], on the principal strain [Fis81] or on the multiaxial distributions of stress and strain [Fis82], gives analogous predictions [Rich85].

2.3.2 Maximal principal stress criterion

In three dimensions, the complete description of the crack growth direction involves two propagation angles, which are described in Fig. 22. The kinking angle θ_0 characterises the relative proportion of mode I and mode II, when the twisting angle ψ_0 illustrates the rotation due to a mode III loading.
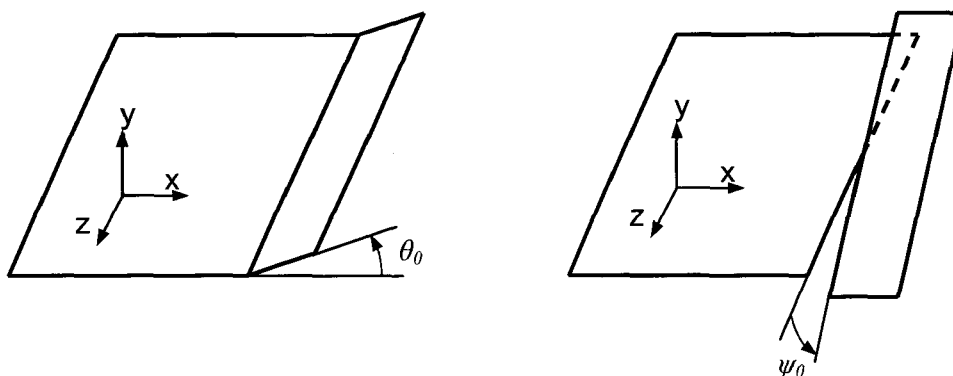
Fig. 22: Crack propagation angles θ_0 and ψ_0

The criterion proposed by Schöllmann [Sch01] and Dhondt [Dho01] is actually an extension to 3D of the maximum tangential stress (MTS) criterion from Erdogan and Sih [Erd63]. The MTS criterion explains that for planar mixed mode situation the crack propagates perpendicular to the direction of the maximum tangential stress $\sigma_{\theta max}$. In the case of a three-dimensional loading, the criterion may also take into account the stress field variation along the z-axis (see Fig. 23*). It postulates that the crack extension appears perpendicular to the direction of the maximum principal normal stress σ_1', which is given by:

$$\sigma_1' = \frac{\sigma_\theta + \sigma_z}{2} + \frac{1}{2}\sqrt{(\sigma_\theta - \sigma_z)^2 + 4\tau_{\theta z}^2} \qquad \text{Eq. 81}$$

with

$$\sigma_\theta = \frac{K_I}{4\sqrt{2\pi r}}\left\{3\cos\left(\frac{\theta}{2}\right)+\cos\left(\frac{3\theta}{2}\right)\right\} - \frac{3K_{II}}{4\sqrt{2\pi r}}\left\{\sin\left(\frac{\theta}{2}\right)+\sin\left(\frac{3\theta}{2}\right)\right\}$$

$$\sigma_z = v(\sigma_r + \sigma_\theta) = \frac{8v}{4\sqrt{2\pi r}}\left\{K_I\cos\left(\frac{\theta}{2}\right)-K_{II}\sin\left(\frac{\theta}{2}\right)\right\} \qquad \text{Eq. 82}$$

$$\tau_{\theta z} = \frac{K_{III}}{\sqrt{2\pi r}}\cos\left(\frac{\theta}{2}\right)$$
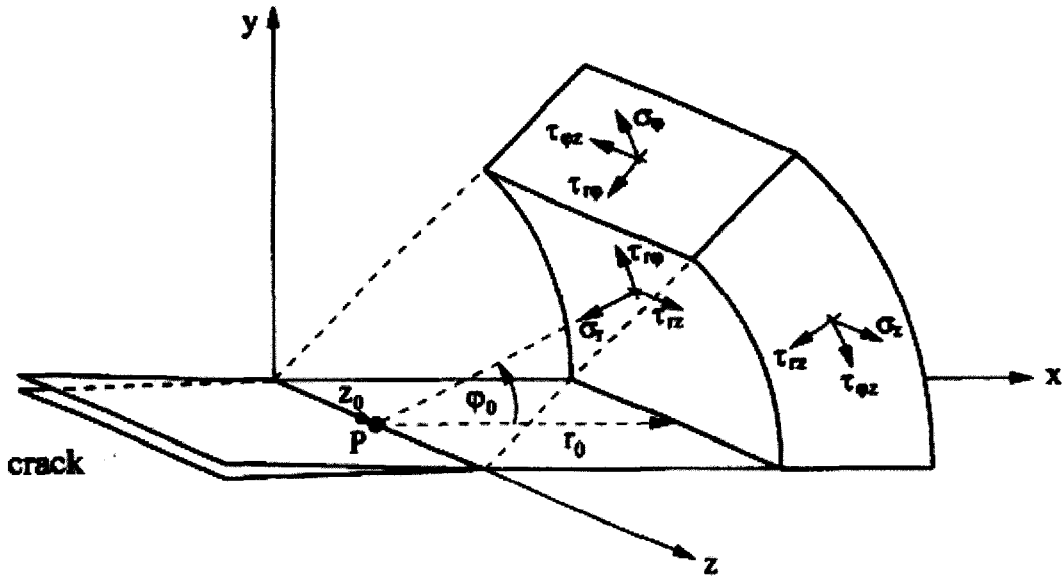
Fig. 23*: Cylindrical coordinate system at a 3D crack front [SFR01]

So the kinking angle θ_0 can be calculated by the partial derivatives:

$$\frac{\partial \sigma_1'}{\partial \theta} = 0 \quad \text{and} \quad \frac{\partial^2 \sigma_1'}{\partial \theta^2} < 0 \qquad \text{Eq. 83}$$

Then, the twisting angle ψ_0 is given by:

$$\psi_0 = \frac{1}{2}\arctan\left(\frac{2\tau_{\theta z}(\theta_0)}{\sigma_\theta(\theta_0)-\sigma_z(\theta_0)}\right) \qquad \text{Eq. 84}$$

* Note: in Fig. 23, angle θ_0 is represented by the angle φ_0 and θ by φ respectively

The solution θ_0 of Eq. 83 can be numerically evaluated under the form:

$$-6K_I \tan\left(\frac{\theta_0}{2}\right) - K_{II}\left[6 - 12\tan^2\left(\frac{\theta_0}{2}\right)\right]$$

$$+ \left\{\left[4K_I - 12K_{II}\tan\left(\frac{\theta_0}{2}\right)\right]\left[-6K_I\tan\left(\frac{\theta_0}{2}\right) - K_{II}\left[6 - 12\tan^2\left(\frac{\theta_0}{2}\right)\right]\right]\right.$$

$$\left. - 32K_{III}^2\tan\left(\frac{\theta_0}{2}\right)\left[1 + \tan^2\left(\frac{\theta_0}{2}\right)\right]^2\right\} \qquad\qquad \textbf{Eq. 85}$$

$$\cdot\left\{\left[4K_I - 12K_{II}\tan\left(\frac{\theta_0}{2}\right)\right]^2 + 64K_{III}^2\left[1 + \tan^2\left(\frac{\theta_0}{2}\right)\right]^2\right\}^{-1/2} = 0$$

As depicted in Eq. 85, the angle θ_0 is not directly dependent on the absolute value of the stress intensity factors, but from the relative proportion of K_I, K_{II} or K_{III}. The introduction of the normalised stress intensity factors (Eq. 86) gives the possibility to represent the solution of Eq. 83 and Eq. 84.

$$K_I^n = \frac{K_I}{K_I + |K_{II}| + |K_{III}|}$$

$$K_{II}^n = \frac{K_{II}}{K_I + |K_{II}| + |K_{III}|} \qquad\qquad \textbf{Eq. 86}$$

$$K_{III}^n = \frac{K_{III}}{K_I + |K_{II}| + |K_{III}|}$$
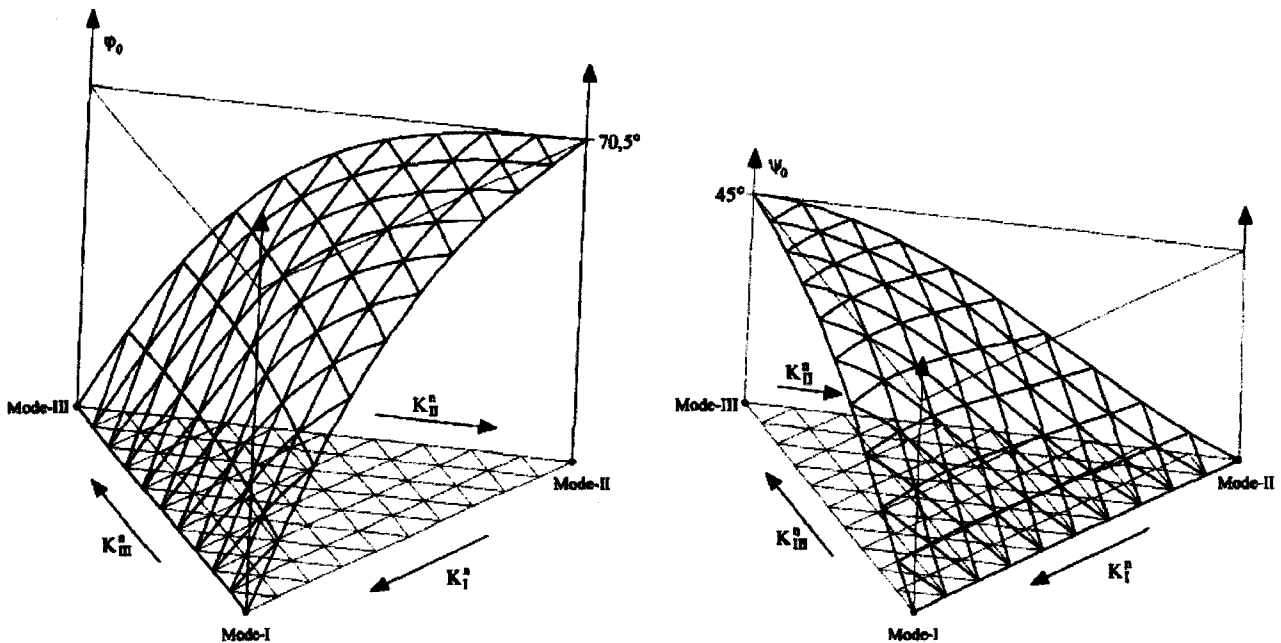
Fig. 24*: Angle θ_0 and ψ_0 depending on mixed-mode ratio [SFR01]

* Note: in Fig. 24, angle θ_0 is represented by the angle φ_0

2.3.3　Maximum tangential stress criterion

If mode III is not preponderant, the problem is reduced to a mode I - mode II configuration. The simplest formulation was suggested by Erdogan and Sih [Erd63]. It proposes that the crack propagates in the direction that maximizes the tangential stress σ_θ. At the crack tip, the analytical solutions for the stress field are:

$$\sigma_r = \frac{1}{\sqrt{2\pi r}}\cos\left(\frac{\theta}{2}\right)\left[K_I\left\{1+\sin^2\left(\frac{\theta}{2}\right)\right\}+K_{II}\left\{\frac{3}{2}\sin\theta-2\tan\left(\frac{\theta}{2}\right)\right\}\right]$$

$$\sigma_\theta = \frac{1}{\sqrt{2\pi r}}\cos\left(\frac{\theta}{2}\right)\left[K_I\cos^2\left(\frac{\theta}{2}\right)-\frac{3}{2}K_{II}\sin\theta\right] \qquad \textbf{Eq. 87}$$

$$\sigma_{r\theta} = \frac{1}{\sqrt{2\pi r}}\cos\left(\frac{\theta}{2}\right)\left[\frac{1}{2}K_I\sin\theta+\frac{1}{2}K_{II}\left(3\cos\theta-1\right)\right]$$

These expressions are valid both for plane stress and plane strain states. The maximum tangential stress $\sigma_{\theta max}$ criterion (MTS) assumes that crack propagation takes place on a plane perpendicular to the direction in which σ_θ is maximum and in which the shear stress component is equal to zero $\sigma_{r\theta} = 0$. From this assumption, the expression of σ_θ and $\sigma_{r\theta}$ compose a system of equation, whose trivial solution is $\theta = \pm\pi$ (from $\cos(\theta/2) = 0$) and a non-trivial solution:

$$K_I\sin\theta+K_{II}\left(3\cos\theta-1\right)=0 \qquad \textbf{Eq. 88}$$

The solutions of this equation depend on the relative proportion of mode I and mode II. For pure mode I loading, $K_{II} = 0$ so that Eq. 88 is reduced to $K_I\sin\theta = 0$ and leads to $\theta = 0$. Experimental tests based on ASTM norms [A-399, A-5045] and performed on CT specimen confirm this value. For pure mode II loading, $K_I = 0$, so that Eq. 88 is reduced to $K_{II}\left(3\cos\theta-1\right)=0$ and leads to $\theta = \pm70.53°$. The mixed-mode intermediary values are found by rewriting Eq. 88:

$$2K_I\sin\frac{\theta}{2}\cos\frac{\theta}{2}+3K_{II}\left(\cos^2\frac{\theta}{2}-\sin^2\frac{\theta}{2}\right)-K_{II}\left(\cos^2\frac{\theta}{2}+\sin^2\frac{\theta}{2}\right)=0 \quad \textbf{Eq. 89}$$

It is essential to notice that $\theta = \pm\pi$ is a trivial solution, which corresponds to the free surface of the crack. With $\theta \neq\pm\pi$ and $\theta \neq 0$, Eq. 89 yields:

$$2K_{II}\tan^2\frac{\theta}{2}-K_I\tan\frac{\theta}{2}-K_{II}=0 \qquad \textbf{Eq. 90}$$

The resulting Eq. 90 is a quadratic equation in $\tan\left(\theta/2\right)$, which solutions are:

$$\theta = 2\arctan\left(\frac{1}{4}\left[\frac{K_I}{K_{II}}\pm\sqrt{\left(\frac{K_I}{K_{II}}\right)^2+8}\right]\right) \qquad \textbf{Eq. 91}$$

Another formulation for the MTS criterion is given by [Aba05]:

$$\theta = \pm \arccos\left(\frac{3K_{II}^2 + \sqrt{K_I^4 + 8K_I^2 K_{II}^2}}{K_I^2 + 9K_{II}^2}\right)$$

Eq. 92

If $\theta < 0$, the term K_{II} takes a positive value ($K_{II} > 0$). Inversely, if $\theta > 0$ then $K_{II} < 0$.

As presented in Eq. 91, it is generally possible to express the direction of crack propagation as a function of the ratio K_{II}/K_I. Considering the diagram $\theta = f(K_{II}/K_I)$, a pure mode II can only be represented by an asymptotic line. In fact, a pure mode II of loading corresponds to $K_{II}/K_I \rightarrow \infty$. The introduction of the factor $K_{II}/(K_I + K_{II})$ facilitates the representation of the crack extension angle, as seen in Fig. 25. A pure mode I corresponds to $K_{II}/(K_I + K_{II}) = 0$ and a pure mode II corresponds to $K_{II}/(K_I + K_{II}) = 1$.
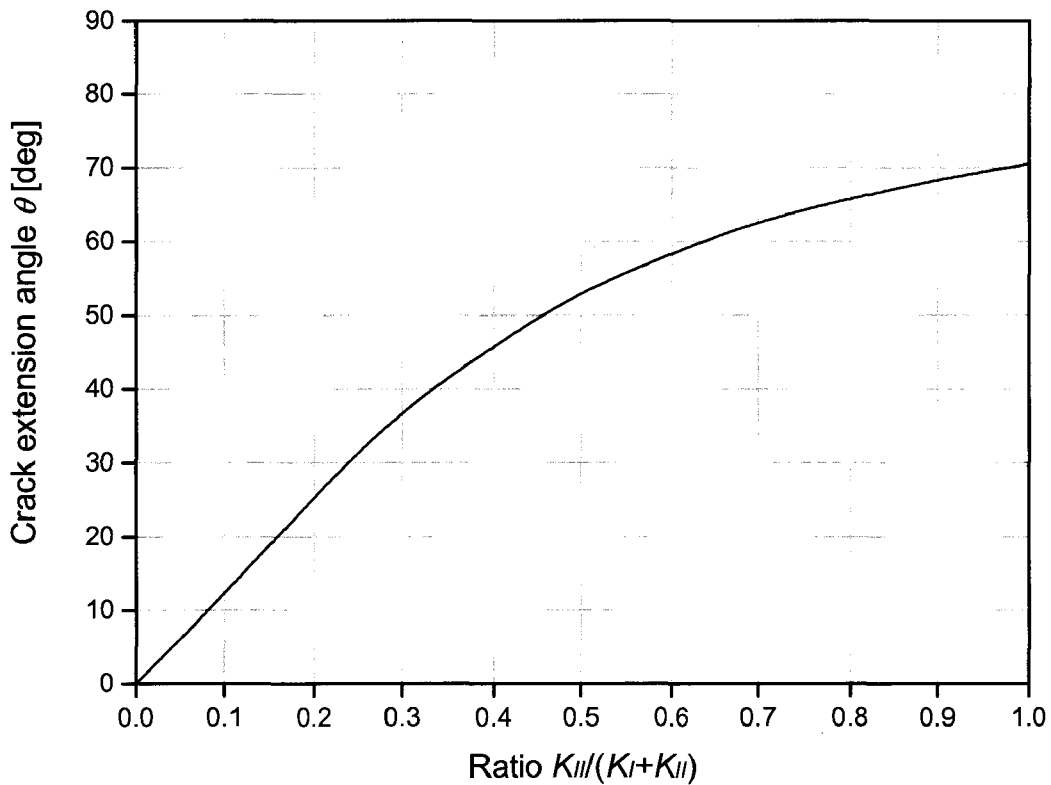
Fig. 25: MTS criterion - crack propagation angle $\theta = f(K_{II}/(K_I + K_{II}))$

2.3.4 Maximum energy release rate criterion

In their original model, Erdogan and Sih [Erd63] report that:
"If we accept the Griffith (energy) theory as the valid criterion which explains the crack growth [...], then the crack will grow in the direction along which the elastic energy release per unit crack extension will be maximum and the crack will start to grow when this energy reaches a critical value [or G(δ, θ) = G$_c$]. The application of the Griffith theory in this form requires the calculation of the elastic energy release rate per unit crack extension in cases for which the crack extension is not colinear with the crack itself. At the moment, the mathematical difficulties [for the evaluation of G(δ, θ)] seems to be insurmountable."

"conventional" stress intensity factors
$[K_I ; K_{II}]$

"angular" stress intensity factors
$[K_I(\theta) ; K_{II}(\theta)]$
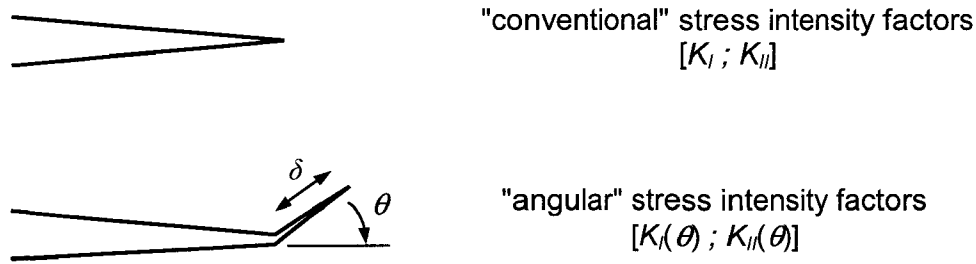
Fig. 26: Conventional and kinking fracture approach

Hussain, Pu and Underwood [Hus74] suggest solving this problem through an approach of infinitesimal kinking fracture. Contrary to the conventional definition, where the crack extension is assumed to occur in the plane of the original crack, the fracture is composed by a main branch and a propagation branch at an arbitrary angle θ, see Fig. 26. Consequently, the expression of the usual stress intensity factors K_I and K_{II} is not more valid. The definition of the "angular" stress intensity factors $K_I(\theta)$ and $K_{II}(\theta)$ near the crack tip, as a function of the "conventional" stress intensity factors K_I and K_{II} is:

$$\begin{Bmatrix} K_I(\theta) \\ K_{II}(\theta) \end{Bmatrix} = \left(\frac{4}{3 + \cos^2(\theta)} \right) \left(\frac{1 - \dfrac{\theta}{\pi}}{1 + \dfrac{\theta}{\pi}} \right)^{\frac{\theta}{2\pi}} \begin{Bmatrix} K_I \cos(\theta) + \dfrac{3}{2} K_{II} \sin(\theta) \\ K_{II} \cos(\theta) - \dfrac{1}{2} K_I \sin(\theta) \end{Bmatrix} \qquad \textbf{Eq. 93}$$

If the crack grows along its initial plane, the Griffith-Irwin energy release rate under mixed mode loading is identified as a function of the "conventional" stress intensity factors:

$$G = \frac{1}{E'}\left(K_I^2 + K_{II}^2 \right) \qquad \textbf{Eq. 94}$$

The deflected crack is considered as infinitesimal and tends to a collinear crack growth, as the propagation branch vanishes. As a result, a general expression of the energy release rate for an arbitrary angle of crack extension is formulated with the help of the "angular" stress intensity factors:

$$G(\theta) = \frac{1}{E'}\left(K_I^2(\theta) + K_{II}^2(\theta) \right) \qquad \textbf{Eq. 95}$$

The combination of the equation Eq. 93 and Eq. 95 leads to:

$$G(\theta) = \frac{4}{E'} \left(\frac{1}{3 + \cos^2 \theta} \right)^2 \left(\frac{1 - \dfrac{\theta}{\pi}}{1 + \dfrac{\theta}{\pi}} \right)^{\frac{\theta}{\pi}}$$

Eq. 96

$$\left\{ \left(1 + 3\cos^2 \theta \right) K_I^2 + 8 \sin \theta \cos \theta K_I K_{II} + \left(9 - 5\cos^2 \theta \right) K_{II}^2 \right\}$$

When θ is equal to zero, it should be remarked that Eq. 93 and Eq. 96 return the "conventional" expression for G, K_I or K_{II}.

The hypothesis of this criterion is that the crack will propagate in the direction along which the elastic energy release $G(\theta)$ is maximal. Thus, the angle of crack propagation verifies:

$$\frac{\partial G(\theta)}{\partial \theta} = 0 \quad \text{and} \quad \frac{\partial^2 G(\theta)}{\partial \theta^2} < 0$$

Eq. 97

The derivation of $G(\theta)$ enables the resolution of this equation system for various ratios K_{II} / K_I. Particularly, for a pure mode I, it is found that $\theta = 0$, i.e. the crack will propagate in the same plan as the crack tip. For a pure mode II ($K_I = 0$), Hussain [Hus74] shown that propagation occur in the direction $\theta = \pm 75.2°$. Finally, the curve $\theta = f(K_{II}/(K_I + K_{II}))$ is represented in Fig. 27.
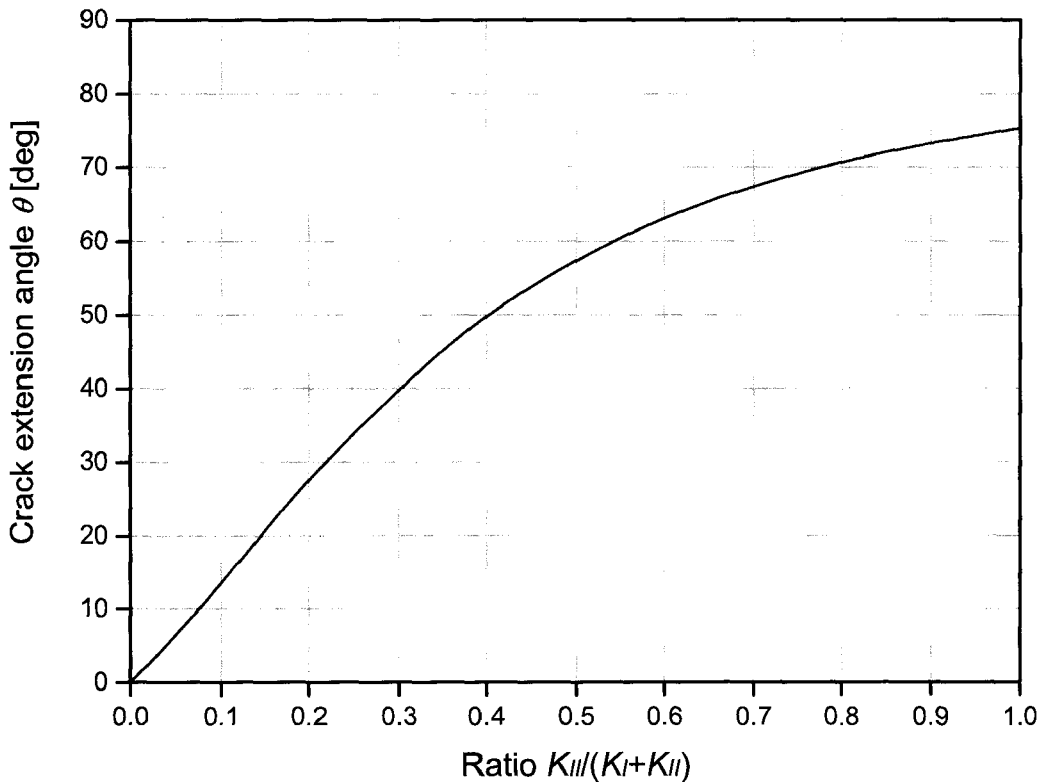
Fig. 27: MERR criterion - crack propagation angle $\theta = f(K_{II}/(K_I + K_{II}))$

2.3.5 Minimum strain energy density criterion

The strain energy density corresponds to the work dW required to deform a body per volume unit dV. The criterion proposed by Sih [Sih74] declares that crack growth occurs in the direction of minimum strain energy density (MSED), which means that crack propagates along path of minimum deformation. This concept firstly requires the expression of the strain energy around crack tip, in function of an arbitrary orientation θ:

$$\frac{dW}{dV} = \frac{1}{2E}\left(\sigma_x^2 + \sigma_y^2 + \sigma_z^2\right) - \frac{v}{E}\left(\sigma_x\sigma_y + \sigma_y\sigma_z + \sigma_z\sigma_x\right) + \frac{1}{2\mu}\left(\sigma_{xy}^2 + \sigma_{yz}^2 + \sigma_{zx}^2\right) \qquad \textbf{Eq. 98}$$

where μ is the shear modulus. From the principle of superposition, the strain energy can be determined for the mixed mode stress field at a crack by adding $\sigma_x = \sigma_{xI} + \sigma_{xII}$, etc ... where σ_{xI} and σ_{xII} are the stresses due to constitutive modes I and II:

$$\sigma_{ij} = \frac{K_I}{\sqrt{2\pi r}} f_{Iij}(\theta) + \frac{K_{II}}{\sqrt{2\pi r}} f_{IIij}(\theta) \qquad \textbf{Eq. 99}$$

Sih introduced the strain energy density factor S, corresponding to the magnitude of the energy field around crack tip, as:

$$\frac{dW}{dV} = \frac{S(\theta)}{r} = \frac{1}{\pi r}\left(a_{11}K_I^2 + 2a_{12}K_I K_{II} + a_{22}K_{II}^2\right) \qquad \textbf{Eq. 100}$$

where

$$a_{11} = \frac{1}{16\mu}\left[(1 + \cos\theta)(\kappa - \cos\theta)\right]$$

$$a_{12} = \frac{1}{16\mu}\sin\theta\left[2\cos\theta - \kappa + 1\right] \qquad \textbf{Eq. 101}$$

$$a_{22} = \frac{1}{16\mu}\left[(\kappa + 1)(1 - \cos\theta) + (1 + \cos\theta)(3\cos\theta - 1)\right]$$

with $\kappa = 3 - 4v$ for plane strain
$\kappa = (3 - v)/(1 + v)$ for plane stress

The magnitude of the energy field depends on θ through the coefficients a_{ij}. Hence, it gives a description of the local energy density on any radial plane intersecting the crack tip. The criterion is based on the hypothesis that fracture takes place in the direction along which the strain energy density reaches a minimum amplitude:

$$\frac{\partial S(\theta)}{\partial \theta} = 0 \quad \text{and} \quad \frac{\partial^2 S(\theta)}{\partial \theta^2} > 0 \qquad \textbf{Eq. 102}$$

For pure mode I ($K_{II} = 0$), it is found that $\theta = 0°$. For pure mode II ($K_I = 0$), it is found that:

$$\theta = \pm\arccos\left(\frac{(\kappa - 1)}{6}\right) \qquad \textbf{Eq. 103}$$

The MSED criterion strongly depends on the material parameter v. The direction of crack propagation θ can be predicted for a pure mode II using Eq. 103. Estimated values varies between $\theta = \pm 70.5°$ to $\theta = \pm 90.0°$ for v included between 0.0 and 0.5, as seen in Tab. 1

	MSED criterion (plane strain assumption)						
	$v = 0.0$	$v = 0.1$	$v = 0.2$	$v = 0.3$	$v = 1/3$	$v = 0.4$	$v \approx 0.5$
Pure mode II	70.53°	74.53°	78.46°	82.34°	83.62°	86.18°	90.00°

Tab. 1: MSED criterion - Extension angle under pure Mode II

In this study, materials have Poisson's ratio included between 0.2 and 0.4 at ambient temperature. Fig. 28 illustrated the influence of the Poisson's ratio for the MSED criterion.
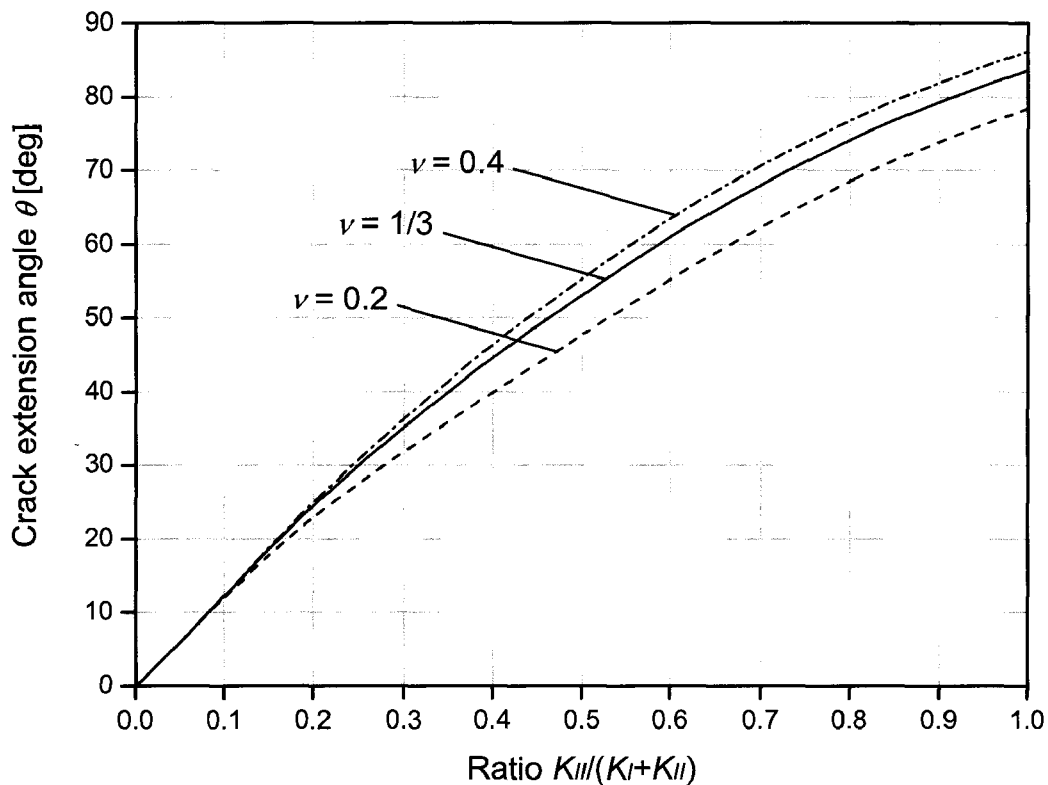
Fig. 28: MSED criterion - crack propagation angle $\theta = f(K_{II}/(K_I + K_{II}))$

2.3.6 Comparison of crack growth direction criteria

In the case of the MTS and MSED criterion, the Irwin's formulation (Eq. 87 and Eq. 99) is used to describe the stress intensity factors in a cylindrical coordinate system. These expressions are valid as r becomes indefinitely small. A critical distance r_0 should be defined as the point of evaluation of σ_θ and S. Whereas this may raise some theoretical questions with regard to the model, it is assume that the critical distance is the same for all angles [Erd63, Sih74, Rich85]. Under this assumption, results are independent of the choice for r_0 as seen in Eq. 91 or Eq. 103.

In the case of the MTS criterion, the angle of crack extension can be expressed as a simple function of the stress intensity factors K_I and K_{II} (Eq. 91). On the opposite, the MSED criterion presents a complex form which depends on the material parameter v. A comparison

between MTS, MERR and MSED criteria is shown in Fig. 29. Only the case of plane strain and for $v = 1/3$ is represented for the MSED criterion.
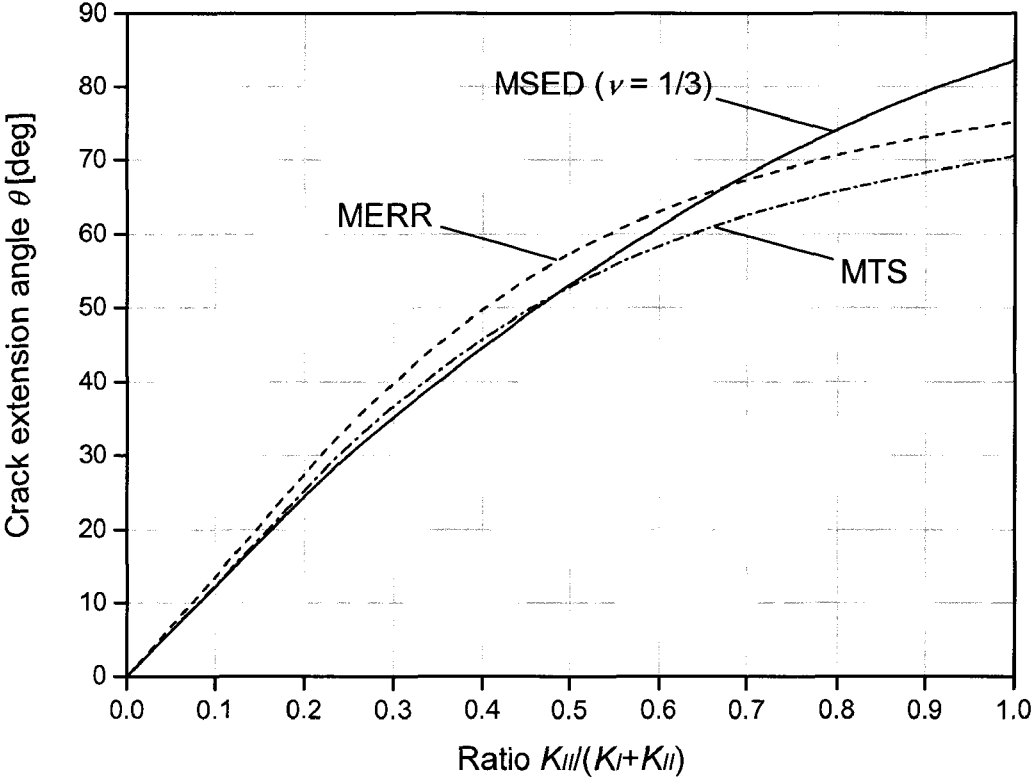
Fig. 29: Comparison between the MTS, MERR, and MSED criteria

Tab. 2 regroups specific values predicted by MTS, MERR, and MSED criteria. In this study, materials have Poisson's ratio included between 0.2 and 0.4 at ambient temperature. For pure mode I, the criteria furnish an extension angle of 0°, independently of applied criteria and of the Poisson's ratio, as experimentally observed. For plane strain conditions, $v = 1/3$ and $K_{II} = K_I$, the MTS and MSED criteria estimate the same angle of crack propagation $\theta = \pm 53.13°$. For pure mode II, the predicted angle of crack growth θ lies in the range $\pm 70.53°$ and $\pm 86.18°$.

| | MTS criterion | MERR criterion | MSED criterion | | |
			$v = 0.2$	$v = 1/3$	$v = 0.4$
Pure mode I	0°	0°	0°	0°	0°
Ratio $K_{II}/K_I = 1$	53.13°	57.33°	47.70°	53.13°	55.37°
Pure mode II	70.53°	75.23°	78.46°	83.62°	86.18°

Tab. 2: Extreme values for MTS, MERR, and MSED criteria

Fig. 30 indicates that for small ratios of K_{II} / K_I, the three criteria have similar trends. The influence of Poisson's ratio for MSED criterion is negligible for small ratio $K_{II} / (K_I + K_{II})$. Taking MTS as reference criterion, the variation between criteria for extension angles between 0° and 15° is less than 5%.
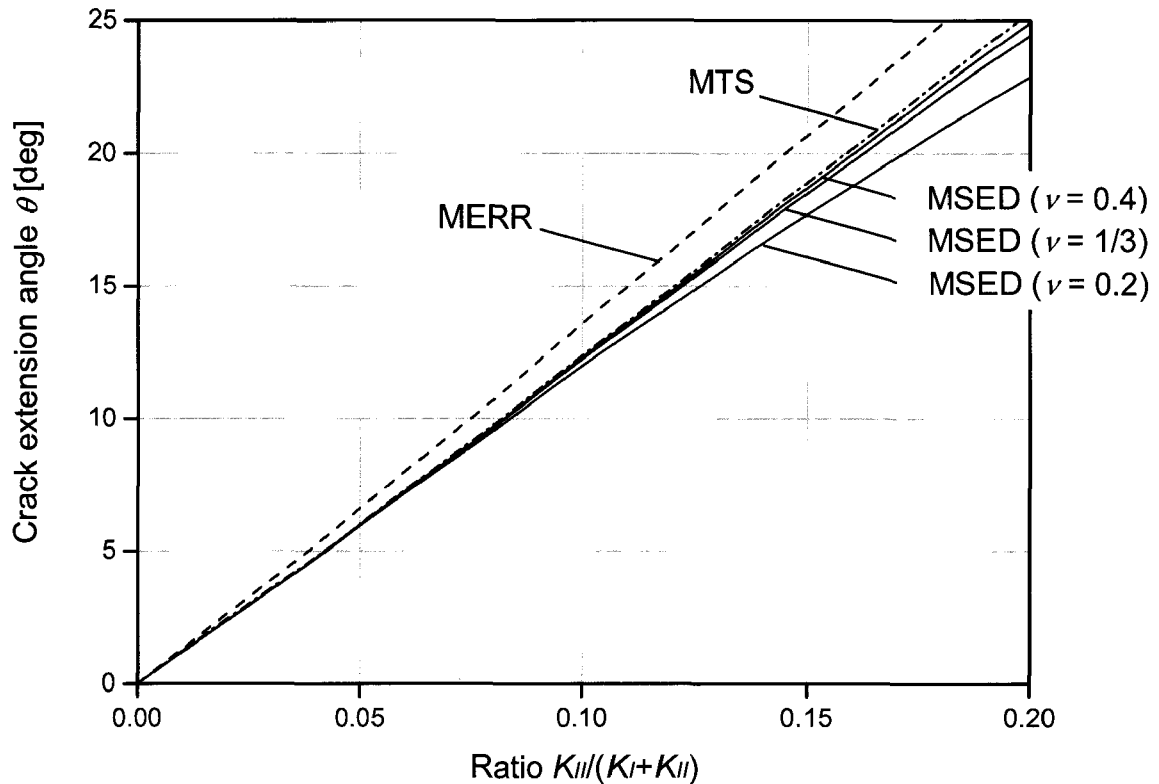
Fig. 30: MTS, MERR, MSED criteria for small ratios K_{II} / K_I

For a specified material, any theoretical assumption enables to define the most appropriate criterion to predict the direction of crack growth. Consequently, an experimental investigation is required. Experimental results are compared with the analytical solutions. For example, Broek [Bro76] presented experimental results for aluminium alloys. The crack growth direction was in accordance with the MTS criterion. Erdogan [Erd63] and Richard [Rich85] have worked with Plexiglas material (PMMA) and showed that experimental results agree very well with the MERR criterion.

Once the criterion is defined, the crack extension direction can be established for complex geometries or extreme loading conditions with the help of simulation. Actually, numerical software packages can evaluate the relative proportion of mode I / mode II at the crack tip.

2.3.7 Fracture criterion under mixed-mode loading

Concept of mixed mode fracture criteria

By analogy to mode I, the stress intensity factor K_{II} associated to a mode II loading under an in-plane shear stress τ takes the following form:

$$K_{II} = \tau \sqrt{\pi a}$$

Eq. 104

As previously defined in chapter 2.2.3, the crack extension for pure mode II occurs, only if the stress intensity factor K_{II} reaches a specific material critical value K_{IIc}:

$$K_{II} = K_{IIc}$$

Eq. 105

Considering a two-dimensional cracked geometry under tensile and shear loading, the relation between the stress intensity factors K_I and K_{II} at the crack tip and the material fracture parameters K_{Ic} and K_{IIc} establishes a fracture criteria of crack growth:

$$f\left(\frac{K_{II}}{K_I}, K_{IIc}, K_{Ic}\right) = 0$$

Eq. 106

Empirical fracture criteria

Although no theoretical model exists, empirical expressions can be found in the literature [Bro82, Erd63, Rich85]. The simplest one is directly derived from the energy release rate approach in LEFM. The global energy release rate G can be decomposed into pure modes I and II as:

$$G = G_I + G_{II} = \frac{K_I^2}{E'} + \frac{K_{II}^2}{E'}$$

Eq. 107

According to Griffith, the crack propagates, if the global energy release rate G equals or exceeds the crack resistance energy R. Assumed that R is a constant material parameter, the fracture criterion is simplified to:

$$K_I^2 + K_{II}^2 = \text{constant} = K_{Ic}^2$$

Eq. 108

In the case of a pure mode I loading, the global energy release rate G is only a function of the fracture toughness K_{Ic}. In the same way, for a pure mode II, G is proportional to K_{IIc}^2. Consequently, Eq. 108 leads to $K_{Ic} = K_{IIc}$. As depicted in Fig. 31, the fracture criterion can be graphically represented in the plane (K_I, K_{II}) as a circle of radius K_{Ic}. In other words, the crack under combined loading propagates, if the point of coordinates (K_I, K_{II}) is on or outside the circle of radius K_{Ic}.
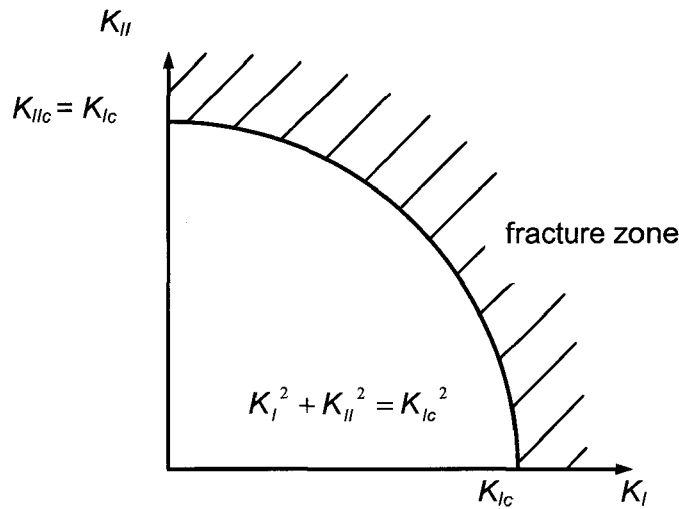
Fig. 31: Mixed-mode loading - Schematic representation of fracture zone

Nevertheless, the relation $K_{Ic} = K_{IIc}$ is not observed experimentally. Broek [Bro82] proposes an extension of the previous fracture criterion, so that the locus of fracture is approximated by an ellipse in the plane (K_I, K_{II}):

$$\left(\frac{K_I}{K_{Ic}}\right)^2 + \left(\frac{K_{II}}{K_{IIc}}\right)^2 = 1$$

Eq. 109
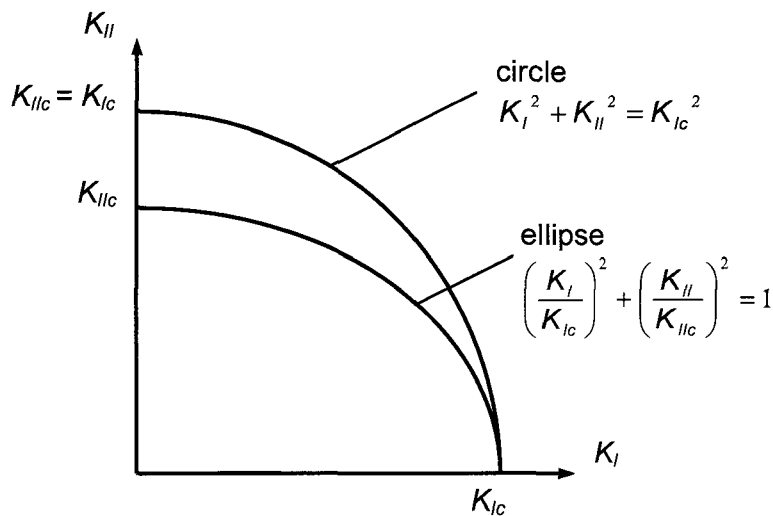
Fig. 32: Mixed-mode loading - Empirical fracture criteria

These two fracture criteria for combined mode follow from the relation between the energy release rate G_k and the associated stress intensity factor K_k. This relation is only valid for pure mode I or mode II). This implies that the crack propagates in the plane of the original crack. However, in the case of mixed mode loading, the crack usually extends in a plane different from the original one.

Criteria based on the direction of crack growth

The criteria developed to determine the crack growth direction offers another way to define the fracture criteria. For example, the maximum tangential stress (MTS) criterion considers that the crack propagates in the direction that maximizes the tangential stress σ_θ. At the crack tip, the analytical solution for the tangential stress σ_θ is:

$$\sigma_\theta = \frac{1}{\sqrt{2\pi r}}\cos\left(\frac{\theta}{2}\right)\left[K_I\cos^2\left(\frac{\theta}{2}\right) - \frac{3}{2}K_{II}\sin\theta\right] \qquad \text{Eq. 110}$$

The evaluation of the propagation angle θ_m was developed in the chapter 2.3.3. The maximum tangential stress $\sigma_{\theta max}$ is obtained for the propagation angle θ_m. Let be $K_{\theta max}$ the relative stress intensity factor:

$$K_{\theta max} = \lim_{r\to 0}\left(\sigma_{\theta max}\sqrt{2\pi r}\right) = \cos\left(\frac{\theta_m}{2}\right)\left[K_I\cos^2\left(\frac{\theta_m}{2}\right) - \frac{3}{2}K_{II}\sin\theta_m\right] \qquad \text{Eq. 111}$$

The crack propagates, if the stress intensity factors $K_{\theta max}$ exceeds a critical value, which is assumed to be equivalent to the fracture toughness K_{Ic}, so that the fracture criterion is:

$$K_{Ic} = \cos\left(\frac{\theta_m}{2}\right)\left[K_I\cos^2\left(\frac{\theta_m}{2}\right) - \frac{3}{2}K_{II}\sin\theta_m\right] \qquad \text{Eq. 112}$$

The same approach can be applied to the minimum strain energy density (MSED) criterion. The chapter 2.3.5 describes the evaluation method of the associated angle of propagation θ_m. The strain energy density factor S in Eq. 100 yields a minimum value for the angle θ_m:

$$S_{min}(\theta) = S(\theta = \theta_m) = \frac{1}{\pi}\left[a_{11}K_I^2 + 2a_{12}K_IK_{II} + a_{22}K_{II}^2\right]_{\theta=\theta_m} \qquad \text{Eq. 113}$$

Crack growth occurs, when the strain energy density factor S_{min} exceeds a critical value $S_{min,c}$, which is associated to the material fracture toughness K_{Ic}:

$$S_{min,c}(\theta) = S_{min}(\theta = 0) = \frac{1}{\pi}\left[a_{11}K_{Ic}^2\right]_{\theta=0} \qquad \text{Eq. 114}$$

Considering the MSED criterion, the fracture criterion is

$$\frac{\left[a_{11}K_I^2 + 2a_{12}K_IK_{II} + a_{22}K_{II}^2\right]_{\theta=\theta_m}}{\left[a_{11}\right]_{\theta=0}} = K_{Ic}^2 \qquad \text{Eq. 115}$$

where coefficients a_{11}, a_{12} and a_{22} are defined in Eq. 101.

The same approach can be applied to the MERR criterion. The maximum energy release rate is attained for the angle θ_m:

$$G_{max}(\theta) = G(\theta = \theta_m) = \frac{1}{E'}\left(K_I^2(\theta_m) + K_{II}^2(\theta_m)\right) = \frac{K_{Ic}^2}{E'} \qquad \text{Eq. 116}$$

A schematic representation of the fracture criteria is shown in Fig. 33.
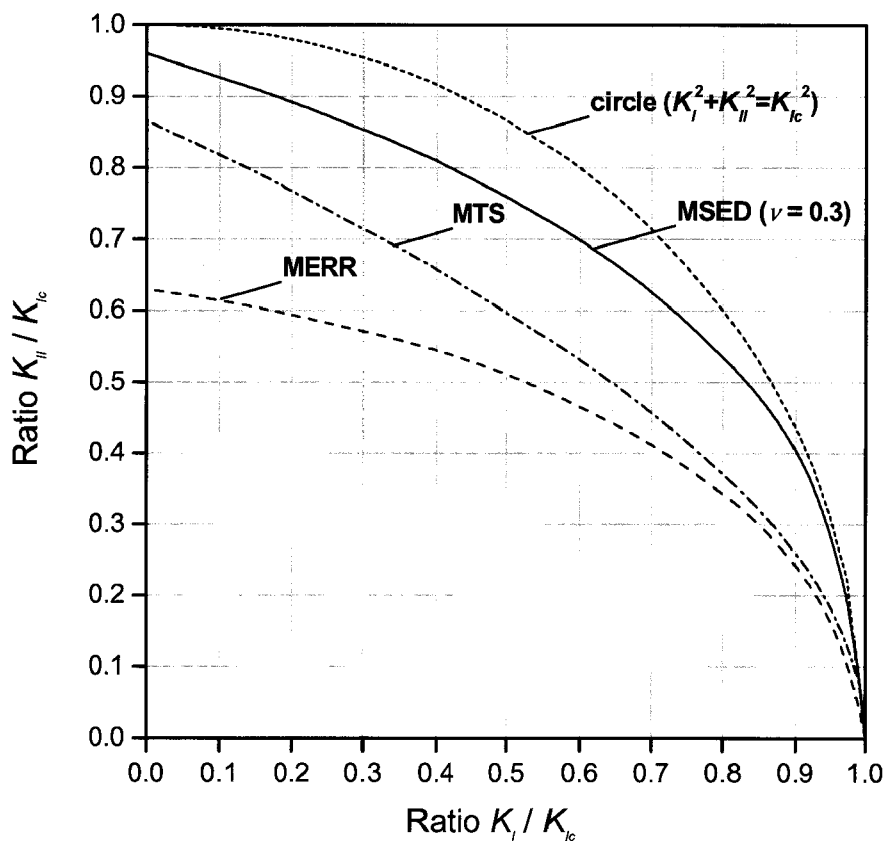
Fig. 33: Mixed-mode loading - MERR, MSED and MTS fracture criteria

For a pure mode I loading, it is obvious that the fracture criterion is directly equivalent to the fracture toughness ($K_I / K_{Ic} = 1$). For a certain mixed-mode loading ($K_I \neq 0$ and $K_{II} \neq 0$), the difference increases between the fracture predictions. For a pure mode II, the variation between the MTS and the MSED fracture criteria is about 10% and about 30% between MSED and MERR criterion. This phenomenon is illustrated by Fig. 33.

Conclusion

In this chapter basics of fracture mechanics are described. Because the studied materials have a brittle behaviour, concepts are restrained to linear elastic fracture mechanics (LEFM). A general overview presents the different parameters available to describe the behaviour of a cracked body. The energy release rate and the J-integral are two global parameters, which are based on the evaluation of the energy dissipated during crack growth. Stress intensity factors and crack tip opening displacement are conversely two local parameters, which are evaluated with the help of the stress and strain distribution near the crack tip. Within the context of LEFM, the equivalence between the different parameters provides various methods to determine if a crack will grow or not. For example, fracture toughness and critical energy are introduced to characterise the capability of a material to resist fracture under mode I. As well, theoretical models for cracks under mixed mode loading conditions are examined. Criteria based on 2D or 3D assumptions are proposed to predict the direction of crack propagation. Moreover, fracture criteria for mixed mode loading are described. The chapter 3 will show the implementation of these concepts in finite element software.

3 Numerical implementation

This study has the ambition to provide a simulation tool able to predict fracture in complex structures. In fact, no simple models are available to prevent the risk of material failure in real structures. For this reason, simulation methods are developed to estimate fracture mechanics parameters, such as stress intensity factors or energy release rate. These computed parameters enable to describe if a crack will grow or not. Additionally, numerical software packages give the possibility to evaluate the magnitude and direction of crack growth. A three-dimensional crack propagation can also be simulated by a sequential approach, in which the crack length is updated step by step. The present chapter gives an overview of the techniques implemented within the context of the Finite Element Method.

3.1 Numerical evaluation of fracture mechanics parameters

A numerical fracture analysis has first to answer the question if the crack will extend or not. This step can only be successful through an accurate evaluation of the fracture mechanics parameters. Analytical solutions exist mainly for simple two-dimensional crack configurations [Mur87, ESI01, A-399]. However, complex curved crack front and assimilated parameters must be investigated with numerical methods. The development of such a numerical model shall be compatible with the theoretical assumptions of fracture mechanics.

3.1.1 Generalities about fracture mechanics parameters

In this study, linear elastic material behaviour will be assumed, as in most cases of crack growth analysis. Within the field of the LEFM, the primary parameters that may be of interest for crack propagation are:
- Stress Intensity Factors SIFs, K_i
- Energy Release Rate ERR, G

The formulation of the stress intensity factor and respectively of the energy release rate encloses directly the effects of loading and geometry of the body near the crack tip:

$$K_i = f(\text{load, crack length, geometry})$$
$$G = f(\text{load, crack length, geometry})$$

Eq. 117

The stress intensity factor directly results from the elastic stress field in the vicinity of the crack front, while the energy release rate corresponds to the elastic energy released during the crack extension. The FE method enables to estimate the strain and stress fields inside a body, and consequently to evaluate the SIF and ERR. However, the accuracy of the strain and stress fields depends on the mesh quality throughout the model. Particularly, stress intensity factors are evaluated from the local stress distribution at the crack front, so that a fine mesh is required near the crack tip to return an accurate value of this fracture parameter.

Moreover, a singularity in the stress and strain fields exists in the vicinity of the crack tip. The asymptotic stress field at the crack tip is usually obtained by performing analytical two-dimensional plane stress or plane strain calculations. For a 2D model, this yields a $1/r^{0.5}$ square root singularity. In the case of a 3D model, the square root singularity prevails along the crack front within the body. Near the free boundary, the singularity slightly differs and takes the form $1/r^{0.4519}$ for mode I stress singularity and $1/r^{0.607}$ for mode II or III stress singularities [Dho01, Yam78]. However, this variation only appears over a small region, so that the square root singularity is here assumed along the entire crack front. In classical finite element software, standard elements return at most a linear stress field. In order to numerically represent the square root singularity, modified elements have to be introduced at the crack tip.

First, the stress field near the crack tip shall be accurately modelled with a mesh refinement near the crack tip and/or with the implementation of modified elements at the crack tip. Once the mesh containing a crack of length a is successfully generated, two approaches are distinguished to extract the fracture mechanics parameters. On the one hand, a direct method -or point matching method- computes the fracture parameters directly from the results of the FE analysis. The direct method is particularly appropriated for the evaluation of stress intensity factors from the computed nodal displacements. On the other hand, an indirect method determines the fracture parameters by considering an infinitesimal variation of the crack length Δa. As seen in section 2, energy-based criteria are based on the same principle, so that the indirect method is usually implemented to compute the energy release rate. Although the indirect method is time-consuming and its implementation is complex, it is generally preferred to the direct method. In fact, indirect methods are less sensitive to the accuracy of stress/strain distribution near the crack tip than the direct methods, and deliver precise results even with coarse meshes.

Relations between SIFs and ERR were shown in section 2. The energy release rate can be easily determined from the stress intensity factors K_i as depicted in Eq. 45. However, the decomposition of the global energy release rate G into stress intensity factors is not trivial. This conversion requires the evaluation of the energy release rate G_i related to each mode of fracture (mode I, II and III), as seen in Eq. 44. The equivalence between the J-integral and the energy release rate for linear elastic material constitutes an alternative way. In fact, Eq. 65 gives an expression to evaluate the K-factors from the J-integral.

The choice between SIF and ERR is generally correlated with the architecture of the numerical procedure. Some FE software packages return fracture mechanical parameters as result values. For example, the FE software Abaqus enables the direct evaluation of the stress intensity factors and the J-integral. On the opposite, the J-integral is not available with the FE software Ansys as direct output values. Another way consists in the evaluation of SIFs or ERR by post-processing of the FE results.

In most studies [RyK77, Bit96, SFR00-03], the fatigue crack growth criterion is based on the evaluation of stress intensity factors. In fact, fatigue laws are commonly expressed in terms of a function $da/dN = f(\Delta K)$. The use of the energy release rate implies a conversion of the energy into stress intensity factors. Moreover, each basic mode of crack extension (mode I, II and III) is associated to one stress intensity factor (K_I, K_{II} and K_{III}) in the case of LEFM. The relative proportions of opening, sliding and tearing mode provide an efficient technique to predict the direction of crack propagation. Direct and indirect methods exist for the evaluation of the SIFs [RyK77, Zen06]. Either, SIFs are directly extracted from the stress/strain field as presented in Eq. 45, or the energy release rate is computed and the SIFs inferred from it.

3.1.2 Stress intensity factors

Stress intensity factors can be directly evaluated from the computed nodal displacements. This direct method is high sensitive to the accuracy of the local strain and stress fields near the crack tip. Consequently, a precise representation of the crack tip singularity in the FE model is required.

Numerical model of the singularity

In the case of LEFM, the order of the singularity is equal to ½ and cannot be modelled by usual FE elements. However, specific "*crack tip elements are unnecessary*", as labelled by Henshell and Shaw in 1975 [Hen75]. Barsoum worked independently on the same subject and established in 1974 [Bar74-76] that a two-dimensional 8-noded isoparametric element (Fig. 34) offers the possibility to model the square root singularity, when the mid-side nodes near the crack tip are moved to the quarter point, as seen in Fig. 35.
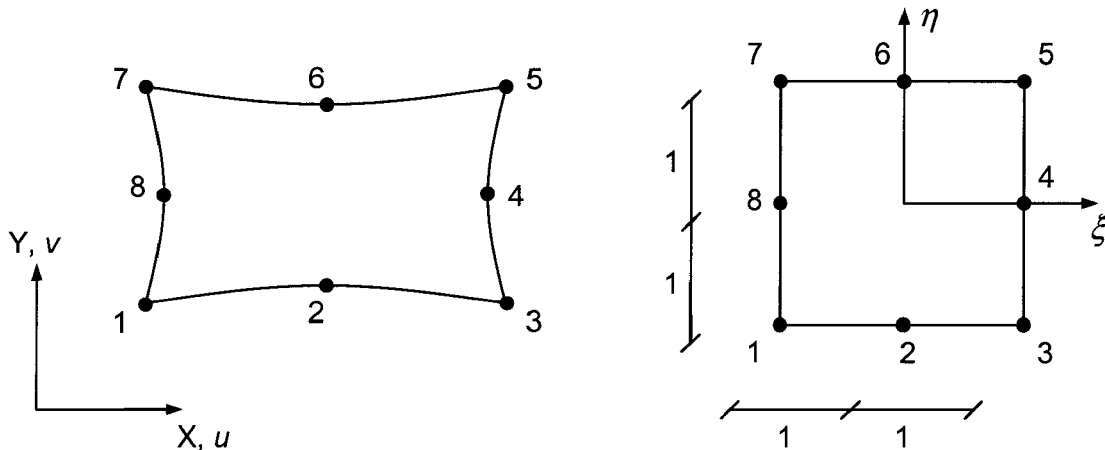
Fig. 34: 2D 8-noded isoparametric element
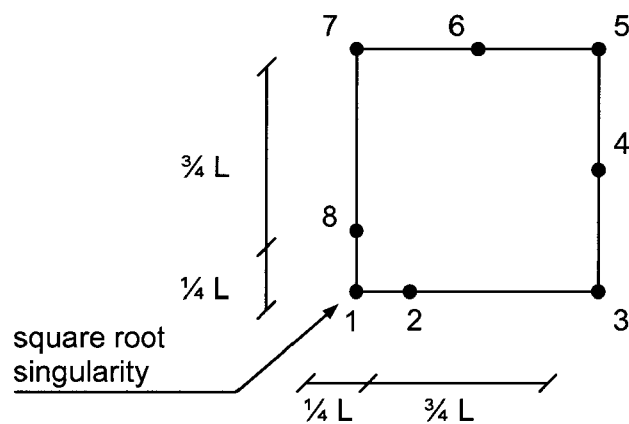
Fig. 35: 8-noded quarter point element

By locating the mid-side nodes 2 and 8 at the distance L/4 instead of L/2, a stress singularity is introduced at the first node. The displacement along the edge 1-2-3 (η = -1) has the following form [Bar74]:

$$u = -\frac{1}{2}\left(-1+2\sqrt{\frac{x}{L}}\right)\left(2-2\sqrt{\frac{x}{L}}\right)\bar{u}_1 + \frac{1}{2}\left(-1+2\sqrt{\frac{x}{L}}\right)\left(2\sqrt{\frac{x}{L}}\right)\bar{u}_2 + \left(4\sqrt{\frac{x}{L}}-4\frac{x}{L}\right)\bar{u}_3 \qquad \textbf{Eq. 118}$$

where $\bar{u}_1$, $\bar{u}_2$ and $\bar{u}_3$ are the displacements at nodes 1, 2 and 3. Eq. 118 can be rewritten:

$$u = A + Bx + C\sqrt{\frac{x}{L}} \qquad \textbf{Eq. 119}$$

In opposite to standard second-order isoparametric elements, the displacement field is not a quadratic polynomial, but a superposition of a linear and a square root terms (cf. Eq. 119). The strain field along the side 1-2-3 is reached by differentiating the displacement field:

$$\varepsilon_x = -\frac{1}{2}\left(\frac{3}{\sqrt{xL}} - \frac{4}{L}\right)\bar{u}_1 + \frac{1}{2}\left(\frac{-1}{\sqrt{xL}} + \frac{4}{L}\right)\bar{u}_2 + \left(\frac{2}{\sqrt{xL}} - \frac{4}{L}\right)\bar{u}_3 \qquad \textbf{Eq. 120}$$

Thus the order of the strain (and stress) singularity is equal to $1/r^{0.5}$ and gives the possibility to model a linear elastic fracture mechanics problem. In 1976, Barsoum [Bar76] established that the triangular element formed by collapsing one side of the quarter point rectangular element led to better results. This is shown in Fig. 36, where the crack-tip nodes (1, 7, 8) are constrained to move together. Moreover, the representation of the crack front is simplified and is reduced to a single node.

isoparametric space   physical space
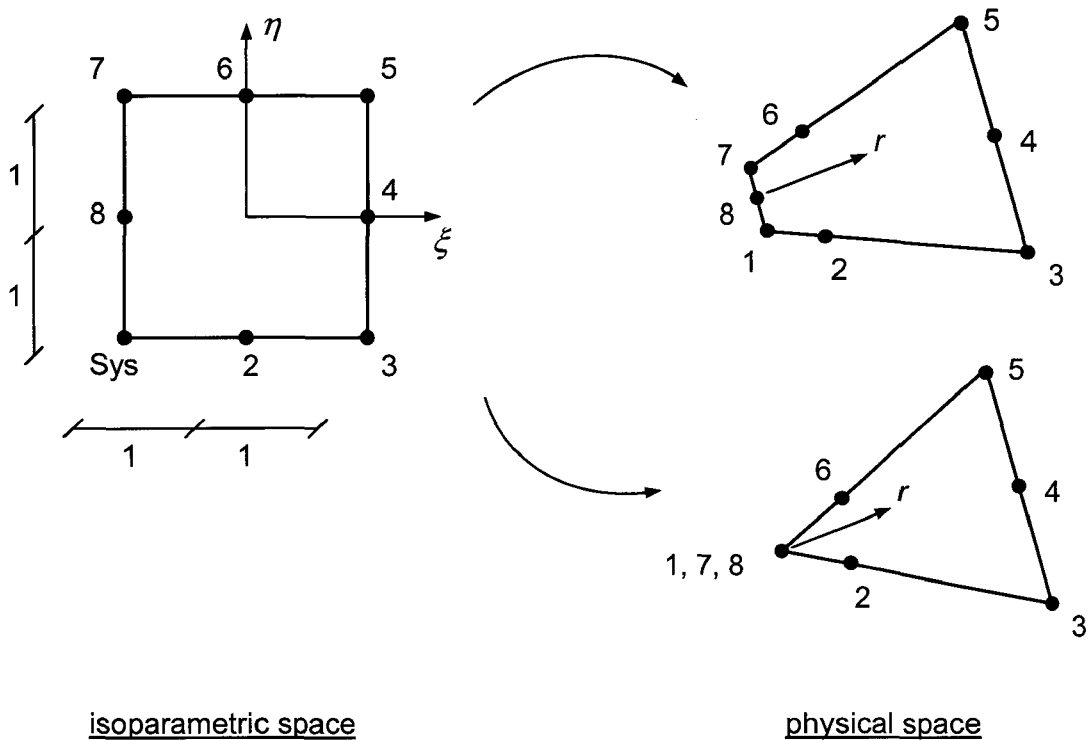
Fig. 36: Collapsed quarter point element

As shown in Fig. 37, the combination of collapsed quadrilateral elements surrounding the crack tip introduces a square root singularity in the finite element mesh. This uniform pattern is commonly named rosette. The size of the crack tip elements influences the accuracy of the solutions: the smaller the radial dimension of the element from the crack tip, the better the results are [Aba05]. In three dimensions, 20-noded or 27-noded brick elements with collapsed nodes are used to create singular fields as depicted in Fig. 38.
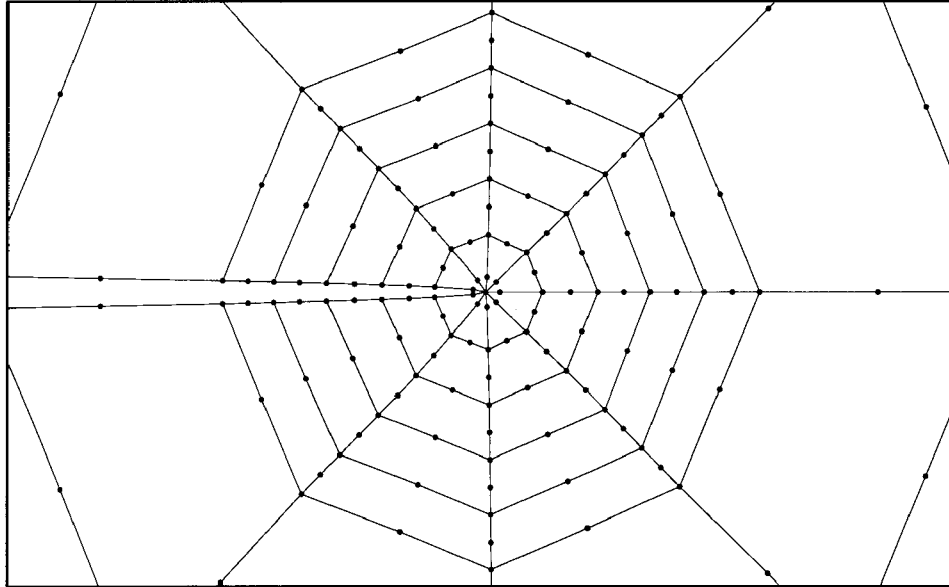
Fig. 37: Crack tip modelled with collapsed 8-noded quarter point elements

2 nodes collapsed to the same location

crack line

3 nodes collapsed   midside nodes moved to ¼ points
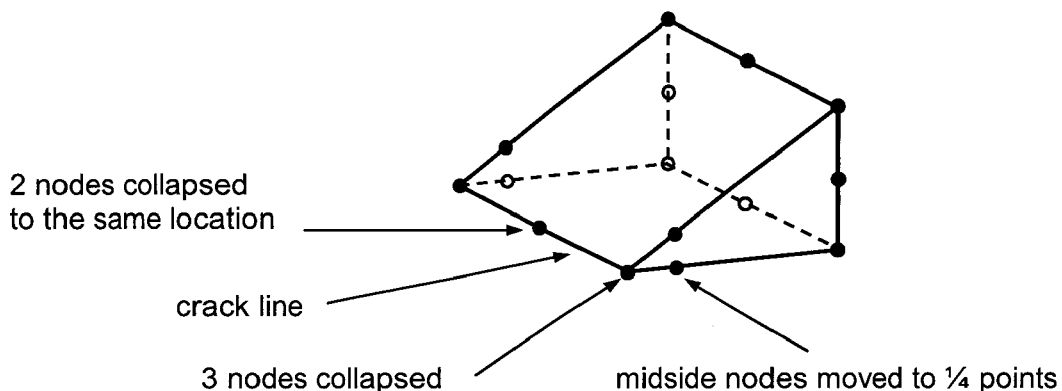
Fig. 38: 20-noded quarter point element [Aba05]

If the mid-side nodes of quadrilateral or cubic collapsed elements remain at the mid-side positions and nodes 1, 7, 8 are allowed to move independently, a $1/r$ singularity is created. This combination is suitable for Elastic Plastic Fracture Mechanics (EPFM).

Displacement based evaluation of the stress intensity factors

As seen in section 2, the stress intensity factors are determined from the local stress or local displacement fields behind the crack tip (see Eq. 23 and Eq. 24). As a result, the stress intensity factors can be directly evaluated from FE simulations. Nearly all finite element codes are displacement based, i.e. the nodal displacements are the primary unknowns, and the stresses are obtained through derivation. Consequently, the element stress values are not as accurate as node displacement results. From this statement, the computation of the

stress intensity factors is based on a direct method using the opening displacements behind the crack tip. To accurate model the singularity in the strain field, collapsed elements are required at the crack tip, as illustrated in Fig. 39.
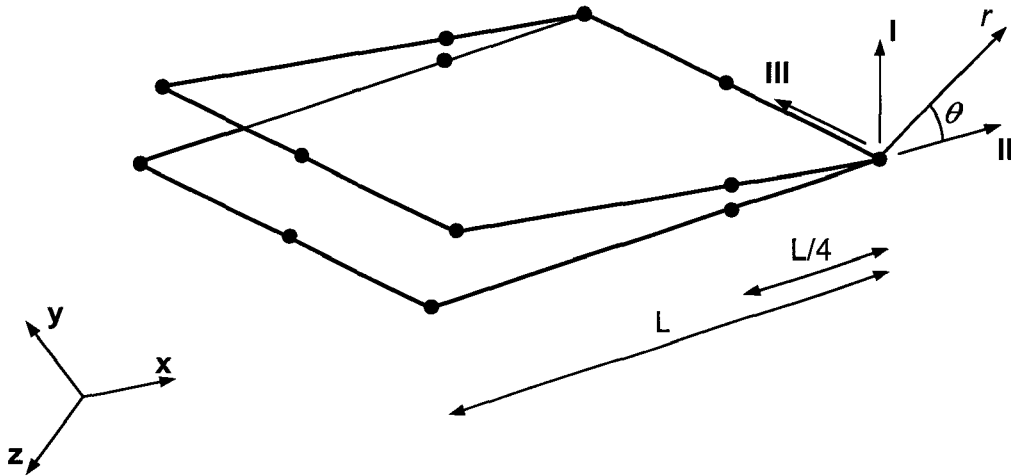
Fig. 39: Local coordinate system at an opened crack front

In the local coordinate system (I, II, III), Westergaard describes the stress field near the crack front as a function of the stress intensity factors and the geometrical parameters (r, θ) [Wes39]. The crack surface ahead the crack front corresponds to an angle $\theta = \pm \pi$. Derived from the Westergaard's equations, the opening displacements V_I, V_{II} and V_{III} for nodes on the crack surface have the following form for linear elastic isotropic material:

$$V_I = \frac{(1+v)(1+\kappa)}{E} \sqrt{\frac{r}{2\pi}} K_I + o(r)$$

$$V_{II} = \frac{(1+v)(1+\kappa)}{E} \sqrt{\frac{r}{2\pi}} K_{II} + o(r)$$ **Eq. 121**

$$V_{III} = \frac{2}{\mu} \sqrt{\frac{r}{2\pi}} K_{III} + o(r)$$

where $\kappa = 3 - 4v$ for plane strain

   $\kappa = (3-v)/(1+v)$ for plane stress

The higher order terms $o(r)$ are negligible so that the stress intensity factors can be written:

$$K_I = \frac{E'V_I}{4} \sqrt{\frac{2\pi}{r}}$$

$$K_{II} = \frac{E'V_{II}}{4} \sqrt{\frac{2\pi}{r}}$$ **Eq. 122**

$$K_{III} = \frac{\mu V_{III}}{2} \sqrt{\frac{2\pi}{r}}$$

The choice of the length r can raise some theoretical difficulties. A simple and accurate solution is to estimate these displacements at the quarter node positions [Zen06].

In addition, the expression of the energy release rate G for linear elastic isotropic materials is suitable and yields:

$$G = G_I + G_{II} + G_{III} = \frac{\left(K_I^2 + K_{II}^2\right)}{E'} + \frac{1}{2\mu}K_{III}^2 \qquad \text{Eq. 123}$$

3.1.3 Energy release rate

In opposite to direct methods, for which the K-factors are directly extracted from the stress/strain field, indirect methods are associated with the evaluation of energy-based criteria. The fracture parameter is here evaluated by considering an infinitesimal variation of the crack length Δa. This implies a mathematical post-processing of the fields computed by the FE analysis.

Finite crack extension method

The energy release rate corresponds to the free energy expended in creating a new crack surfaces. Discretisation of Eq. 5 for a small crack surface extension from A to $A+\Delta A$ yields:

$$G = -\frac{dU_M}{dA} = -\lim_{\Delta A \to 0} \frac{U_M\big|_{A+\Delta A} - U_M\big|_A}{\Delta A} \qquad \text{Eq. 124}$$

The simplest method for the evaluation of G is a geometrical transcription of this mathematical expression. Two finite element models are generated with respective crack surfaces A and $A+\Delta A$, which represent the cracked surfaces before and after crack extension. For the two FE analyses, the applied displacements are maintained constant, so that the energy from the external loading is equal to zero (cf. chapter 2.2.2). For each model, the elastic energy is evaluated and the difference leads to an estimation of G [Kru02].

This method consists in a simple approach, but it has the disadvantage to require two FE analyses. Among others, the generation of two FE models is time-consuming. In addition, the stiffness matrix of the entire model has to be compiled for each analysis, although only elements near the crack front are modified. In the case of large structures, this method is not recommended.

Virtual crack extension method

The Virtual Crack Extension or VCE method was developed by Hellen [Hel75]. This technique is based on the evaluation of the mechanical energy change dU_M. The mathematical formulation was already presented in chapter 2.2.2 and is here adjusted to FE formulation. The mechanical energy U_M is equal to:

$$U_M = U_E + U_A = \frac{1}{2}u^T K u - u^T P \qquad \text{Eq. 125}$$

where K is the stiffness matrix of the system
            u is the vector of nodal displacements
            P is the vector of external forces applied to the nodes

Then, a small change of the mechanical energy is:

$$dU_M = \frac{1}{2} u^T dK u + du^T K u - du^T P - u^T dP$$

<div align="right">Eq. 126</div>

With the assumption that the external forces are maintained constant during crack extension and considering a linear elastic system $P = Ku$, the mechanical energy is reduced to:

$$dU_M = \frac{1}{2} u^T dK u$$

<div align="right">Eq. 127</div>

For a system with a unit thickness $B = 1$, in which a crack grows of a small amount da, the energy release rate is finally given by:

$$G = -\frac{dU_M}{da} = -\frac{1}{2} u^T \frac{dK}{da} u$$

<div align="right">Eq. 128</div>

As described in Eq. 17, the energy release rate is expressed as a function of displacement and stiffness. The term dK/da vanishes for elements, which are not in the vicinity of the crack front. In fact, no change in the geometry is observed for these elements in the case of a small crack increment da. Hence, the energy release rate is computed locally in the neighbourhood of the crack front. To evaluate the term dK/da, only an accommodation of the crack growth by moving elements near the crack tip and leaving the rest of the mesh intact is required. The elements between the paths Γ_1 and Γ_2 are distorted (see Fig. 40), such that their stiffness changes. This allows the determination of the energy release rate from:

$$G = -\frac{1}{2} u^T \frac{dK}{da} u = -\frac{1}{2} u^T \left(\sum_{i=1}^{N_e} \frac{dK_i}{da} \right) u$$

<div align="right">Eq. 129</div>

where K_i are the elemental stiffness matrices and N_e the number of elements between the contours. It was demonstrated by Parks [Pak74] that this expression of G is independent of the inner and outer contours.
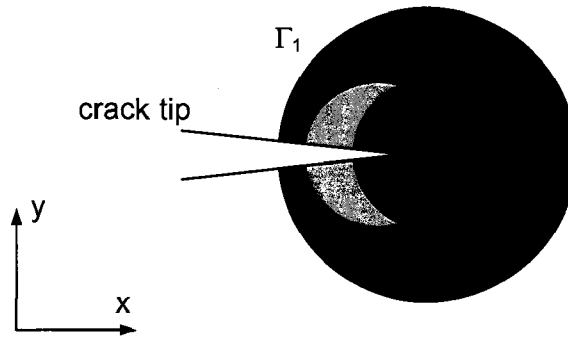
Fig. 40: Two-dimensional body containing a notch

With this method, only one FE analysis of the structure is required; the evaluation of the energy release rate follows with an additional computation of the stiffness matrix of the elements affected by the virtual crack extension. In comparison to the finite crack extension method, the VCE method constitutes a time-efficient solution. Moreover, the energy release rate is expressed as a function of the direction in which the crack was virtually extended and yields the most likely direction of crack propagation.

3.1.4 J-integral and contour integral evaluation

The J-integral method was proposed by Rice [Ric68] in order to determine the rate of change of potential energy for linear elastic, as well as for non-linear elastic material behaviour. The J-integral can be applied with elastic-plastic material behaviour, but only for monotonic loading. Moreover, for a linear elastic material, J is equivalent to the energy release rate G.

The definition of the J-integral in three dimensions is directly extended from the two-dimensional definition. From this remark, this chapter will focus on the evaluation of J-integral for two-dimensional FE models. With simple adaptations due to the third dimension, the techniques are then available for three-dimensional FE models. In the case of an elastic material behaviour, the J-integral is path-independent. To evaluate the J-integral, appropriate contours and/or domains shall be defined. As described in chapter 2.2.5, various expressions exist for the J-integral. The formulation based on domain integral (Eq. 61) is preferred to the formulation with a vanishing path Γ (Eq. 56). In fact, stresses and strains inside a vanishing path Γ can not be accurately determined and as a result, this formulation is not appropriate for a numerical evaluation.

Some FE programs directly returns the J-integral as output value, like Abaqus [Aba05]. Although the J-integral is path-independent, a fine mesh at the crack tip improves the representation of the stress and strain field and consequently the accuracy of the J-integral values. Generally, the J-integral is not evaluated on a unique path, but on different contours (near or far from the crack tip). Resulted path dependence in the evaluation of the J-integral may be an indication that the mesh is not sufficiently refined. To calculate the J-integral vector in two dimensions, the FE software Abaqus [Aba05] defines the domain in terms of rings of elements surrounding the crack tip. The first contour Γ_1 consists of those elements directly connected to crack tip nodes, as seen in Fig. 41. The next contour Γ_2 is composed of the ring of elements in contact with the first contour, as well as the elements in the first contour. Each subsequent contour is defined by adding the next ring of elements in contact with the previous contour.

Γ_2-contour
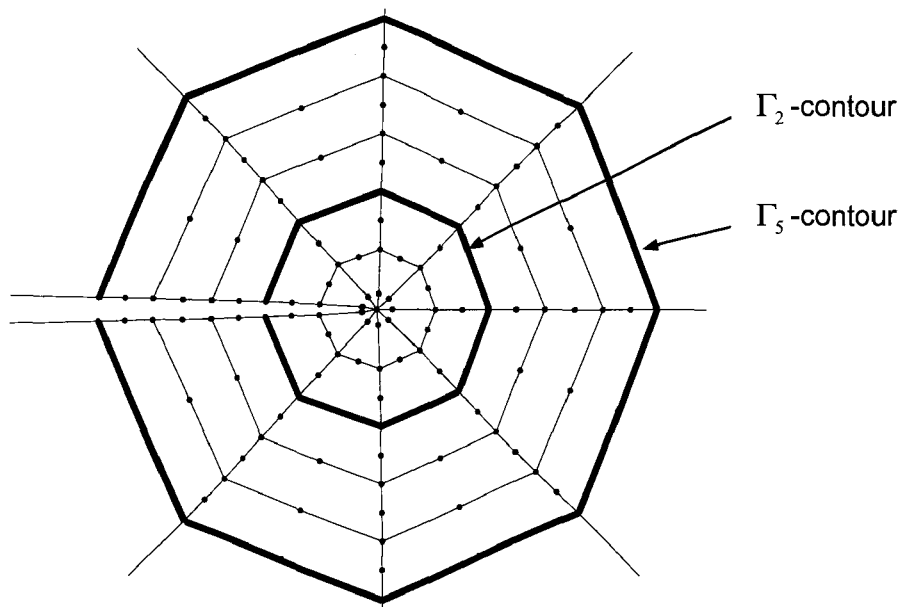
Γ_5-contour

Fig. 41: Contour used by Abaqus for the J-integral evaluation

Within the context of LEFM, the J-integral evaluation is an accurate method to obtain the values of the energy release rate.

3.1.5 Virtual crack closure technique

The virtual crack closure technique (VCCT) was first proposed by Rybicki and Kanninen [RyK77] as the numerical implementation of Irwin's crack closure integral. The Irwin's theory [Bro82] considers that the energy ΔE released during a small crack extension Δa (from a to $a+\Delta a$) is identical to the work required to close a crack with the same extension. Based on a unique 2D or 3D finite element analysis, the VCCT enables to evaluate the energy release rates related to each mode of loading (mode I, II and III).

According to the modes of crack propagation, the global strain energy release rate can be decomposed into G_I, G_{II}, G_{III}, the three corresponding fracture modes:

$$G = G_I + G_{II} + G_{III}$$

Eq. 130

Using a local polar coordinate system placed at the crack tip, the corresponding stresses are respectively σ_y, τ_{xy} and τ_{zy}, and the related displacements behind the crack tip are v, u and w.

$$G_I = \lim_{\Delta a \to 0} \frac{1}{2\Delta a} \int_0^{\Delta a} \sigma_y (\Delta a - r) v(r,\pi) dr$$

$$G_{II} = \lim_{\Delta a \to 0} \frac{1}{2\Delta a} \int_0^{\Delta a} \tau_{xy} (\Delta a - r) u(r,\pi) dr$$

Eq. 131

$$G_{III} = \lim_{\Delta a \to 0} \frac{1}{2\Delta a} \int_0^{\Delta a} \tau_{zy} (\Delta a - r) w(r,\pi) dr$$

The VCCT approach can be implemented in FE codes by discretising the crack closure integral (Eq. 131). Thus, the VCCT depends on the type of element used to model the crack front. The simplest case was depicted by Rybicki and Kanninen [RyK77] for planar problems using 4-noded elements in the vicinity of the crack tip.
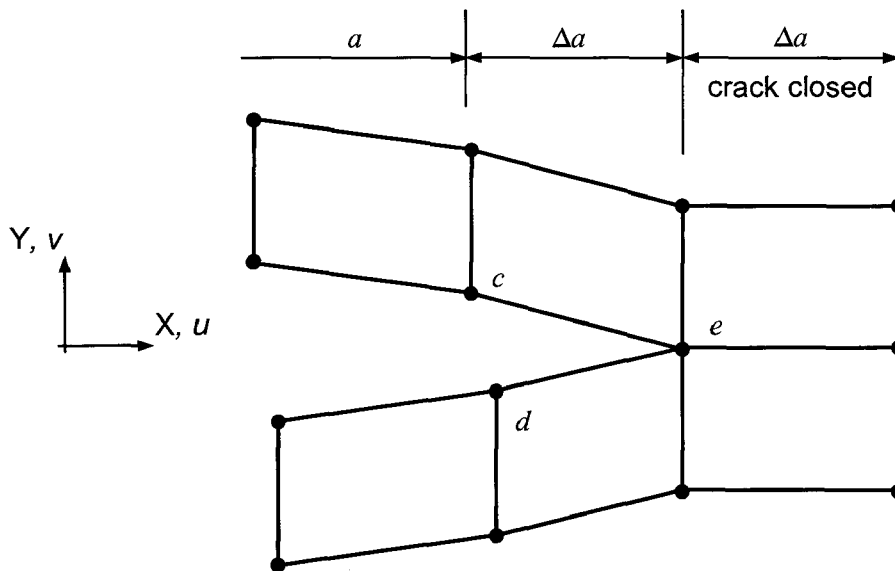
Fig. 42: VCCT - 4-noded element model at the crack tip

The energy ΔE released during the crack extension Δa from node c to node e is equal to the energy required to close the crack between the same locations, which yields:

$$G_I = \frac{1}{2\Delta a}\left[F_{Yc}\left(v_c - v_d\right)\right] \quad \text{and}$$

$$G_{II} = \frac{1}{2\Delta a}\left[F_{Xc}\left(u_c - u_d\right)\right]$$

Eq. 132

u_c and u_d are the displacements along the axis X of nodes c and d, where v_c and v_d are the displacements along the axis Y, respectively. F_{Xc} and F_{Yc} are the nodal forces necessary to hold nodes c and d together. However, the evaluation of F_{Xc} and F_{Yc} requires a second FE analysis. If Δa is small compared to the crack length a and if the elements around the crack tip are the same size Δa, it is assumed that the forces F_{Xe} and F_{Ye} required to hold the nodes e and f together are approximately equal to F_{Xc} and F_{Yc} and leads to [Kru02]:

$$G_I = \frac{1}{2\Delta a}\left[F_{Ye}\left(v_c - v_d\right)\right] \quad \text{and}$$

$$G_{II} = \frac{1}{2\Delta a}\left[F_{Xe}\left(u_c - u_d\right)\right]$$

Eq. 133

The ideal case of identical element lengths Δa for the element in front of and behind the crack tip is not always assumed, due to the use of automatic mesh generators or in the case of crack propagation through an irregular mesh. A first solution is to introduce a correction factor proportional to the element crack lengths in the expressions of G_i [RyK77, Kru02]. A second solution consists in the use of a submodeling technique. As used in the software ADAPCRACK3D [Ful02], a submodel with a regular mesh at the crack tip allows the evaluation of the diverse ERRs.

The VCCT is formulated for 8-noded elements on the same assumptions and yields:

$$G_I = \frac{1}{2\Delta a}\left[F_{Ye}\left(v_c - v_d\right) + F_{Yh}\left(v_f - v_g\right)\right] \quad \text{and}$$

$$G_{II} = \frac{1}{2\Delta a}\left[F_{Xe}\left(u_c - u_d\right) + F_{Xh}\left(u_f - u_g\right)\right]$$

Eq. 134
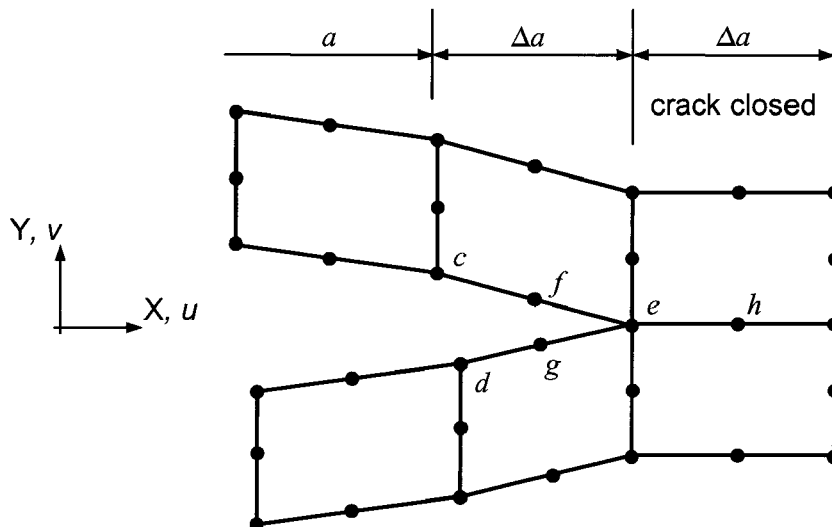
Fig. 43: VCCT - 8-noded element model at the crack tip

The combination of 2nd order elements and the VCCT can lead to an incompatible interpenetration of the elements due to the quadratic shape functions [Kru02]. That is why debonding of nodes, which models the opened crack, should be realised over the entire length of the element.

In the precedent formulations, the crack tip is modelled with conventional elements. A compatible alternative consists in modelling the crack tip with collapsed quarter point elements, in order to numerically represent the singularity of stress and displacement fields near the crack tip, as defined in chapter 3.1.2. Only the position of the mid-side node changes in the configuration of "quarter point" elements, so that Eq. 134 is still valid [Kru02].

The previous models are limited to planar analyses and do not take into account the mode III. Consequently the VCCT formulation was extended to three dimensional problems for the investigation of mixed mode loading [Kru02-03, JiM03]. For example, Jimènez and Miravete describe the implementation of the VCC technique in the software Abaqus using "quarter point" 27-noded brick elements. It yields the opening energy release rate G_I, as expressed in Eq. 135. G_{II} and G_{III} take a similar form:

$$G_I = \frac{1}{2 l_{n3} \Delta}\left\{F_{z_{n3}}\left[t_{11}\left(w_{d3} - w_{d3'}\right) + t_{12}\left(w_{\theta3} - w_{\theta3'}\right)\right]\right.$$

$$+ F_{z_{p3}}\left[t_{21}\left(w_{d3} - w_{d3'}\right) + t_{22}\left(w_{\theta3} - w_{\theta3'}\right)\right]$$

$$+ \frac{1}{2}\left\{F_{z_{n2}}\left[t_{11}\left(w_{d2} - w_{d2'}\right) + t_{12}\left(w_{\theta2} - w_{\theta2'}\right)\right]\right.$$

$$\left. + F_{z_{p2}}\left[t_{21}\left(w_{d2} - w_{d2'}\right) + t_{22}\left(w_{\theta2} - w_{\theta2'}\right)\right]\right\}$$

$$+ \frac{1}{2}\left\{F_{z_{n4}}\left[t_{11}\left(w_{d4} - w_{d4'}\right) + t_{12}\left(w_{\theta4} - w_{\theta4'}\right)\right]\right.$$

$$\left.\left. + F_{z_{p4}}\left[t_{21}\left(w_{d4} - w_{d4'}\right) + t_{22}\left(w_{\theta4} - w_{\theta4'}\right)\right]\right\}\right\}$$

Eq. 135

where $l_{n3} = \frac{1}{2}\left(l_{j-1} + l_j\right)$ $t_{11} = 6 - \frac{3}{2}\pi$ $t_{12} = 6\pi - 20$ $t_{21} = \frac{1}{2}$ $t_{22} = 1$
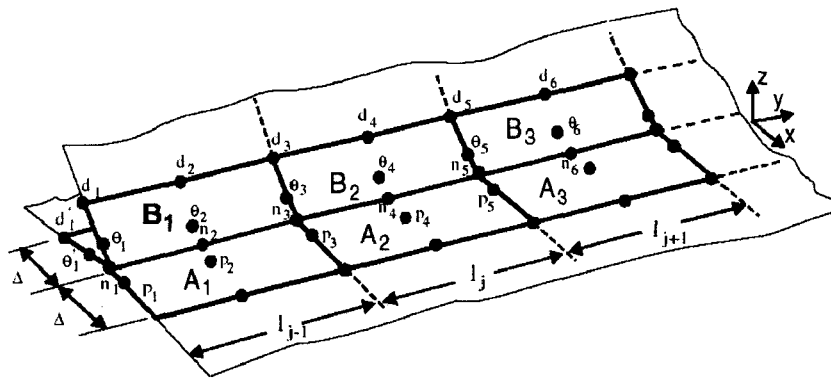
Fig. 44: VCCT - 27-noded brick element model [JiM03]

Since the material properties do not appear in the formulation, the VCCT is convenient either for crack analysis in bulk materials or at the interface between two materials. Nevertheless, slight modifications are necessary due to the oscillatory character of the singularity at an interfacial crack [Sun89, Kru02, Har01]. Other advantages of this method are that it requires only one simulation step, and that the ERR components for mode I, mode II and mode III can be distinguished.

3.2 Numerical crack growth

The precedent section described different techniques available for the evaluation of stress intensity factors or energy release rates. A comparison between the computed fracture mechanics parameters and the material parameters, such as the fracture toughness, delivers a useful criterion for crack propagation. Numerical software packages give the possibility to establish if a crack will propagate or not. Moreover, they enable to evaluate the magnitude and direction of crack growth. A three-dimensional crack propagation can also be simulated by a sequential approach, in which the crack length is updated step by step.

3.2.1 Numerical approach

The extension of a crack front is controlled by the initial shape, the specimen geometry, the applied loading and materials data. Since the energy release rate or the stress intensity factors encloses all these parameters under a unique variable, they are appropriated parameters to control a numerical crack growth. The Finite Element Method (FEM) proposes various solutions to evaluate numerically the stress intensity factors and energy release rate, as seen in chapter 3.1. Consequently, a crack growth analysis can be modelled by a sequential approach, in which the crack length is updated step by step. This study focused on fatigue crack growth analysis, as presented in next chapters. A time-dependent subcritical crack growth can be simulated with the same approach.

Fig. 45 illustrates schematically this incremental approach. First, the specimen geometry, the crack position in the structure and the structural material behaviour have to be specified as input data. From these, a three-dimensional FE model containing the initial crack is generated. High stress and strain gradients involve a very refined mesh near the crack tip. Then, a standard FE analysis is run. From the computed stress and strain values derive the fracture mechanics parameters along the crack front. The stress intensity factors or the energy release rate are calculated to determine the magnitude of crack growth Δa and the direction of extension for the next step. In fact, the crack growth increment is represented as a vector. This fracture criterion allows the front to be advanced through the model. In the case of a fatigue crack growth, an additional input data is the material fatigue law $da/dN = f(\Delta K)$. The discretisation of da/dN into $\Delta a/\Delta N$ gives the possibility to evaluate the amount of crack growth Δa for a given number of cycles ΔN. The global geometry is then updated and remeshed automatically with the new crack length $a+\Delta a$. The next analysis step can be run.

During the procedure, three operations are critical:
- Evaluation of the stress intensity factors and/or the energy release rate along the crack front. These values are used as crack growth criteria.
- Numerical prediction of the growth magnitude and the direction of crack extension, with the help of the stress intensity factors and/or the energy release rate. This allows the crack to be advanced through the model.
- Extension of the crack position. The global geometry is updated and remeshed automatically.

For each operation, various technical solutions are available. These numerical, theoretical or structural tools will be explained in details in the next chapters. Particularly, the solutions implemented in the software codes ADAPCRACK3D and Zencrack are presented.
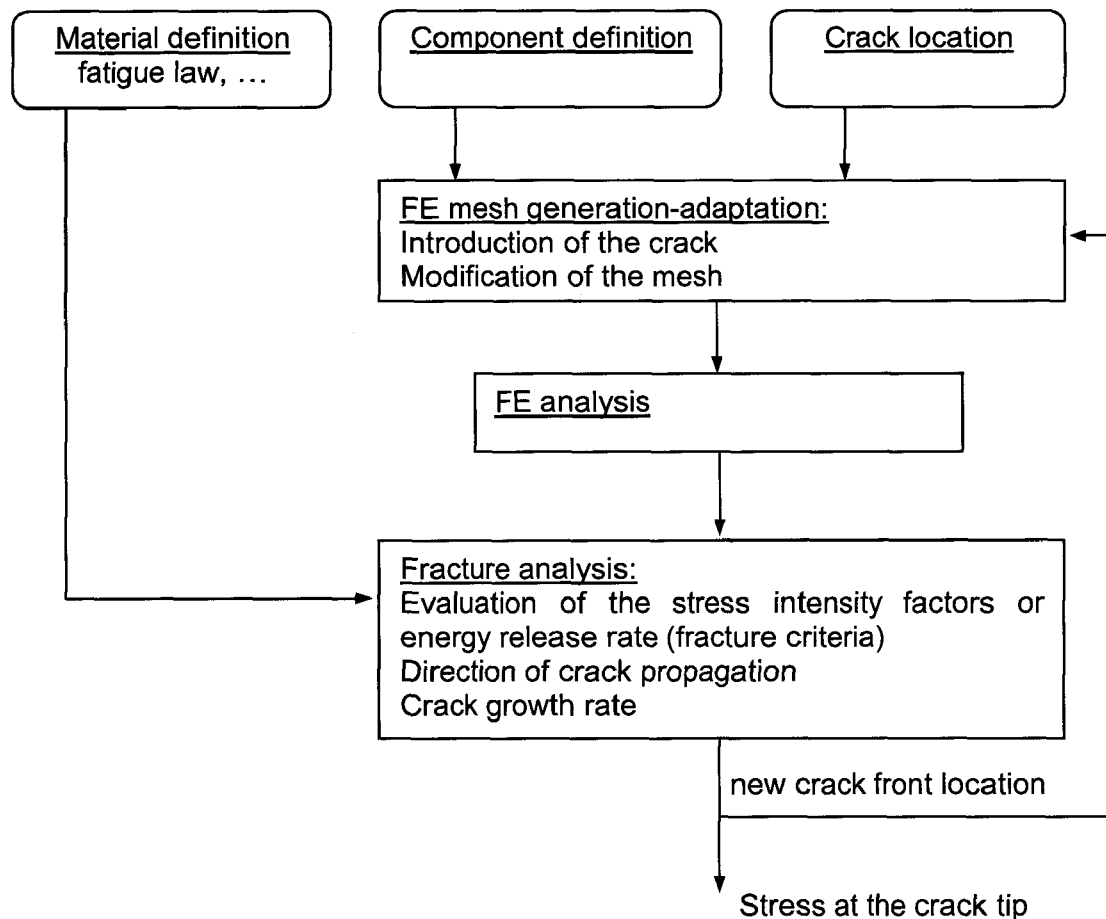
Fig. 45: Incremental crack propagation process

3.2.2 Software ADAPCRACK3D

The software ADAPCRACK3D has been developed at the Institute of Applied Mechanics from the University of Paderborn, Germany, in order to predict fatigue crack growth in complex three-dimensional geometries under general mixed-mode loading conditions [SFR00, Ful02]. ADAPCRACK3D proposes a fully automatic simulation of crack propagation based on the FE solver Abaqus.

The process used during an ADAPCRACK3D analysis is divided into two parts. The module NETADAPT3D performs all the required adaptations of the mesh, resulting from the modification of the global geometry after the crack propagation. Each step is composed by a global cracked model analysis and a submodel analysis of the crack tip. The both analyses are performed by Abaqus, as seen in Fig. 46.

The results are then investigated by the module NETCRACK3D. The energy release rates G_i and associated stress intensity factors K_i are evaluated with the help of the Virtual Crack Closure Technique (VCCT) from the stress field of the submodel analysis, as presented in chapter 3.1.5. The stress intensity factors are used in combination with the maximum principle stress criterion to predict the direction and the magnitude of crack propagation and finally to estimate the new crack front location.
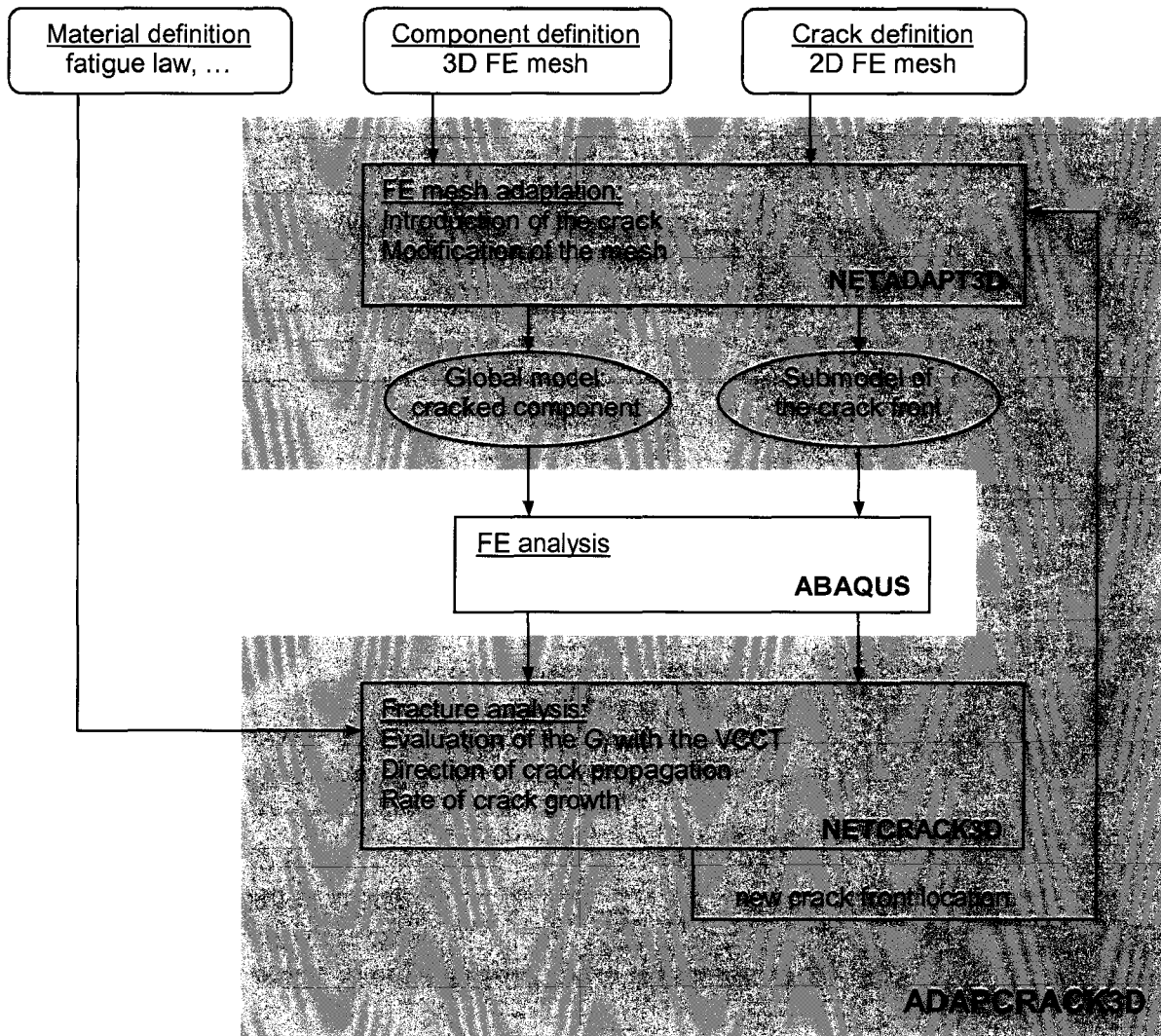
Fig. 46: ADAPCRACK3D procedure

3.2.3 Software Zencrack

The Zencrack program is a proprietary software product of Zentech International Ltd., which can be used in three ways:

- for cracked mesh design: generation of 3D finite element meshes containing multiple crack fronts from a finite element model of an uncracked component.
- for initial crack state analysis: determination of the maximum energy release rates and stress intensity factors distribution along crack fronts.
- for crack growth analysis: automatically calculation of a fatigue crack growth in a general 3D body under arbitrary loading.

The FE analysis itself is computed by external FE codes. Zencrack is interfaced to the Ansys, Finas, MSC.Marc or Abaqus (in this work) finite element packages. A user-defined script controls where the crack will be introduced, and determines the size of the generated crack front section. Once started, each analysis is completed fully automatically following the procedure described in Fig. 47.
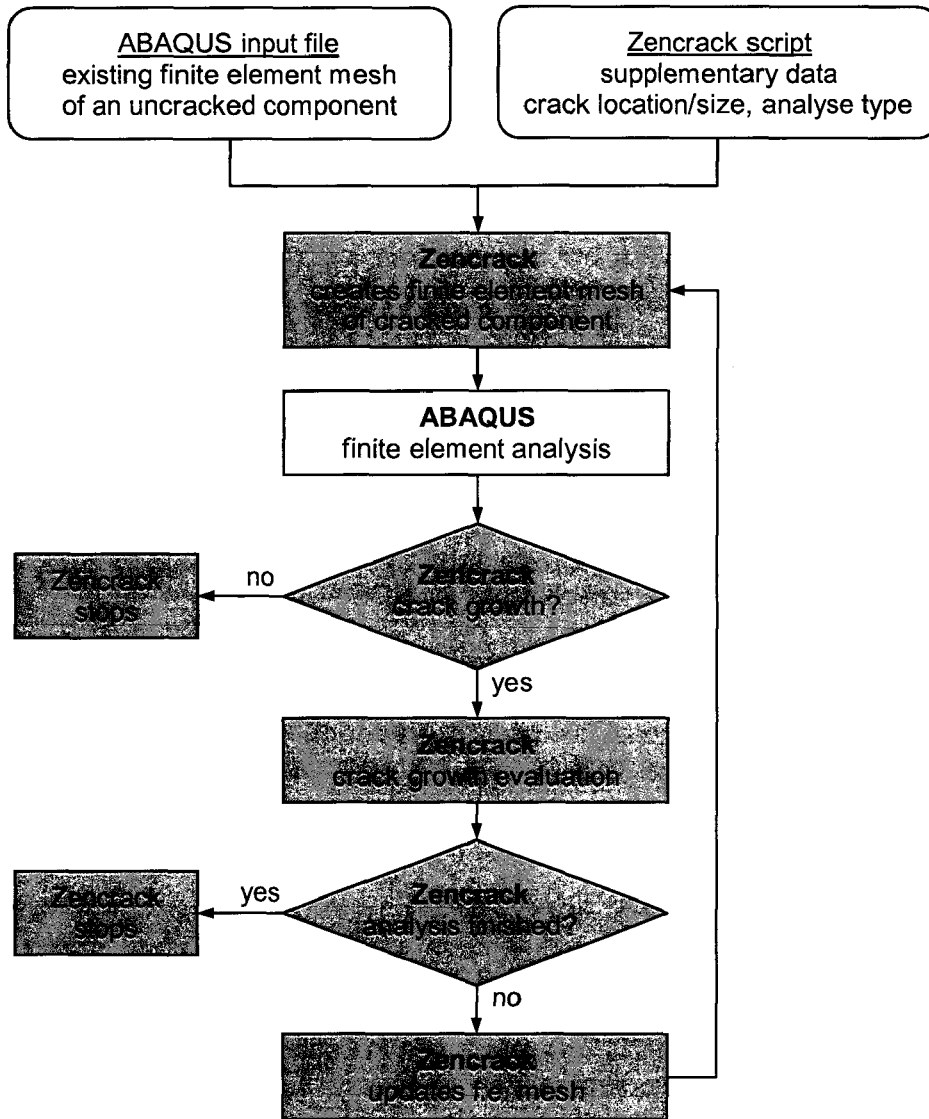
Fig. 47: Zencrack procedure

Zencrack calculates ERR along 3D crack fronts and/or SIFs using direct or indirect methods. The user has the possibility to evaluate the SIFs by using the nodal displacements close to the crack tip in the case of linear elastic materials (chapter 3.1.2). Or, the change in strain energy for various virtual crack extensions at the crack front(s) can be selected. This indirect method (J-integral) is described in chapter 3.1.4.

3.2.4 Numerical evaluation of the propagation direction

The software packages ADAPCRACK3D and Zencrack are based on an incremental procedure. The central operation is the evaluation of fracture mechanics parameters. Available methods are summarised in Tab. 3.

	Zencrack		ADAPCRACK3D	
parameter	K_i	G	K_i	G
FE method	Nodal displacements	J-integral	VCCT	VCCT
formulation	$K_i = \dfrac{E'V_i}{4}\sqrt{\dfrac{2\pi}{r}}$	$G = J$	$K_i^2 = E'G_i$	$G = G_I + G_{II} + G_{III}$

Tab. 3: Numerical methods used to evaluate SIFs or ERR in Zencrack and ADAPCRACK3D

The direction of crack propagation can also be deduced from the stress intensity factors or the energy release rates. This step is essential in the case of mixed-mode loading at the crack tip, as the predicted crack path is closely related to the direction of crack extension. As presented in chapter 2.3, various criteria exist and the available criterion differs from one software codes to another.

Criteria implemented in ADAPCRACK3D

The three-dimensional approach implemented in ADAPCRACK3D is based on the maximal principal stress criteria suggested by Schöllmann [Sch01] and Dhondt [Dho01], which is described in chapter 2.3.2. The VCCT enables the evaluation of energy release rates G_I, G_{II}, and G_{III}, which are converted into stress intensity factors K_I, K_{II}, and K_{III} as seen in Eq. 45. Then, Eq. 85 and Eq. 84 are successively used to evaluate the kinking angle θ_0 and the twisting angle ψ_0.

Criteria implemented in ZENCRACK

The software Zencrack proposed two approaches to estimate the direction of crack propagation. Both criteria consider that mode III is not preponderant. Only the direction of crack propagation θ induced by mode I and mode II is evaluated.

The first way is based on the maximum tangential stress (MTS) criterion. As stated in Eq. 91, the direction of crack propagation is directly related to the ratio K_{II} / K_I. Within the context of LEFM, the stress intensity factors are evaluated from the relative opening displacements as described by Eq. 122. Zencrack estimates these displacements at the quarter point node positions [Zen06].

The second approach considers the maximum energy release rate (MERR) criterion. Hellen assumes for a 2D case that the direction of fatigue crack growth is very close to the direction of the maximum energy release rate G_{max} [Hel75]. For this, a series of virtual crack extensions (VCE) in the normal plane is estimated using the J-integral parameter. It yields a distribution of energy release rates. Zencrack applies seven VCE vectors for each node on the crack front and ERRs are evaluated in these multiple directions [-60°, -40°, -20°, 0°, +20°, +40°, +60° in the local coordinate system]. This is shown schematically in Fig. 48 as energy

release rate values G_1 to G_7. From this data, Zencrack extracts the maximum energy release rate G_{max} and the corresponding direction θ_{max}.
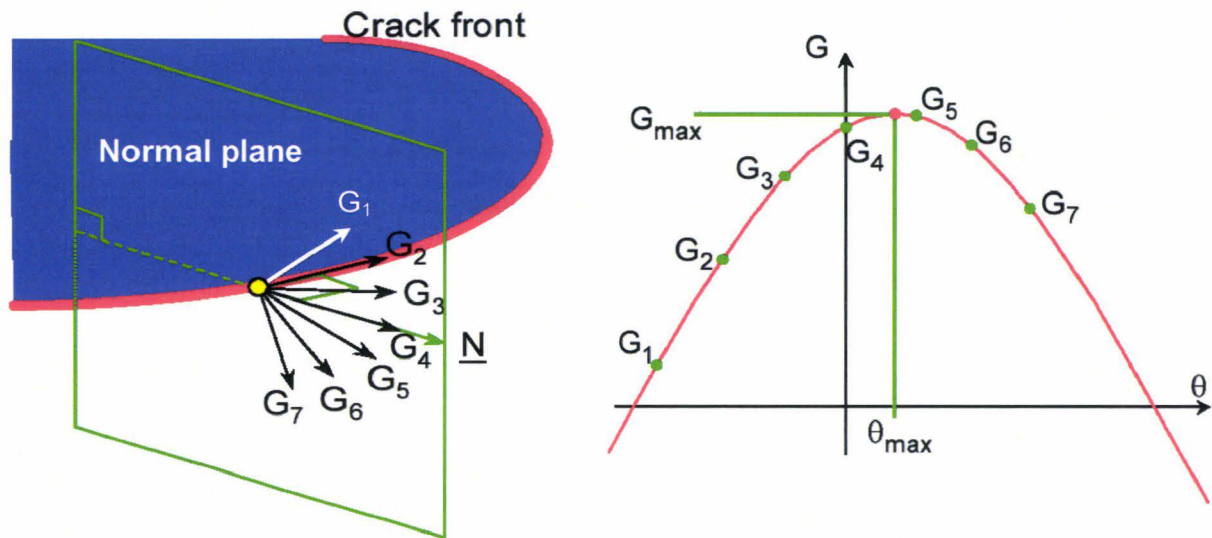
Fig. 48: Energy based calculation of G_{max} and growth direction [Zen06]

The implemented method is either a displacement-based technique (MTS criterion) or relies on an energy-based method (MERR criterion). Actually, the selected method depends upon the Finite Element package to which Zencrack is interfaced. The nodal displacements behind the crack tip are accessible with all FE codes, so that the first method is available with all interfaced FE solvers (Ansys, Finas, MSC.Marc and Abaqus). On the other hand, the energy-based method requires the evaluation of the J-integral. This output variable is only available in the software codes Finas and Abaqus. In this study, Abaqus is used as FE solver and one of the two approaches has to be specified by the user. As the J-integral is less sensitive to the mesh quality at the crack tip, the MERR criterion is generally preferred.

As referred in Tab. 4, neither Zencrack nor ADAPCRACK3D propose the MSED as available criterion. In fact, MTS, MERR and maximum principle stress criterion are simpler to implement in FE packages and return similar crack propagation direction (see Fig. 29).

	Zencrack	ADAPCRACK3D
Crack growth direction criterion	MERR [Hus74] or MTS [Erd63]	Maximum principal stress [Sch01]

Tab. 4: Crack growth direction criterion implemented in Zencrack and ADAPCRACK3D

3.3 Finite-Element mesh generation

The extraction of the fracture mechanics parameters and the evaluation of the crack propagation direction from a discrete crack model are insufficient to predict the lifetime of a structure. In fact, the entire crack advance has to be modelled. The extension of the crack position is modelled with the help of successive FE analyses and the position of the crack has to be updated between each FE analysis. This step requires a partial or global remeshing of the geometry. The finite mesh generation constitutes the central originality of each software structure. As they cannot be dissociated, the software and the implemented remeshing approach are here described together.

3.3.1 Objectives

The procedure of mesh generation should satisfy conditions, which are imposed either by the extraction of parameters or by the update of the crack position.

First, a fine mesh near the crack tip is required to ensure a precise evaluation of the fracture mechanics parameters. Moreover, a specific mesh geometry is recommended at the crack tip. For example, the presence of quarter-point elements at the crack tip was justified in chapter 3.1.2 in order to numerically represent the singularity. As well, the rosette design (see Fig. 37) improves the accuracy for the J-integral evaluation. In the case of the Virtual Crack Closure Integral technique, only a regular mesh with hexahedron elements is required at the crack tip (Fig. 43).

Two phases have to be described in the definition of the crack position: the introduction of the crack front in the original mesh and the automatic update of the crack position. A simple generation of the first mesh by the user is associated to a logic and understanding process. The first way is to consider the crack as a geometrical default and to directly mesh the structure with crack surfaces using a classical meshing tool. The second method is based on the generation of a virgin mesh, in which a crack is afterwards introduced by modifying the FE model. The location of the crack is here defined by a user-script.

Once the magnitude and the direction of crack growth are extracted, the crack position can be updated automatically. Techniques differ from one software code to another. Either a complete new mesh containing the crack is generated or the mesh of the previous FE analysis is modified. As the latter technique is less time-consuming, it is preferred in software packages ADAPCRACK3D and Zencrack.

3.3.2 Complete re-meshing

The crack propagation is numerically modelled with a succession of discrete FE analyses. Before the next FE analysis runs, the FE model has to be modified in order to reflect the current crack configuration. The simplest solution consists in the generation of a complete new mesh. It means that the crack advance is considered as a geometrical modification. This operation can be done automatically, but is considered as costly and timely expensive.

The strategy of complete meshing can be applied to update the mesh between two FE analyses, and also to generate the original mesh. A fine mesh has to be produced along the crack front in order to accurately model the stress field. The rest of the geometry is generally modelled with a coarse mesh. The recursive spatial decomposition methods seem to be particularly adapted to satisfy these two conditions [Bit96, Mir03]. Another simple method of

complete meshing is based on an advancing front algorithm, which meshes the structure from the outer to the inner domain. In general, the quality of the generated mesh is improved by using a smoothing algorithm.

Quadtree algorithm

The principle of quadtree algorithms is to partition a two-dimensional surface (Fig. 49-a) by recursively subdividing it into four quadrants. The repartition of nodes is naturally adapted to the required refinement (Fig. 49-b). The octree algorithms realise the same function for three-dimensional models by dividing the space into eight octants. After the subdivision, nodes are placed along the border of the structure and at the center of each square. Triangle elements are then generated (Fig. 49-c). A smoothing algorithm enables a homogeneous repartition of nodes (Fig. 49-d). This method is implemented into the software Quebra2D, which means 2D fracture in Portuguese [Bit96, Mir03].
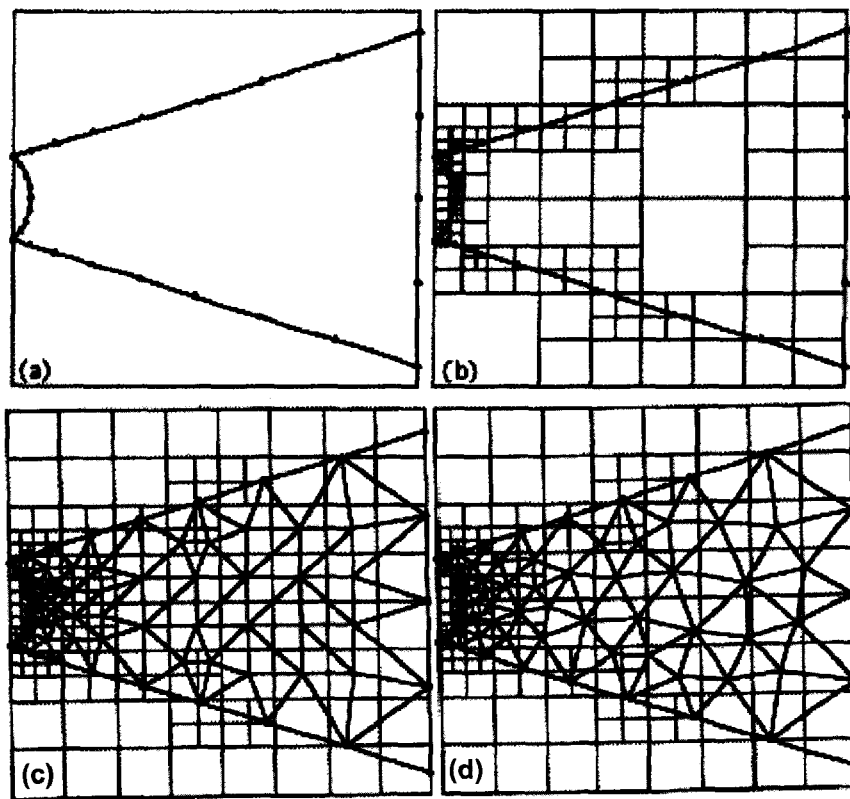
Fig. 49: Complete meshing using quadtree algorithms [Bit96]

Advancing front algorithm

Another strategy to generate surface (or space) meshing is achieved with advancing front methods. The surface or space will be discretised by triangle or tetrahedral elements. Elements are generated one-by-one, starting from the outer edges or surfaces and growing toward the interior of the domain. First, the algorithm divides the borders of the structure into edges (2D) or into triangles (3D). Furthermore, locations where loads, displacements or other boundaries conditions are applied have to be taken into account. These discretised boundaries form the initial front. Then, nodes are inserted in the inner domain and are connecting to the existent front. This operation is reiterated, as depicted in Fig. 50. The successive generation of triangular or tetrahedral element layers is name crack front advance. The domain to be meshed is progressively reduced, which fact results in a

conjunction of the advancing front(s) at the centre of the mesh. Fronts have to be merged together in a manner that does not compromise the quality of elements. A connection between small elements of a front and large elements of an adjacent front will require a wide smoothing zone. That is why the size of the generated elements has to be controlled throughout the procedure. Advancing front methods typically create adapted triangular or tetrahedral mesh near the boundaries, but are less effective where fronts collide [She99].
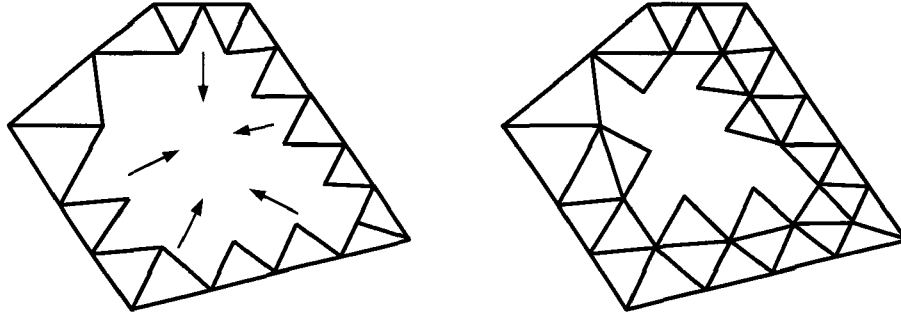
Fig. 50: Complete meshing using advancing front algorithm

3.3.3 ADAPCRACK3D

The numerical crack growth is characterised by small increments of crack propagation between two FE analyses. The crack extension can be interpreted as a local change of the geometry, so that a complete remeshing of the structure containing the new crack front is not required. ADAPCRACK3D proposes a standard technique, which is based on a local mesh adaptation and enables to update the FE model from the previous analysis. Besides, ADAPCRACK3D evaluates the stress intensity factors or the relative energy release rates using the VCCT. This operation necessitates a regular mesh at the crack tip, which is composed by hexahedral elements. However, the special mesh at the crack tip (hexahedral elements) and the global mesh of the structure (tetrahedral elements) can not be connected without developing complex algorithms. The application of the special mesh as a submodel is an original solution suggested by ADAPCRACK3D. A valid connection is also ensured between the stress and strain fields of the two meshes and the submodeling technique simplifies the procedure of mesh generation [Ful02].

Mesh generation

During the generation of the initial mesh, the geometry is first considered as an uncracked mesh. The main difficulty is then to introduce the crack in the virgin global geometry. The structure containing the initial crack is actually modelled from two original FE meshes: the uncracked structure is defined as a three-dimensional FE mesh composed by first order tetrahedrons and the initial crack as a two-dimensional FE mesh (3-noded triangles). Using this simple representation, the requirement of a complex algorithm, which realises the introduction of the crack in the global geometry, is reduced to the insertion of a three-noded elements surface in the global mesh to model the crack surface. In all subsequent steps, NEPADAPT3D realises the crack propagation by extension of the existing crack on basis of the calculated new crack front coordinates.
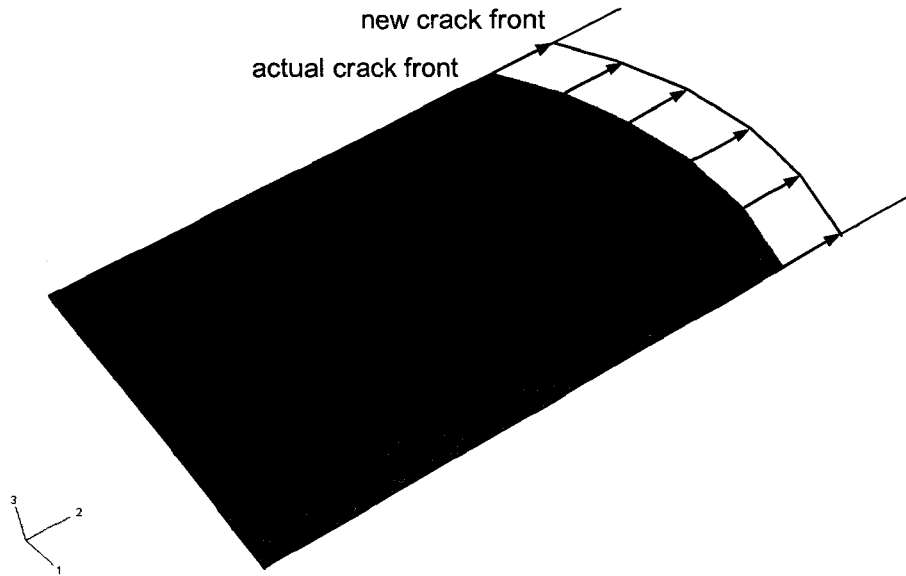
Fig. 51: ADAPCRACK3D - Crack definition (2D FE mesh)

As depicted in Fig. 51, the crack surface is meshed by an assembly of 3-noded triangles. The mesh adaptation algorithm creates FE-faces in the global mesh by an iteration of inserting each triangular element, which itself is divided into three parts:

1.   *Insertion of crack nodes:* This algorithm has the purpose of inserting a unique crack node at a certain position within the mesh in case of not having any FE node at this position yet. The result is the introduction of all three nodes of the particular crack face.

2.   *Insertion of crack edges:* Hereafter, the three edges connecting the three nodes are inserted. The insertion of additional nodes is generally necessary to create the edges. The position of these nodes depends on the strategy of the insertion process and will be discussed later.

3.   *Insertion of faces:* The last step consists in an explicit creation of the face. As in the precedent step, the addition of nodes is sometimes required.

a) Insertion inside an element   b) Insertion on an edge

c) Insertion on a face
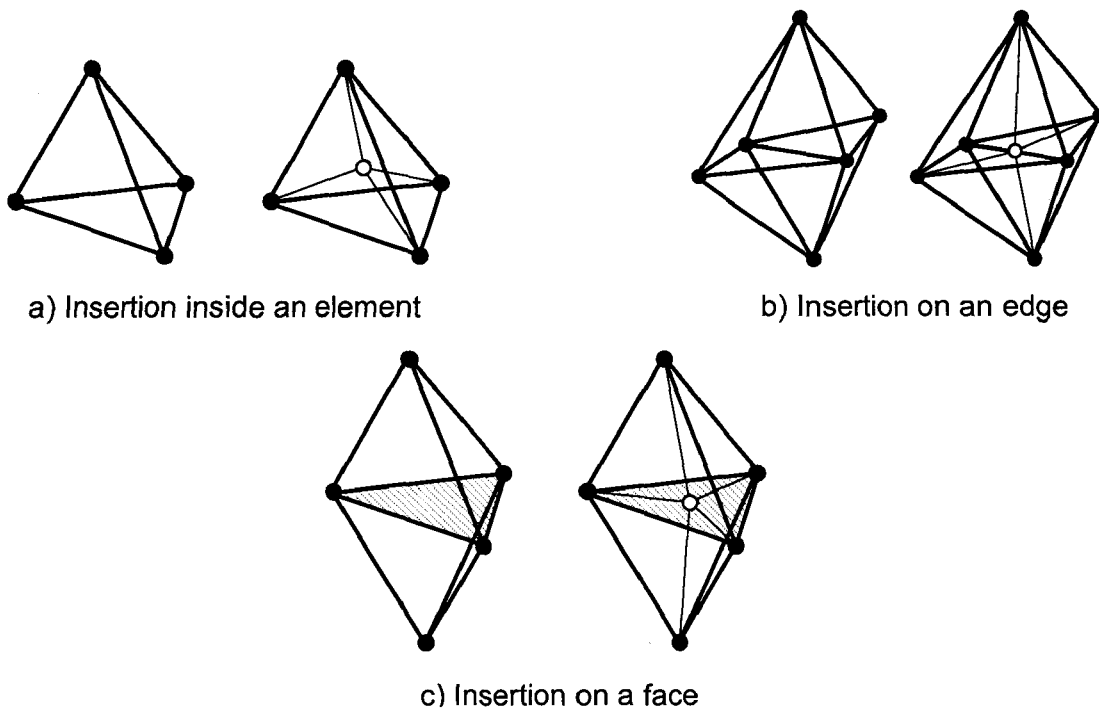
Fig. 52: ADAPCRACK3D - Vertex insertion

The critical phase of this iterative procedure can be resumed to the insertion of additional nodes (see Fig. 52) and can be investigated by two approaches. The first technique is a *direct way*, which consists of a direct insertion and follows the precedent steps. This simple methodology has the disadvantage to produce worse mesh quality. The second method uses the Delaunay algorithm [She99]. Its main idea is to find all elements, whose circumradii contain the new node, erase those elements (the so-called cavity) and create new ones under inclusion of the new node. It is important to notice that the 3D Delaunay algorithm creates at least a valid, but in contrast to 2D algorithm not necessarily a high quality mesh. The Delaunay algorithm does not respect already existing FE-objects (edges, faces), which means that inserting a node in order to create an edge might destruct another edge. That is why a *modified Delaunay algorithm* was developed for this purpose.

Although the insertion of vertex is realised by high-developed algorithm, the mesh quality has to be ensured and is the first stage in the way of a mesh improvement. Within ADAPCRACK3D the so called *mean ratio* quality criterion was implemented: Let V be the volume of a tetrahedron T and $Vmax$ the volume of an equilateral tetrahedron T' having the same circumradius as T. Then the quotient $Q = V / Vmax$ defines a quality measure satisfying the standard definition of tetrahedron shape measures given by [Dom98]. In this work, the ratio $Q = 0.02$ is used as upper bound for elements that have to be improved. A first method consists in removing nodes by melting them. In fact, the density of nodes in the surrounding crack region is higher as necessary to mesh this area with quality. Nodes, which are not describing the crack mesh, can be merged with adjacent nodes. Moreover in order to obtain a better distribution of the nodes and consequently better mesh quality, an algorithm of controlled displacement has been implemented. Its mode of action is comparable to the Laplacian algorithm, apart from the fact that the final position of a node is not determined by the coordinates of the adjacent nodes but by the optimum quality of elements adjacent to this node. This algorithm is developed as optimisation software. In fact, this simple strategy of relocating nodes is expected to find only a local optimum of elements qualities. That is why another local optimum is searched and compared with the first one. The best found distribution of nodes is always stored. Finally the least (and better) local optimum or even the global one is taken into account. If necessary the whole mesh can automatically be reinitiated with those best node positions. This algorithm is very time costly, but gives excellent results in finding good meshes.

Finally, the correct crack description consisting of two surfaces lying directly at one another can easily be obtained by doubling those nodes, edges and faces and unstitching the FE-model along the crack face. Only nodes defining the crack front should not be debonding.

Submodeling technique

Once the mesh adaptation is realised, the Finite Element solver Abaqus carries out the mechanical analysis. To accurately evaluate the energy release rates related to each mode of fracture, ADAPCRACK3D applies the Virtual Crack Closure Technique (VCCT) technique [Ful02]. Although this method has a simple mathematical formulation, its application is only accurate with a regular mesh at the crack tip. Thus a submodel technique is proposed to study the stress field at the crack tip with a mesh composed by hexahedral elements. The aspect of the associated submodel is represented in Fig. 53. In consequence, two FE analyses have to be performed by Abaqus. The advantage of the submodeling technique is both to present a fine regular mesh near the crack in the submodel and to conserve a coarse mesh far from the crack in the global model preferable to attain a reduced computational time. The second analysis imposed by the submodeling only takes very little computational time due to the limited number of nodes.
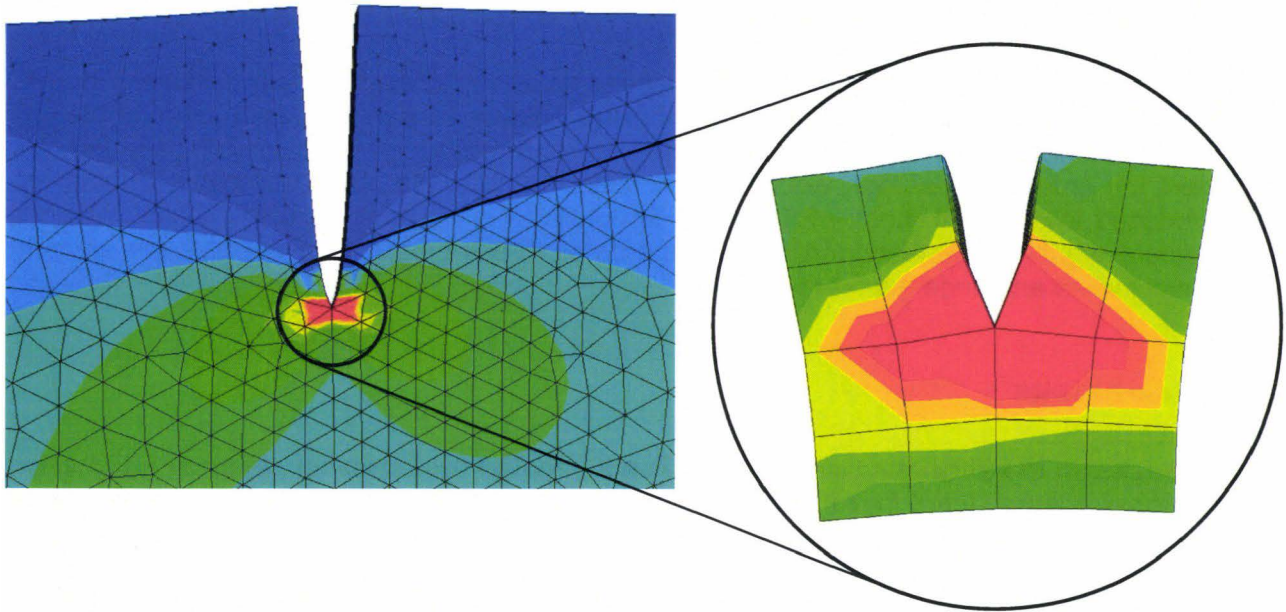
Fig. 53: Submodeling technique- Global model and associated submodel

From the results of the FE analysis, the software NETCRACK3D computes the energy release rates and corresponding stress intensity factors, whose magnitude are required to characterise the crack growth magnitude and direction. The crack front is then updated and the next FE analysis is run.

3.3.4   Zencrack - mesh generation

The principle employed to automatically mesh and remesh the global model constitutes the particularity of the software Zencrack. In fact, pre-defined element arrangements are used to describe the crack region. The method works by replacing one or more elements in the uncracked mesh by crack-blocks that contain section of crack front.
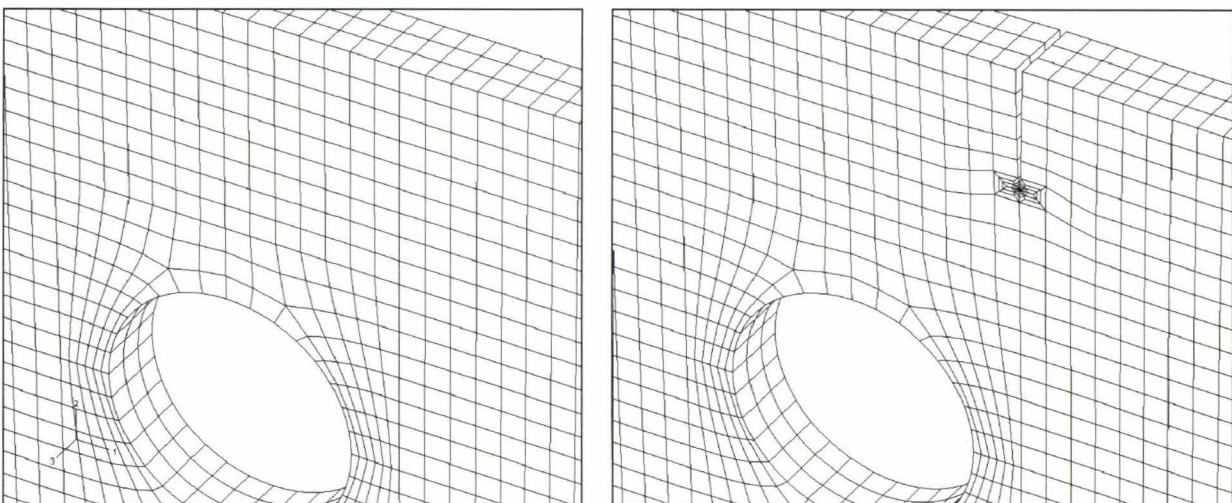
Fig. 54: Details of the uncracked and cracked front model

Mesh generation

In this work the design of the various specimens as three-dimensional finite element models is achieved with the pre-processor I-DEAS™ and Abaqus version 6.6, using eight or twenty-noded hexahedral elements. First, a simple mesh without crack is generated, see Fig. 54. Then, the software Zencrack version 7.4 is used to model the crack geometry. Cracks are introduced into a valid mesh of the intact structure by a mapping scheme, which replaces standard eight- or twenty-noded brick elements by "crack-blocks" and updates the element connectivities and node numbers [Tim00].

Crack-blocks

As defined in the Zencrack User Manual [Zen06], the term *crack-block* refers to a collection of brick elements stored in a unit cube. The arrangement of these crack-blocks is such that the cube form represents either a quarter circular or straight-through crack front on one face. Part of this face is allowed to open up under loading giving the opening crack face within the crack-block. Examples of unit cube crack-blocks are shown in Fig. 55 with their opening crack faces shaded for clarity.
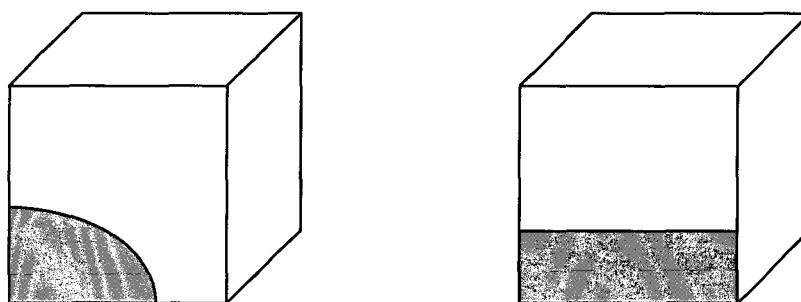
Fig. 55: Quarter circular or straight crack-block

The internal mesh of the crack-block has to fulfil two functions. The first one is to assure the connectivity with the surrounding user-supplied mesh composed of standard brick elements. The second is to closely model the fine crack tip. That is why the mesh of the crack-block coarsens away from the crack front. In the simplest case of all, a cracked mesh may contain only a single crack-block (and therefore a single crack front). If there is a single crack-block then only one side of the crack is modelled and symmetry constraints should be applied. If both sides of the crack are to be modelled, then pairs of crack-blocks are used with a *face-to-face* match of the crack-blocks, as shown in Fig. 54. In some cases, an initial crack should be inserted deep in the structure. For this special configuration, Zencrack introduces the notion of element split pairs. The crack face is then composed by crack-block and standard elements, as seen in Fig. 54. To separate pairs of standard elements that are on the crack faces, the nodes located on the common surface between the two elements are duplicated. The nodal definition of one element is updated, which leads to the creation of a new surface. To model a single sophisticated crack front, crack-blocks can be connected to other compatible crack-blocks, as in Fig. 56, where a quarter circular and a straight-through crack-block are merged or as in Fig. 54 where straight crack-blocks describe a through crack front.

Finally, the mesh containing the initial crack is submitted for analysis to Abaqus. During a growth analysis, new cracked meshes are automatically generated on the same way.
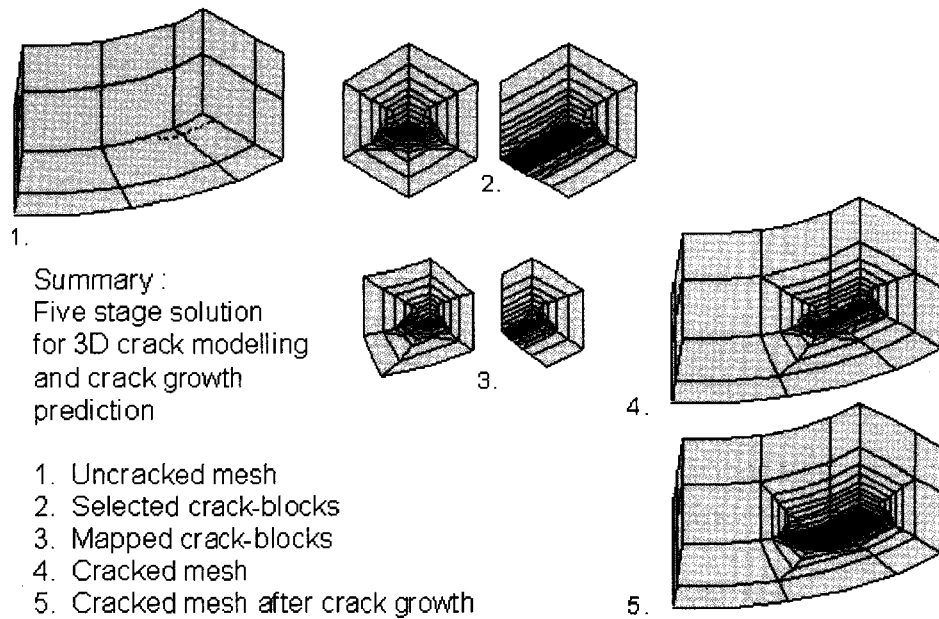
Fig. 56: Example of meshing using crack-blocks [Zen06]

Crack-blocks are composed by brick elements. Consequently, cracks can only be introduced in 3D virgin model. However, the application of supplementary boundary conditions offers the possibility to reduce the 3D FE model to a 2D model.

Singularity at the crack front

Crack-blocks enclose collapsed 8 or 20-noded brick elements at the crack tip. In order to closely model the singularity, the rosette geometry (see Fig. 37) constitutes the mesh pattern at the crack tip, what enables the evaluation of the J-integral on regular contours (see chapter 3.1.4). With collapsed 20-noded brick elements, the user has the possibility to control the position of the midside node and to allow the generation of quarter point nodes if the context of LEFM is expected. The crack front itself is seen as a line of nodes on the crack-block surface [Zen06].

Mesh relaxation and boundary shifting

Crack-blocks are geometrically parameterised so that the user can completely defined the profile of the crack front. Especially, the user-defined script describes the position of the crack front inside the crack-block. However, the distortion of the crack-block elements has to be limited in order to ensure the greatest accuracy. That is why the definition of a crack-block is associated to the ideal ratio of crack size to crack-block edge length. Keeping the crack size at an ideal position within the crack-block contributes to minimise element distortion.

Nevertheless, this ideal position is not always compatible with the original mesh and the real crack position. The following procedure is applied: First, elements of the virgin mesh are replaced by crack-blocks. In a second step, the elements surrounding the crack-block are moved, such that the crack-block takes a minimal distortion geometry (see Fig. 57). This relaxation zone has to be defined by the user. The relaxation algorithm uses Laplacian smoothing to minimise distortion of elements surrounding the crack-blocks [Zen06].
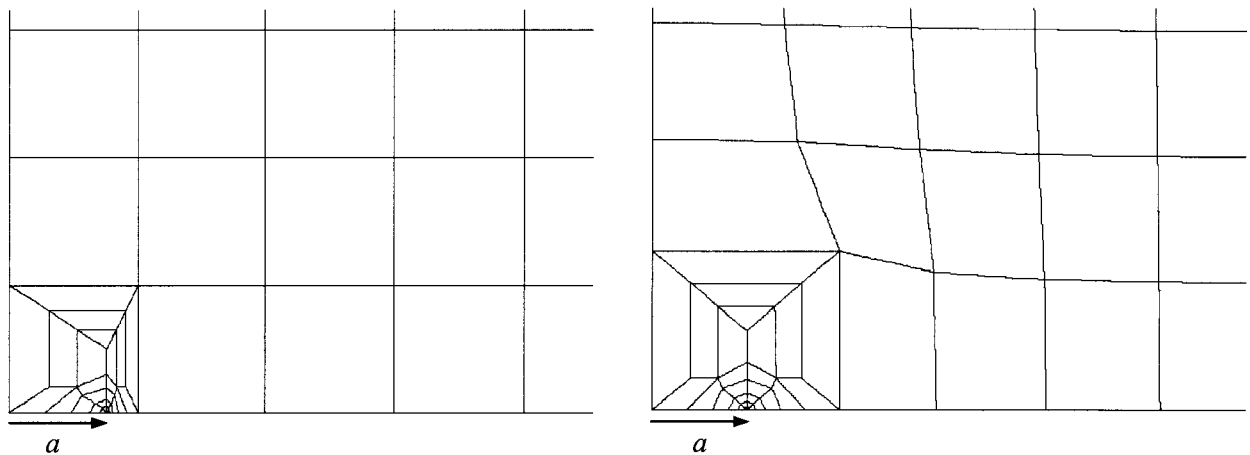
Fig. 57: Zencrack - Mesh relaxation [Zen06]

The numerical crack growth is generally characterised by small increments of crack propagation. A complete remeshing is not required and this step can be reduced to a small displacement of the crack-block. In this case, the relaxation algorithm is applied to update the surrounding mesh. The algorithm attempts to move element boundaries and resize the crack-blocks to maintain the crack at the ideal position [Zen06]. However, the surrounding mesh cannot be infinitely relaxed. Zencrack allows crack-blocks to transfer from one position to another, as seen in Fig. 58.
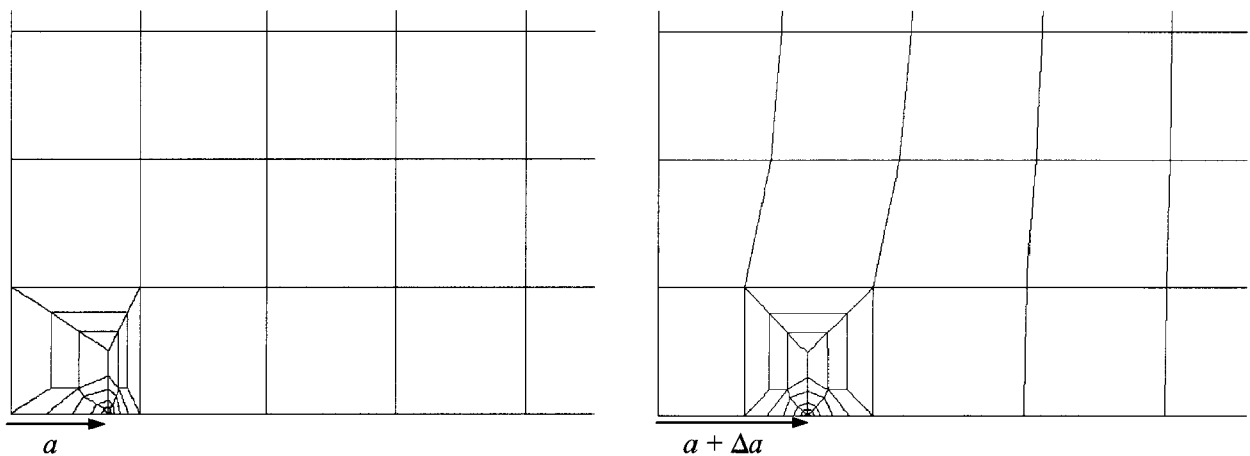
Fig. 58: Zencrack - Crack-block transfer [Zen06]

The combination of these two approaches improves the quality of the generated mesh and enables the crack advance in the structure, even if the techniques are time-consuming. As well, the mesh quality depends strongly on the surrounding mesh, where the distortion may become severe enough to cause high-deformed mesh or worst inside-out elements. This phenomenon appears in the case of significant non-planar crack growth.

Conclusion

After presenting the basic concepts of fracture mechanics, their implementation in Finite Element Method (FEM) is exposed. It covers the numerical methods available to evaluate the fracture mechanics parameters. For example, local parameters, such as SIFs are evaluated from nodal displacements behind the crack tip. Consequently, the crack tip singularity should be accurately represented using quarter-point elements. Moreover, the virtual crack extension or the contour integral methods enable to evaluate the ERR by considering an infinitesimal variation of the crack length Δa. Using a regular mesh at the crack tip, the virtual crack closure technique is also a numerical technique used to compute the energy released from nodal displacements and nodal forces. In a second part, the numerical techniques implemented to evaluate the magnitude and direction of crack growth are described. Three-dimensional crack propagation can also be simulated by updating the crack length step by step. The sequential approach applied in software packages Zencrack and ADAPCRACK3D is explained. In a third part, general techniques of re-meshing are described. As well, special methods developed in Zencrack (crack block advancement) and in ADAPCRACK3D (insertion of nodes in the existing mesh) are presented.

4 Experimental methods

In order to correctly predict the behaviour of a crack in a real component, material parameters specific to fracture mechanics are required. For example, the fracture toughness corresponds to the capability of a material containing a crack to resist fracture. The fracture toughness is commonly determined under an opening quasi-static loading. Similar parameters are also available to characterise subcritical crack propagation or fatigue crack propagation. The determination of material parameters requires accurate and reproducible experimental techniques. For this reason, experiments are generally performed with basic specimen geometries under simple loading conditions. Unfortunately, a specific test returns only one typical material parameter, what multiply the number of tests to completely characterise a material. Historically, the fracture mechanics tests were developed for metallic materials and then extended to plastics, as epoxy resins or thermoplastics. This chapter presents usual standard test methods, as a selection of original test geometries.

4.1 Fracture toughness - Mode I

4.1.1 Static test

The American Society for Testing and Materials (ASTM) [A-399, A-5045] or European Structural Integrity Society (ESIS) [ESI01] propose standardised test methods to evaluate the fracture toughness K_{Ic}. The indexes I and c indicate that the stress intensity factor K is evaluated for the critical state, at which the crack extension occurs, in the configuration of a mode I loading condition. The ASTM and ESIS standards suggest specimen geometries and loading conditions, which minimise the introduction of mode II and III. The Compact Tension (CT) specimen and the Single Edge Notched (SEN) specimen satisfy this condition. Specimens contain a crack front, which is generally manufactured at a notch position by applying appropriate periodic loading. The stress field from Eq. 25 is solved analytically. Experimentally, the critical stress intensity factor K_{Ic} is calculated with [Gro96]:

$$K_{Ic} = \frac{P_c}{B\sqrt{W}} f\left(\frac{a}{W}\right)$$

Eq. 136

The crack length a, the critical load P_c, at which the crack propagation occurs, and the fracture toughness K_{Ic} are related through the dimensionless function f, which depends upon the specimen geometry. The definition of the fracture toughness as material parameter imposes a reproducible testing method. It means that the estimated parameter K_{Ic} is independent on the specimen dimensions, and particularly on the crack length a. In order to fulfil LEFM conditions, the plastic zone at the crack tip shall be clearly smaller than other dimensions of the geometry. From this small scale yielding restriction results the size criteria:

$$a, B, W - a \geq 2.5 \left(\frac{K_{Ic}}{\sigma_y}\right)^2$$

Eq. 137

As presented in chapter 2.2.3, the term fracture toughness K_{Ic} is commonly employed in place of plane strain fracture toughness [A-399]. In fact, the value obtained in the case of a dominant plane strain condition is more conservative than in the case of prevailing plane stress state. In the case of a thin specimen, a dominant plane stress state exists along the crack tip and the plastic zone is not negligible. For this reason, thick specimens are preferred, as their geometry reproduces a plane strain condition along the crack front [And95, Wal03].

The fracture toughness depends on various parameters, like the microstructure of the material (size of particles, orientation of fibres ...) or the environmental conditions (temperature, humidity, corrosive medium ...) [Gro96, Wal03].

Material	K_{Ic} [MPa.m$^{1/2}$]
From literature:	
Titanium Allow Ti$_6$Al$_4$V	77 – 116
Steel alloy	50 – 115
Aluminium	14 – 28
AL$_2$O$_3$ – Ceramic	3 – 5
Tests performed internally:	
Epoxy resins	1 – 2
Thermoplastics	5 – 8

Tab. 5: Fracture toughness for some materials [Gro96, Wal03, Leb04]

4.1.2 CT specimen

Geometry and sample preparation

The test described in this chapter is in accordance with the ASTM standard E399-90 [A-399], which involves a standard test method for measurement of plane strain fracture toughness. This standard method was initially developed for metals, but is valid for other materials too, like epoxy resins [A-5045, ESI01]. The standard proportions are presented in the following figure. Additional recommendations are $W/4 \leq B \leq W/2$ and $0.55 \leq a/W \leq 0.65$. Generally, it is recommended to take the thickness $B = W/2$.
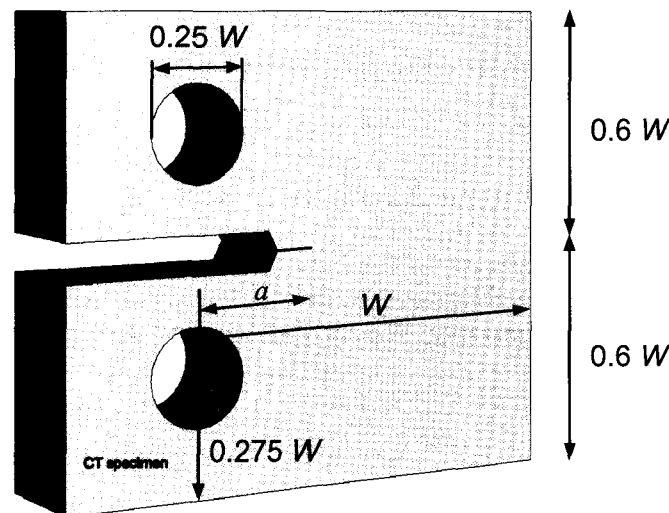

Fig. 59: Compact Tension specimen dimensions

In this study, dimensions are $W = 20$ mm, $B = 6$ mm and $a \geq 6$ mm. For CT specimens made of epoxy resins and with similar dimensions ($W = 20.3$ mm), it was shown that a state of plane strain is only verified if the thickness is larger than $B = 4$ mm [Wal03].

Specimen dimensions shall conform to the proposed tolerances, which are inferior to 0.1%. To minimise the perturbations due to Mode II and III, holes should be collinear and should follow the same orientation as the crack surface.

Another essential step in the sample preparation is the precrack generation. As formulated by Williams [ESI01], the ideal case corresponds to a natural crack which is re-initiated. In fact, a "non-ideal" precrack leads to an overestimation of K_{Ic} values. Yet, experience has shown that it is impractical to obtain a reproducible sharp. The ASTM [A-399] recommends for metals to machine a sharp notch and subsequently to extending it into a fatigue crack. In the case of plastics, sufficiently sharp precrack can be introduced by other techniques. In the case of mould compounds, the precrack can be directly embedded. For instance, a razor blade is positioned in the mould as insert [Wal03]. Additional publications propose to introduce the crack by tapping on a razor blade placed in the notch [Her80] or by sliding and sawing a razor blade across the machined notch [ESI01].

Test procedure

Both ends of the specimen are held in a clevis and loaded through pins (radius 0.24 W) in order to allow rotation of the specimen during testing. Standards recommend performing the tests with a tensile machine at a rate of 10 mm/min [A-399, ESI01]. Alternative rate shouldn't reach over 1 m/s and loading time shouldn't reach under 1 ms to avoid dynamics effects [ESI01]. To ensure a quasi-static loading condition, the fracture toughness is measured in this study under a loading rate of 0.1 mm/min. Measurements of applied displacement directly results from the position transducer of the machine (traverse displacement) or using a special displacement gage. The resulting load is recording by a load cell. In our case, experimental data are acquired using the traverse displacement of a Zwick-Roell tensile machine. The load is measured by a 500 N load cell capacity. The resolution is 1 µm and 0.25 N for displacement and load, respectively.

As a result, a load versus displacement curve is obtained. Theoretically, a linear behaviour is observed and the force drops abruptly to zero, as the crack propagates. Fig. 60 is representative of the load-displacement curves obtained during the experimental campaign at ambient temperature. In fact, epoxy resins are brittle materials, whose behaviour is considered as linear elastic. The maximal force P_{max} corresponds to the force at which the crack propagates. The critical load P_c in Eq. 136 is taken equal to the maximal load P_{max}.

In this study, tests are also performed at high temperatures. Small non-linearities appear on the load-displacement diagram. In worth cases, the instant at which the crack propagation occurs can not be easily identified. To determine precisely the critical load, the domain of linear behaviour and the associated compliance C are first determined. Then, an arbitrary compliance obtained by a 5% increase of the initial compliance is evaluated. The respective lines are drawn in Fig. 60. The intersection of the line with compliance $C+5\%$ and the experimental load curve returns the load $P_{5\%}$. In the case of non-linearities, the critical load P_c is taken equal to the load $P_{5\%}$.
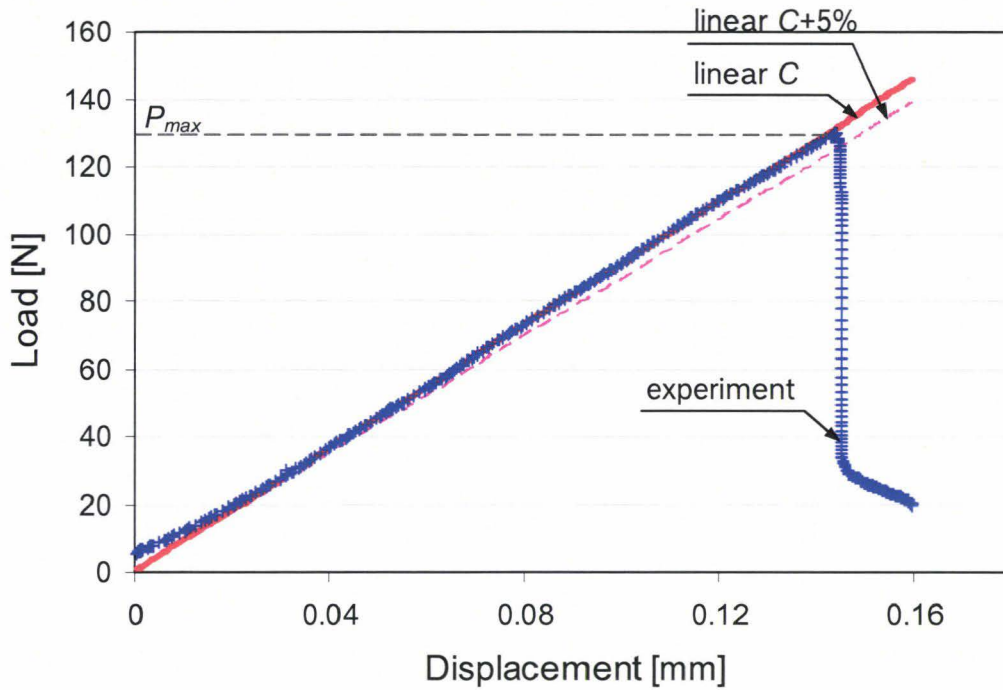
Fig. 60: Load-displacement curve
(test realised with an epoxy resin material at T = 23°C)

From the critical load P_c and the crack length a, the fracture toughness is then determined from Eq. 136, where the dimensionless function f is given by:

$$f_{CT}(\alpha) = \frac{(2+\alpha)}{(1-\alpha)^{3/2}} \left(0.886 + 4.64\alpha - 13.32\alpha^2 + 14.72\alpha^3 - 5.6\alpha^4 \right)$$

Eq. 138

$$\text{with} \quad \alpha = \frac{a}{W}$$

This expression is considered to be accurate to ±0.5% for any crack length satisfying $0.2 < a/W < 0.8$ [A-399].

It is recommended that at least three tests be performed for each material condition [ESI01]. Statistical methods, like standard deviation or Weibull distribution, enables to determine the confidence of experimental results.

4.1.3 SEN specimen and other geometries

The previous recommendations about the sample preparation, the precrack introduction, the test procedure or the critical load extraction are also suitable for other geometries. Geometries under a bending load required smaller sizes to achieve a state of plane strain along the crack tip [A-399, A-5045, ESI01]. The single edge notched specimen is loaded in three-point bending with a support span $S = 4W$. The dimensions of the cracked beam are presented in Fig. 61. The load P is applied on the upper cylinder and the two supports are fixed. Similar load-displacement curves are similar to those obtained with CT specimen. Consequently, the extraction of the critical load P_c follows the same process.
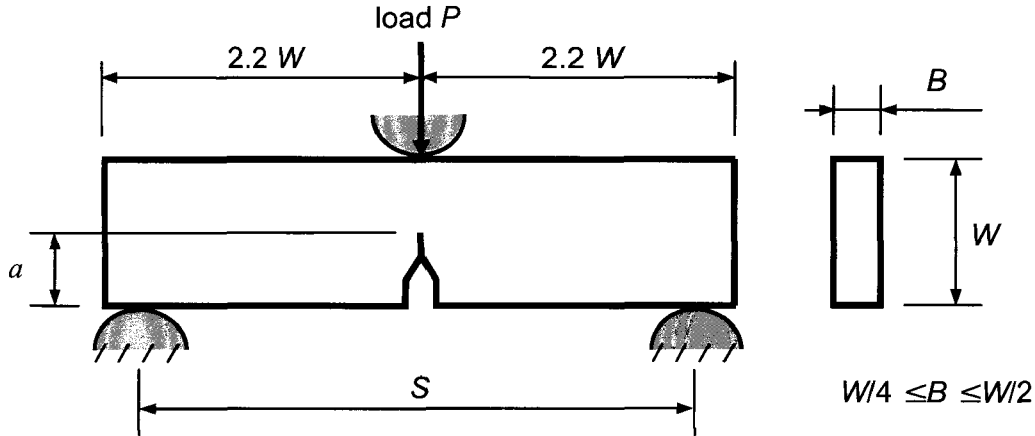
Fig. 61: Single Edge Notched SEN specimen dimensions

For a single edge notched specimen, the fracture toughness is evaluated from Eq. 136 using:

$$f_{SEN}(\alpha) = 6\alpha^{\frac{1}{2}} \frac{\left[1.99 - \alpha(1-\alpha)(2.15 - 3.93\alpha + 2.7\alpha^2)\right]}{(1+2\alpha)(1-\alpha)^{\frac{3}{2}}}$$

$$\text{with} \quad \alpha = \frac{a}{W}$$

Eq. 139

This expression is considered to be accurate within ±0.5% for any crack length satisfying $0 < a/W < 1$ [A-399].

For bar or hollow cylinder, a derived form of the CT specimen is proposed. The proportions of the disk-shaped compact and the arc-shaped tension specimens simplify the manufacturing of these samples [A-399, Mur87].

4.1.4 Crack length measurement

As the critical load P_c, the crack length a is an experimental parameter (see Eq. 136). For fracture toughness measurement, the crack length can be evaluated after fracture. This step is combined with the verification of the precrack profile, which shall present a regular geometry after fatigue. However, optic or electronic systems can be applied for the evaluation of the crack length in-situ during the test. For example, the crack length can be extracted from the opening displacement behind the crack tip (see Eq. 67) with the help of a displacement gages positioned near the crack tip and measuring the relative displacement of the crack surfaces [Kus04].

On the other side, optical systems are contact-free measurement techniques. This advantage is particularly interesting in the case of fatigue crack growth, for which the crack growth rate da/dN is measured during the test duration. Moreover, this method is independent of the specimen geometry. Optical techniques, like laser extensometer [Wal03] or photoelastic determination [Bro82], have an excellent precision. Yet, classical optical methods (picture or video recording) are preferred, as their accuracy is sufficient and their utilisation simple.

In this work, the procedure is based on a digital recording of the lateral sample surface. A straight crack front is assumed, which means that the crack length is considered as constant through the sample thickness. Thanks to a 2-million-pixel CCD camera, which is combined with a 70-180 mm (1:4.5-5.6) zoom lens, the pixel size is about 0.015 mm and the crack length can be determined with a precision less than 0.1 mm. This equipment is used not only for static tests, but for fatigue crack propagation too. Especially in the case of fatigue crack propagation, a post-processing of the images allows an accurate detection of the crack tip at regular intervals. The optical crack tracing (OCT) process is based on the variation of contrast between two consecutive images, as seen in Fig. 63.
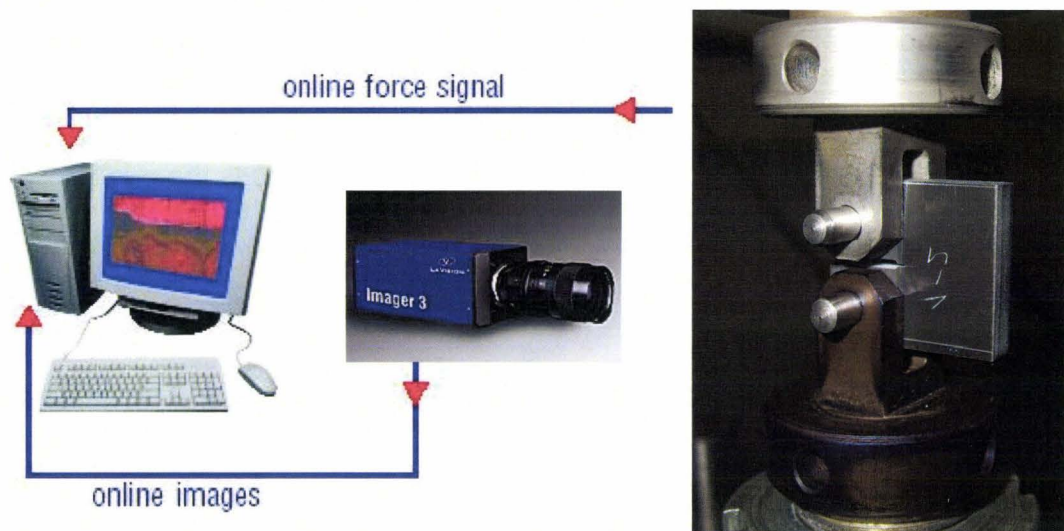

Fig. 62: Optical crack tracing (OCT) equipment
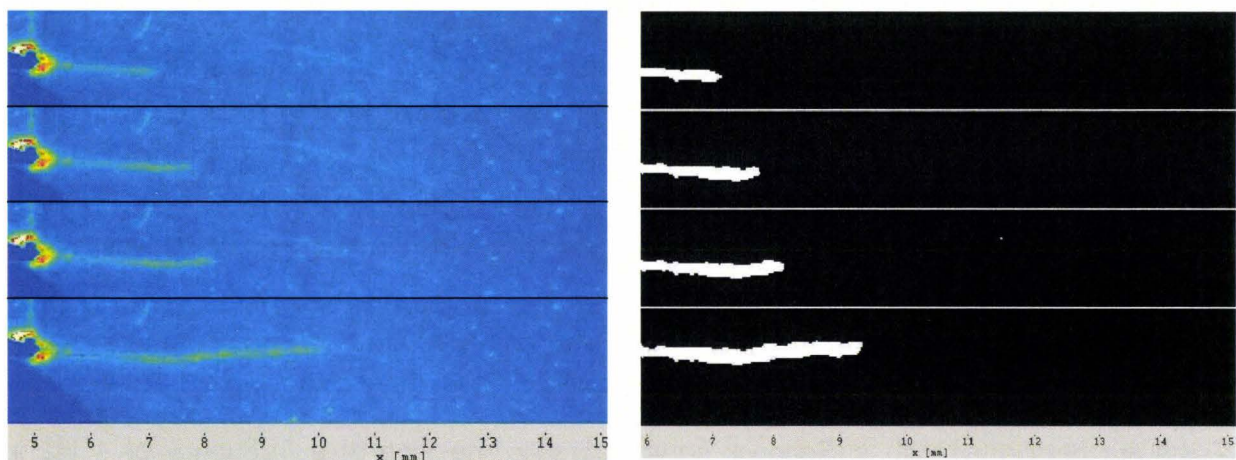
Fig. 63: Set of images recorded during a test and after post processing

4.2 Fatigue crack growth

In materials science, fatigue describes the progressive, localised, and permanent structural damage of material. The resistance to repeated loading or endurance limit of a material is characterised with the help of S-N or Wöhler's curve, where S and N stands for cyclical stress magnitude and the cycles to failure, respectively.

Similar to this definition, fatigue crack propagation results from the application of cyclic or fluctuating stresses or strains at the crack tip. The applied maximal stresses are thus below the critical value of fracture toughness, yet may still cause a crack propagation. The fatigue crack growth is generally represented by the crack growth rate da/dN as a function of stress intensity factor range ΔK.

4.2.1 Fatigue test

Tests described in this study are in accordance with the ASTM standard E 647-95, which involves a standard test method for measurement of fatigue crack growth rates [A-647]. This standard method was initially developed for metals, but is also valid for other materials [ESI01]. The study is confined to cyclic opening mode. The conditions of LEFM are satisfied, so that the concept of stress intensity factor K is appropriate. For periodic loading, the notion of stress intensity factor range ΔK is introduced. Eq. 140 describes the relation between the stress intensity factor range ΔK and the crack length a. The stress intensity factor K_{max} (respectively K_{min}) is associated with the maximal stress σ_{max} (resp. minimal stress σ_{min}):

$$\Delta K = K_{max} - K_{min} = (\sigma_{max} - \sigma_{min})\sqrt{\pi a} / Y = \Delta\sigma\sqrt{\pi a} / Y \qquad \textbf{Eq. 140}$$

While the crack length is measured with an optical system, a cyclic traction loading is applied to a CT specimen.

$W = 20$ mm
$B = 6$ mm
$a \geq 6$ mm
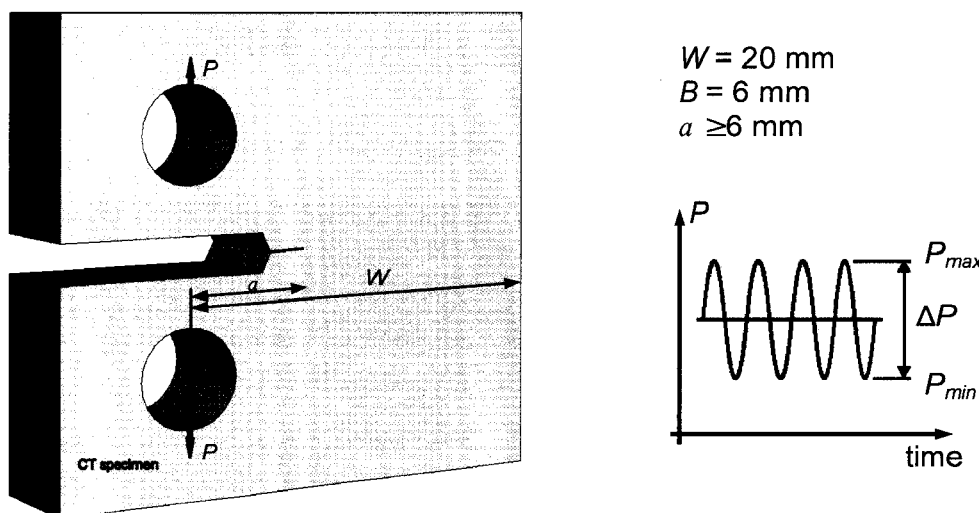
Fig. 64: Fatigue crack growth with CT specimen

Tests are performed with a Schenck servo-hydraulic machine at a frequency of 1 Hz at ambient temperature. A 40 mm-length position transducer records the position of the cylinder, as a load cell of 10 kN returns the applied load. An electronic system (Instron Labtronic 8400) coupled with a computer interface allows a fine control of the machine and counts the elapsed cycles. The sinusoidal load oscillates between a maximal load P_{max} and a

minimal load P_{min}. The load range ΔP has a constant amplitude during the test. The stress ratio R is fixed to 0.1:

$$\Delta P = P_{max} - P_{min} \quad \text{and} \quad R = \frac{P_{min}}{P_{max}} = \frac{\sigma_{min}}{\sigma_{max}} = \frac{K_{min}}{K_{max}} \qquad \text{Eq. 141}$$

Each crack length corresponds to a stress state at the crack tip. An analytical solution from the ASTM standard [A-647] provides the expression $\Delta K = f(a)$ for CT specimen:

$$\Delta K = \frac{\Delta P}{B\sqrt{W}} f_{CT}(\alpha) \quad \text{with} \quad \alpha = \frac{a}{W} \qquad \text{Eq. 142}$$

The function f_{CT} is defined by Eq. 138. Geometric dimensions (B and W) and loading parameters (frequency, ΔP and P_{max}) are maintained constant during the test. Consequently, the measurement of crack length as function of the cycle number constitutes the main information. During the experiment, the crack length is expressed as a function of the number of elapsed cycles N. The crack growth rate da/dN, i.e. the amount of crack growth da after a certain number of cycles dN, is derived from the curve $a = f(N)$. The crack growth rate is associated to a corresponding ΔK for a given crack length a.
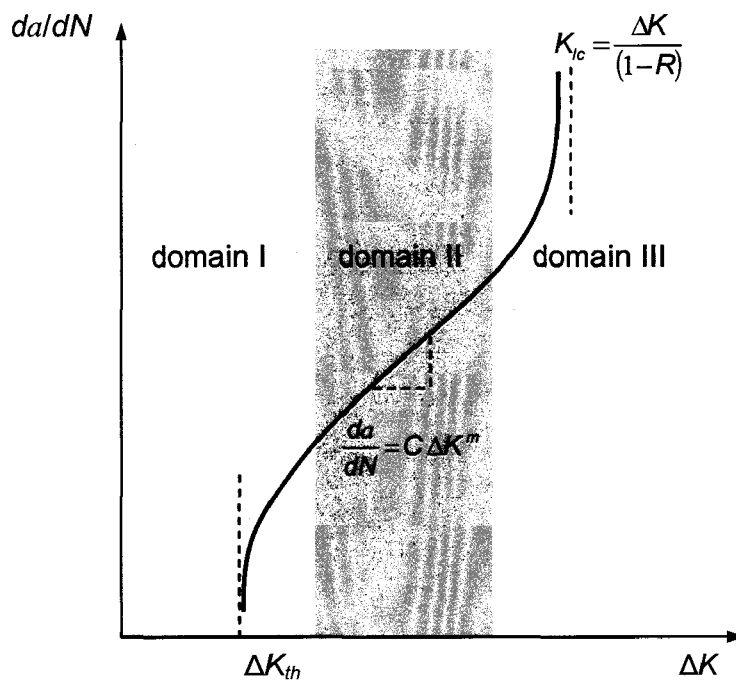
Fig. 65: Cyclic loading - Crack growth rate da/dN
as a function of stress intensity factor range ΔK

4.2.2 Fatigue law

The measurement of the crack growth rate as a function of the stress intensity factor range yields the da/dN - ΔK curve, as qualitative represented in Fig. 65. It is considered that no crack propagation occurs below the threshold ΔK_{th} (domain I). Experimental verification of this threshold is difficult. In the case of high amplitude (domain III), the loading condition approaches the configuration of a static test and ΔK tends to K_{Ic} (for $R = 0$). If a logarithmic scale is used for the representation, the da/dN - ΔK curve can be approximated by a straight

- 95 -

line in the intermediate domain (domain II). Paris et al. [Par61-63] propose to fit the curve to a power law:

$$\frac{da}{dN} = C \, \Delta K^m$$

Eq. 143

where C and m are material parameters. Although this law is purely phenomenological, it provides a suitable fit for many materials [Her80, Oso83, Wil84, Azi96]. The Paris exponent m has typically values between 2 and 4 for metallic materials [Law93, Gro96]. Similar experiments on epoxy resins were performed by Osorio [Oso83] and the resulted Paris exponents m were found in a range of [7.41 - 10.77]. The Paris relationship was later modified by Forman in 1967 to introduce the effects of the stress ratio R and of the fracture toughness K_{Ic}:

$$\frac{da}{dN} = \frac{C \, \Delta K^m}{(1-R)K_{Ic} - \Delta K}$$

Eq. 144

The evaluation of such a fatigue law enables the prediction of lifetime using an integration procedure. Let define a_d the minimal detectable crack length or the existing crack length and a_c the critical crack length. The lifetime or critical number of elapsed cycles N_c is given by:

$$N_c = \int_{a_d}^{a_c} \frac{da}{f(\Delta K)}$$

Eq. 145

4.3 Mode II and mixed mode

Standardised methods propose to evaluate the fracture toughness K_{Ic}, as seen previously. Introduced for a pure mode I, this concept of fracture criteria can be extended to pure mode II (respectively to mode III). However, no standard really exists to evaluate the critical stress intensity factors K_{IIc}. As well, the case of a mixed mode loading is rarely investigated.

4.3.1 Mode II

The critical stress intensity factor K_{IIc} can be experimentally determined with the help of adapted specimen geometries or modified loading fixture [Rid83, Erd63]. For example, Richard [Rich81, Rich85] designs a Compact Tension Shear (CTS) specimen to characterise the pure sliding mode of loading.

$0.6 \leq a/W \leq 0.7$
$b = 0.85\ W$
$c = 0.6\ W$
$D = 0.15\ W$
$f = 0.2\ W$
$P_{max} = N = Q = F$
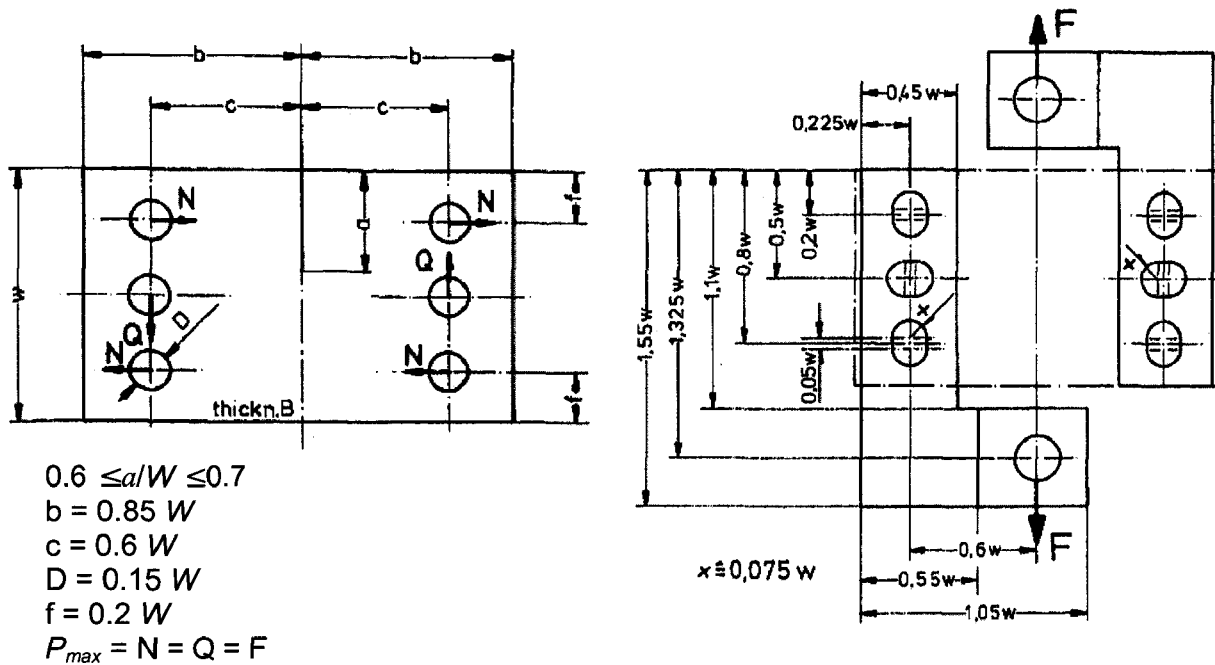
Fig. 66: Compact Tension Shear CTS specimen dimensions [Rich81]

As the simple geometry derives from the CT specimen, the conditions of plane strain state along the crack tip and of small scale yielding are also suitable. The loading frame enables a pure shear loading at the crack tip. For a thickness $B = W/2$ and $0.6 \leq a/W \leq 0.7$:

$$K_{IIc} = \frac{P_{max}}{BW} \frac{\sqrt{\pi a}}{1 - \frac{a}{W}} \sqrt{\frac{\left[-0.23 + 1.40 \frac{a}{(W-a)} \right]}{\left[1 - 0.67 \frac{a}{(W-a)} + 2.08 \left(\frac{a}{(W-a)} \right)^2 \right]}}$$

Eq. 146

Using the same specimen geometry, a mixed mode loading can be investigated with the help of a modified Arcan type fixture [Rich85]. The direction of the applied load can be adjusted, in order to generate a pure mode I, a pure mode II or a combination of these two modes.

4.3.2 Mixed mode loading

In a general way, a combined tensile-shear loading at the crack tip can be achieved using various geometries. The coupling mode effects between modes I, II and III was investigated by Dhondt [Dho01]. For example, a three point bending specimen with a crack inclined to the mid plane between the supports was used to describe the behaviour of a crack with a non-negligible mode III of loading.

However, most of geometries are limited to the study of combined mode I and II, as presented by Murakami [Mur87]. As defined earlier, mixed mode can be also investigated using the Compact Tension Shear (CTS) specimen. In this case, the load is applied with the help of a modified Arcan type fixture [Rich85]. This configuration enables to reach a pure mode II of loading. However, the centre cracked tension (CCT) specimen is preferred in this study, because of the simplicity of the sample geometry and the existing loading equipment. Due to the fact that for pure mode II, sliding of the crack flanks may occur (depending of the roughness of the flanks [Gil86, Gro96]), only mixed mode loading with $K_I > 0$ is considered in this work.

Centre cracked tension specimen

A crack of length $2a$ is inserted into a rectangular plate subjected to a uniform uniaxial tensile stress, as drawn in Fig. 67. The direction of the crack is inclined with an angle φ to the loading direction [Mur87]. Wilson [Wil71] and Kitagawa [Kit77] used boundary collocation analyses, as numerical methods to determine the expression of stress intensity factors as a function of geometry and applied loading for CCT specimens. This method gives results with an accuracy of $\pm 0.5\%$. As depicted in Fig. 67, for an angle $\varphi = 0$, the geometry is equivalent to the Middle Tension (MT) specimen [A-647]. The configuration of a pure mode II can not be reached with this sample geometry. In fact, for an angle φ close to 90°, the mode I and the mode II vanishes. Mode II is maximum for an angle φ near 45°. The ratio K_{II} / K_I increases with φ.

For $a/W = 0.5$ and $H = 2W$:
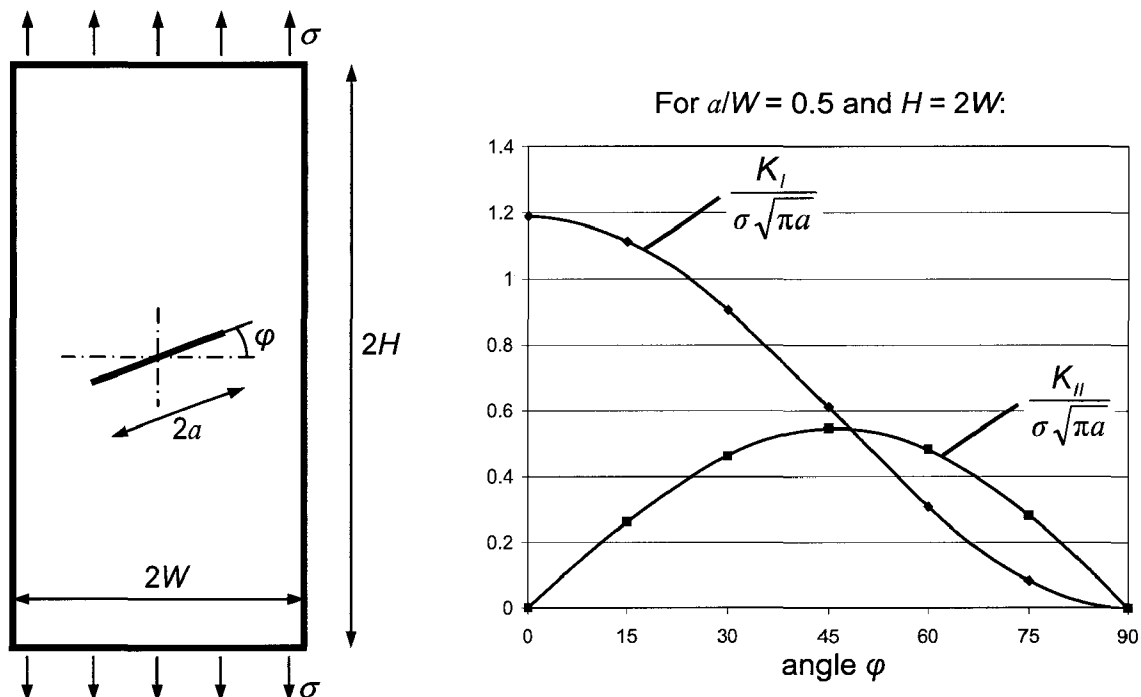
Fig. 67: Centre cracked tension CCT specimen [Wil71, Kit77, Mur87]

Perforated single edge notched specimen

In the previous geometries, the relative proportion of mode I and mode II is only known at the crack tip, as the crack propagates. To investigate the configuration of a curved crack front, a new specimen was developed, which have to meet some conditions. First, the geometry and loading conditions are simple. A unique crack front is inserted. Moreover, the proportion of mode II is non-negligible during the fatigue test and varies with the crack length.

The geometry used for this test is a rectangular tensile specimen containing a circular hole and a through thickness crack, which is named perforated single-edge-notched (SEN) specimen. Miranda [Mir03] realised similar tests with a 4-point bending specimen, for which Timbrell computed the crack path using a 2D plane strain model [Tim05]. In the present work, a cyclic uniaxial tension is applied. The crack deviates from its path due to the presence of the hole. The initial distance L between the crack tip and the hole centre is fixed to 7 mm as described in Fig. 68, but can be varied to study other crack bifurcations. The sample has a thickness of 3 mm.
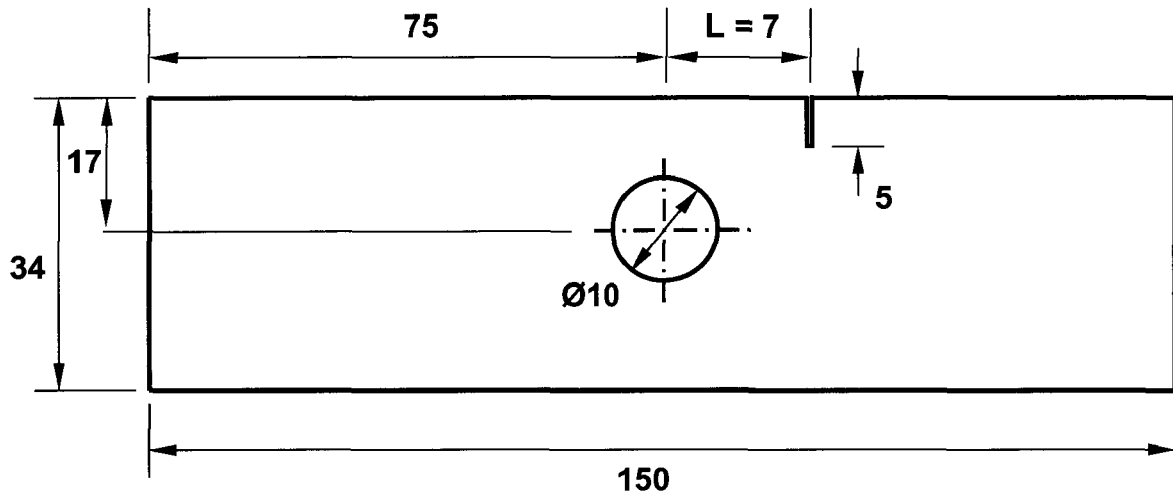
Fig. 68: Geometry of the perforated SEN specimen (dimensions in mm)
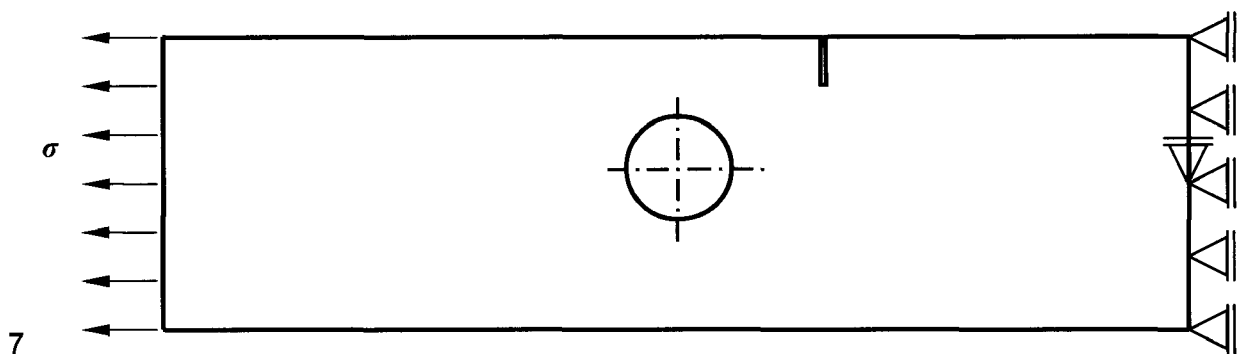
Fig. 69: Boundary conditions applied on the perforated SEN specimen

No analytical solution exists for this geometry. Consequently, the proportion of mode I and mode II is evaluated numerically as described in the next chapter.

Conclusion

Fracture criteria are introduced in chapter 2, the application of which required an evaluation of material parameters. Experiments on basic samples enable to characterise the crack propagation under pure mode I. Standards are proposed by the ASTM [A-399, A-5045] and ESIS [ESI01] societies to measure the plane strain fracture toughness with CT and SEN specimens. Analytical solutions exist to estimate the fracture toughness, which required the measurement of crack length and critical applied load. In a second part, methods to perform fatigue crack experiments are explained. Fatigue models like Paris law enable the identification of material parameters. Cracks are not only subjected to tensile, but also to shear loadings. Specimen geometries are proposed to study the material behaviour under pure mode II or mixed mode.

5 Numerical study of used test specimens

Analytical solutions can be established for specific geometries, as shown in section 4. Finite element models of these basic geometries are here generated, in order to verify the accuracy of numerical methods. First, the basic case of cracks under pure mode I is investigated with two-dimensional and three-dimensional models. Then, cracks subjected to mixed mode loading are submitted to analysis. Finally, a comparison between the software packages ADAPCRACK3D and Zencrack extends the discussion to the different numerical approaches and techniques, which can be implemented to predict the direction of crack propagation.

5.1 Procedure

Numerical models for CT, CCT and perforated SEN specimens are generated in this chapter. CT specimens introduce only mode I, where CCT and perforated SEN specimens create mixed mode loading conditions at the crack tip. Numerical methods are described within the context of LEFM in chapter 3. Tab. 6 lists the different FE methods used to estimate the investigated parameter for each model.

	investigated parameter	FE software	FE method	note
CT specimen	G, K_I	Zencrack	J-integral	pure mode I: $K_I^2 = E'G$
CCT specimen	G	Zencrack	J-integral	
	(K_I, K_{II})	Zencrack	nodal displacements	
Perforated SEN specimen	G	Zencrack	J-integral	
	(K_I, K_{II})	Zencrack	nodal displacements	
		ADAPCRACK3D	VCCT	$K_i^2 = E'G_i$

Tab. 6: FE methods used to estimate the parameters K_I, K_{II} or ERR for CT, CCT and perforated SEN models

5.2 Numerical evaluation of K_I based on 2D assumptions with Zencrack

5.2.1 FE model for CT specimen

The ASTM standard [A-399, A-5045] provides an expression to analytically evaluate the stress intensity factor K_I in CT specimens. This value, noted K_{ASTM}, is evaluated using Eq. 136 and Eq. 138. An estimation of the stress intensity factor can also be numerically computed and compared to the reference quantity K_{ASTM}. First, a 3D mesh of the uncracked CT specimen is generated with twenty-noded brick elements. From this virgin model and a user-defined script describing the crack front location, the Zencrack program generates a 3D finite element mesh containing the expected crack (Fig. 70a). As mentioned earlier, cracks

are introduced into the mesh of the intact structure using a mapping scheme, which replaces standard twenty-noded brick elements by crack-blocks and updates the element connectivities and node numbers (Fig. 70b). A behaviour corresponding to LEFM is assumed, so that collapsed quarter point elements are used at the crack tip in order to numerically reproduce the square root singularity, as seen in Fig. 38.

The ASTM standard [A-647] derives from a two-dimensional theory: a straight crack front and a plane strain state through the sample thickness are considered. In order to be consistent with these assumptions, all displacements in the z-direction are suppressed. Moreover, crack-blocks are geometrically parameterised, so that the user can completely define the profile of the crack front. Here, a straight front is modelled as initial crack profile.
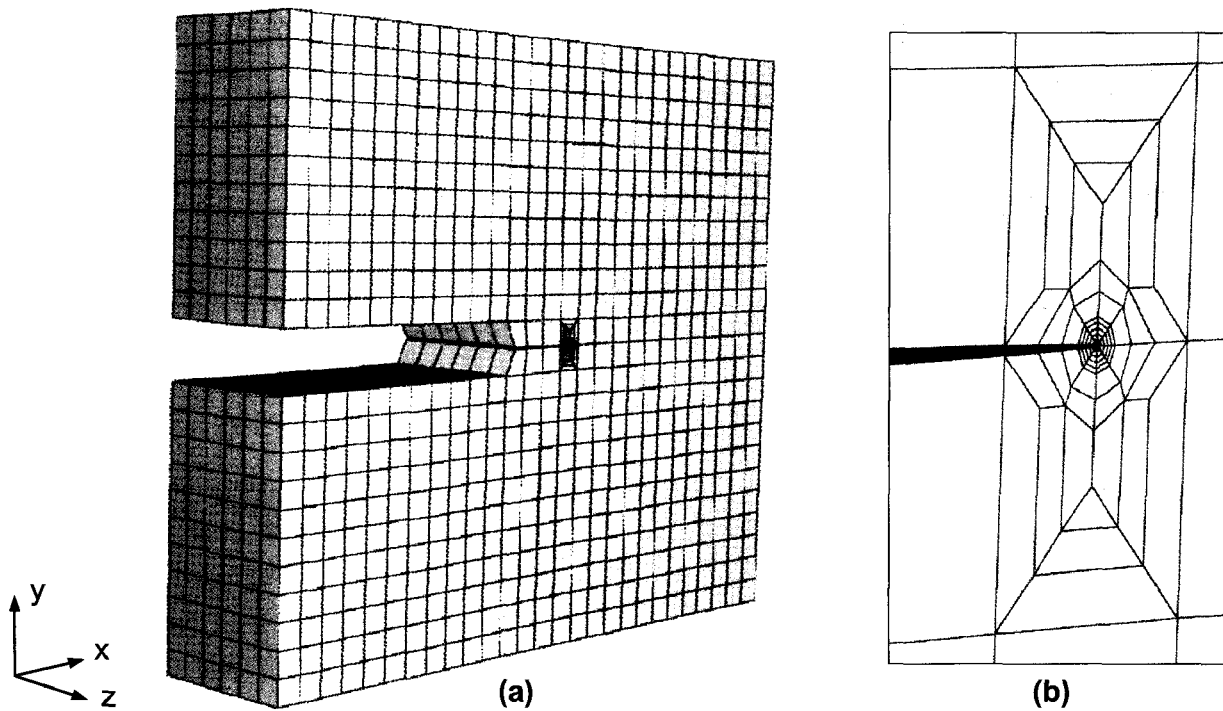
Fig. 70: (a) Numerical model of CT specimen; (b) crack-block at the crack tip

The CT specimen is modelled with a crack length of a = 7.5 mm. CT specimen dimensions (W = 20 mm, B = 6 mm) are defined in Fig. 59. The applied load is fixed to P = 110 N. As seen in Fig. 70a, loading pins and holes are not represented in the model. The applied load is distributed on nodes, the position of which corresponds to the centre of the pin hole.

The generated model is then submitted for analysis to the finite element code Abaqus. The Abaqus option *Contour Integral* enables to evaluate the J-integral, which is equivalent to the energy release rate G in the framework of LEFM [Aba05]. The respective stress intensity factor K_{FEM} can be numerically evaluated as indicated in Eq. 43 using $E' = E/(1-v^2)$ the effective Young's modulus for plane strain state.

Thanks to crack-blocks, the mapping scheme represented in Fig. 41 is reproduced at each node positioned on the crack front. This pattern creates regular contours in the plane (x, y). A value of J-integral is computed along each contour. Results are identical from one contour to the other. This is a very good indicator for mesh quality, i.e. the mesh refinement can be considered as sufficient. As a result, a unique value of J-integral is associated to each node along the crack front. Moreover, the energy release rate G takes a constant value along the crack front, due to forced plane strain conditions. In fact, the boundary condition u_z = 0 enforces a plane strain state over the sample, so that the FE model is equivalent to the 2D analytical solutions [Buc04, Dho01].

5.2.2 Accuracy of the CT specimen model

For the CT model with $a = 7.5$ mm and $P = 110$ N, a value of 28.3 MPa.mm$^{1/2}$ is computed for the stress intensity factor K_{FEM}. The reference value K_{ASTM} is equal to 27.9 MPa.mm$^{1/2}$. The relative difference between K_{ASTM} and K_{FEM} is only about 1.3%. The same procedure is reiterated for various crack lengths. Models are generated for crack lengths included between 6.5 and 15.5 mm. In terms of ratio a/W, the interval covers the range [0.325, 0.775]. The applied load is fixed to 110 N for each crack length.
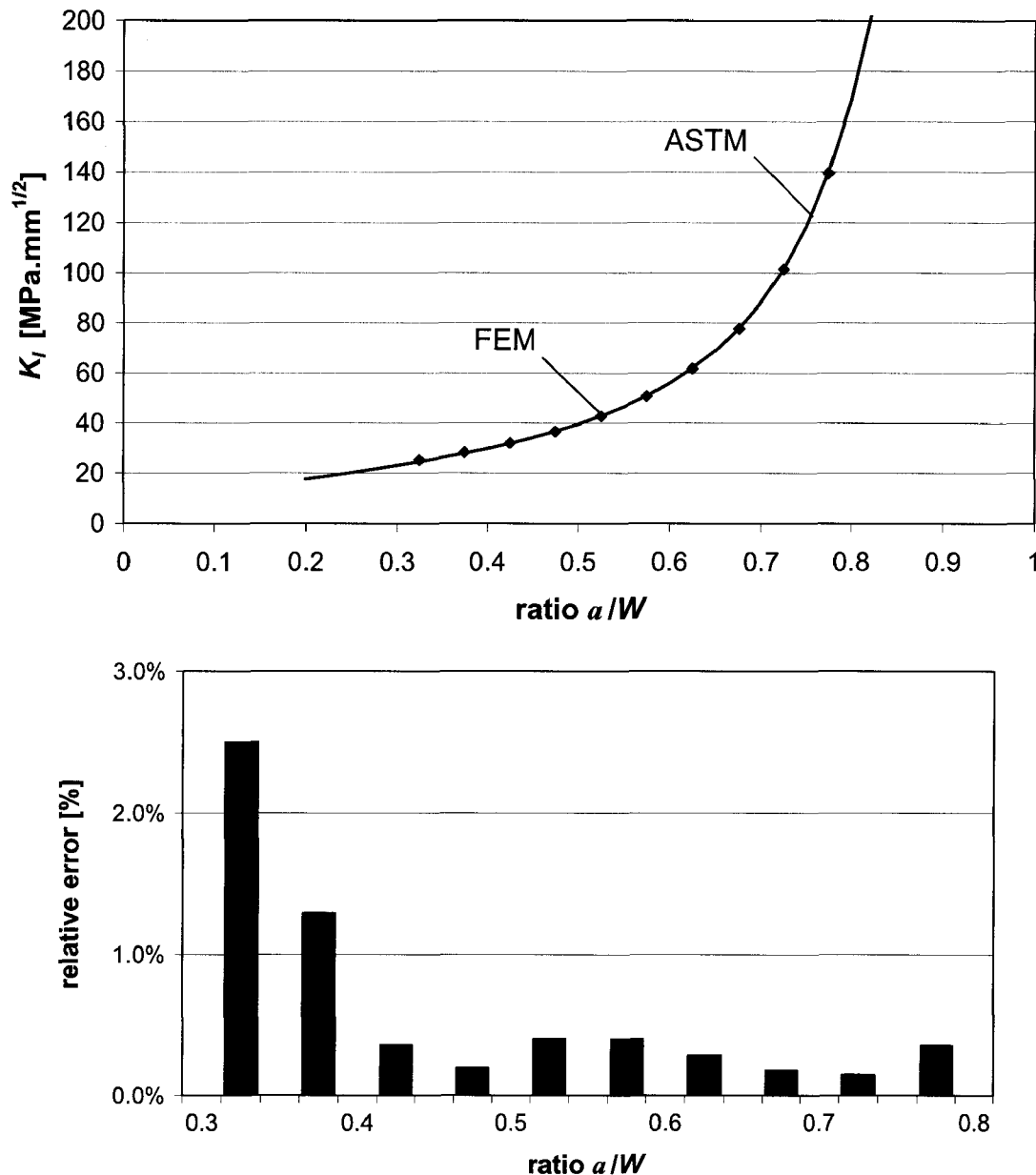
Fig. 71: CT specimen - Comparison between FE model and ASTM solution

As seen in Fig. 71, the stress intensity factors computed with the FE model are in accordance with the ASTM solution. The relative error is less than 0.5% for ratio a/W in the interval [0.4, 0.8]. For crack lengths included in the range a/W [0.3, 0.4], error decreases from 2.5% to 0.5%, and is due to the proximity of the loading pin holes to the crack front.

5.3 Numerical evaluation of K_I based on 3D assumptions with Zencrack

As real products have generally complex design, a restricted model with plane strain boundary conditions is not sufficient: the investigation of a full 3D model is required.

5.3.1 Through-thickness effects in 3D

It was shown in chapter 5.2 that the energy release rate G takes a constant value along a straight crack front. The corresponding stress intensity factor K_{FEM} is in agreement with the ASTM solution K_{ASTM} (see Fig. 72). A 3D model without plane strain conditions imposes to reconsider the distribution of stress intensity factors along the crack front. For this, the same FE model with a straight crack front through the sample is generated. In this case, the displacements on u_z are not constrained. Abaqus computes the energy release rate G at each node on the crack front. The stress intensity factors along the crack front are extracted from Eq. 43 with $E' = E/(1-v^2)$ and normalised with the analytical ASTM solution. The material parameters used for the simulation are E = 7000 MPa and v = 0.37. Fig. 72 presents the results of the two numerical models (with or without plane strain boundary conditions) for a crack length a = 7.5 mm.
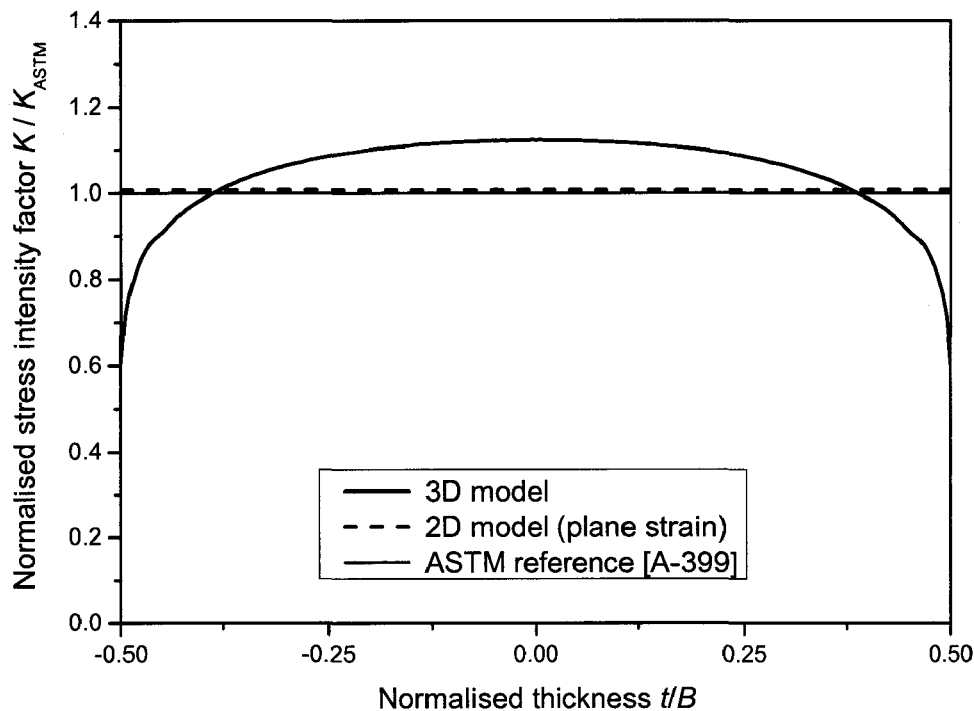
Fig. 72: SIF along the crack front for a FE model with a straight front profile

As previously described, the model with plane strain boundary conditions returns a constant stress intensity factor along the crack front, the value of which corresponds to the ASTM reference. Without plane strain boundary conditions, the variation of the SIF along the crack front points out a through-thickness effect in 3D [Yam78, Swe88]. Fig. 72 shows that the stress intensity factors in the centre of the CT specimen are higher than on the free surfaces for a straight crack front. So a larger extension of the crack is expected inside the sample. Experimentally, this phenomenon is revealed with the evolution from an initial straight crack front to a curved crack profile during the test [Dho01, Buc04].

5.3.2 Influence of the Poisson's ratio on the crack front curvature

As described by Yamamoto [Yam78], the shape of the crack front is directly related to the Poisson's ratio. This influence can be numerically demonstrated. Based on the previous 3D FE model (initial straight crack front and without plain strain boundary conditions), fatigue crack propagations are simulated with Zencrack. The Poisson's ratio takes alternately the values 0.15, 0.30, 0.37 and 0.45. Here, only the geometrical evolution of the crack front is investigated, so that the Paris law has no influence on the result. Each FE analysis returns successive computed crack fronts.

a_0 → direction of crack propagation →

$v = 0.15$

$v = 0.30$

$v = 0.37$

$v = 0.45$
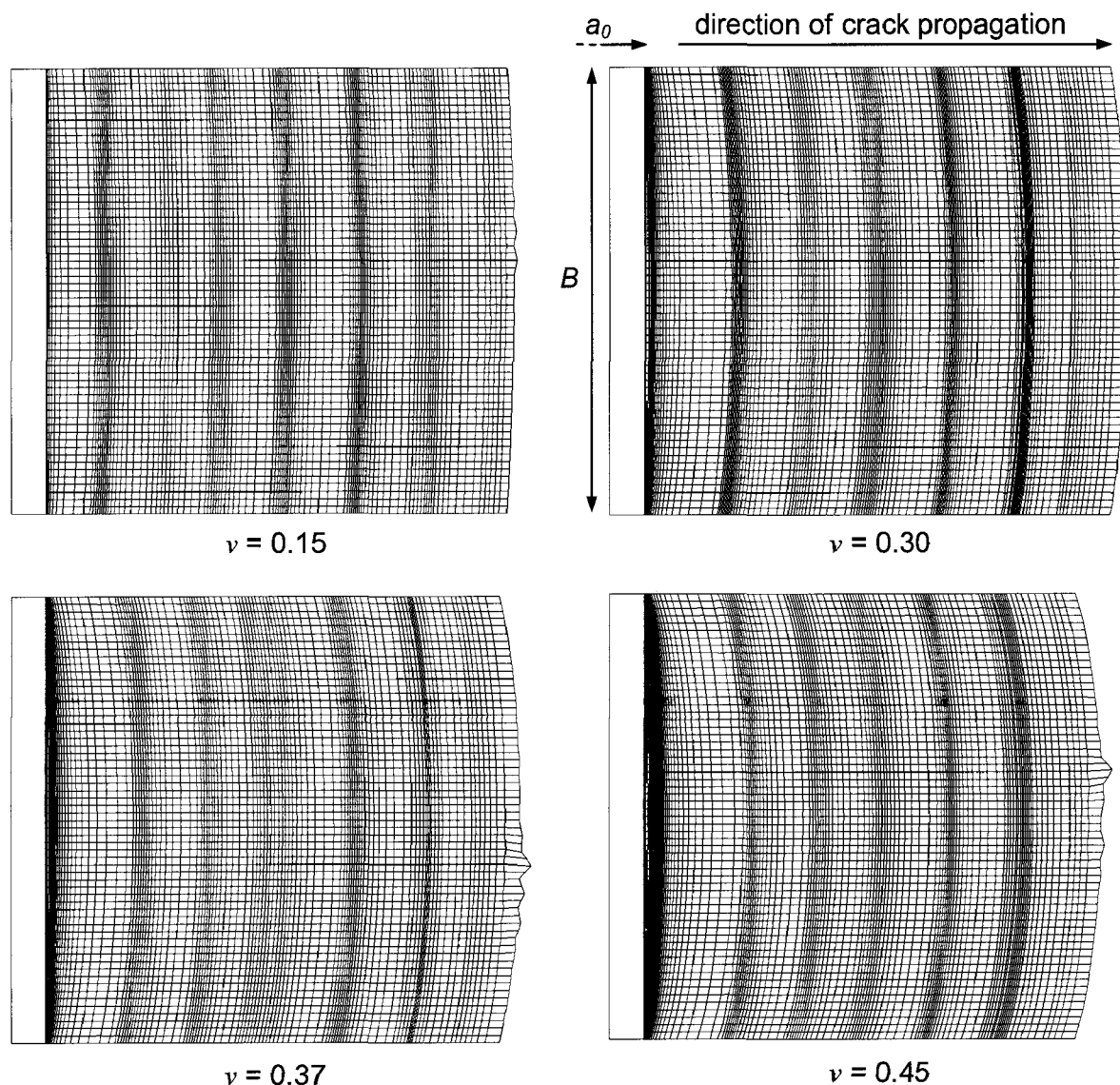
Fig. 73: Influence of the Poisson's ratio on numerical crack front curvature (fatigue crack propagation using a 3D model with an initial straight crack front and without plain strain boundary conditions)

On Fig. 73, the crack propagates from left to right. The initial straight crack front has a length a_0 in the FE model and the white surface on the left symbolises the precrack. The last computed crack front is drawn on the right side. As earlier stated, for a constant load ratio ΔP, the crack growth rate da/dN takes higher values, as the crack length increases. During the simulation, the amount of crack growth Δa is limited to a maximal crack increment Δa_{max}.

The simulation is stopped after the computation of almost 100 successive crack fronts, since the amount of crack growth Δa cannot be larger than Δa_{max} for a unique cycle $\Delta N = 1$.

The computed crack front evolves rapidly from the initial straight profile to a curved crack profile. Once the transition phase is over, the curvature is reproduced uniformly till the end of the analysis. The curvature is strongly dependent on the Poisson's ratio and can be characterised by the crack depth, which is defined by the difference between the crack length at the surface and in the middle of the specimen. The higher the Poisson's ratio, the higher the crack depth is. For a thickness $B = 6$ mm, a crack depth equal to 0.36 mm was computed for $v = 0.45$. The case $v = 0.0$ returns a straight crack front, i.e. the crack length is maintained constant through the thickness during the analysis.

Different crack profiles, which are described through elliptical or polynomial mathematical functions, are investigated. It is found that a profile, which is based on a 4th degree polynomial, fits closely the numerical crack front. This numerical crack front can be introduced in the FE model, as initial front design.

5.3.3 FE model with initial curved crack front

The FE model has the following properties:
- three-dimensional FE model
- displacements on u_z are not constrained (no plane strain boundary conditions)
- initial crack front is curved (4th degree polynomial)

As in chapter 5.3.1, the material has a Poisson's ratio equal to $v = 0.37$. The numerical model is generated with a crack length of 7.5 mm at the surface. With a profile based on the polynomial function, the crack length attains progressively a maximum of 7.76 mm in the middle of the specimen. The FE analysis returns a constant value for the energy release rate G along the crack front. The conversion into stress intensity factor is assumed with a plane strain state (see Eq. 43). The resulted stress intensity factor is named effective stress intensity factor K_{eff}.

The effective stress intensity factor can be compared to the ASTM solution. The stress intensity factor K_{ASTM} is evaluated with the surface crack length equal to $a = 7.5$ mm. In fact, the crack length is optically measured on the extern surface during the experiments. To be consistent with experiments, the reference crack length is chosen as the surface crack length. Results are plotted in Fig. 74a.

As expected, the effective stress intensity factor K_{eff} takes a constant value through the thickness. The effective stress intensity factor K_{eff} is about 10% higher than the ASTM value K_{ASTM} for the ratio $\alpha = a/W = 0.375$. This analysis is repeated for different crack lengths in order to characterise the influence of the crack length parameter a. FE models are generated for ratios α included in the range [0.3 - 0.6]. The difference between the stress intensity factors K_{eff} and K_{ASTM} is presented in Fig. 74b. A regular trend is observed for the relative difference, which attains a minimum around 9% for α included in the range [0.45 - 0.52].

The FE model shows that the energy release rates, respectively the stress intensity factors, are distributed uniformly along the crack front, as suggested from Broek [Bro82]. However, the extracted stress intensity factor K_{eff} differs from the ASTM solution K_{ASTM}. The ASTM standard was developed from 2D assumptions, so that the effect due to the thickness in 3D analysis is not taken into account. This explains a difference of about 10% between the current FE model and the ASTM solution.
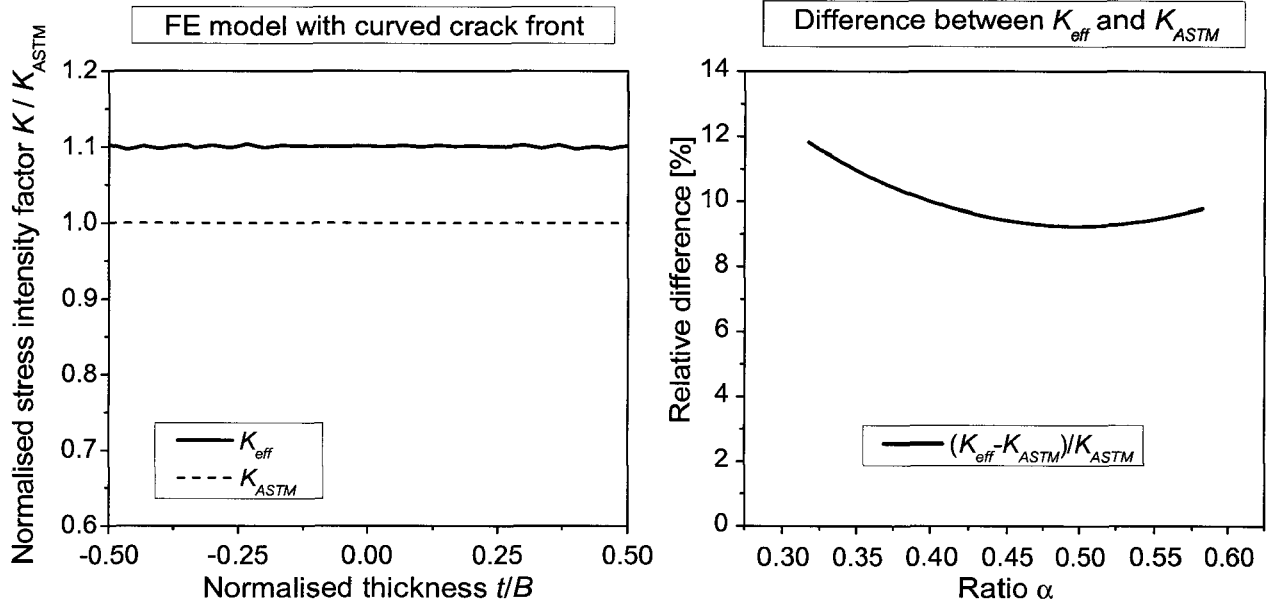
Fig. 74: (a) SIF along the crack front for a FE model with a curved front profile;
(b) Relative difference between K_{eff} and K_{ASTM}

5.3.4 Dimensionless function F

The ASTM norm [A-647] describes the relation between the stress intensity factor and the crack length with the help of a 4th order polynomial, as seen in Eq. 147.

$$K_{Ic} = \frac{P_c}{B\sqrt{W}} \frac{(2+\alpha)}{(1-\alpha)^{3/2}} F_{ASTM}(\alpha) \quad \text{with} \quad \alpha = \frac{a}{W}$$

Eq. 147

$$F_{ASTM}(\alpha) = 0.886 + 4.64\alpha - 13.32\alpha^2 + 14.72\alpha^3 - 5.6\alpha^4$$

As mentioned earlier, the function F_{ASTM} was formulated using 2D assumptions [Sra76, A-647]. Based on the previous numerical results, an extension to 3D is here proposed. The dimensionless function F is inherently related to the CT specimen geometry. As the curved crack front constitutes a geometrical characteristic, this effect can be integrated in a similar dimensionless function F_{eff}, which is defined as follows:

$$\frac{F_{eff}}{F_{ASTM}} = \frac{K_{eff}}{K_{ASTM}}$$

Eq. 148

The parameters F_{ASTM} and K_{ASTM} are evaluated from Eq. 147, in which the crack length a is chosen as the surface crack length. The effective stress intensity factor K_{eff} is extracted from FE models. The simulated data F_{eff} are evaluated for different crack lengths and fitted to a 4th order polynomial. For example, simulations are completed with the material parameter $v = 0.37$. The resulting form $F_{eff}(\alpha) = 1.511 + 1.74\alpha - 6.71\alpha^2 + 7.25\alpha^3 - 1.9\alpha^4$ furnishes a modified expression for the stress intensity factor as a function of the crack length $K_{eff} = f(a)$, as plotted in Fig. 75.
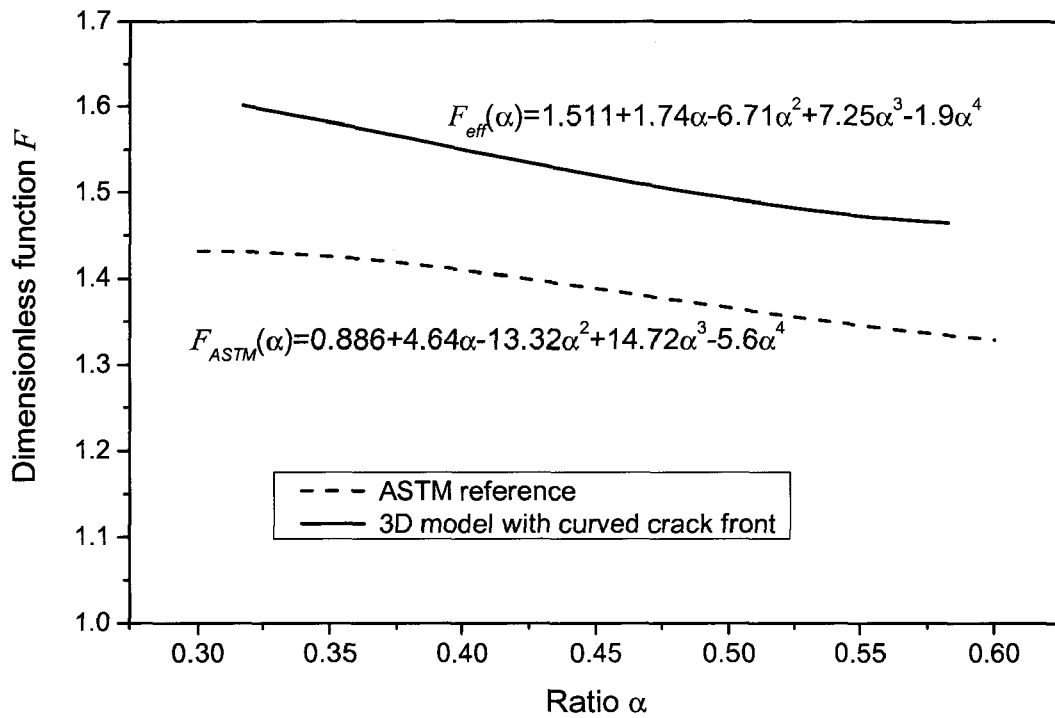
Fig. 75: Dimensionless functions F_{ASTM} and F_{eff}
(from FE models of CT specimen with B = 6 mm and W = 20 mm, v = 0.37)

The function F_{eff} is defined for a given Poisson's ratio (here v = 0.37). The same numerical method is used to provide the effective dimensionless functions for various Poisson's ratios. Results for v = 0.0, 0.15, 0.30, 0.37 and 0.45 are represented in Fig. 76.
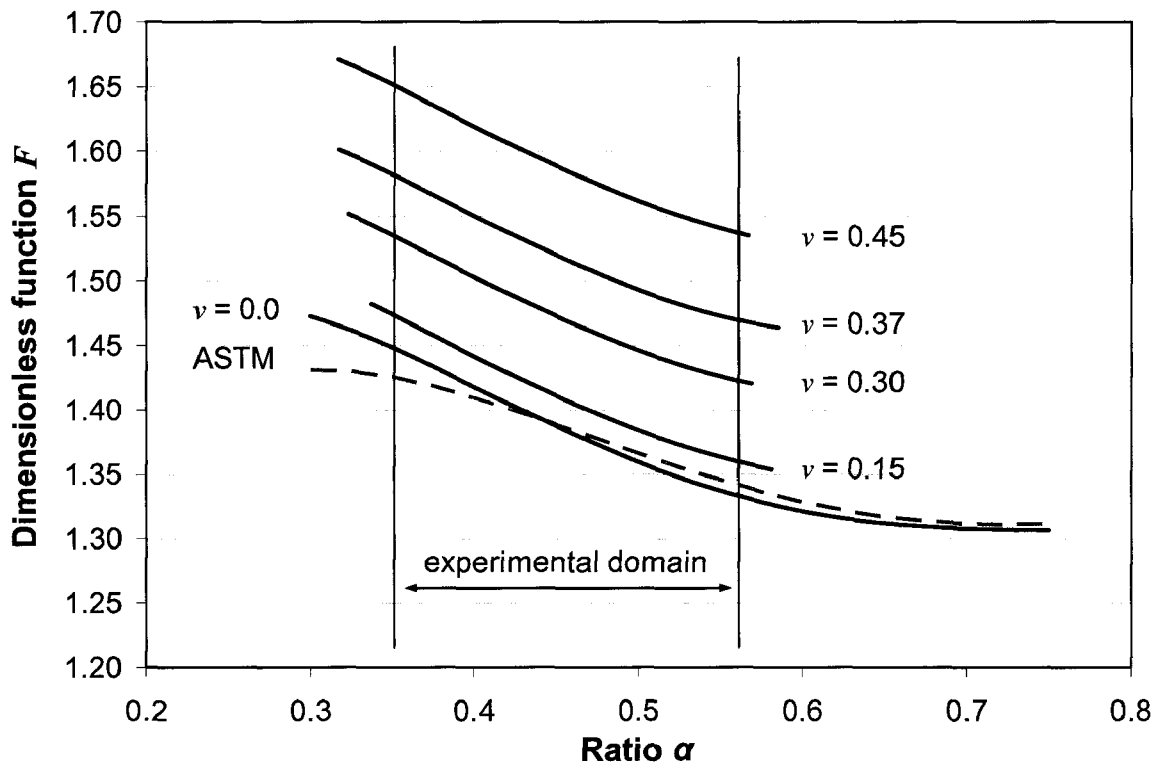
Fig. 76: Influence of Poisson's ratio on effective function F_{eff}
(from FE models of CT specimen with B = 6 mm and W = 20 mm)

The numerical investigation is limited to crack length ratios α in the range [0.32, 0.6], corresponding to the experimental domain. As expected, the function $F_{eff,v=0.0}$ gives a good representation of the ASTM function F_{ASTM}. In fact, no thickness effect is caused by a Poisson's ratio equal to $v = 0.0$. By increasing values of v, the difference between effective function F_{eff} and reference function F_{ASTM} increases.

5.4 Numerical evaluation of mixed mode with Zencrack

Cracks may have an arbitrary orientation with regard to the loading applied to the structure [Dho01]. Mixed mode loading conditions also occur at the crack tip. The Appendix presents a numerical study of an infinite plate, containing a crack inclined of an angle φ to the applied tensile loading. Stress intensity factors and energy release rate estimated with Zencrack are consistent with analytical solutions [Erd63]. The centre cracked tension (CCT) specimen is adapted from the infinite plate. Due to the approximation of a finite plate, the evolution of the stress intensity factors K_I and K_{II} and of the energy release rate slightly differs to the case of an infinite plate.

5.4.1 FE model for CCT specimen

In order to experimentally characterise the direction of propagation for cracks under mixed mode loading conditions, CCT specimens were introduced in chapter 4.3.2. Wilson [Wil71] and Kitagawa [Kit77] used the boundary collocation method to determine the expression of K_I and K_{II} as a function of geometry and applied loading (see Fig. 67). These numerical solutions are here taken as reference value [Mur87].

Specimens are 100 mm long, 50 mm width and 3 mm thick. In its middle, the rectangular plate contains a crack of length $2a = 25$ mm, the direction of which is inclined with an angle φ to the loading direction (see Fig. 67). Plates with angles $\varphi = 0°$, 15°, 30°, 45°, 60°, 70° and 75° are modelled with Zencrack. A load of 10 MPa is applied. Reference analyses are based on a two-dimensional model [Kit77]. Consequently, nodal displacements on u_z are constrained to enforce a plane strain boundary condition. After analysis, stress intensity factors are extracted with the crack tip opening displacement method (see chapter 3.1.2). Independently, the energy release rate is also estimated with the J-integral method. Both are constant along the crack front, due to the constraint on nodal displacement.

Results of the FE analysis are in agreement with values from the boundary collocation analysis (see Fig. 67). For the stress intensity factors K_I and K_{II}, the difference is less than 1.6%. The variation on ratio K_{II} / K_I is even less than 1.4%, as seen in Tab. 7. These results confirm that the crack tip opening displacement method returns a good estimation of the stress intensity factors and of the ratio K_{II} / K_I respectively.

Crack orientation φ	Reference value K_{II} / K_I [Kit77]	FE results K_{II} / K_I	FE results Difference
0°	0.000	0.000	0.0%
15°	0.235	0.232	1.4%
30°	0.510	0.507	0.7%
45°	0.892	0.887	0.5%
60°	1.558	1.562	0.3%
70°	2.481	2.470	0.4%
75°	3.375	3.398	0.7%

Tab. 7: CCT specimen - Comparison between FEM results and reference values

The accuracy of the J-integral approach is investigated with the same FE models. Eq. 45 gives the possibility to estimate a reference value for the ERR with the stress intensity factors from the boundary collocation method (see Fig. 67). Difference is less than 2.7%. The computed energy release rates present a good agreement with those from the literature.

5.4.2 Direction of crack growth

As stated in chapter 3.2.4, Zencrack can be used to predict the direction of crack propagation with the help of the Maximum Tangential Stress or the Maximum Energy Release Rate criterion. Each configuration of the CCT specimen is characterised for an angle φ, which corresponds to a ratio K_{II}/K_I according to the work of Kitagawa [Kit77] or $K_{II}/(K_I+K_{II})$, as seen in Tab. 8. The analytical solutions for MTS [Erd63] and MERR [Hus74] criteria are presented in Fig. 29 and are here expressed as a function of the angle φ in Fig. 77. Moreover, the numerical prediction is extracted from FE analyses and shown in Fig. 77.

	$\varphi = 0°$	$\varphi = 15°$	$\varphi = 30°$	$\varphi = 45°$	$\varphi = 60°$	$\varphi = 70°$	$\varphi = 75°$
K_{II}/K_I	0.000	0.235	0.511	0.892	1.558	2.482	3.380
$K_{II}/(K_I + K_{II})$	0.000	0.190	0.338	0.471	0.609	0.713	0.772

Tab. 8: CCT specimen - Equivalence between φ, K_{II} / K_I and K_{II} / (K_I + K_{II})
(for a CCT geometry with a/W = 0.5 and H = 2W)
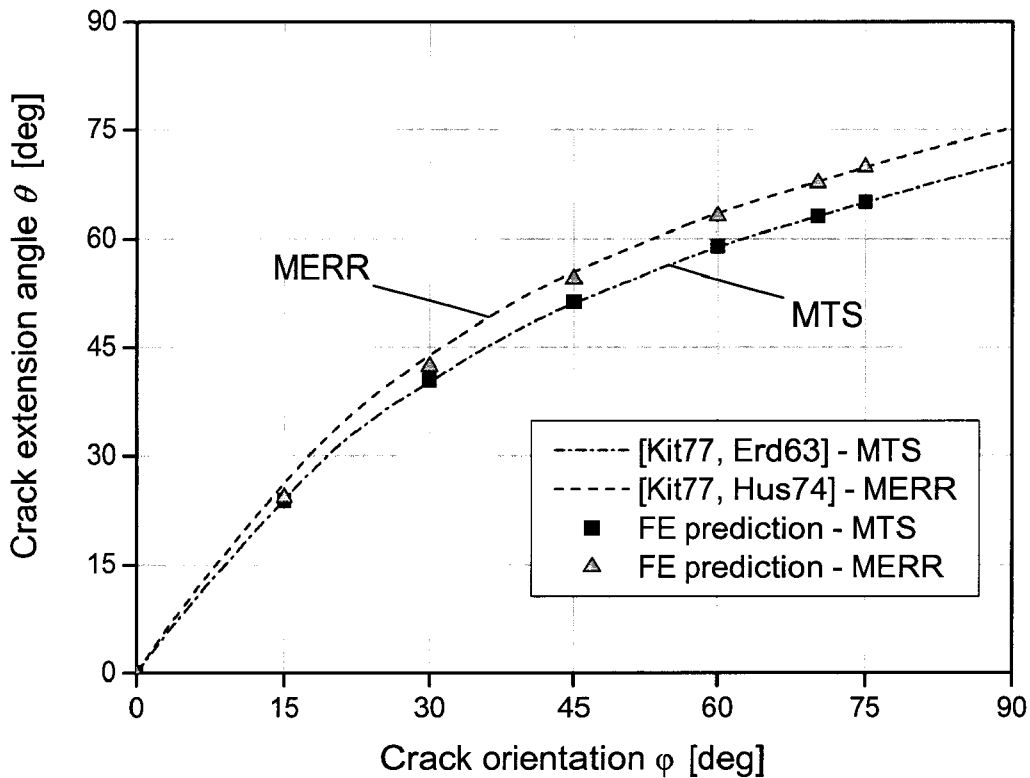
Fig. 77: CCT specimen - Prediction of the crack propagation direction

The difference between FE prediction and reference value does not exceed 3° for each model. The MTS criterion directly uses the ratio K_{II} / K_I (Eq. 91), while the MERR approach is based on the distribution of J-integrals for different virtual crack extension directions (see chapter 3.2.4). In the previous section, it was shown that the nodal displacement method accurately estimates the ratio K_{II} / K_I. As well, the error on the energy release rate is less than 3%. Therefore, numerical predictions with the MTS and MERR criteria are in good agreement with solutions based on the boundary collocation method [Kit77]. In conclusion, the prediction of the crack propagation direction is accurately implemented in FE models. Consequently, the MERR and MTS criteria, which are implemented in the software Zencrack, can be used as criterion during numerical simulations.

5.5   Prediction of a curved crack path

The capability to predict a curved crack path is studied through a comparison of two crack propagation software packages, ADAPCRACK3D and Zencrack. The perforated single edge notched specimen is selected as reference geometry for the analysis, dimensions of which are described in chapter 4.3.2. A succession of FE analyses returns a curved crack path, which is specific of the geometry.

5.5.1   Results from ADAPCRACK3D

The initial mesh is generated from a three-dimensional uncracked mesh composed by first order tetrahedrons. The definition of the initial crack is realised through the insertion of three-noded element surface in the global mesh. At the initial state, the global FE model is composed approximately by 33000 nodes and 20000 elements, as seen in Fig. 78. Once the global mesh is generated, a standard FE analysis is run.
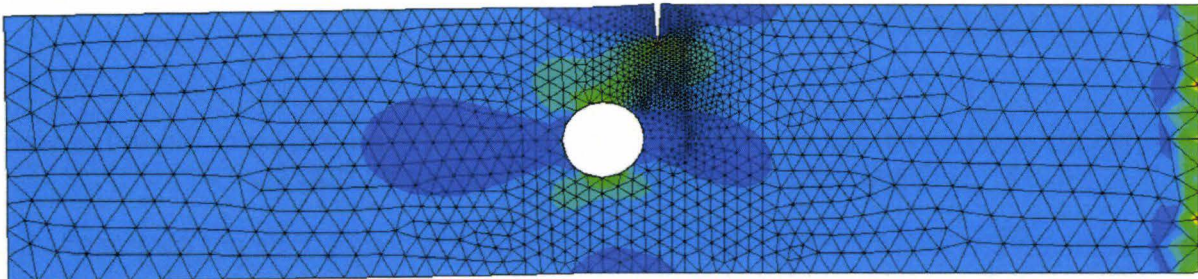
(a) Entire FE model
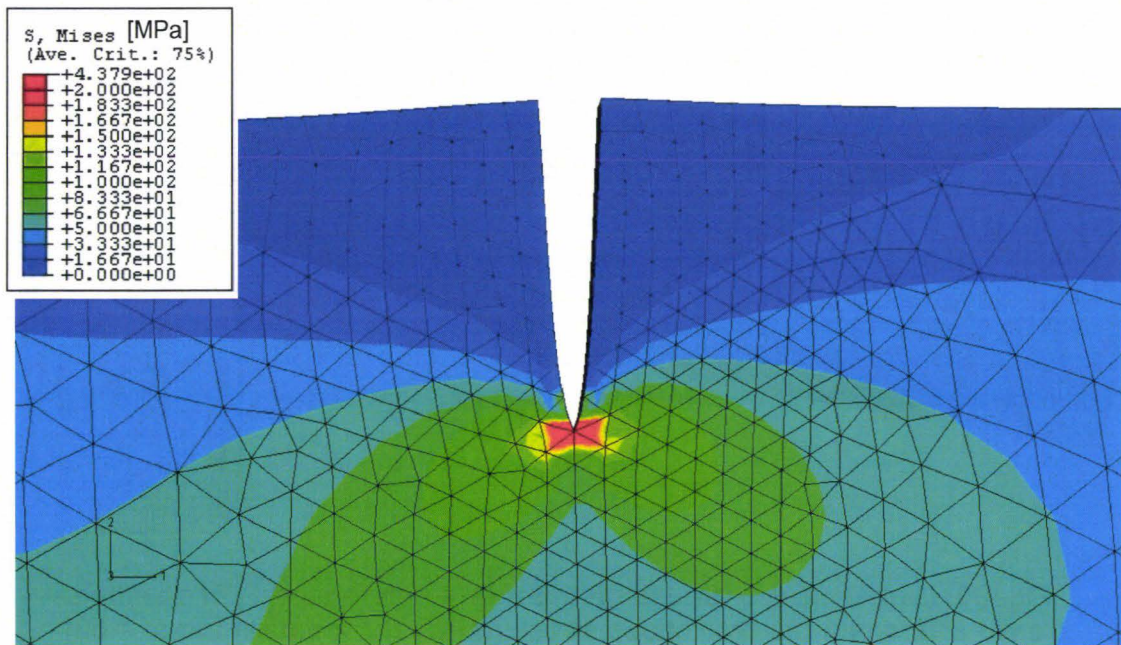
(b) Zoom on the crack tip zone

**Fig. 78: Global model - Stress distribution in perforated SEN specimen
at the initial state (von Mises stress [MPa], deformation factor = 50)**

- 113 -

As previously stated in chapter 3.2.2, ADAPCRACK3D uses the VCCT-method (Virtual Crack Closure Technique) to extract the stress intensity factors at the crack tip. Although this method has a simple mathematical formulation, its application is only accurate with a regular mesh at the crack tip. For this reason, a submodel technique is proposed to study the stress field at the crack tip with a mesh composed by hexahedral elements. The aspect of the associated submodel is represented in Fig. 79.
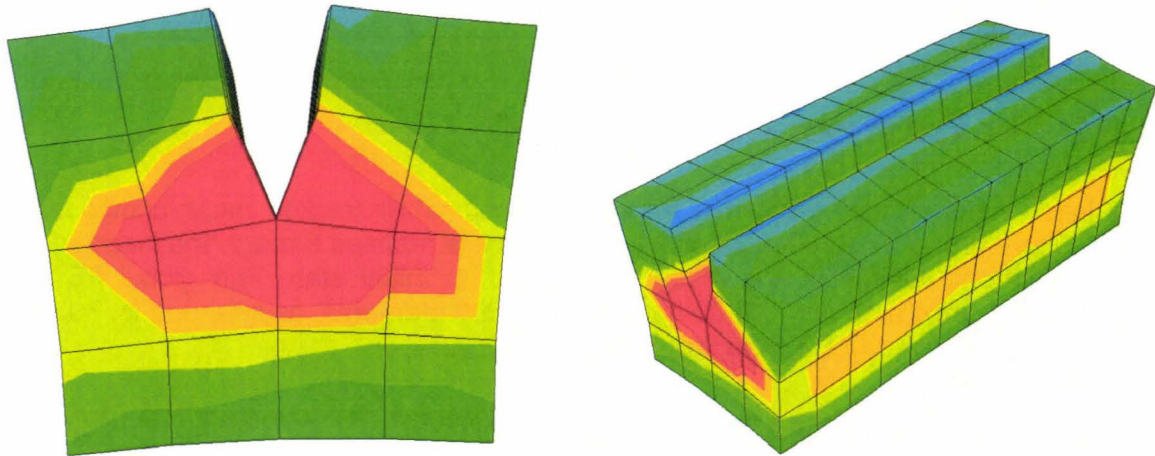
Fig. 79: Submodel - Stress distribution in perforated SEN specimen at the initial state (Hexahedron elements in order to apply VCCT)

At each increment, the crack extension and the direction of propagation are computed using the stress intensity factor distribution at the crack tip. A new crack front is defined, which is used to update the existent mesh. The simulation is achieved in 27 increments until the crack front attains the interior hole. The last FE increment is represented in Fig. 80.
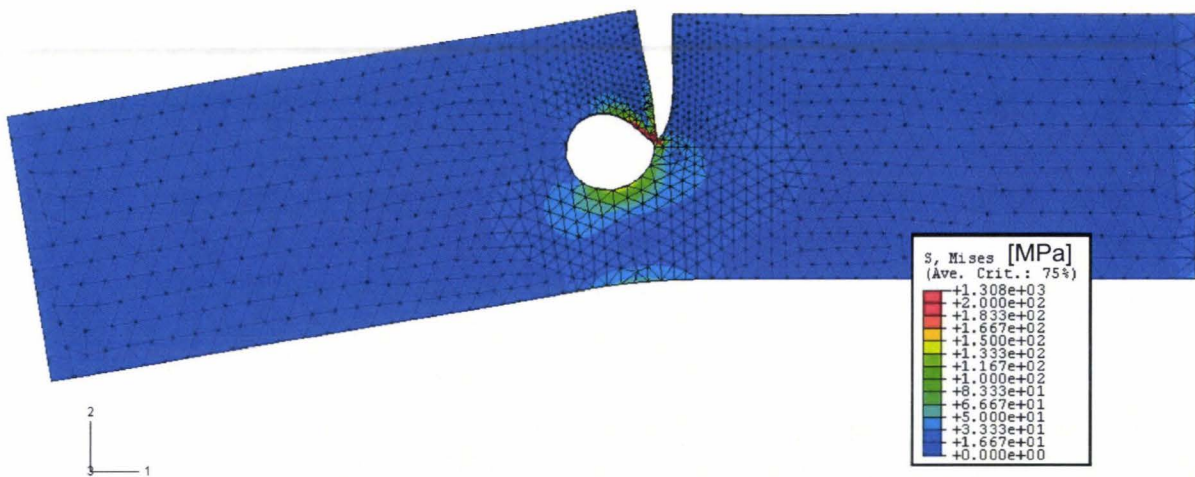
Fig. 80: Global model - Stress distribution in perforated SEN specimen after 27 increments (von Mises stress [MPa], deformation factor = 50)

Fig. 81 shows the development of the crack front in the SEN specimen during the simulation. It appears that the crack path is not dependent on the Z-coordinate (direction of the specimen thickness). In fact, the specimen is only 3 mm thick, so that through-thickness effects are negligible. Moreover, mode III is not predominant, due to the tension loading conditions. On this account the position of the computed crack front can be averaged over the specimen thickness.
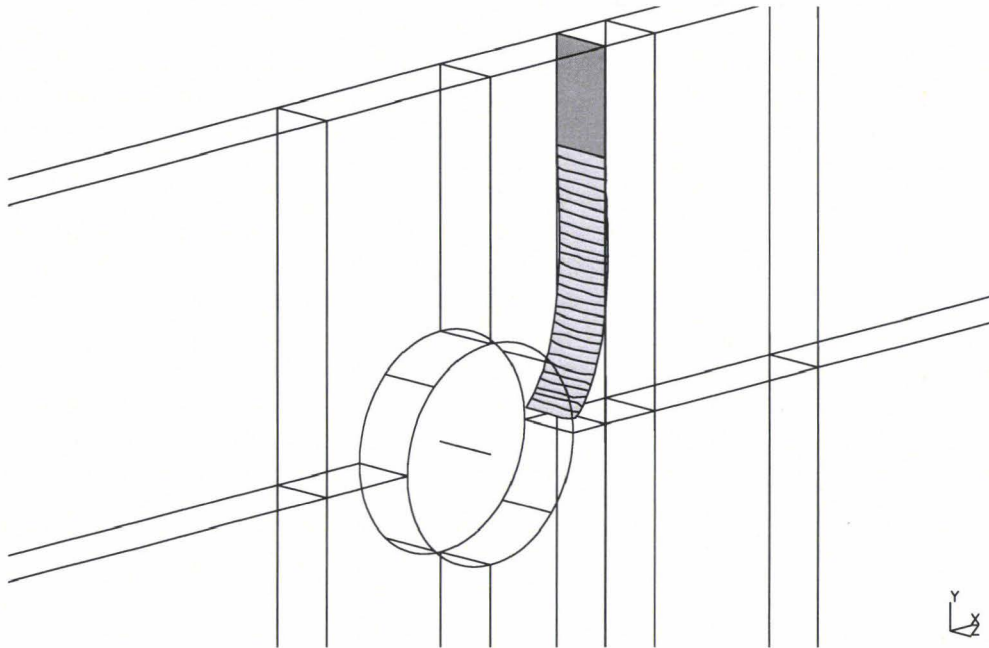
Fig. 81: ADAPCRACK3D - Simulated crack path
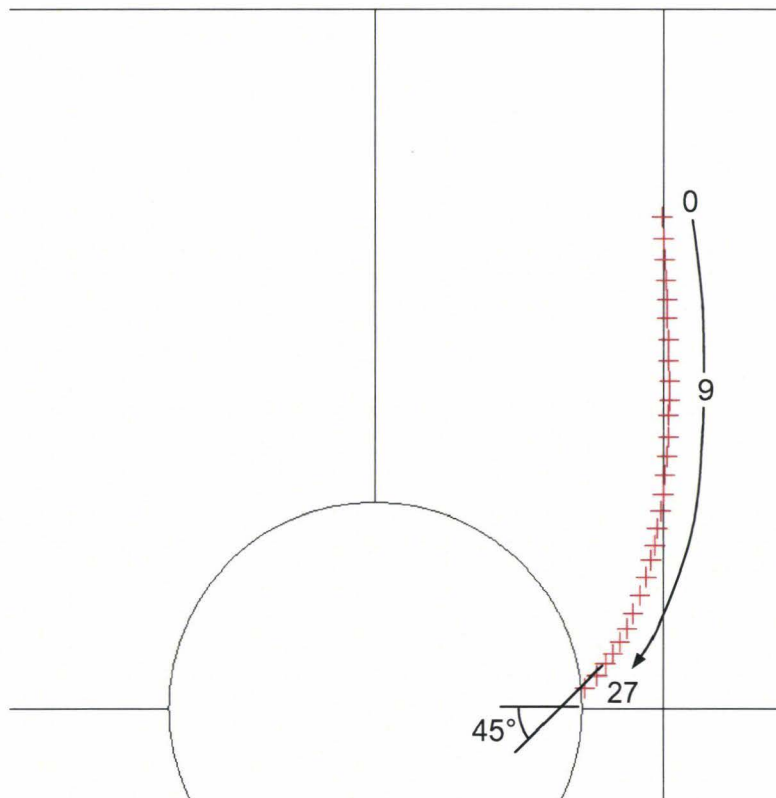
**Fig. 82: ADAPCRACK3D - Projection of the crack front on the X-Y plane
(from initial state 0 to increment 27)**

A projection on the X-Y plane of the average crack front is illustrated in Fig. 82. During the simulation the crack length increment da takes values between 0.29 and 0.50 mm. The maximum crack increment da is limited to 0.50 mm in order to ensure a regular crack growth. It is apparent that the crack front first slightly moves away from the hole (increments 1-9), to then deviate in the direction of the hole in the next steps. Finally, the crack meets the cavity inclined with an angle of 45° to the original crack direction.

The curvature of the crack is characteristic of a mixed mode loading condition. The evolution of the stress intensity factors K_I and K_{II} demonstrates that the proportion of mode II varies during the crack advance. In Fig. 83, the stress intensity factors K_I and K_{II} are normalised by the stress intensity factor K_I evaluated at the first increment. As the crack advances and the applied load is held constant, the value of K_I increases during the analysis. The amount of K_{II} is small, but sufficient to create a curved crack front. The positive values of K_{II} at the beginning (till y = 9 mm) are in accordance with the crack propagation away from the hole, whereas the following negative values are consistent with the change of direction and the inflexion point in the curved path.
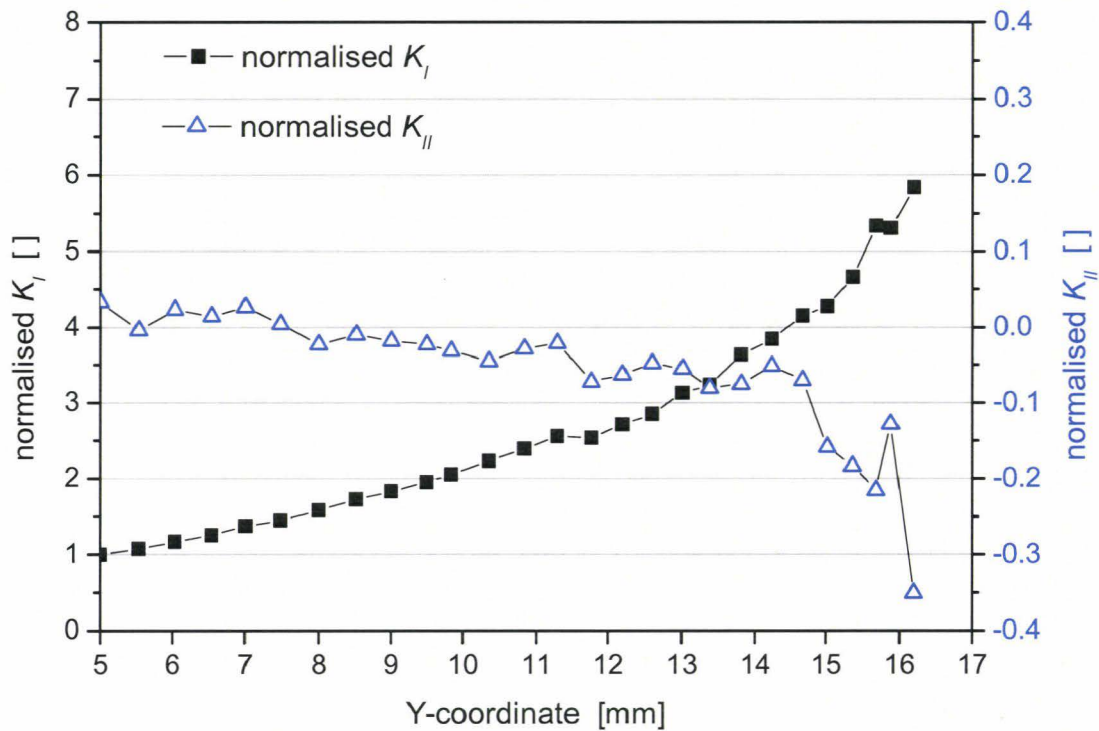
Fig. 83: ADAPCRACK3D - Normalised K_I and K_{II} as function of the Y-coordinate (normalised by K_I at the first increment)

5.5.2   Results from Zencrack

A similar analysis is performed with Zencrack. The FE model is generated with identical dimensions and boundary conditions. First, a virgin mesh is generated with second-order hexahedron elements. In order to investigate the influence of mesh refinement, two FE meshes are generated. The first one is composed by 14000 nodes and 2500 elements. An amount of 12000 elements with 60000 nodes is enumerated for the second mesh. The mesh in the centre of the specimen (cracked zone) is regular and square elements have a side length of 1 mm for the fine mesh and 1.5 mm for the coarse mesh. In the second FE model, the mesh refinement in this zone is comparable with the mesh quality investigated in ADAPCRACK3D. Then, the initial crack is introduced in the virgin mesh. Crack-blocks ensure a fine mesh and the representation of the singularity at the crack tip. As depicted in Fig. 54, three brick elements are positioned over the thickness in the second FE model and enable the insertion of three crack-blocks on each side of the crack front. In the coarse FE model, only two crack-blocks are introduced on each side of the crack front.

(a) coarse mesh   (b) fine mesh
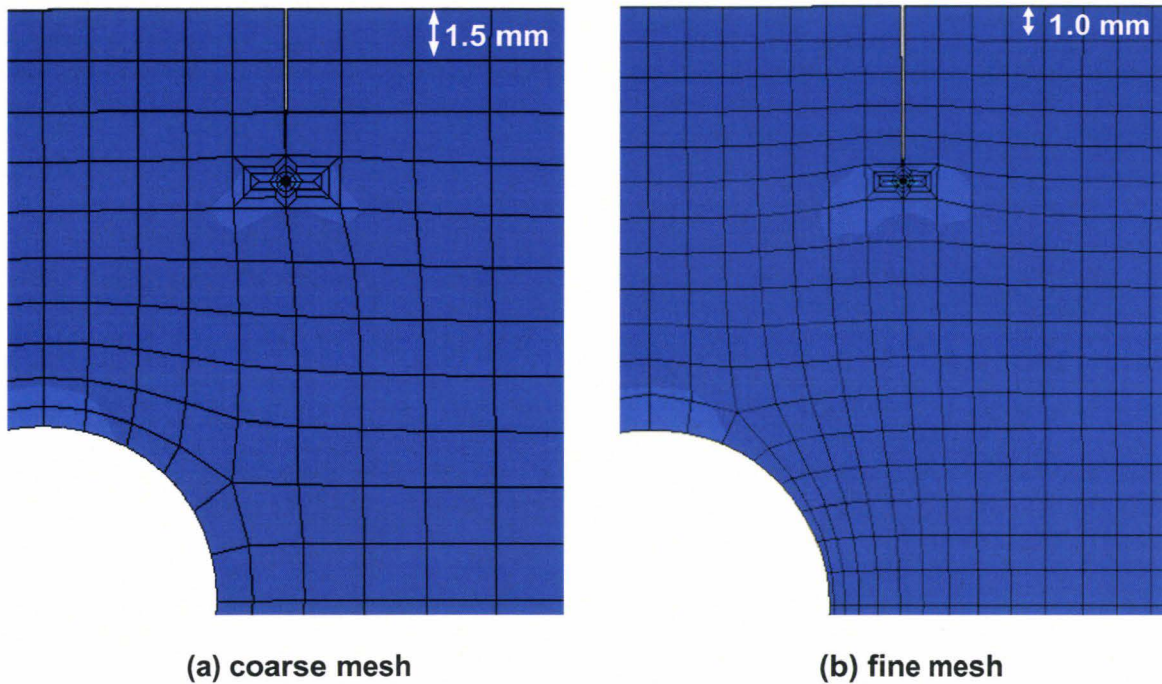
Fig. 84: Zencrack - Details of the coarse and fine FE models (initial crack length)

During the analysis, the crack front geometry is updated at the beginning of each increment. As described in chapter 3.3.4, the position and dimensions of crack-blocks are adjusted in order to fit the shape of the crack. If required, a crack-block transfer is done. In the case of non-planar crack growth, distortions can appear in elements surrounding the crack-blocks, as seen in Fig. 85.
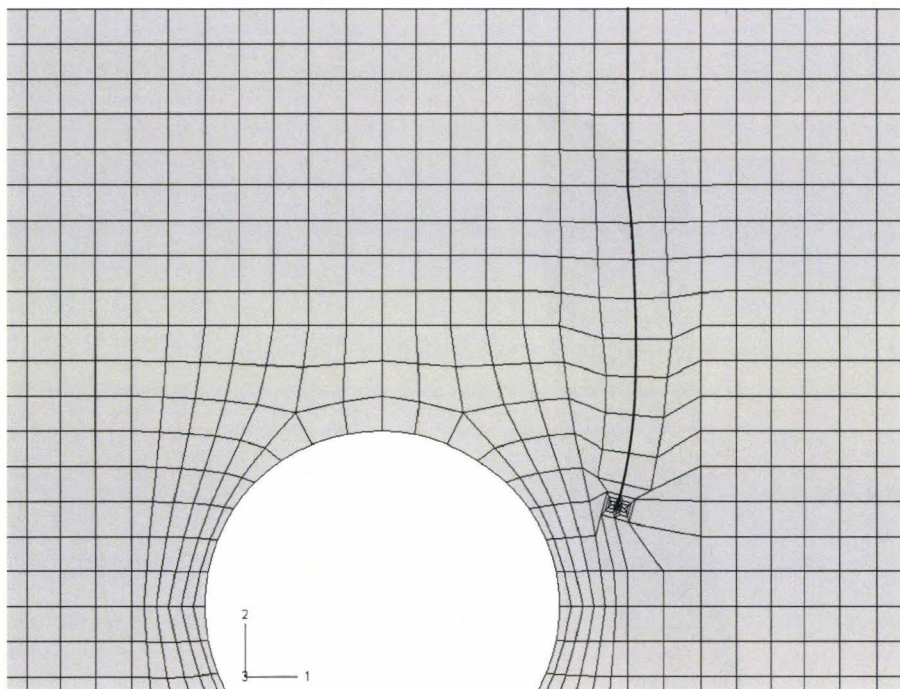
Fig. 85: Zencrack - Crack path obtained without relaxation (fine mesh)

As explained in chapter 3.3.4, boundary shifting and mesh relaxation are Zencrack options, which enable to improve the quality of the surrounding mesh. This gives the potential for the analysis to develop additional growth with greater accuracy. Nevertheless, mesh relaxation

has its limits and may not always be able to produce valid elements. In extreme cases, the distortion in the surrounding elements may become severe enough to cause inside-out elements [Zen06]. This problem happens as the crack front comes close to the hole. As seen in Fig. 86, the crack-blocks intersect the element layers near the surface, what leads to an invalid FE mesh and to the analysis interruption.
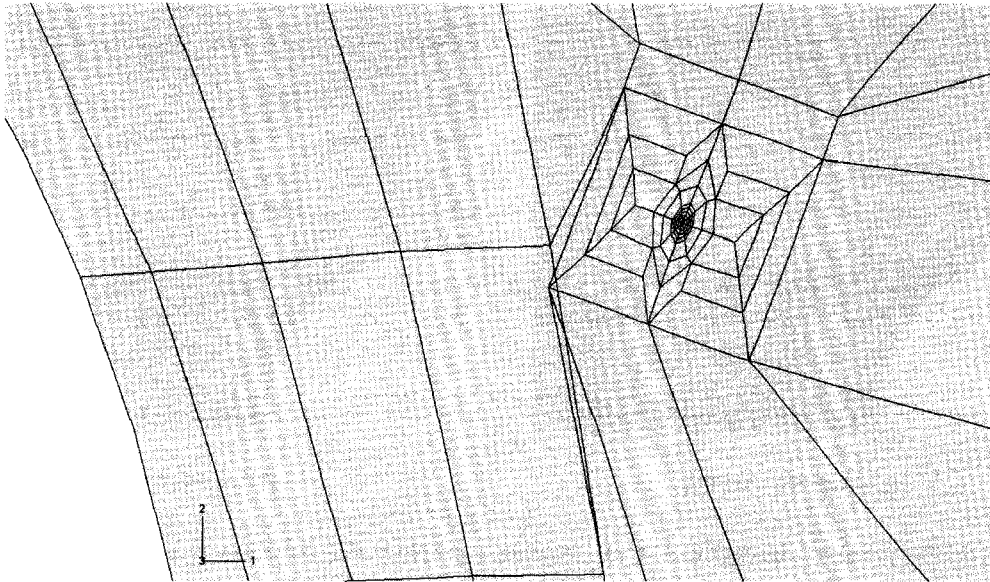
Fig. 86: Zencrack - Mesh distortion near the crack front (fine mesh)

Before the analysis aborts, a succession of 50 increments is run with the coarse mesh. In the case of the fine mesh, a total of 66 increments is attained. For a fine mesh, the quantity of crack transfer is higher. This increases the number of increments and consequently the computation time. At the end of the analysis, the form of the crack front can be extracted.
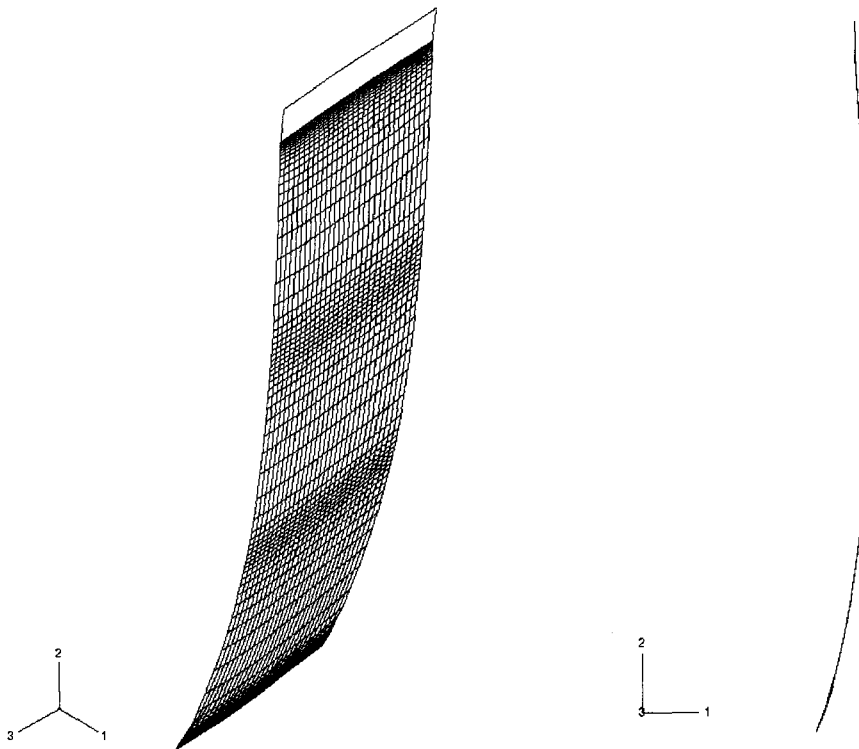
Fig. 87: Zencrack - Computed crack path (fine mesh)

The crack path is not dependent on the Z-coordinate. Fig. 87 represents the profile of the crack path and shows that the crack front is not twisted. On this account, the position of the computed crack front can be averaged over the specimen thickness for each analysis step.

Let consider simulation results obtained with the MTS criterion. Both FE models describe a similar crack path. As a result, the mesh quality of the coarse mesh is sufficient to obtain a suitable prediction of the crack path. Moreover, a simple mesh reduces the risk of mesh distortion, so that valid meshes can be generated when the crack is close to the border of the hole. As seen in Fig. 88a, the predicted crack path is 1.2 mm longer in the case of the coarse mesh. For this reason, the coarse mesh is used in the rest of the study. As seen in Fig. 88b, either the maximum energy release rate or the maximum tangential stress criteria deliver similar curved shapes. As documented in Fig. 30, the MERR criterion predicts an angle of crack propagation bigger than the MTS criterion for a given ratio K_{II} / K_I. That is why the crack path computed with the MERR shows a stronger curvature.
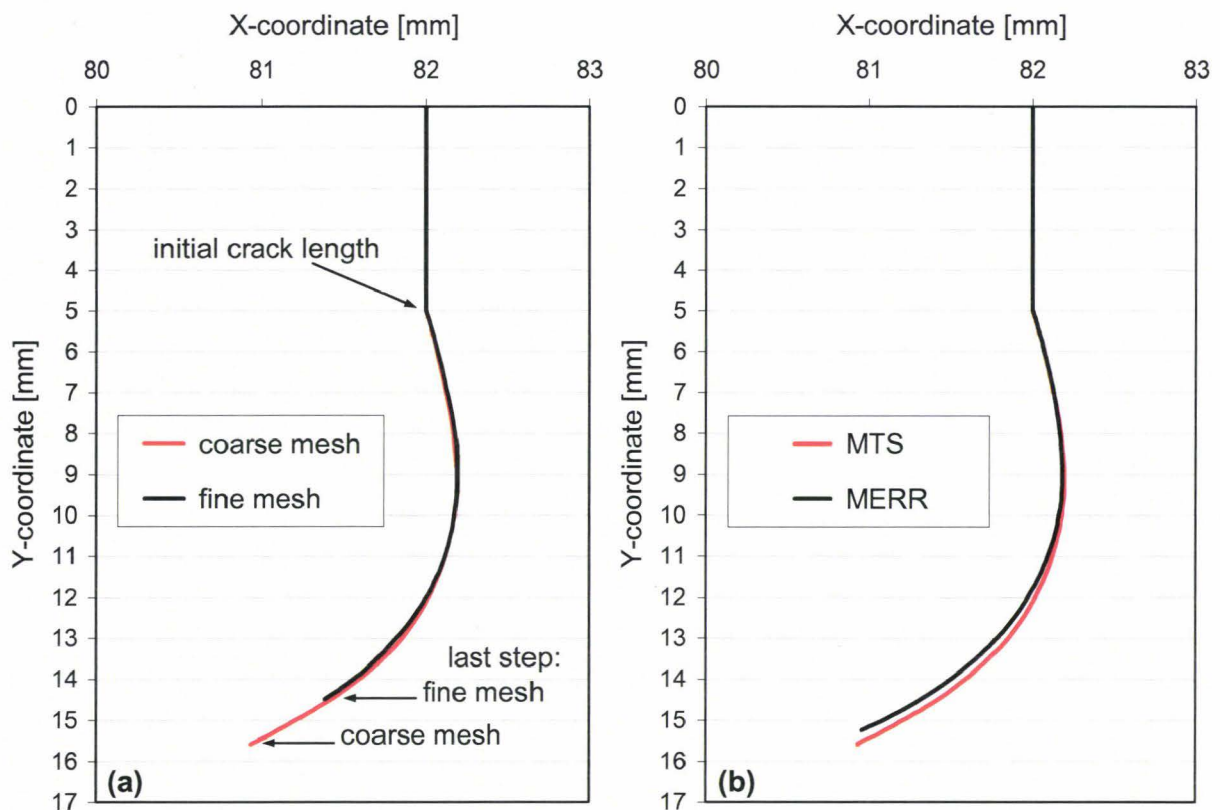
Fig. 88: Zencrack - Computed crack path
(a) for fine and coarse mesh (with MTS criterion);
(b) with MTS and MERR criterion (for coarse mesh)

5.5.3 Comparison Zencrack / ADAPCRACK3D

One of the goals of this analysis is to compare the different numerical methods implemented in software Zencrack and ADAPCRACK3D. Various parameters are examined, like the effort required to create a model, the computation time or the accuracy of results.

First, the creation of the initial FE model requires equivalent efforts for both software packages. A classical mesh of the uncracked geometry has to be generated. The position and geometry of the crack are additionally defined by the user. These two input data are then combined to automatically design the cracked FE model. In order to facilitate the introduction of the initial crack, the virgin FE model has to be prepared. In Zencrack, crack-blocks replace

hexahedron elements, which have to be adequately positioned on each side of the future crack tip. In ADAPCRACK3D, the insertion of the initial crack consists in the creation of three-noded elements surface in the global 3D mesh. As well, the crack surface can be defined in advance in the 3D uncracked mesh, so that introduced nodes are already on the surface of a tetrahedron element (see Fig. 52).

The total time computation is also similar for both models. Analyses are run on similar workstations. A crack growth increment is run in approximately 20 min (clock time) with ADAPCRACK3D. A total time of 540 min was required for the complete analysis. With Zencrack, a period of 12 min flows between two steps. For the coarse mesh, 50 successive steps are computed, which corresponds to a total time of 600 min. An increment in ADAPCRACK3D is composed by a first FE analysis for the global model and a second one for the submodel. Consequently, the elapsed time between two increments is longer. Besides, the amount of increments is controlled by the maximal crack extension da allowed per increment. A length of 0.5 mm was fixed in ADAPCRACK3D, so that the average crack extension da over the 27 increments is equal to 0.44 mm. On the other hand, crack-block transfers enforce small crack extensions da in the software Zencrack. The average crack extension da is here equal to 0.20 mm. Consequently, the total computation time with Zencrack is slightly longer.

Fig. 89 depicts paths computed with ADAPCRACK3D (maximum principle stress criterion) and otherwise with Zencrack (MERR or MTS criteria). A first observation reveals that the different approaches lead to a single crack profile (Fig. 89a). Only small variations have to be pointed out in the design (Fig. 89b). A second examination demonstrates the limitation of the software Zencrack. The crack path computed with ADAPCRACK3D is actually more extended than the crack path performed with Zencrack. In the case of high-curved crack, the transfer of crack blocks is sometimes difficult to be executed.
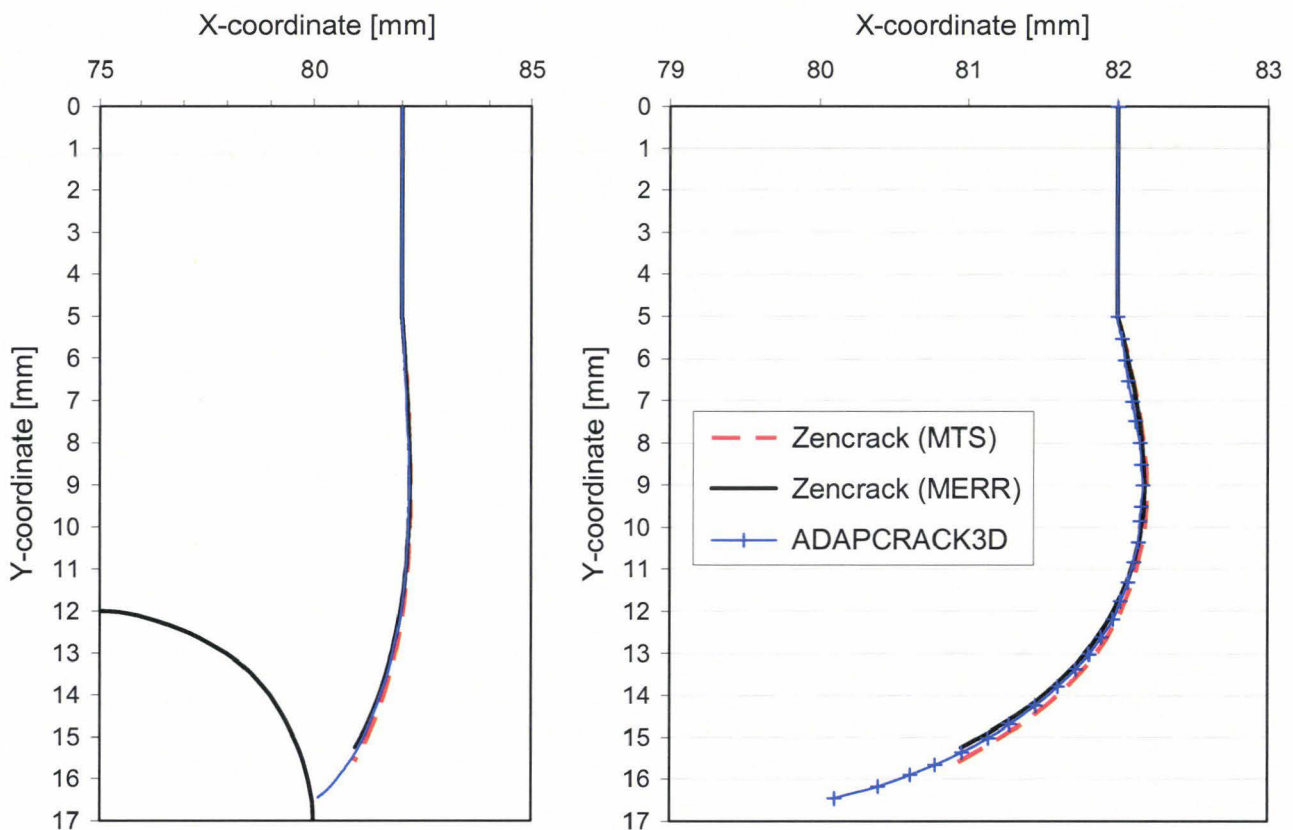
Fig. 89: Simulated crack path from ADAPCRACK3D and Zencrack:
(a) real X-coordinates; (b) deformed X-coordinate

The FE software ADAPCRACK3D and Zencrack offer dissimilar ways to compute the crack growth direction. However, the simulated crack paths are similar. This can be explained by the accuracy of the numerical procedures. As described in chapter 5.4.1, the J-integral can compute the energy release rate with a precision better than 3%. As well, the nodal displacements method returns precise evaluation for the stress intensity factors. The VCCT technique presents analogous accuracy in the evaluation of stress intensity factors [RyK77]. Moreover, the various criteria used to predict the propagation direction provide similar angles of crack extension, especially for small ratio K_{II} / K_I (see Fig. 30). Afterwards, the direction of crack propagation is adjusted from one increment to the next. So, small crack extensions da limit the influence of an error on the direction of crack propagation. Finally, it is obvious that the mesh quality has to be fine enough.

Conclusion

In this chapter, test specimens used for this study are numerically investigated. First, a CT specimen under static loading conditions is modelled for various crack lengths. The stress intensity factors are first computed with a 2D plane strain model. Estimated values are in good agreement with the analytical solutions [A-399]. This validates the capability of FE methods to accurately evaluate the stress intensity factor K_I. Additionaly, a 3D model of the CT geometry is created. A through-thickness effect is pointed out by a variation of the SIF along the crack front. The curvature of the crack front is also characterised as a function of the Poisson's ratio. Finally, the concept of effective stress intensity factor and effective function F_{eff} is introduced to integrate this 3D effect in the evaluation of SIF. In a second part, the case of mixed mode loading is studied with a model of CCT specimen. As well, FE results for SIFs and ERR are in accordance with the reference solution [Mur87]. Then, the perforated SEN specimen is considered in order to verify the capability of simulation to provide curved crack front. Although Zencrack and ADAPCRACK3D propose different numerical procedure to evaluate SIFs or ERR, the computed amplitude and direction of crack extension are analogous. Consequently, both software packages predict similar paths.

6 Fracture resistance of epoxy resins

Previous chapters described experimental and numerical methods to characterise the fracture resistance of materials. The notion of fracture resistance involves the definition of a critical value above which the crack propagates. For example, measurement of the fracture toughness provides a simple parameter to compare different epoxy resins within the context of mode I. As well, a similar criterion can be identified for cracks under mixed mode loading conditions. The direction of crack propagation, as the path followed by a crack can be determined from similar concepts. Tests are generally completed on basic specimens under static loading, whose results can be compared with analytical and numerical models. This chapter presents experimental results measured on epoxy resin materials used for the protection of electronic components.

6.1 Fracture toughness measurement (Mode I)

It was shown in chapter 5.3, that a three-dimensional effect exists through the thickness of CT specimens. The presented model takes into account the shape of the crack front. Indeed, the crack front curvature is controlled by the Poisson's ratio. Consequently, the application of this model requires the measurement of the Poisson's ratio for each material. Alternatively, ASTM standards [A-399, A-5045] propose a method based on a 2D assumption to evaluate the plane strain fracture toughness. With this simple formulation (see Eq. 138), no tests are required to determine further material parameters. Moreover, the fracture toughness is used to compare the fracture resistance of materials. In order to compare the following tests with values from literature, the ASTM procedure is applied to evaluate the fracture toughness.

6.1.1 CT specimen preparation

Tests are realised on epoxy resin materials at ambient temperature. Four different filled epoxy resins are characterised, which are labelled Mat1 to Mat4. Moreover, CT specimens are prepared to characterise the fracture toughness of the epoxy resin Mat1 without filler particles (named unfilled Mat1). Epoxy resins are primarily composed of two materials: resin and hardener. The epoxy resin basis for Mat1 and Mat2 is a bisphenol A, while the basis for Mat3 and Mat4 is a cycloaliphatic epoxy resin. The hardener is an anhydride compound. The proportion of resin and hardener is optimised for Bosch products and are considered as confidential data. The amount of filler particles is about 40 to 50% by weight for each filled epoxy resin. Filler material is composed of calcium silicate and carbonate particles with a maximal size of 100 µm. The proportion of modifiers, like mineral fillers or adhesion promoters, and the manufacturing process are different from on material to the other. As mechanical property, the E-modulus is representative to show the difference between Mat1-4.

	Mat1	Mat2	Mat3	Mat4
E-modulus [MPa]	6900	7000	8800	9000

Tab. 9: E-modulus for Mat1 to Mat4 (at ambient temperature)

In order to obtain a good homogeneity of the mixture and to avoid air bubbles, a dissolver is used under vacuum. The mixture is placed in a pre-heated metal mould and placed in an oven for the gelification and hardening phases. CT specimens are machined from the potted plates. The notch preparation is performed in two steps. A first crack is introduced by tapping a razor blade into the machined notch provided in the specimens. Then, the specimen is loaded at a very slow rate of 0.01 mm/min, until crack propagation is noticed (detected by a force drop of 0.3%). Finally, tests are performed conform to the procedure presented in chapter 4.1.2.

6.1.2   Statistical method of data extraction

For each material, a minimum number of 12 specimens is tested. Each CT specimen returns a fracture toughness value. From this, it is possible to extract the average value K_{avg} and the standard deviation. The maximal error is defined by the maximal difference between the measured value and the mean value. The maximal error is generally reported as a percentage of the average value. The relative standard deviation or coefficient of variation is defined by the quotient of the standard deviation divided by the mean value.

$$\text{relative standard deviation} = \frac{\text{standard deviation}}{\text{mean value } K_{avg}}$$ **Eq. 149**

More than an average value combined with a standard deviation factor, statistics offer the possibility to represent the results by a continuous probability distribution. The Weibull distribution is widely used in reliability data analysis due to its versatility [Leb04, Dep05]. Advantages of such a formulation are its mathematical simplicity and its ability to fit most lifetime data with a great confidence. The cumulative density function is a two-parametric function F:

$$F(K) = 1 - \exp\left(-\left(\frac{K}{K_0}\right)^{m_0}\right)$$ **Eq. 150**

where m_0 denotes the Weibull modulus and K_0 is the scaling parameter. Indeed, K_0 is named scaling toughness. For $K = K_0$, the cumulative failure probability equals $F(K_0) = 0.632$. In other words, the toughness is lower or equal to K_0 with a probability of 63.2%. The cumulative failure probability expresses the probability that the cracked specimen doesn't resist to a loading equivalent to K, i.e. the probability that the variable K_{Ic} takes a value less or equal to K:

$$F(K) = \Pr(K_{Ic} \leq K)$$ **Eq. 151**

Experimentally, N values of K_{Ic} are measured. Each value of K_{Ic} is ranked in ascending order and is associated to a failure position i. In this analysis, the expected plotting position $i/(N+1)$ is used to estimate the sample's cumulative probability function denoted F_i, as displayed in Tab. 10. Weibull proposes to fit the curve $F_i = f(K_{Ic})$ as presented in Eq. 150. A modified form of the Weibull cumulative probability function facilitates the data fit by evaluating:

$$\ln(-\ln(F_i)) = f(\ln(K_{Ic}))$$ **Eq. 152**

A linear regression allows the evaluation of the parameters (K_0; m_0). These two parameters enable to plot the probability density and cumulative distribution functions, as seen in Fig. 92 for Mat1. It is possible to determine the 90% confidence interval for K_{Ic}, namely by evaluating the distribution function for which a cumulative probability of 5% and 95% are reached.

6.1.3 Tests on CT specimens with filled epoxy resin

Since filled epoxy resins are opaque materials, the curved nature of the crack front cannot be directly observed. The crack length is measured on the sample surface with an optical system and is supposed constant through the thickness. The technique of data extraction is here presented for Mat1 with a set of 14 CT specimens (see Fig. 90) in accordance with the ASTM standard [A-399]. Measurements are performed at ambient temperature. For Mat1, the average value is equal to 1.15 MPa.m$^{1/2}$. A relative standard deviation of 5.5% and a maximal error of 13.5% for the sample n°13 show a low variation of the gathered data.
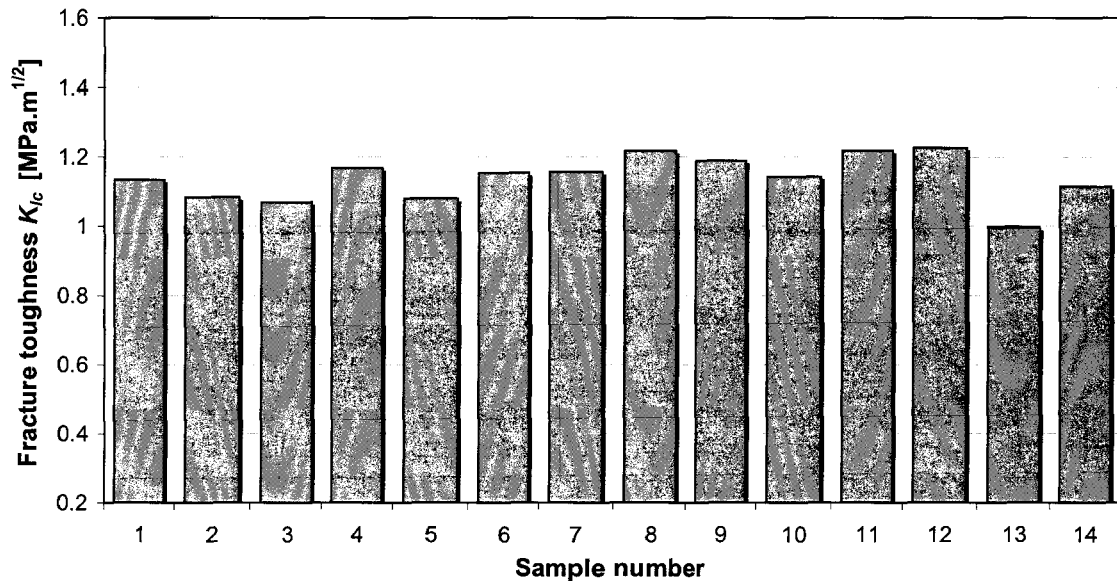
Fig. 90: K_{Ic} measurement for Mat1 (ambient temperature)
(evaluation of K_{Ic} based on Eq. 138 [A-399])

Additionally, the Weibull statistic method is applied to draw the probability distribution of these tests. Tab. 10 presents the data extraction for Mat1 and Fig. 91 the respective linear fit of the Weibull distribution.

K_{Ic} [MPa.m$^{1/2}$]	$\ln(K_{Ic})$	failure position i	$F_i = \dfrac{i}{N+1}$	$\ln(-\ln(F_i))$
0.997	-0.0025	1	0.0666	-2.6737
1.069	0.0672	2	0.1333	-1.9442
1.080	0.0771	3	0.2	-1.4999
...	...	...	...	...
1.217	0.1968	13	0.8666	0.7006
1.225	0.2032	14	0.9333	0.9962

Tab. 10: Weibull plotting data for Mat1
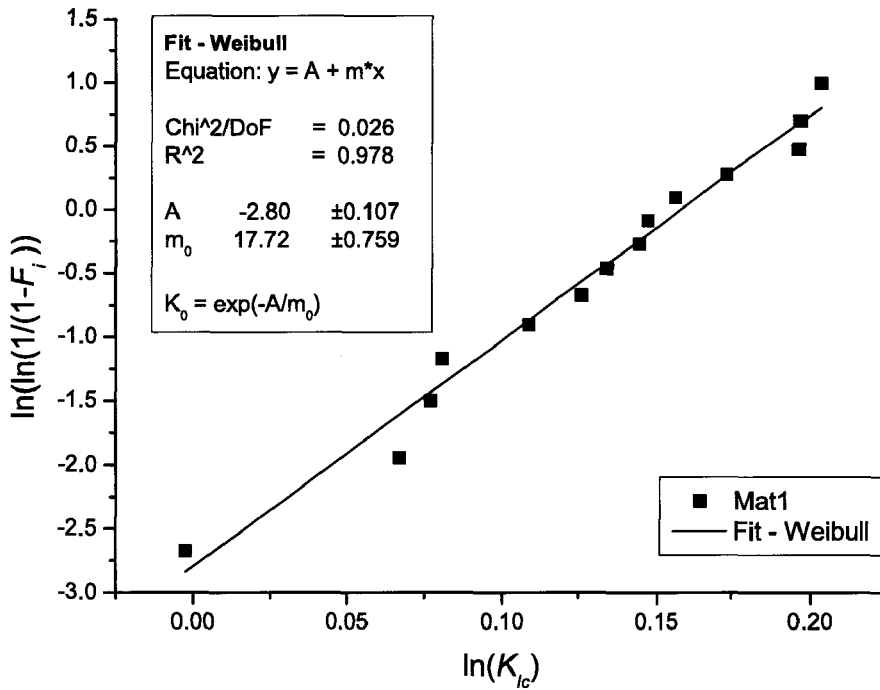
Fig. 91: Weibull distribution for Mat1 - Linear fit to extract m_0 and K_0

Given that R^2 = 0.978, the linear regression describes reasonably the experimental data. The scaling toughness is equal to K_0 = 1.17 MPa.m$^{1/2}$ and the Weibull modulus to m_0 = 17.71. These two parameters enable to plot the probability density and cumulative distribution functions, as seen in Fig. 92. The 90% confidence interval is in the range [0.99; 1.24] for Mat1 at ambient temperature.
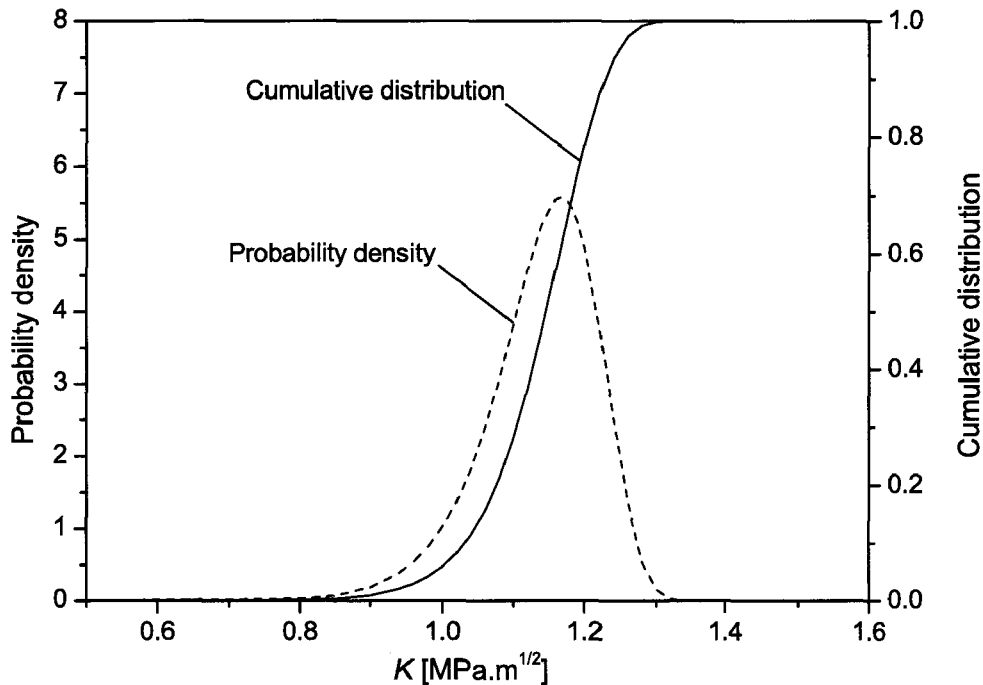
Fig. 92: Probability density and cumulative distribution functions for Mat1 at ambient temperature

6.1.4 Tests on CT specimens with unfilled epoxy resin

Fracture toughness tests are realised at ambient temperature on the unfilled Mat1 [A-399]. The statistical methods of data extraction are analogous. The fracture toughness measured with 12 CT specimens are presented in Fig. 93.
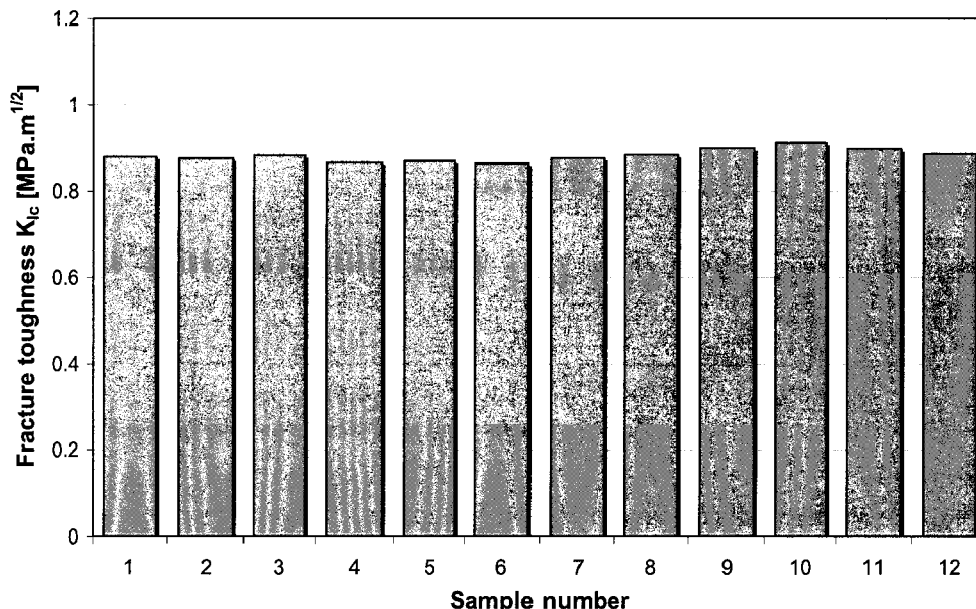
Fig. 93: K_{Ic} **measurement for unfilled Mat1**
(evaluation of K_{Ic} based on Eq. 138 [A-399])

The mean value is equal to 0.88 MPa.m$^{1/2}$. Graphically, it is obvious that the scatter reduces in comparison to filled epoxy resins. A relative standard deviation of 1.5% and a maximal error of 3.3% for the sample n°10 confirm the small dispersion. In addition, the experimental data can be represented by a Weibull distribution.
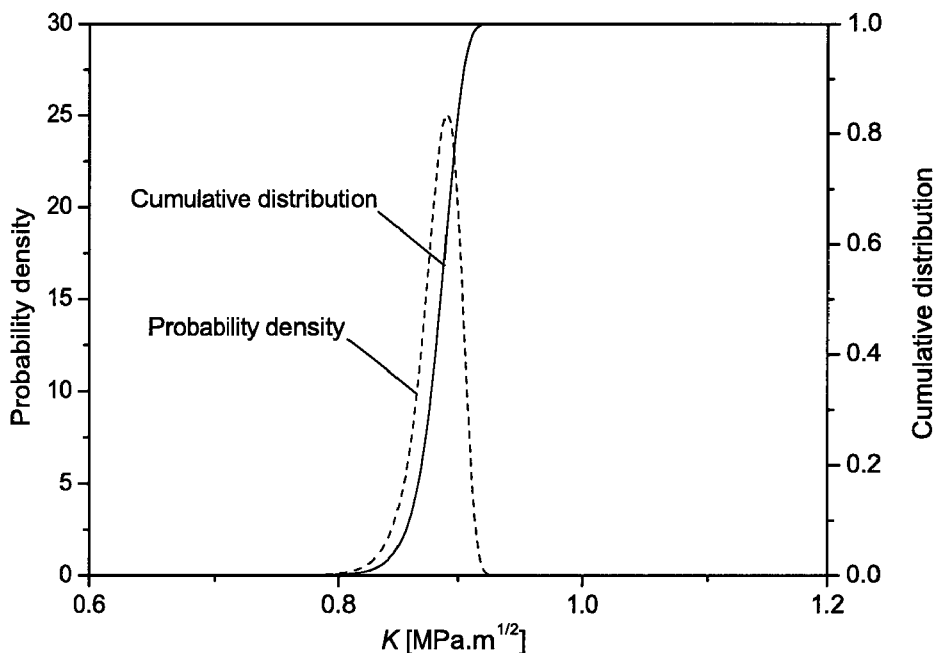
Fig. 94: Probability density and cumulative distribution functions
for unfilled Mat1 at ambient temperature

The linear regression (R^2 = 0.89) describes reasonably the data set. The scaling toughness is equal to K_0 = 0.89 MPa.m$^{1/2}$ and the Weibull modulus to m_0 = 60.65. The probability density and cumulative distribution functions for unfilled Mat1 at ambient temperature are plotted in Fig. 94. From these statistical results, it is possible to advance that the dispersion involved by the test procedure itself is less than 2% in terms of standard deviation. This fact validates the reproducibility of the test method for epoxy resins.

6.1.5 Epoxy resin comparison

Influence of filler particles

A campaign of tests is achieved with filled and unfilled Mat1. As expected, the addition of filler significantly increases the fracture toughness of epoxy resin [Dep05]. As listed in Tab. 11, the mean value K_{avg} is equal to 0.88 MPa.m$^{1/2}$ without filler and attains 1.15 MPa.m$^{1/2}$ with filler particles. As seen in Fig. 95, it is obvious that fracture toughness values measured for filled Mat1 are higher than for the unfilled Mat1. In fact, the scaling toughness is 30% higher for Mat1 with filler particles.

	Unfilled Mat1	Filled Mat1
mean value K_{avg} [MPa.m$^{1/2}$]	0.88	1.15
relative standard deviation	1.5%	5.5%
maximal error	3.3%	13.5%
m_0	60.65	17.71
K_0 [MPa.m$^{1/2}$]	0.89	1.17
90% confidence interval	0.84 - 0.91	0.99 - 1.24

Tab. 11: Influence of filler particles on the fracture toughness measurement (tests performed with filled and unfilled Mat1 at ambient temperature)
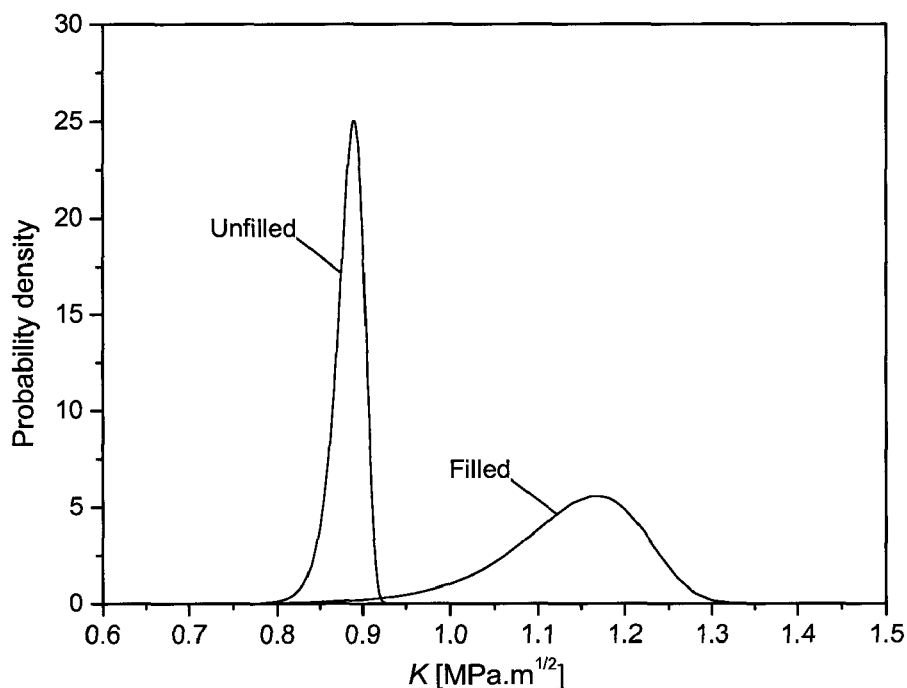
Fig. 95: Probability density function for filled and unfilled Mat1 at ambient temperature

Moreover, the dispersion of the measured fracture toughness is higher for a material with filler particles. The relative standard deviation is equal to 1.5% for unfilled Mat1, compared to 5.5% for filled Mat1. As well, the high value of the Weibull modulus (m_0 = 60.65) indicates a small variability of the measured data for filled Mat1, in comparison with the data measured for the filled Mat1 (m_0 = 17.71). Graphically, the probability density function is concentrated on the interval [0.84; 0.91] for unfilled Mat1, while the probability density function for filled Mat1 defines a large 90% confidence interval [0.99 - 1.24].

The standard deviation observed for filled epoxy resins is mainly due to filler particles. Actually, particles are source of material inhomogeneities. The quantity and size of particles can be inhomogeneously distributed in the moulded plates. Cracks can be deviated by the presence of particles [Gro96]. The interface between matrix and particles is also a source of damage, which can improve the scatter [Dep05]. In addition, the precrack introduction is achieved by taping a razor blade. The generation of the precrack is less reproducible in the case of filled epoxy resins, as their hardness is higher due to the presence of silicate and carbonate particles.

Comparison of filled epoxy resins

The same statistical method is applied to characterise the measured data for filled epoxy resins Mat2 to Mat4. Results are summarised in Tab. 12.

	Mat1	Mat2	Mat3	Mat4
tested specimen number	14	31	11	19
mean value K_{avg} [MPa.m$^{1/2}$]	1.15	1.37	1.57	1.68
relative standard deviation	5.5%	9.8%	6.8%	7.2%
maximal error	13.5%	27.3%	11.5%	12.82%

Tab. 12: Parameters for filled epoxy resins Mat1-4 at ambient temperature

A first classification of the different epoxy resins can be reached by comparing the average value K_{avg}. Mat4 has an average resistance to fracture higher than Mat1-3.

Within the context of fracture investigation, one of the troublesome drawbacks is the variability of measured data. For example, relative standard deviations for tensile strength are commonly in the range of [1 - 10%]. Values over 10% may indicate an abnormality in the experiments or specimen preparation. To validate our fracture toughness tests, the same indicator is applied. For filled epoxy resins, the relative standard deviation was included in a range of [5.5 - 9.8%]. The material inhomogeneities or the precrack initiation step partially explain the difficulty to manufacture reproducible specimens and to obtain constant results for the fracture toughness [ESI01].

Weibull parameters K_0 and m_0 like the 90% confidence interval are extracted for Mat2-4, values of which are recapitulated in Tab. 13.

	Mat1	Mat2	Mat3	Mat4
m_0	17.71	12.66	14.04	14.41
K_0 [MPa.m$^{1/2}$]	1.17	1.43	1.62	1.73
90% confidence interval	0.99 - 1.24	1.13 - 1.55	1.31 - 1.75	1.41 - 1.87

Tab. 13: Weibull parameters for Mat1-4

Fig. 96 represents the probability density functions for Mat1 to Mat4 and provides a precise tool to compare the fracture toughness of the four materials. If the described domains are completely distinct, the comparison between materials is trivial. For example, Mat4 is characterised by a fracture toughness whose scaling toughness is approximately 45% higher than the toughness of Mat1 (see Tab. 13). Since the overlapping zone between Mat1 and Mat3 is small, the materials can also be easily differentiated from each other. Mat3 is characterised by a fracture toughness whose scaling toughness is about 35% higher than the toughness of Mat1 and the 90% confidence intervals do not intersect.
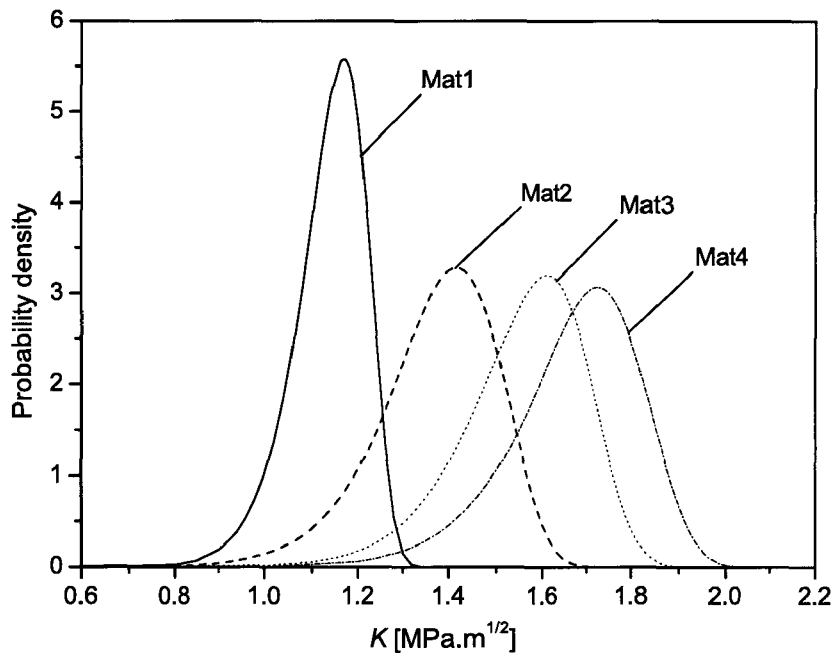
Fig. 96: Probability density function for Mat1-4

In the case of Mat2, the surface overlapping with Mat3 can not be considered as insignificant (see Fig. 96). The relative 90% confidence intervals intersect in a large common domain [1.31; 1.55]. In fact, a unique fracture toughness test for each material can lead to the same value for the two materials. The value for Mat2 may also be higher than the value for Mat3. In this case, it is necessary to repeat the number of tests to confirm the tendency that statistically Mat3 is more resistant than Mat2. In the case of Mat3 and Mat4, the plotted domains are globally equivalent. Statistically, the average value and Weibull scaling toughness of Mat4 are higher than those of Mat3. However, materials cannot be clearly distinguished due to a high dispersion. In this case, it is assumed that the two materials have a similar behaviour regarding the fracture resistance.

This databank is particularly useful during the development of new components. The determination of the optimal epoxy resin is a frequent topic. Filled epoxy resins are brittle materials and their resistance to crack propagation has a direct impact in term of reliability and lifetime. The energy release rate G is sometimes chosen to characterise the resistance to fracture, as G integrates the stiffness and the fracture toughness under a unique parameter. Tab. 14 presents the critical energy release rate evaluated from E and average K_{Ic} with Eq. 43. As E-modulus does not vary significantly from one resin to the other (see Tab. 9), results with G and K_{Ic} return similar variation.

	Mat1	Mat2	Mat3	Mat4
Critical G [J/m^2]	192	268	280	364

Tab. 14: Critical energy released G for Mat1 to Mat4 (at ambient temperature)

Minimum number of tested specimens

Tests are time-consuming and costly expensive (material, machine ...) and call for a limited number of specimens. Standards suggest a minimum of 3 tests [A-399, ESI01], which seems to be insufficient to accurately characterise filled epoxy resins.

For Mat2, a total of 31 specimens were tested. This amount of tests assures a consistent statistical analysis of the data. Subsequently, the mean value K_{avg} and the Weibull modulus K_0 are taken as representative reference value. In order to illustrate the dependence of the results with the number of tested specimens, the precedent statistical methods are applied to a reduced number of specimens. For example, sets of 3, 6 and 10 specimens are extracted from the global population of 31 samples. Specimens with the highest values are chosen (descending ranking), as they return the highest variation and can be defined as "worst case". In fact, values measured consecutively or picked randomly in the global population are more representative of the global population. For each set (3, 6 or 10 samples), the mean value K_{avg} and the Weibull modulus K_0 are evaluated. A comparison with the reference values is presented in Tab. 15. If a minimum number of 10 specimens is tested for each material, the mean value K_{avg} and the Weibull modulus K_0 will be determined with a precision less than 11%. For this reason, it is recommended to test 10 specimens for each material.

	reference samples 1-31	10 samples	6 samples	3 samples
mean value K_{avg} [MPa.m$^{1/2}$]	1.37	1.52	1.58	1.67
relative difference		10.6%	15.1%	21.8%
K_0 [MPa.m$^{1/2}$]	1.43	1.58	1.64	1.71
relative difference		10.7%	14.9%	19.9%

Tab. 15: Influence of the specimen number for Mat2

6.1.6 Temperature influence

Epoxy resins are particularly used as encapsulating materials to protect automotive electronic components from extreme loadings. For example, temperatures in the engine compartment vary frequently between +150°C and -40°C. Epoxy resins are sensitive to temperature variation, so that material parameters are specified as a function of temperature. Standard values of fracture toughness are evaluated at ambient temperature. For epoxy resins, effects due to temperature are not negligible, as the glass transition temperature can be less than 100°C.

E-Modulus and glass transition temperature T$_g$

Dynamic Mechanical Analyses (DMA) are generally used to characterise the viscoelastic nature of polymers and enables to evaluate the dynamic storage modulus $E'(T)$ as a function of the temperature. The Young's modulus $E(T)$ can be approximated by the storage modulus $E'(T)$ [Wit04, Dep05]. DMA allows the determination of glass transition temperature T$_g$ too. The glass transition temperature is the temperature below which the physical properties of amorphous material are similar to those of glass or crystalline phase (high *E*-modulus), and above which amorphous materials behave like liquids or rubber (low *E*-modulus).
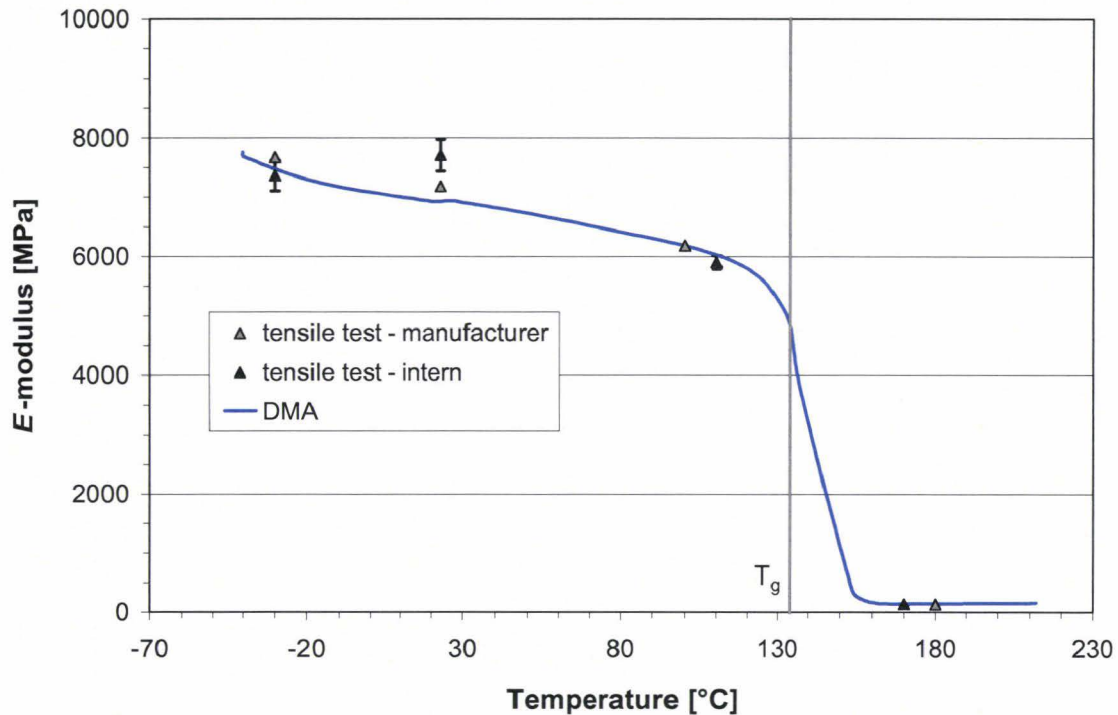
Fig. 97: Temperature dependence of the E-modulus for Mat2

Standardised tensile tests were performed for Mat2 at different temperatures. The evaluated E-moduli are comparable with the results from the DMA. Fig. 97 shows that the E-modulus decreases with increasing temperature, especially with an abrupt drop near the glass transition temperature (T_g = 132°C for Mat2). As the stiffness of the material strongly decreases above T_g, it is not recommended that components reach such temperature. For example, if the component is subjected to a constant mechanical stress, a warm up phase from low temperatures to over T_g leads to high deformations.

Fracture toughness

As well, the variation of the fracture toughness K_{Ic} with the temperature can be characterised by processing tests on CT specimens at a fixed temperature. The same fixture and tensile machine are used in combination with a climatic chamber, which minimal and maximal working temperatures are -40°C and +250°C. For each temperature, a minimum of 10 specimens is investigated. For low temperature, the crack propagation is identified by an abrupt load reduction in the load-displacement diagram and the maximal load is taken as critical load $P_c = P_{max}$, as seen in Fig. 60. For high temperature, non-linearities appear before the crack grows. As seen in Fig. 98, the determination of the compliance $C+5\%$ is required to evaluate the critical load $P_c = P_{5\%}$.

Non-linearities for high stress can be partially explained by small plastic deformations around crack tip. In fact, this phenomenon is only detectable for high temperature (near T_g) when the load approaches the critical point of crack propagation. Below T_g, the yield stress σ_y reduces considerably with increasing temperatures, in comparison to the fracture toughness. The process zone size is evaluated with Eq. 34. There is a direct proportionality between increasing temperature and process zone size. Furthermore, creep phenomena are particularly common in polymers. Creep is the term used to characterise the deformation of a material under a load applied over a long period until the material ultimately fails. In general, the higher the temperature is, the larger the creep deformation is [Dep05]. As the loading rate is slow (0.1 mm/min) and the temperature is heavy, creep damage can generate additional deformations.

- 131 -
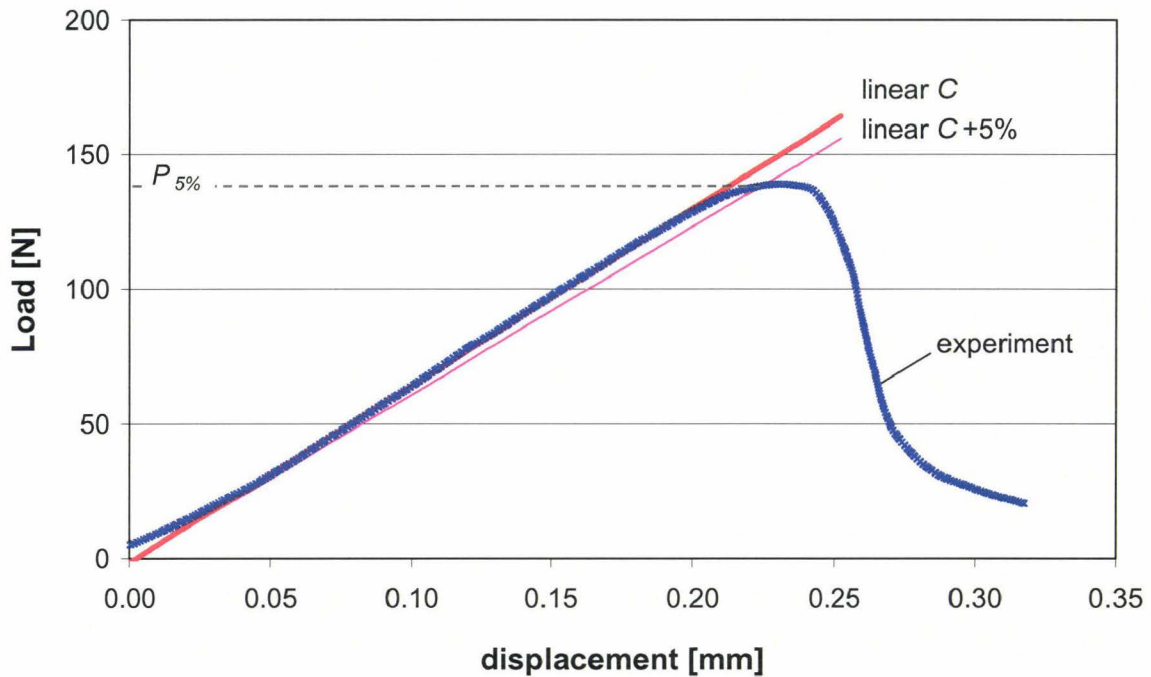
Fig. 98: Load-displacement curve for Mat2 at T = 130°C

The mean value K_{avg} and the 90% confidence interval are extracted as presented in the precedent chapters. For Mat2, temperatures T = [23, 60, 100, 130, 150°C] are investigated. Results are represented in Fig. 99. The fracture toughness globally decreases with an increasing temperature. As for the Young's modulus, a drop occurs near the glass transition temperature. A similar behaviour was observed by Wittler [Wit04].
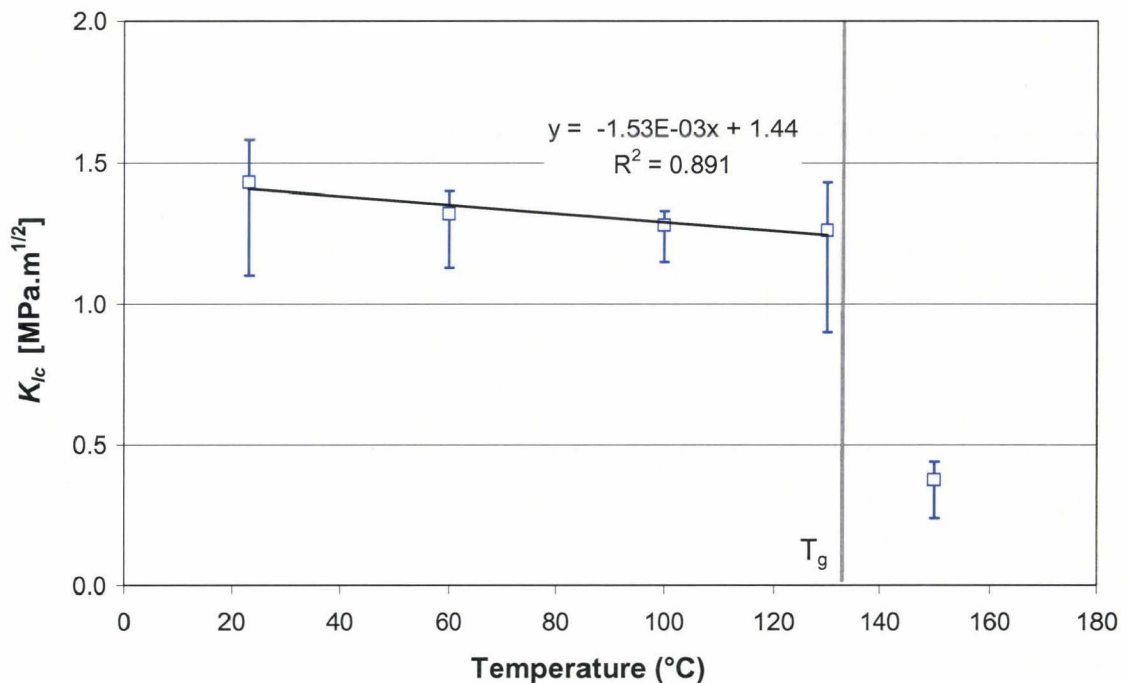
Fig. 99: Temperature dependence of K_{Ic} for Mat2

The glass transition temperature corresponds to a change in the physical properties of an amorphous material from a glassy to a rubbery state or reciprocally. In other words, the soft material undergoes high deformation above T_g (10 times higher than at room temperature)

until fracture occurs. As the stiffness falls down above T_g, the critical stress and the related fracture toughness follows the same variation.

The plasticity and creep phenomena can be interpreted as a dissipation of the elastic energy, which would not be released in creating the new crack surfaces. Below T_g, the plasticity and creep effects grow with the increasing temperature, so that the fraction of dissipated energy increases slowly and that the fracture toughness value progressively declines. Considering the mean values below T_g, the fracture toughness can be approximated by a linear behaviour, as seen in Fig. 99.

A reduction of the dispersion is observed with the increasing temperature. This effect can also be explained by the plasticity phenomenon at the crack tip, before the crack extends. The process zone can be considered as a damaged zone, at which borders the stress is homogeneous and approximated by the yield stress, as postulated in Irwin's model (Fig. 3). The larger scatter observed at T = 130°C for Mat2 is due to the strong variation of the material behaviour approaching the glass transition temperature.

Similar tests were performed with Mat4 and confirm the effects observed with Mat2. The glass transition of Mat4 is equal to $T_g = 235°C$ (see Fig. 100).
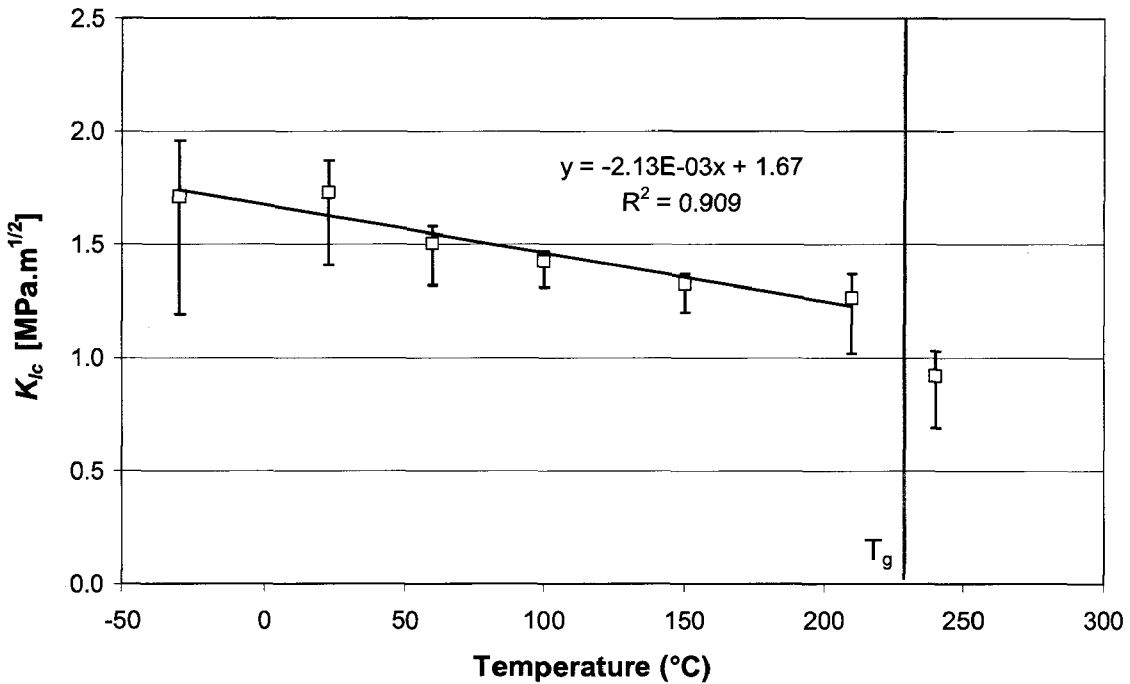
Fig. 100: Temperature dependence of K_{Ic} for Mat4

Thermal variations, like cooling down, generate strain and indirectly stress fields in epoxy resins. If cracks (or defaults modelled as crack) exist, stresses at the crack tip can attain a critical intensity, which leads to a crack propagation. Thermo-mechanical simulations enable the computation of stress intensity factors. A comparison between the computed stress intensity factors evolution and the experimental fracture toughness $K_{Ic}(T)$ is able to predict if the structure will fail and if it fails at which temperature.

6.2 Fracture resistance under mixed mode loading

6.2.1 Centre Cracked Tension specimen preparation

In this study, CCT specimens are 160 mm long, 50 mm width and 3 mm thick.
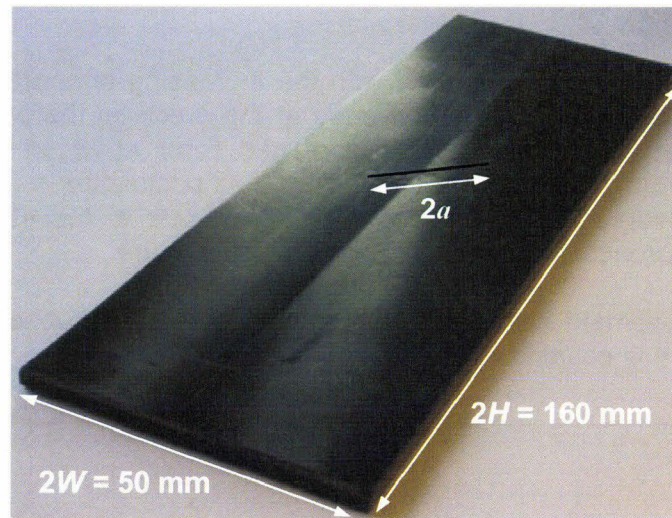
Fig. 101: Moulded CCT specimen

The method used to initiate the precrack in CT specimens requires a machined notch, in which a razor blade is positioned. With CCT specimens, the crack is enclosed in the specimen, so that taping a blade to generate the crack is impracticable. For this reason, a special metal mould is designed.
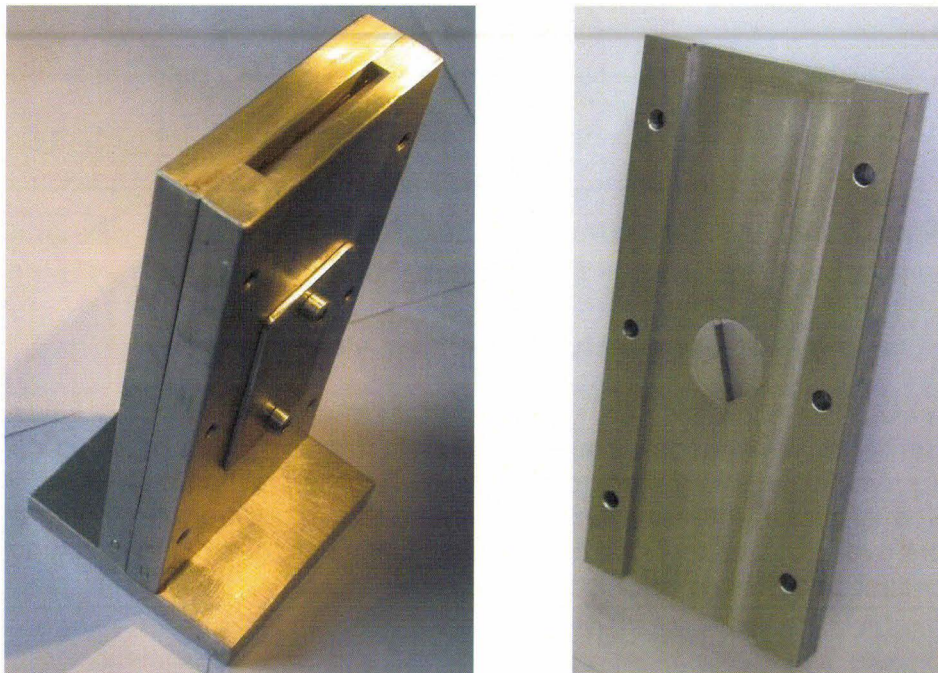
Fig. 102: a) Mould for CCT specimen; b) Inside part with adjustable blade orientation

A 25 mm-length blade is inserted in the centre of the mould. The blade is fixed on a circular piece, so that the crack orientation can be precisely adjusted between 0° and 90°. As seen in Fig. 67, the direction of the crack is inclined with an angle φ to the loading direction. The preparation of epoxy resins follows the standard procedure (mixing, potting and hardening). Removing the specimen from the mould is a difficult step, because epoxy resins are brittle materials. Specimens are here manufactured with Mat2 for angles φ equal to 0°, 15°, 30°, 45°, 60°, 70° and 75°.

6.2.2   Test procedure with CCT specimen

Thanks to the specimen geometry, tests are reduced to classical quasi-static tensile tests. A distance of 100 mm is set up between the two clamping devices. The sample has to be precisely aligned with the machine axes, because the direction of the applied displacement directly influences the proportions of K_I and K_{II} at the two crack fronts. A displacement rate of 0.1 mm/min is applied, until crack propagates. During the test, the load cell returns the resulting force P.

Two phenomena may be characterised with this test:
-    the direction of crack propagation under mixed mode loading
-    the fracture criterion for mixed mode problems based on stress intensity factors.

Consequently, the angle of crack propagation and the critical load, at which the crack extends, are investigated. The load-displacement curve is similar to the curve observed for CT specimens (see Fig. 60). As the material is brittle, the critical load corresponds to the maximal applied load $P_c = P_{max}$. The direction of crack growth is optically measured after the test, as shown in Fig. 103.
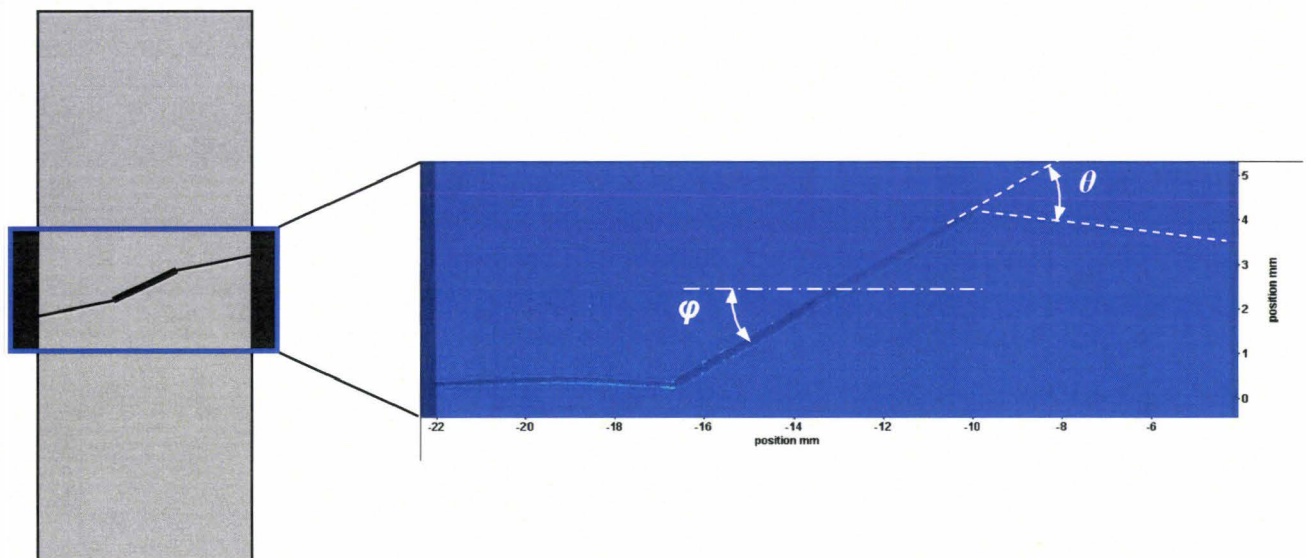
Fig. 103: Crack orientation φ and direction of crack propagation θ

6.2.3 Direction of crack propagation

The direction of crack propagation is optically measured at the fractured specimen.
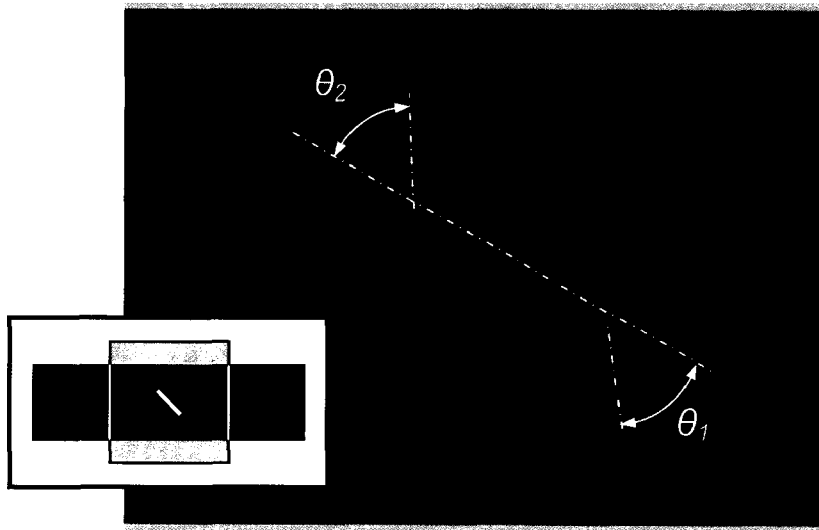
Fig. 104: Measurement of the crack propagation angle (CCT specimen φ = 60°)

As seen in Fig. 104, each sample contains two crack fronts, i.e. each test provides two angles θ_1 and θ_2. The test configuration (sample geometry and applied load) is symmetric. Therefore, the two crack fronts hypothetically propagate simultaneously. With the help of the Optical Crack Tracer (see OCT in Fig. 62), it is possible to follow the development of the crack. If the two crack fronts extend simultaneously, angles θ_1 and θ_2 are measured. One side propagates earlier, due to small asymmetry in the applied load direction and material inhomogeneity. The consequence of a non-symmetric propagation is a modification of loading conditions at the second crack front (referred by θ_2). As the second angle θ_2 does not correspond to the initial mixed mode of loading, only the first angle θ_1 is considered.
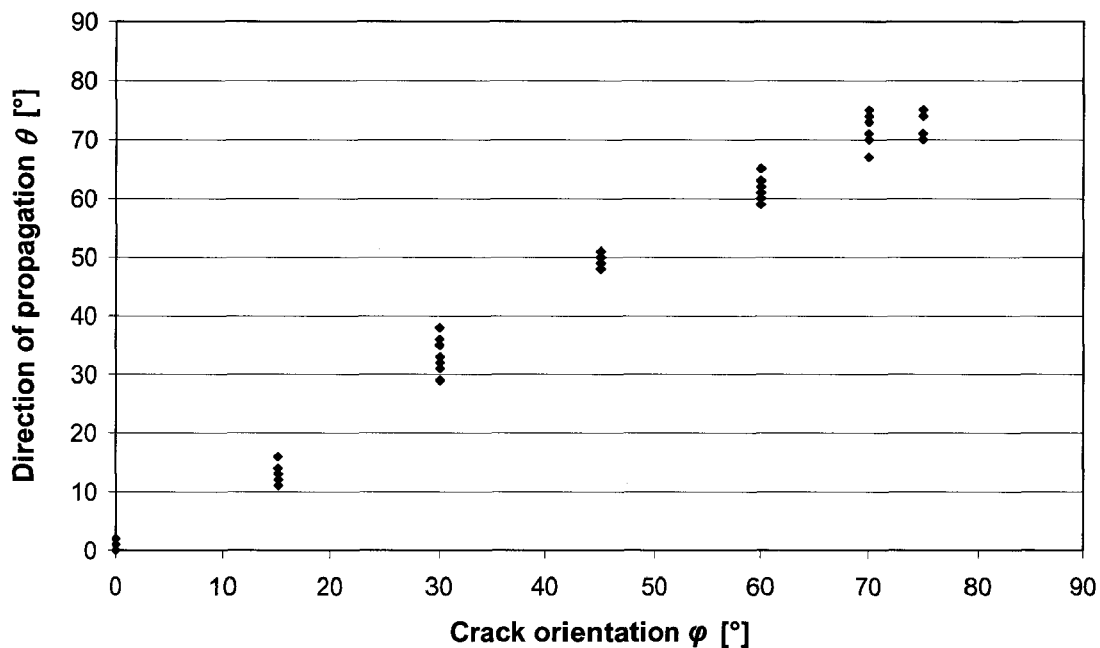
Fig. 105: Angle of crack propagation measured on CCT specimens $\theta = f(\varphi)$

The relation between the angle of crack propagation θ and the geometrical angle φ directly characterises the mixed mode crack propagation from experimental results. Nevertheless, Fig. 105 is specific for the CCT geometry with the angle φ. General form applicable for cracks under mixed mode loading is the use of the ratio K_{II} / K_I. The conversion between the crack orientation φ and the ratio K_{II} / K_I is shown in Tab. 8 [Mur87]. Finally, a set of crack propagation angles is associated to each value of K_{II} / K_I, as seen in Fig. 106.
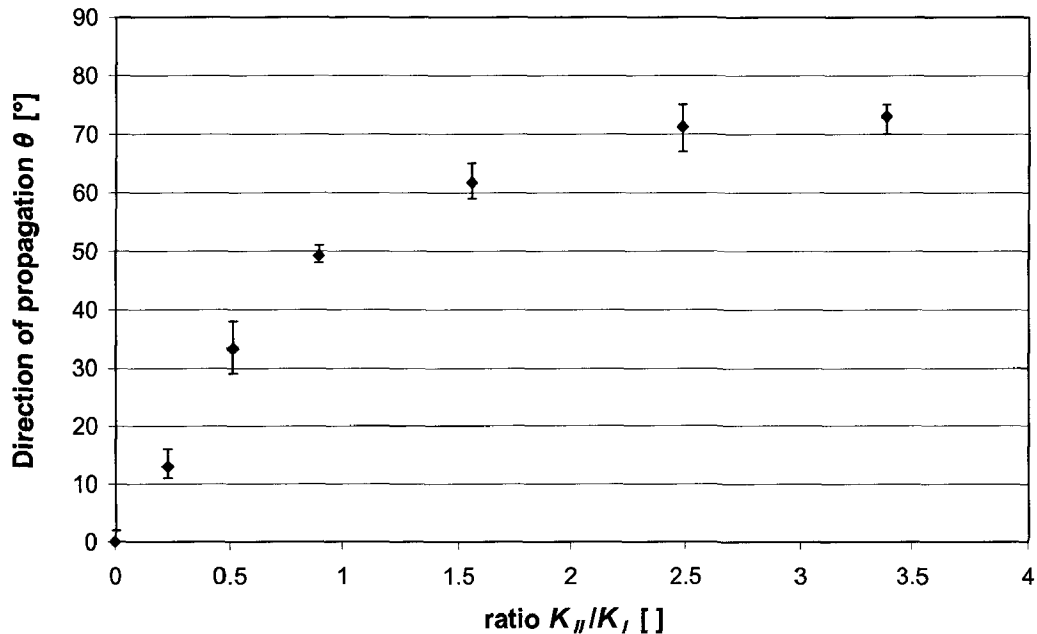
Fig. 106: Angle of crack propagation $\theta = f(K_{II} / K_I)$
(mean, minimal and maximal values measured for each set)

Three theoretical models of crack propagation under mixed mode conditions are presented in chapter 2.3.6: the Maximum Tangential Stress (MTS), the Maximum Energy Release Rate (MERR) and the Minimum Strain Energy Density (MSED). As seen in Fig. 107, the angle of crack propagation θ is represented as a function of the factor $K_{II} / (K_I + K_{II})$, which varies from 0 for a pure mode I to 1 for a pure mode II.

A similar trend is observed between experimental results and theoretical models. The Minimum Strain Energy Density (MSED) criterion shows the best representation of the experimental results. However, the MSED criterion is not implemented in numerical packages, like Zencrack. Since the MTS and MERR are also suitable criteria, they are used to compute the direction of crack propagation.
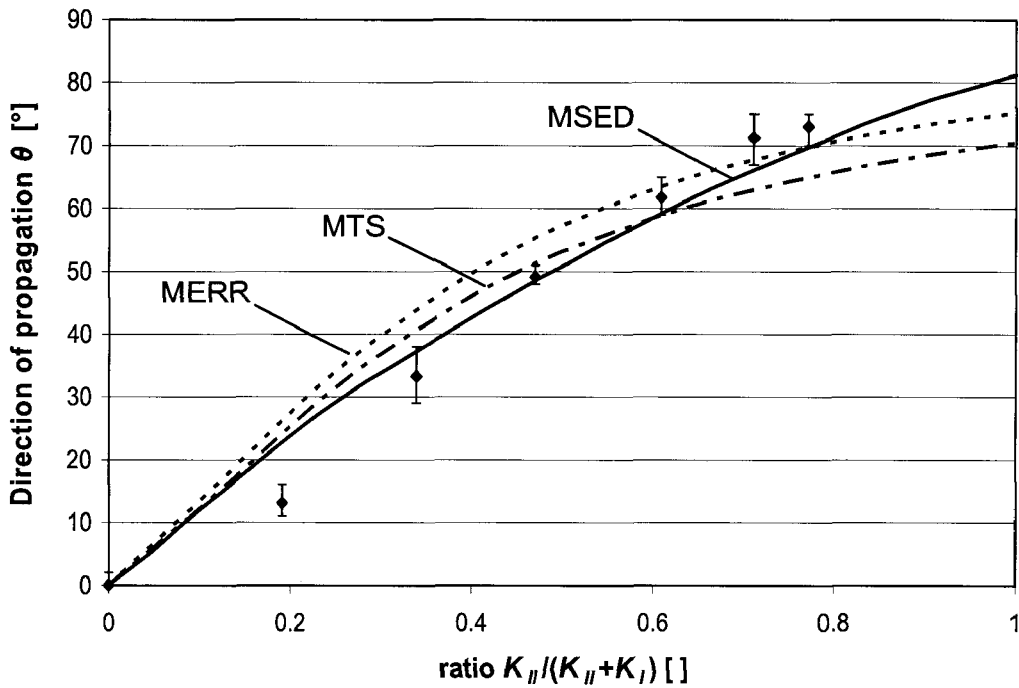
Fig. 107: Direction of crack propagation - Experiments and theoretical models

6.2.4 Fracture criterion for mixed mode loading conditions

The fracture toughness concept defines a useful criterion for pure mode I of fracture. The extension of such a criterion to mixed mode (mode I and II) requires the evaluation of both stress intensity factors K_I and K_{II}. Consider a mixed mode loading at the crack tip: the crack propagates, only if a critical combination of shear and tensile stresses is reached [Gro96]:

$$f(K_I, K_{II}) = 0$$

Eq. 153

The CCT geometry is parameterised by the angle φ. For a given angle φ, the stress intensity factors K_I and K_{II} at the crack tip are directly proportional to the uniaxial stress (see Fig. 67). The extracted stress enables the evaluation of the critical SIFs combination (K_I^c, K_{II}^c) for a given angle φ.
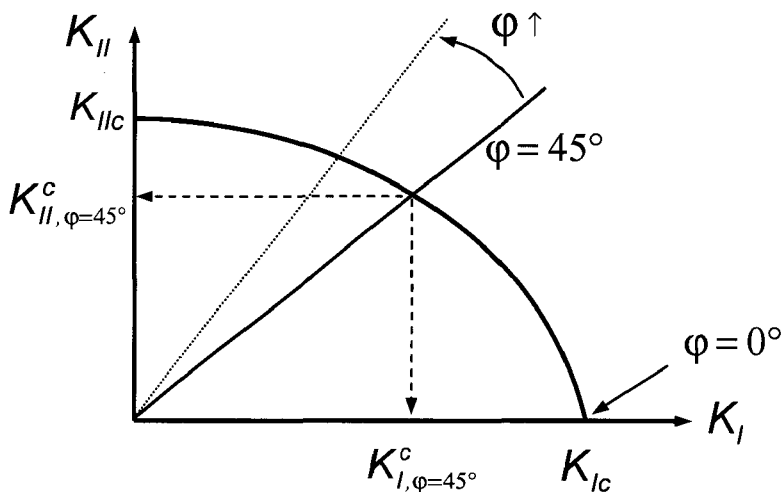
Fig. 108: Mixed-mode loading - Design of fracture criterion

As depicted in Fig. 108, the fracture criterion can be graphically represented in the plane (K_I, K_{II}). Each angle φ is associated to a couple (K_I^c, K_{II}^c) and is used as parameter to plot the curve. For example, the angle $\varphi = 0°$ corresponds to a pure mode I, so that $K_I^c = K_{Ic}$ and $K_{II}^c = 0$. As well, an increasing angle φ tends to generate a pure mode II, so that $K_I^c = 0$ and $K_{II}^c = K_{IIc}$.

Stress intensity factors K_I^c and K_{II}^c are normalised by the fracture toughness K_{Ic}. Experimental results for Mat2 are presented in Fig. 109: in dark, the average curve, and in grey the corridor of experimental dispersion. The scatter zone is globally thin, and tends to reduce for high proportion of K_{II}. An absolute value of K_{IIc} can not be extracted from experiments, but an estimated value near 0.83 K_{Ic} can be approximated.
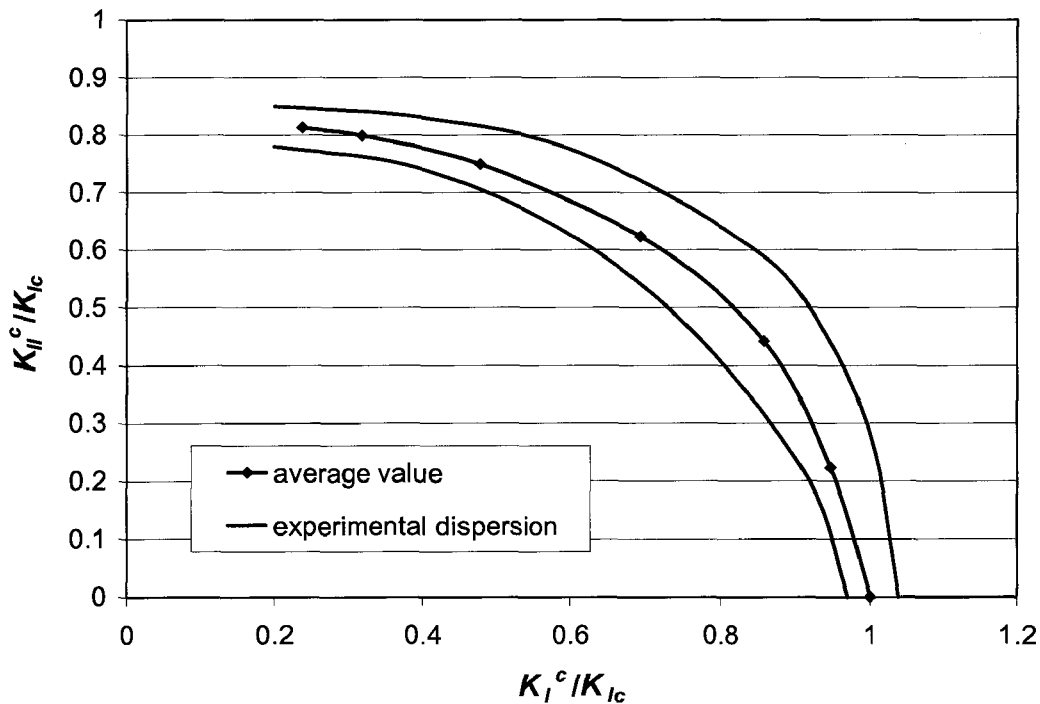
Fig. 109: Critical combinations (K_I^c, K_{II}^c) according to experimental tests

Fig. 110 proposes a comparison between experimental results and theoretical fracture criteria, like MSED, MTS and MERR criterion. The MTS and MERR criteria return a conservative prediction of crack propagation. As previously observed for the direction of crack propagation, the MSED criterion ($v = 0.37$ for Mat2) describes experiments with a good agreement.

In the case of a complex structure under extreme loading conditions, the stress intensity factors K_I and K_{II} can be computed with the help of simulation (see chapter 5.4). Then, the point with coordinates (K_I, K_{II}) can be positioned in the diagram representing the fracture criterion (Fig. 110). If the point is below the limit curve, no crack will propagate. On the other hand, a crack will extend if the point is outside the delimited zone. As a result, the experimental curve divides the plane into a *safe zone* and an *unsafe zone*.
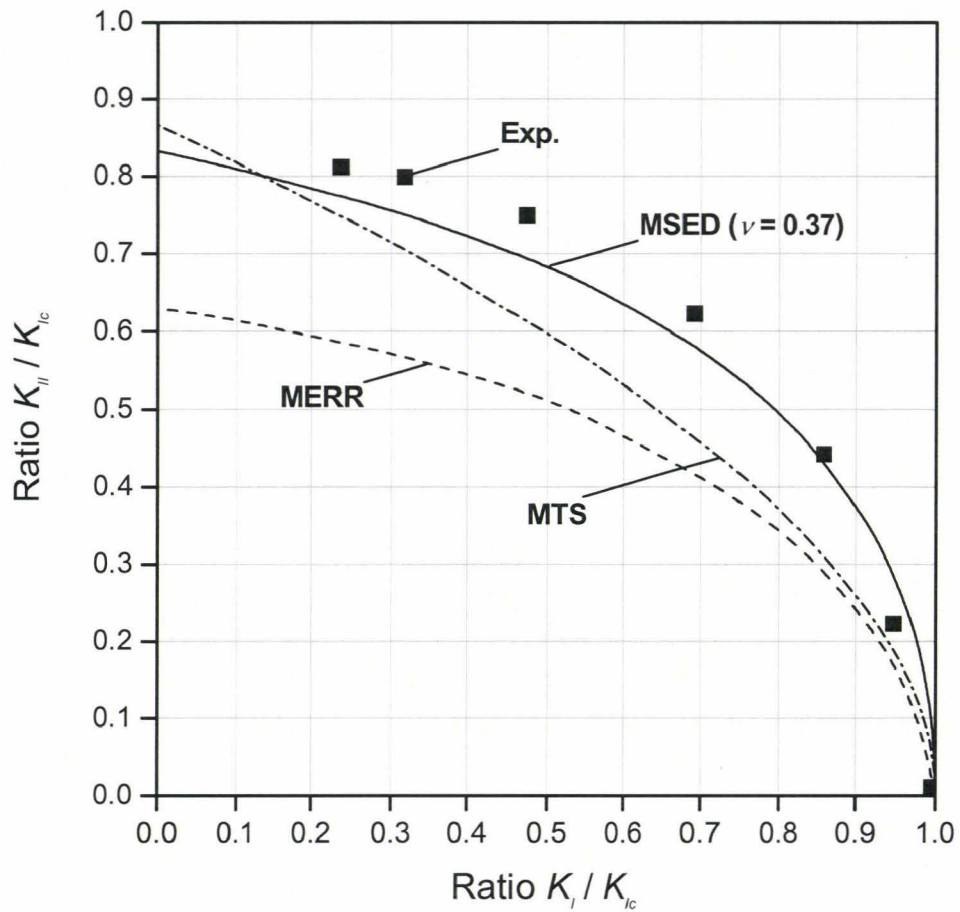
Fig. 110: Fracture criterion - Experiments and theoretical models

6.2.5 Tests on perforated single edge notched specimen

Experimental tests are performed on perforated single edge notched (SEN) specimens.
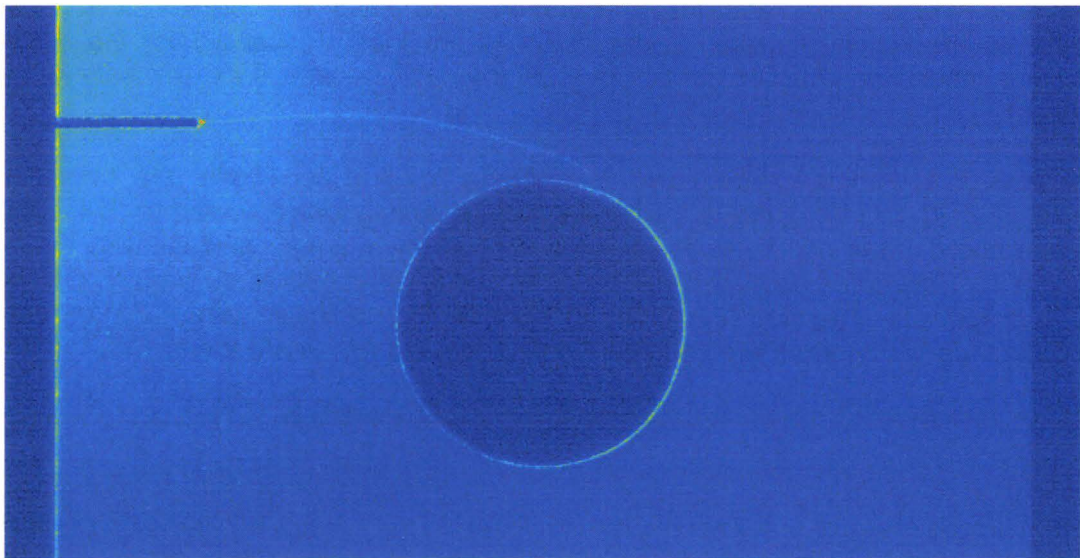
Fig. 111: Experimental crack path (L = 7 mm)

Specimens are machined from 3 mm-thick potted plates of material Mat2. Sample dimensions are described in Fig. 68. Static tests are conducted on a tensile machine with a displacement rate of 5 mm/min. A similar curved crack front is observed for the set of 9 samples. The reproducible curvature is represented in Fig. 111.

Tests are also performed on samples manufactured with Mat3. The observed curved crack front takes the same form as in Fig. 111. This confirms that the curved crack front is specific of the specimen geometry and applied loading and not dependent on material parameters.

6.2.6 Experimental and numerical curved crack front

The perforated single edge notched specimen can be used as model to verify the capability of FE simulations to predict curved crack front. A comparison between software ADAPCRACK3D and Zencrack was achieved in chapter 5.5.3. Both simulations give an analogous prediction. Fig. 112 shows an excellent correlation between the simulated and the experimental shapes.
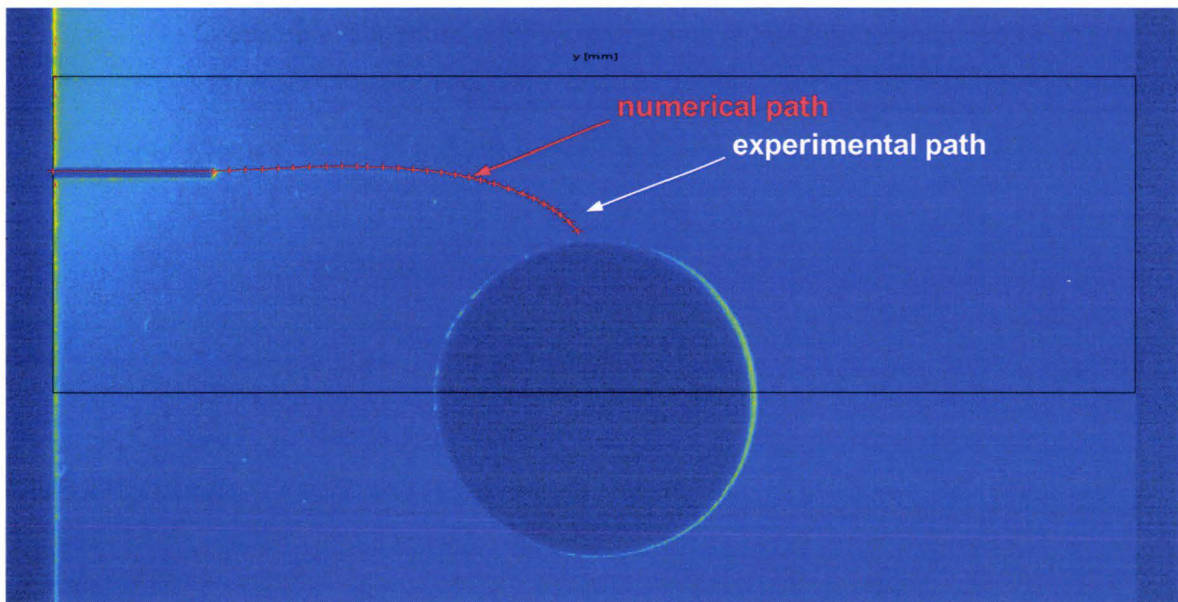
Fig. 112: Experimental and simulated crack path

In conclusion, the ability of FE software to accurately calculate the propagation of a crack under mixed mode loading conditions is validated.

Conclusion

The fracture resistance is characterised by a critical value above which the crack propagates. The fracture toughness is particularly adapted to describe the case of a pure mode I loading. Experiments are performed on CT specimens at ambient temperature in accordance with the ASTM standard [A-399]. The test dispersion is estimated with a statistical method based on a Weibull distribution. The presence of filler particles has the effect to increase the fracture toughness. Therefore, tests on filled and unfilled materials show the difficulty to prepare reproducible crack fronts for filled epoxy resins. Then, a database with four filled epoxy resins (Mat1 to Mat4) is realised, which enables a comparison between the various materials. Finally, the influence of the temperature on the fracture toughness is determined. In a second part, the mixed mode configuration is considered. Tests on CCT specimen allow the representation of the direction of crack propagation as a function of the couple K_I and K_{II}. Moreover, a fracture criterion for cracks under mixed mode loading conditions is extracted for one material (Mat2). The theoretical model MSED is the most appropriate to represent the mixed mode fracture behaviour. However, the MSED criterion is not implemented in FE codes. Since the MTS and MERR return suitable results, they can also be used to numerically predict the direction of crack propagation. The generation of curved crack paths in perforated SEN specimens is numerically studied in chapter 5.5. Experimental paths are in agreement with the numerical prediction.

7 Fatigue crack growth

Fracture criteria for cracks under pure mode I or under mixed mode loadings are identified for epoxy resins in the previous chapter. Although products are generally dimensioned to resist fracture under extreme static loading, progressive crack propagation can appear under repeated loading. As it can strongly reduce the lifetime of components, fatigue crack growth is investigated in this chapter. First, experimental tests are performed with epoxy resins. As a result, parameters of the Paris law are extracted. On the other hand, the behaviour of a structure under cyclic loading can be described with FE analysis. A comparison between simulation and experiments enables to verify the accuracy of the numerical prediction.

7.1 Experimental fatigue crack growth

7.1.1 Test specification

As described in section 4.2.1, tests are realised with CT specimens on Mat2 at ambient temperature. Results published in [Rog07b] are completed in the present chapter.

The notch preparation is performed in two steps. A first crack is introduced by tapping a razor blade into the machined notch provided in the specimen. A fatigue precrack of 0.5 mm is then initiated in situ with the help of the hydraulic machine. This step enables to obtain a similar sharp for each tested sample. The original crack length is generally included between 6.8 mm and 7.4 mm. If during the test the crack deviates more than ±20° from the plane of symmetry over a distance of 0.1 W, the data are considered as invalid.

Cyclic tests are performed at a frequency of 1 Hz. Two sets of data are generated with a load ratio $R = 0.1$: the first under a maximal load $P_{max} = 110$ N and the second with $P_{max} = 140$ N. Maximal values 110 N and 140 N are determined using the fracture toughness K_{Ic} of the material. At ambient temperature, the fracture toughness for Mat2 is evaluated with an average value of 1.37 MPa.m$^{1/2}$, as listed in Tab. 12. For a CT specimen with a crack length of 7 mm, the crack will propagate, when the applied load attains a critical value P_c of 182 N, according to the ASTM analytical solution (see Eq. 136 and Eq. 138). To perform the cyclic tests, the maximal applied loads P_{max} are chosen equal to 60% and respectively 75% of the critical value P_c. This ensures that the crack does not propagate abruptly at the beginning of the test.

The test procedure is here explained for one representative sample under a maximal load of $P_{max} = 110$ N. The applied load oscillates between the maximal load P_{max} and the minimal load P_{min} as depicted in Fig. 64. Geometric dimensions (B and W) and loading parameters (frequency, ΔP and P_{max}) are maintained constant during the test. Consequently, the measurement of crack length as function of the cycle number constitutes the central information. Thanks to the optical system, the crack length can be determined with a precision less than 0.1 mm. The monitored crack lengths are presented in Fig. 113.
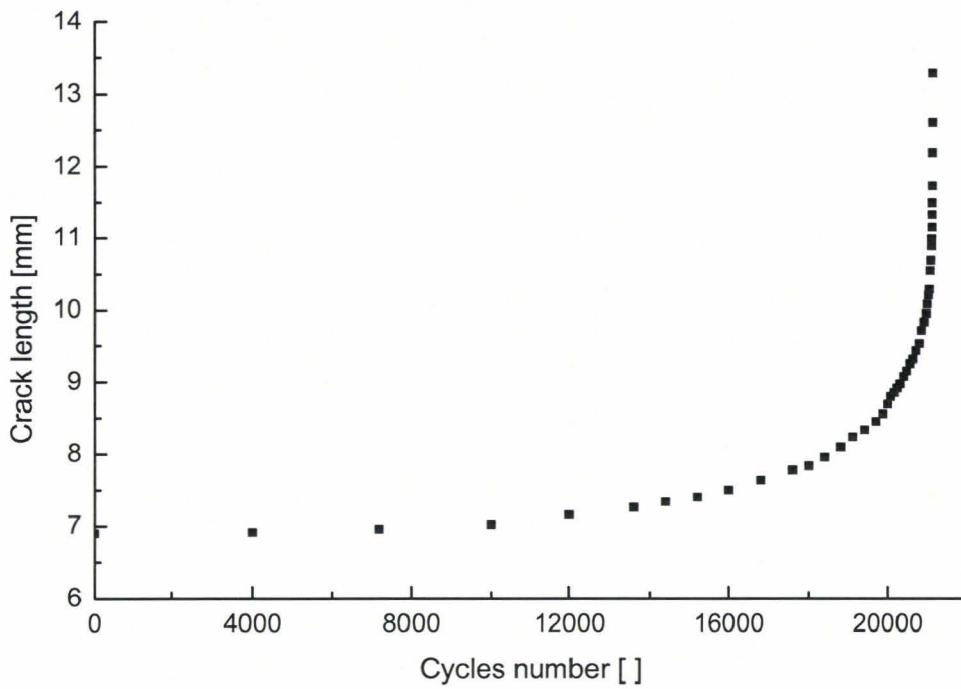
Fig. 113: Measured crack length

7.1.2 Data extraction

The first step consists in the verification of the measured data. While the load stays constant during the experiment and the crack propagates, the stress intensity factor range ΔK increases (cf. Eq. 140). Thus, at the end of the test, the stress intensity factors along the crack tip approach the critical value of the fracture toughness K_{Ic} and leads to unstable crack propagation.
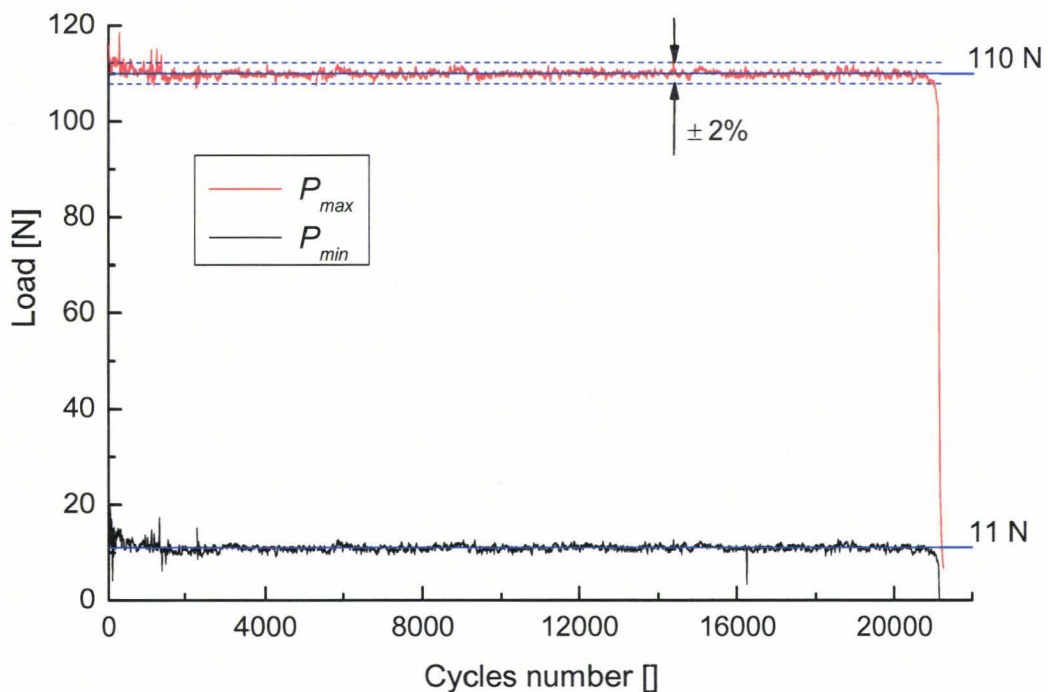
Fig. 114: Force applied and limits for valid data (R = 0.1, frequency 1 Hz)

The applied load ΔP and P_{max} shall be controlled throughout the test with a precision of ±2% [A-647]. As seen in Fig. 114, the machine regulation cannot satisfy this recommendation at the end of the test, because the crack extension between two cycles is too high. This condition sets the upper limit for valid data. The inferior limit for valid data is reached, when a fatigue precrack of 0.5 mm is observed.

The raw data extend from 6.90 to 13.30 mm. The application of the upper and lower limits reduces the valid range of crack length a to [7.40 - 10.20 mm]. For each set of samples, the array of validity is included between 0.3 a/W and 0.55 a/W. The crack growth rate is derived from the curve $a=f(N)$. For that purpose, different mathematical techniques are available. The secant method basically evaluates the amount of crack growth da and the elapsed number of cycles dN between two recorded values:

$$\left.\frac{da}{dN}\right|_{\bar{a}} = \frac{(a_{i+1} - a_i)}{(N_{i+1} - N_i)} \quad \text{for} \quad \bar{a} = \frac{(a_{i+1} + a_i)}{2} \qquad \textbf{Eq. 154}$$

The average crack length $\bar{a}$ is associated to the average crack growth rate and is used to calculate the corresponding ΔK. A second way is based on a linear regression applied to sets of $(2n + 1)$ successive data points. The crack growth rate at the middle data point corresponds to the slope of the fitting curve. This method was successfully tested with $n = 2$, as seen in Fig. 115. Actually, discontinuities of the crack propagation are reduced in comparison to the secant method and to the case $n = 1$.
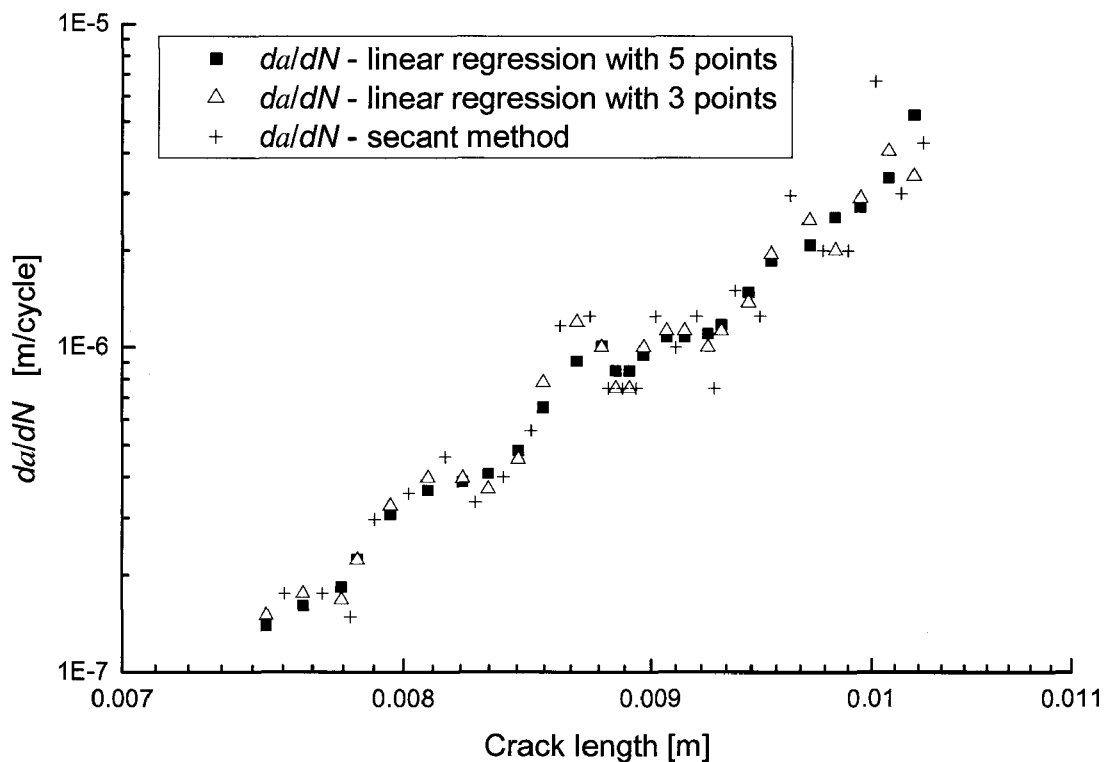
Fig. 115: Results from the linear regression and secant methods to extract da/dN

- 146 -

Each crack length corresponds to a stress state at the crack tip. Eq. 142 provides an analytical expression $\Delta K = f(a)$ for CT specimen [A-647]. Based on a 2D assumption, this formulation assumes a plan strain state and a straight crack front through the specimen. Introduced in chapter 5.3, the through-thickness effect is first not considered. In fact, the use of the ASTM standard [A-647] enables the comparison of the extracted fatigue law with other works.

For each crack length, a crack growth rate da/dN is related to a stress intensity factor range ΔK. In order to characterise the material in terms of fatigue, Paris et al. [Par63] suggest fitting these data to a power law. A logarithmic scale is used to represent the curve as a straight line. Thus the material parameters C and m are determined from the linear regression:

$$\ln\left(\frac{da}{dN}\right) = m \ln(\Delta K) + \ln(C)$$

Eq. 155

As depicted in Fig. 116, the experimental data are fitted to a Paris law with good agreement. The coefficient of determination R^2 is here equal to 0.96, which means that 96% of the variation in $\ln(da/dN)$ can be explained by the linear relation between $\ln(\Delta K)$ and $\ln(da/dN)$. The coefficient m presents the maximal variation and is determined with ±3.1%. A strong correlation is observed for each tested sample.
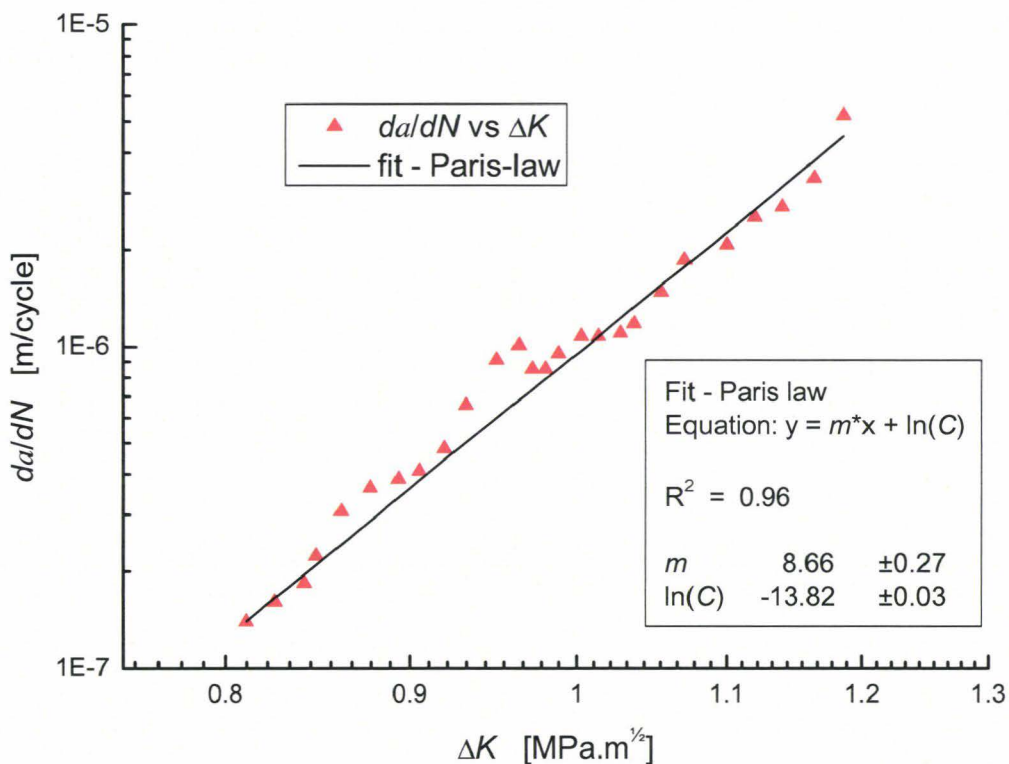
Fig. 116: Fitting of experimental data with a Paris law (evaluation of ΔK based on Eq. 142 [A-647])

7.1.3 Material fatigue behaviour - Paris law

This method of data extraction returns for each sample the da/dN - ΔK curve and the couple of material parameters C and m. Results for a set of samples under a load ratio $R = 0.1$ and a maximal load of $P_{max} = 110$ N are presented in Fig. 117. Fitting coefficients slightly differ from one sample to the other, but a common trend is observed. For a given ΔK, the dispersion is less than a single decade. The scatter comes from material inhomogeneities and from experimental measurement. Particularly during the crack length evaluation, the assumption of a straight crack front through the sample leads to a small difference. Furthermore, a slight variation in the initial crack geometry cannot be avoided between the samples. As well, the load P_{max} is applied with a variation of ±2%.

Sample	m	C
1	9.29	2.55 E-06
2	11.00	2.56 E-06
3	10.66	2.13 E-06
4	10.14	2.16 E-06
5	9.76	1.26 E-06
6	9.64	1.68 E-06
7	8.66	1.00 E-06
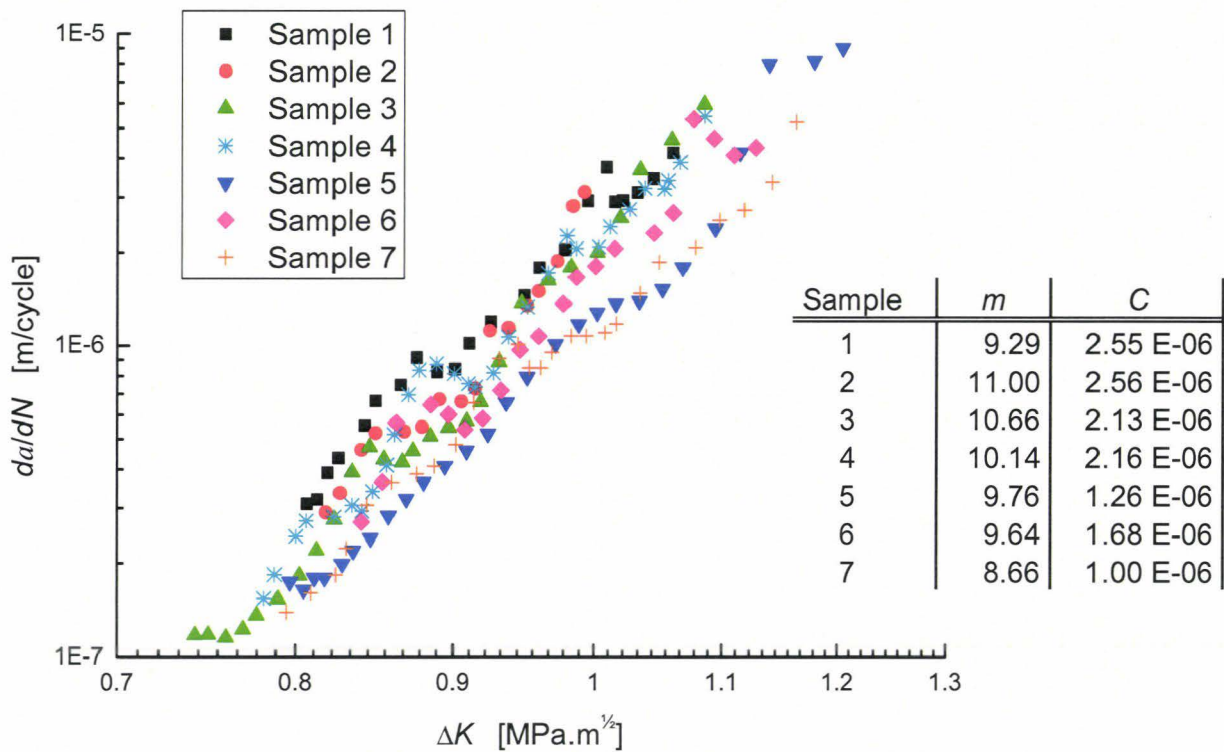
Fig. 117: da/dN - ΔK curve and material coefficients for $P_{max} = 110$ N with $R = 0.1$ (evaluation of ΔK based on Eq. 142 [A-647])

A second set of samples is tested with the same load ratio $R = 0.1$, but under a maximal load of $P_{max} = 140$ N. Due to a higher maximal load, a higher range of crack growth rates is obtained, which extends the results achieved with $P_{max} = 110$ N. The dispersion for the coefficient m is bigger in the case $P_{max} = 140$ N (see Tab. 16), because of a restrained number of experimental points available for the linear regression.

Sample	m	C
8	9.34	1.70 E-06
9	11.34	1.01 E-06
10	12.87	0.92 E-06
11	10.59	1.23 E-06
12	8.67	1.45 E-06

Tab. 16: Material coefficients for $P_{max} = 140$ N with $R = 0.1$

As depicted in Fig. 118, results under P_{max} = 110 N or P_{max} = 140 N follow the same trend. Considering all the experimental points for the fixed load ratio R = 0.1 a global curve fitting provides the Paris coefficients C and m.
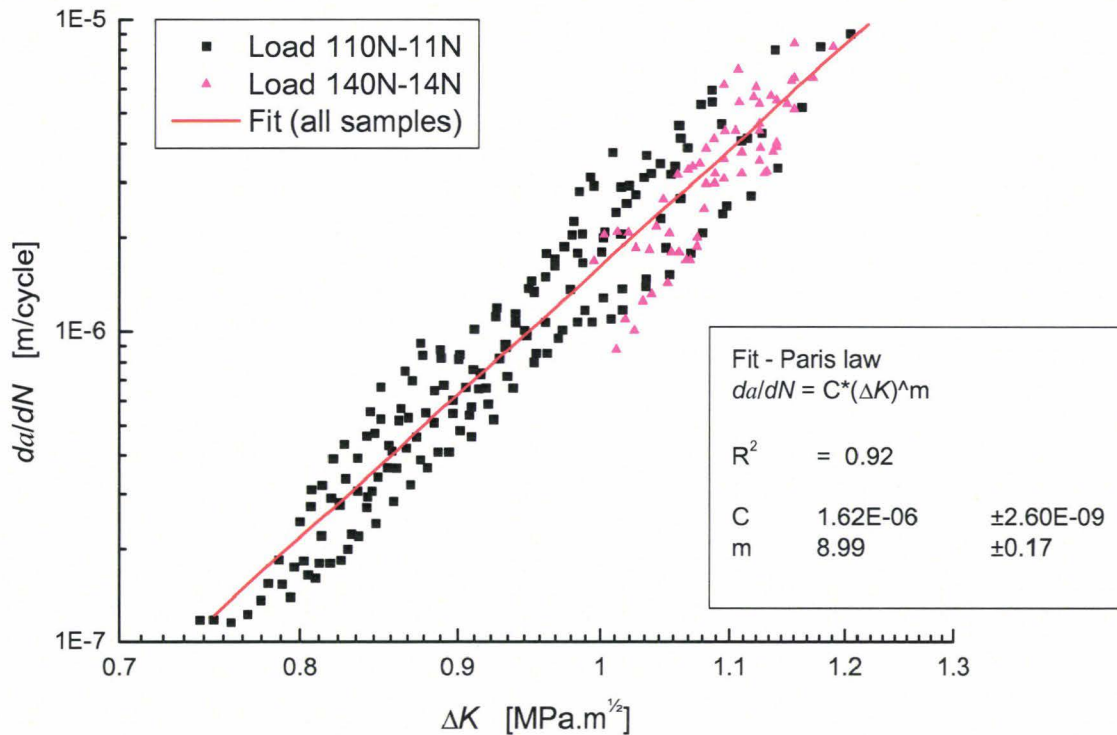
Fig. 118: Fitting of experimental data with R = 0.1 under P_{max} = 110 N and P_{max} = 140 N (evaluation of ΔK based on Eq. 142 [A-647])

For the tested material, the couple (C; m) = (1.62 E-6; 8.99) describes the fatigue crack growth for a load ratio R = 0.1. The coefficient of determination value is close to 1 (R^2= 0.92), which means that the fatigue crack growth in epoxy resins can be explained by the given variables, i.e. a da/dN - ΔK curve, and well represented by a power law. Similar experiments on epoxy resins were performed by Williams [Oso83, Wil84]. The resulted Paris exponents m are found in a range of [7.41 - 10.77] and are in accordance with this work. The extracted Paris exponent m has a high value compared to metallic materials, whose Paris exponent m takes typically values between 2 and 4 [Bro82, Law93]. As well, the fracture toughness for metallic materials is in most cases 50 times higher (see Tab. 5). The fracture toughness is used as parameter to characterise the resistance to fracture of a material under static loading. The coefficient m has the same function for cracks under fatigue loading.

7.1.4 Domain I, II and III of the curve da/dN - ΔK

Previous results describe the behaviour of the crack growth in the linear part of the curve da/dN - ΔK (see Fig. 65). As depicted in Fig. 118, upper and lower limits are applied to restrict the data range to the domain II. The border domains (domains I and III) of the curve da/dN - ΔK are not described.

Domain III

Domain III describes the crack growth for high amplitude of ΔK. The loading conditions are close to the configuration of static tests. The extracted ΔK tends to an asymptotic value ΔK_∞, which is approximated by K_{Ic} (1-R):

$$\Delta K_\infty = (K_{max} - K_{min}) \approx K_{Ic}(1-R) \qquad \text{Eq. 156}$$

Filled epoxy resins are brittle materials with a fracture toughness K_{Ic} about 1.5 MPa.m$^{1/2}$. Consequently, the potential domain of experiments is small in comparison to metals, whose fracture toughness is bigger than 10 MPa.m$^{1/2}$ (see Tab. 5).

The average fracture toughness for Mat2 is equal to K_{Ic} = 1.37 MPa.m$^{1/2}$ and from Eq. 156, the asymptotic value is ΔK_∞ = 1.24 MPa.m$^{1/2}$. This value agrees with results of Fig. 118, whose maximal loading is obtained with ΔK = 1.20 MPa.m$^{1/2}$. Moreover, the upper limit corresponds to a force drop, which is due to an important crack extension in the specimen. Above the upper limit, the experimental values describe the domain III.

Domain I

The domain I of the curve da/dN - ΔK corresponds to slow crack growth rates. Particularly, it is considered that no crack propagation occurs below a threshold ΔK_{th}. The existence and characterisation of the threshold require further experimental tests. The K-decreasing procedure recommends a decrease of the load as the crack grows [A-637].

In this study, the inferior limit for valid data was fixed for a fatigue precrack of 0.5 mm. Arbitrarily defined, the value of 0.5 mm ensures by far the creation of a well-defined fatigue crack front and an established crack growth. Indeed, crack growth rate are greater than 10^{-7} m/cycles.

If the fatigue precrack is fixed equal to 0.2 mm, the crack front can be a priori considered as established. As seen in Fig. 119, additional points are obtained if the precrack length is assumed to be 0.2 mm, instead of 0.5 mm. These points (gray in Fig. 119) are not more aligned with the points used for the fit with the Paris law (black in Fig. 119). As a result, the domain II seems to be defined for crack growth rate superior to 10^{-7} m/cycles, which can experimentally be associated with a stress intensity factor range of ΔK = 0.8 MPa.m$^{1/2}$.

Below 10^{-7} m/cycles, the curve da/dN - ΔK reproduces the characteristic pattern of the domain I. A fatigue crack growth threshold ΔK_{th} equal to 0.73 MPa.m$^{1/2}$ can be asymptotically evaluated. The formulated interpretations should be carefully taken into account, since they are based on the assumption that the fatigue crack is already established for a precrack of 0.2 mm.
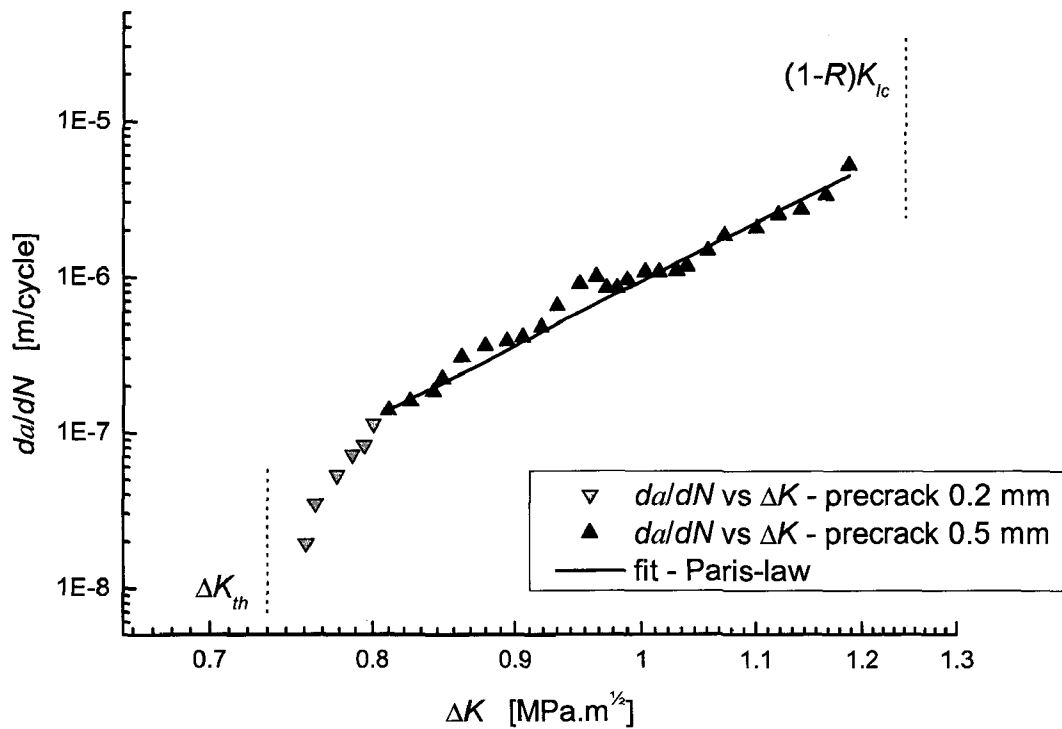
Fig. 119: Fatigue crack growth threshold (evaluation of ΔK based on Eq. 142 [A-647])

Limits of domains II

As drawn in Fig. 65, domain II describes the linear behaviour of the curve da/dN - ΔK. The definition of the upper limit of domain II is related to the fracture toughness of the material and the load ratio. A maximal value corresponding to 95% of $\Delta K_\infty = K_{Ic}$ (1-R) seems to be suitable. As well, the lower limit can be precised. Instead of an arbitrary crack extension of 0.5 mm, the consideration of a minimal crack growth rate da/dN of 10^{-7} m/cycles is more appropriate. Thanks to these upper and lower limits, the current method enables to extract the parameters of the Paris law.

7.2 Numerical fatigue crack growth based on 2D assumption

Fatigue crack growth in epoxy resins is experimentally investigated in the previous part. Data are extracted considering a straight crack front and a plane strain state through the sample as indicated in the ASTM standard [A-647]. As result, parameters of the Paris law are identified, which allow to describe the crack behaviour under fatigue loading. As presented in chapter 3.2, fatigue crack propagation can be simulated by a sequential approach, in which the crack length is updated step by step. The experimental conditions (geometry, loading condition, fatigue behaviour ...) are used to create a numerical model with the commercial software Zencrack. The analysis is here restricted to a 2D representation of the CT specimen. A comparison between simulation and experiments enable to verify the accuracy of the numerical prediction. This work was partly examined and discussed in [Rog07a].

7.2.1 FE analysis

A FE model for CT specimen is generated in part 5.2 with the help of the software Zencrack. For this model, energy release rate and stress intensity factors at the crack tip are evaluated with a difference less than 3% with the ASTM solution. Consequently, the same model can be used to analyse a numerical fatigue crack growth. To be consistent with the ASTM assumptions [A-647], the FE model has the following properties:
- three-dimensional FE model
- displacements on u_z are constrained to enforce a plane strain boundary condition
- straight initial crack front

The experimental characterisation of fatigue crack growth is presented in chapter 7.1. A representative sample is chosen to explain the complete procedure from test to identification of the Paris parameters. The current section proposes to create a numerical model of the same sample, with the objective to compare numerical results and experimental data. Experiments are realised on Mat2, for which a Young's modulus E = 7000 MPa and a Poisson's ratio v = 0.37 are measured at ambient temperature. Dimensions of CT specimens (W = 20 mm, B = 6 mm) are defined in Fig. 59. During the initiation phase, the crack reached a length of 7.4 mm in the experiments, which is set as initial crack length in the simulation. A mesh of the CT specimen with a crack length a = 7.4 mm is generated with Zencrack, as seen in Fig. 70. The cracked mesh is then submitted for analysis to the FE software Abaqus.

During experiments, samples are subjected to a load oscillating between P_{max} = 110 N and P_{min} = 11 N. For the FE analysis, only the maximal load P_{max} = 110 N is introduced as boundary condition. The resulting energy release rate G_{Pmax} is evaluated with Abaqus. The application of the Paris law requires a conversion of G_{Pmax} into ΔK. Zencrack converts G_{Pmax} into K_{max} using Eq. 43 with $E' = E/(1-v^2)$ for plane strain state, which yields:

$$\Delta K = (1-R)K_{max} = (1-R)\sqrt{E'}\sqrt{G_{Pmax}} \qquad \text{Eq. 157}$$

The load ratio R = 0.1 is mentioned in the Zencrack script, as it is required to evaluate the crack growth rate. At this point, Zencrack converts the calculated stress intensity factor range ΔK into a crack growth rate da/dN with the help of the implemented Paris law (Eq. 143). For the tested specimen, the Paris parameters $(C; m)$ = (1.00 E-6; 8.66) were experimentally identified for a load ratio R = 0.1. The discretisation of da/dN into $\Delta a/\Delta N$ gives the possibility to evaluate the amount of crack growth Δa for a given number of cycles ΔN.

The direction of crack propagation derives from the stress distribution. As described in chapter 5.4.2, the MERR or MTS criterion rate can be used to predict the direction of propagation in Zencrack [Hus74, Sih80]. In the case of a CT specimen, normal stresses are preponderant at the crack tip, and an opening mode of crack fracture is observed: the crack propagates along the middle plane of the CT specimen.

In the case of a FE model with a crack length a, the direction of crack extension and the crack growth magnitude Δa can be evaluated. This allows the crack to be advanced through the model from a to $a+\Delta a$. The global geometry is then updated and remeshed automatically with the new crack length $a+\Delta a$. The next analysis step can be run. With this technique, the crack length is updated step by step. As the software Abaqus is used as FE processor, the software Zencrack controls the crack advance through the sample.
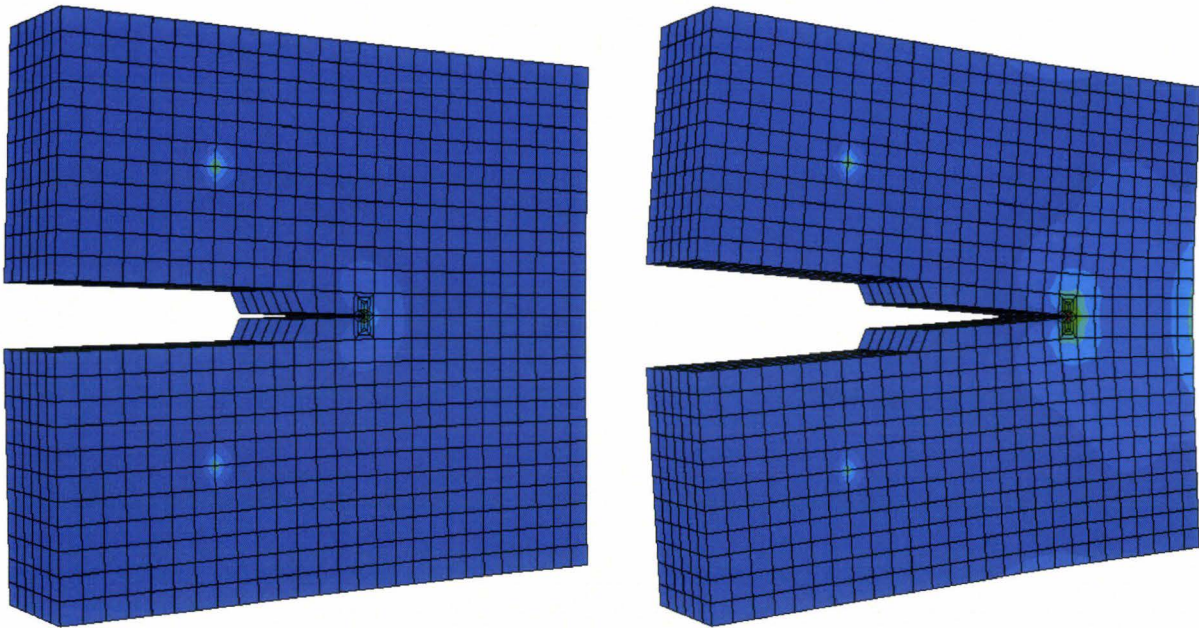
Fig. 120: Numerical fatigue crack growth in CT specimen- First and last increment (FE model with 2D plane strain assumption)

7.2.2 Validation of the FE model with 2D assumption

The Paris law takes a high exponent in the case of epoxy resins. If a value of 9 is considered for the exponent m, a variation of 1% in ΔK leads to a relative error of 10% for the crack growth rate da/dN. For this reason, the numerical model has to be as precise as possible. For example, the thickness B can strongly influence the values obtained for ΔK, and consequently the accuracy of lifetime prediction. As described in Fig. 64, the samples have a nominal thickness of 6 mm. However, the sample, which was considered as the representative sample, has a real thickness of 5.88 mm. Two meshes were generated with the respective thicknesses and submitted to a fatigue crack growth analysis in order to illustrate the thickness influence.

Fig. 121 represents a plot of the crack length evolutions during the simulation for thicknesses of 5.88 and 6.0 mm. Both curves show the same trend as experimental results. The time-to-failure can be defined as the number of cycles achieved before a complete rupture of the sample. Compared to the experimental time-to-failure, the model with the ideal thickness overestimates the lifetime by about 14.9%, while the model with the real thickness returns a difference of only 3.8%. This underestimation can be explained by the assumption of plane

strain state, which is applied in the numerical model. However, the real sample is influenced by the free surfaces and deviates therefore from the assumed plane strain state. As the plane strain state is not a conservative assumption compared to the plane stress [Yam78, Dho01], the simulated stress intensity factor range is higher than expected and yields a slight underestimation of the time-to-failure.
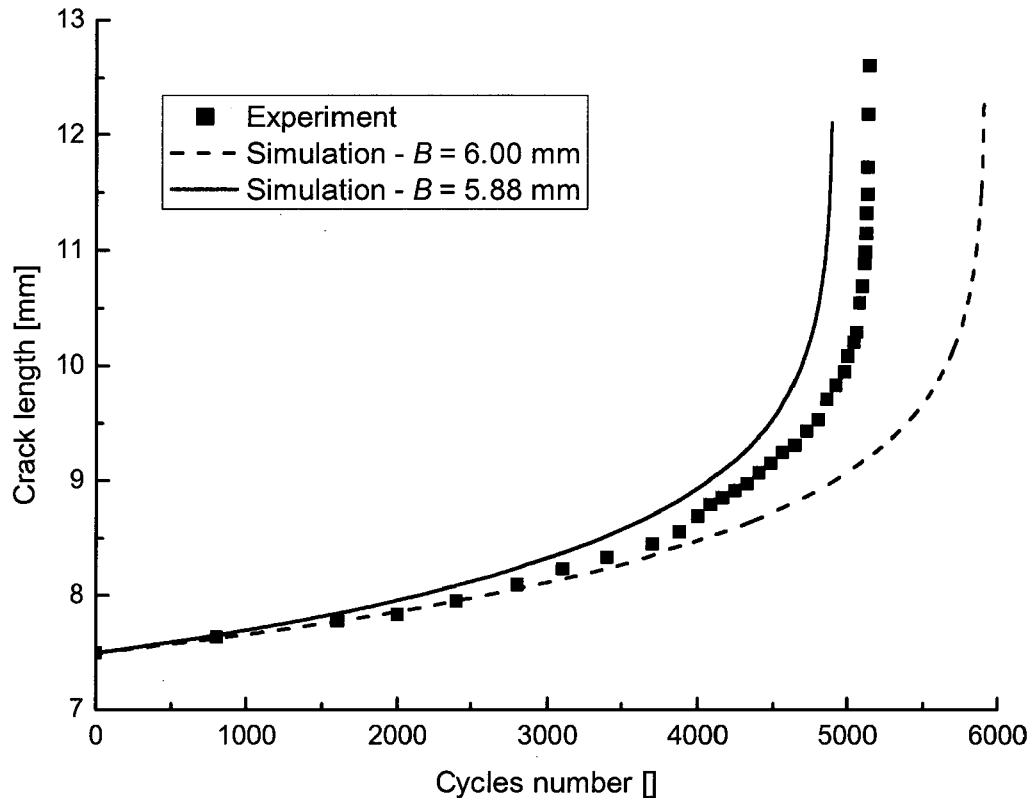
Fig. 121: Experimental and simulated crack length evolution (FE models with 2D plane strain assumption)

As indicated earlier, a plane strain state is imposed through the sample by constraining displacements in the thickness direction. As a result, effects due to the thickness are not more apparent, i.e. the FE model is equivalent to a 2D model. Simulation results are in agreement with experiments, so that a fatigue crack growth can be effectively predicted in CT specimens using this FE model.

7.3 Numerical fatigue crack growth based on 3D assumptions

The case of non-symmetric components requires the investigation of fatigue crack growth with 3D models. The precedent model with the restriction of plane strain state and straight crack front is not more valid. Moreover, a through-thickness effect occurs in three-dimensional models. This is numerically described in chapter 5.3 for the CT specimen geometry. Particularly, the curved nature of the crack front influences the computed values of the stress intensity factor along the crack front. Tests on epoxy resin enable a comparison between experimental and numerical crack curvature.

7.3.1 Crack front geometry in unfilled epoxy resin

Without filler particles, epoxy resins are commonly in a form of a transparent material, which enables to observe the geometry of the crack front. For this, a CT specimen of unfilled Mat1 is subjected to successive load-unload cycles. A controlled displacement generates growing stresses at the crack tip and as soon as a force drop is detected, the specimen is unloaded. The procedure is repeated until the specimen fails.

The inspection of the created crack surface with an optical microscope lets distinguish the consecutive crack extensions. Fig. 122 clearly shows the two steps of the notch preparation. Tapping with a razor blade into the machined notch creates a straight crack front. After that, the specimen is loaded at a very slow rate, until crack propagates. As expected, this second step introduces a well-defined crack front. After a rapid transition from an initial straight crack front (razor blade) to a slight curved crack profile (initial precrack), the curvature of the crack front is kept during the test [Daw92]. The crack presents a symmetric front through the thickness, so that crack lengths at the two free surfaces are equal. The crack in the middle of the specimen is about 0.16 mm longer than at the surface. This represents a variation of 2% for a precrack length of 8 mm.
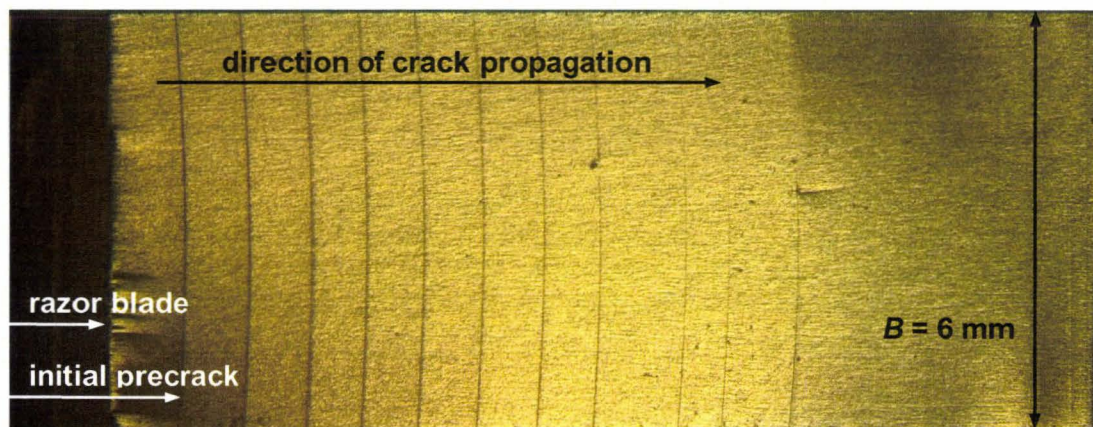
Fig. 122: Crack front geometry after successive load-unload cycles for unfilled Mat1 at ambient temperature

Fig. 122 shows crack fronts created after consecutive static loading/unloading phases. The loading was applied at a rate of 0.01 mm/min, so that crack propagates slowly. This enables the creation of regular consecutive crack fronts, comparable with those obtained during a fatigue test. Actually, repetitive shapes indicate that crack growth rate at each point along the crack front was constant, as explained by Dawicke [Daw92].

For unfilled Mat1, the Poisson's ratio is assumed equal to 0.3. The curvature of the crack front can be numerically estimated from a fatigue crack growth simulation with $v = 0.3$, as seen in Fig. 73. The superposition of experimental and numerical crack fronts is shown in Fig. 123. Simulated crack fronts provide excellent agreements with experiments.
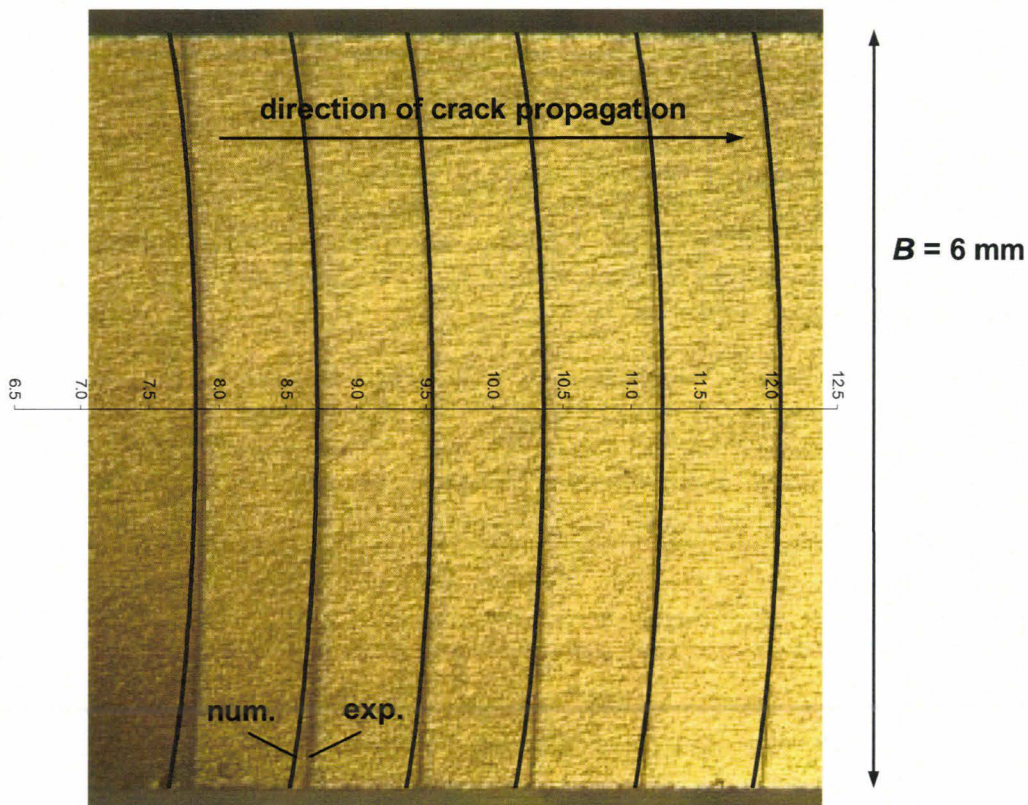
Fig. 123: Superposition of experimental and numerical crack fronts for unfilled Mat1

The simulation procedure is based on the assumption that the distribution of the energy release rate is constant along the crack front. The accordance between experimental and numerical results indicates that the crack front tries to take a shape that establishes a homogeneous energy release rate distribution through the thickness [Bro82, Yam78].

7.3.2 Curved crack front in filled epoxy resins

In the previous section, a comparison between experimental and computed crack fronts establishes that simulation can accurately predict the front curvature in the case of an unfilled material. In order to confirm this result for filled epoxy resins, additional experiments are performed on Mat2.

Since the current material Mat2 is opaque, direct observations of the crack front are impossible during a fatigue test. An examination of the crack front with optical microscopes is only possible after the test. To make evident the curved nature of the crack front, additional experiments are required: three fatigue tests are started as indicated in chapter 7.1.1, but are stopped before the crack attains a length of 9 mm. Specimens are then subjected to a tensile loading at a rate of 1 mm/s. Consequently, the crack front generated during the fatigue step can be easily observed.
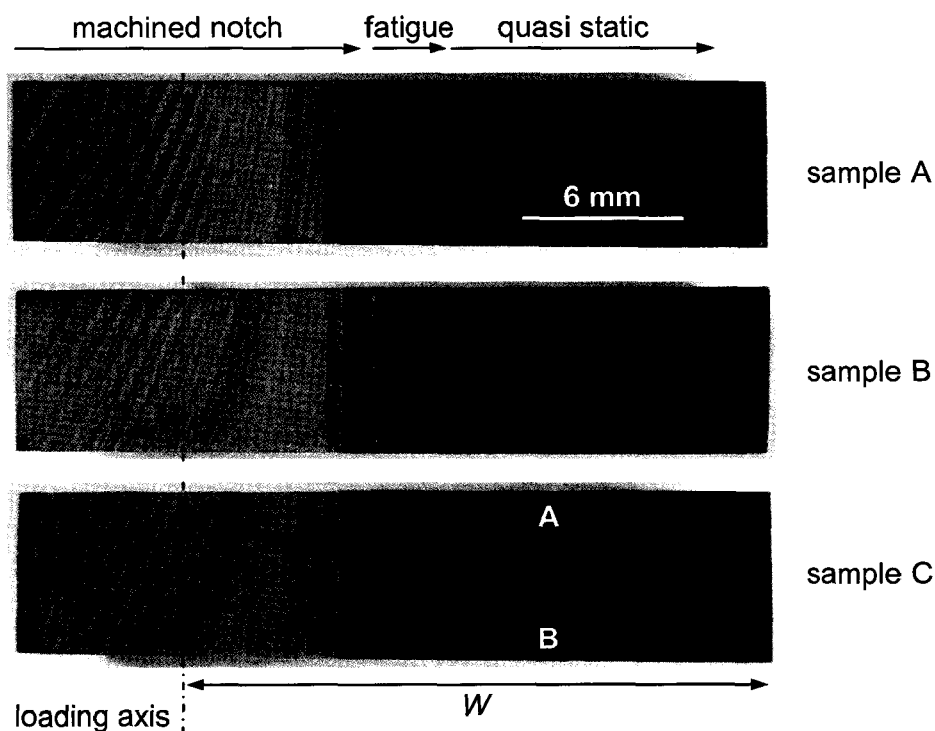
Fig. 124: Curved crack front in Mat2

Fig. 124 shows the crack planes created by fatigue for three different specimens (zone in light grey in the middle of the specimen). It is obvious that crack fronts are curved, but geometries slightly differ from one sample to the other. For example, the crack length on side A is smaller than on side B for the sample C. For each sample, the crack front is extracted.

For Mat2, the Poisson's ratio is equal to 0.37. As seen in Fig. 73, a fatigue crack growth simulation returns a crack front curvature specific to $v = 0.37$. Experimental crack fronts are superimposed to the numerical crack front. The crack length in the middle of the specimen is taken as reference point to plot the graph in Fig. 125. Globally, the numerical crack front is in accordance with the experimental crack shapes. The error is maximal for samples B and C, whose crack fronts are slightly dissymmetric. In fact, reproducible symmetric crack fronts are difficult to generate with filled epoxy resins, in comparison with unfilled epoxy resins.
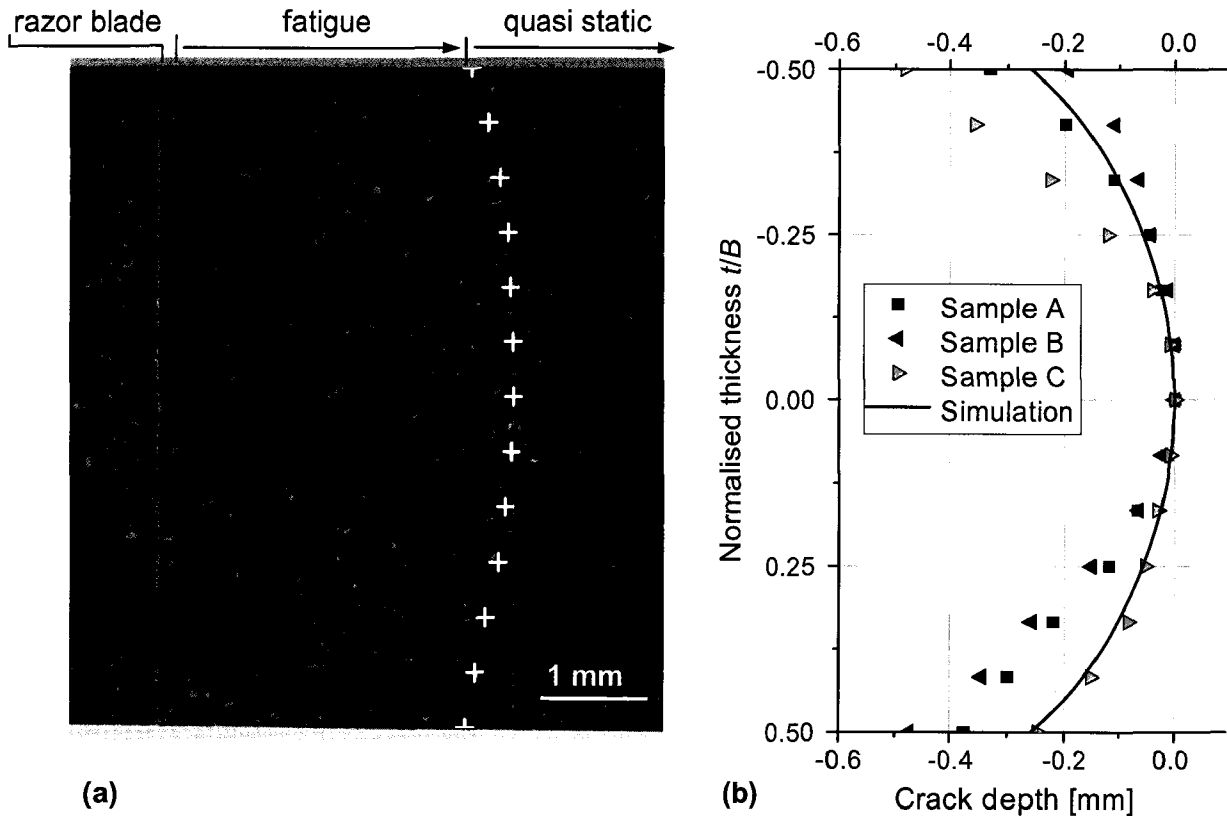
Fig. 125: (a) Extraction of experimental crack front;
(b)Comparison between experimental and numerical crack fronts for Mat2

According to Fig. 123 and Fig. 125, the assumption of an initial straight crack front in the three-dimensional FE model is not appropriate for fatigue crack growth prediction.

7.3.3 FE model with initial curved crack front

To accurately model the fatigue crack propagation, an initial curved crack front have to be inserted in the 3D FE model, instead of a straight configuration. As explained earlier, the direct observation of the crack front is impossible during classical fatigue tests, so that an extraction of the initial crack shape for each sample is not viable. On the other hand, simulation provides a good estimation of the experimental crack shape. As described in chapter 5.3.2, different crack profiles are investigated. It is found that a profile, which is based on a 4th degree polynomial, fits closely the numerical crack front. The FE model introduced in chapter 5.3.3 integrates this numerical crack front as initial front design.

In the next sections, the FE model has the following properties:
- three-dimensional FE model
- displacements on u_z are not constrained (no plane strain boundary conditions)
- initial crack front is curved (4th degree polynomial)

Up to now, the investigation of the numerical model is based on a representative specimen. For this sample, a crack length of 7.4 mm is measured at the surface after fatigue precrack during experiments. With a curved front profile, the crack length attains progressively a maximum of 7.66 mm in the middle of the specimen. In fact, a Poisson's ratio of 0.37 for Mat2 induces a crack depth of 0.26 mm for the CT specimen geometry. As seen in chapter 5.3.3, a constant stress intensity factor is extracted along the crack front through the thickness, which is named effective stress intensity factor K_{eff} (see Fig. 74a). As seen in Eq. 140, the stress intensity factor range ΔK is evaluated from the applied load ΔP and

geometrical parameters (W, B and crack length a). Assuming a straight crack front, a dimensionless function f is proposed by the ASTM to establish the relation between the different parameters. Based on the same concept, a formulation which considers the curved crack front in 3D model is presented in chapter 5.3.4. The dimensionless function F_{eff} is introduced to express K_{eff} as a function of crack length (see Fig. 75).

7.3.4   Effective material parameters

During experiments on Mat2, the crack advances progressively, taking the form of a curved shape. The influence of the crack front curvature should also be considered in the identification of the material parameters. For this, a modified expression for the stress intensity factor as a function of the crack length $K_{eff} = f(a)$ was proposed in chapter 5.3.4. Application of the expression $K_{eff} = f(a)$ to the original set of experimental data provides a new couple of material parameters (C_{eff}, m_{eff}), which takes into account the through-thickness effect.

The classical method based on the ASTM expression was presented in chapter 7.1.2. The coefficients (C, m) = (1.00E-6; 8.66) are estimated for the representative sample. The same experimental data are now converted with the expression $K_{eff} = f(a)$, as seen in Fig. 75. The extraction of the Paris law coefficients (C_{eff}, m_{eff}) = (4.46E-7; 8.89) is depicted in Fig. 126.
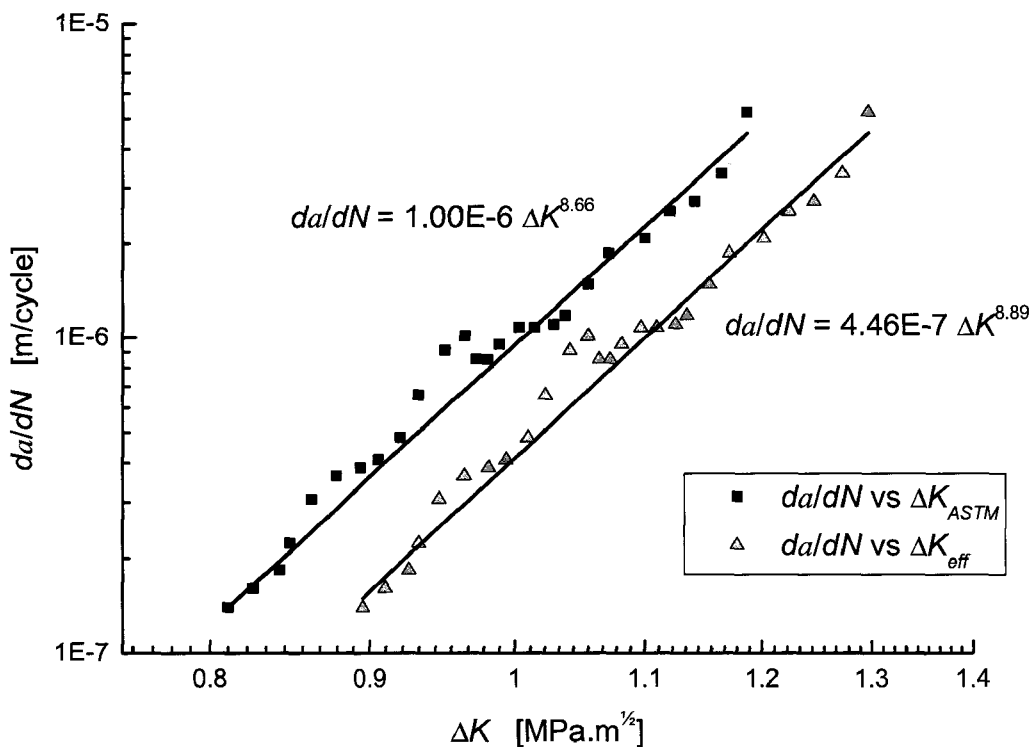
Fig. 126: Conventional and effective da/dN - ΔK curves
(P_{max} = 110 N with R = 0.1)

Though the coefficient C_{eff} is two times smaller than the parameter C, only a small variation is detected for the coefficients m and m_{eff}. Graphically, the two fit curves appear parallel in a diagram with logarithmic scales. The da/dN - ΔK_{eff} curve is globally obtained from the conventional da/dN - ΔK_{ASTM} after a translation of ΔK = 0.09 MPa.m$^{1/2}$. As seen in Fig. 74a, K_{eff} is about 10% higher than the reference K_{ASTM}, so that ΔK_{eff} is approximately 0.09 times higher than ΔK_{ASTM} for R = 0.1. For a given loading condition ΔK, a smaller crack growth rate da/dN will be evaluated with the effective model.

7.3.5 Lifetime prediction in three-dimensional FE models

A three-dimensional model of the CT specimen is generated considering the real thickness of the sample B = 5.88 mm. Displacements on u_z are not constrained. An initial curved crack front is introduced, whose geometry is defined by a 4th order polynomial function. In order to take into account the through-thickness effects, the modified Paris law da/dN - ΔK_{eff} is implemented. A complete fatigue crack growth simulation is run. The surface crack length is chosen as characteristic crack length and compared with the experimental measurements in Fig. 127. A satisfying correlation is observed.
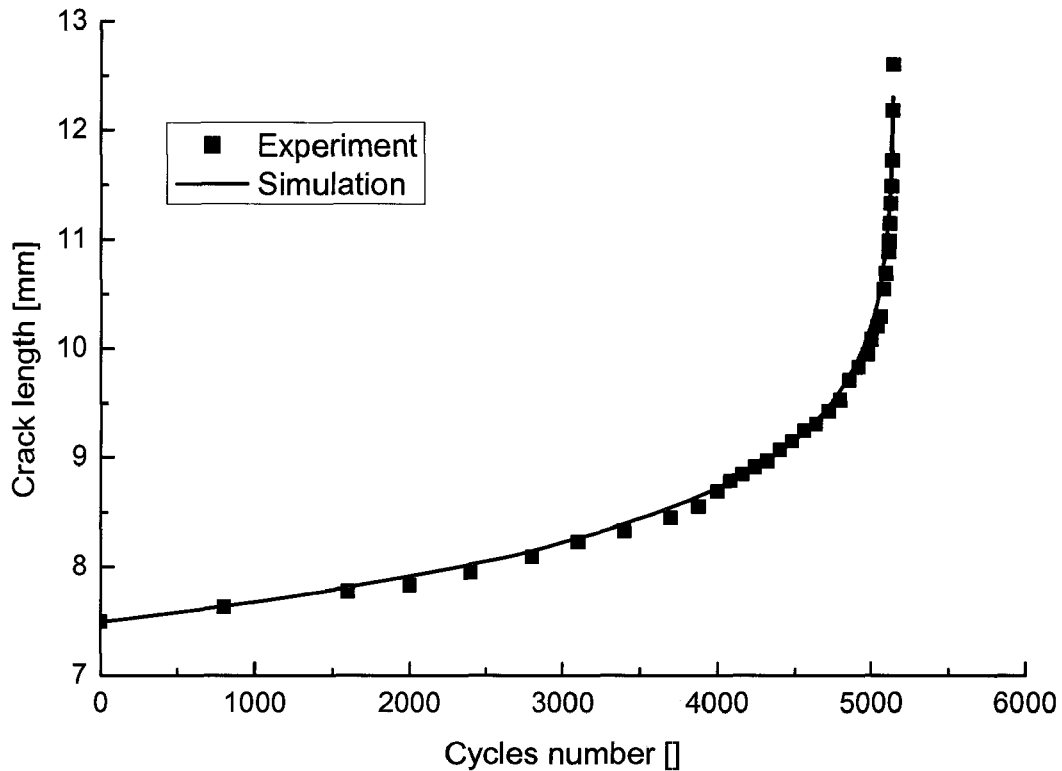
Fig. 127: Lifetime prediction vs. experiment - FE Model with curved crack front and effective material parameters

Numerical results are here depicted for a unique specimen. The entire procedure is reproduced for each specimen of the part 7.1.3. As well, an excellent agreement is found between experimental crack advancement and numerical prediction.

The same FE model is considered but using the conventional Paris law da/dN - ΔK_{ASTM} with the coefficients (C, m) = (1.00E-6; 8.66), as evaluated in chapter 7.1.2. As well, a fatigue crack growth simulation is run. Results are compared with the simulation using the effective material parameters in Fig. 128.
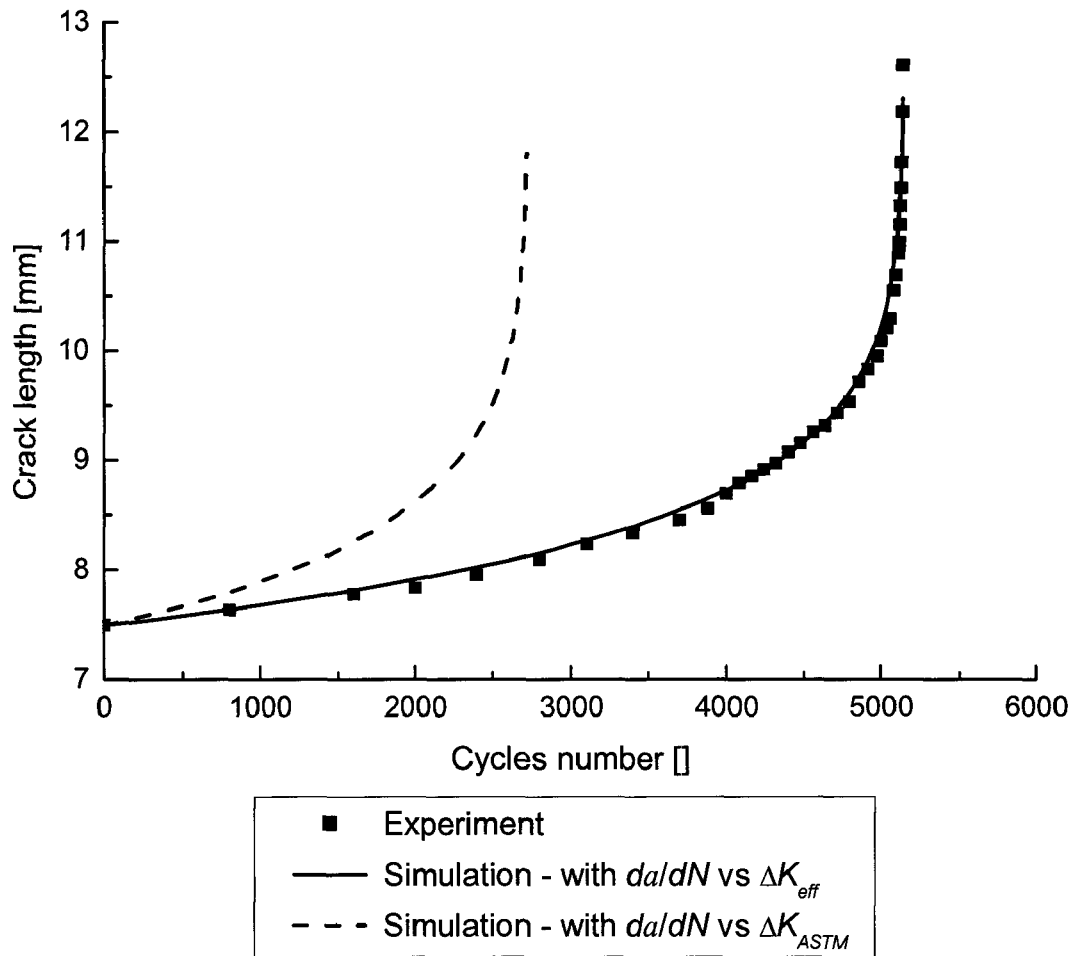
Fig. 128: Lifetime prediction vs. experiment - FE Model with curved crack front using conventional or effective material parameters

The lifetime computed using the conventional Paris law da/dN - ΔK_{ASTM} is underestimated in comparison with the measured data. Though this prediction is conservative, a variation of 50% is observed. For this reason, the conventional Paris law da/dN - ΔK_{ASTM} is not adapted for 3D model. To accurately predict the fatigue crack growth with 3D models, the use of the effective Paris law da/dN - ΔK_{eff} is recommended.

Conclusion

Methods to characterise the fatigue crack growth in filled epoxy materials are explained in this chapter. Experimentally, a cyclic load with constant amplitude is applied on CT specimens, while the crack length is optically measured on the sample surface. Data are evaluated according to the ASTM formulation [A-647]. A fit of the curve da/dN - ΔK_{ASTM} to a Paris law enables the identification of material parameters. Paris exponent m, which is a characteristic value to describe the crack behaviour under fatigue loading, is found about 9 for the tested filled material. Experimental coefficients are then used as input data for FE analysis. During the simulation, the crack is updated step by step. To be consistent with ASTM standards [A-647], a model is generated with a straight crack front and a plane strain state through the sample. A comparison between simulation and experiments enables to verify the accuracy of the numerical prediction with 2D models. However, some complex structures can not be reduced to two-dimensional models. For this reason, fatigue crack growth is investigated in 3D. First, the shape of the crack front through the thickness is experimentally characterised with filled and unfilled epoxy resins. A good correlation is observed with the computed crack front geometries. As described by Yamamoto [Yam78], the crack front curvature depends on the Poisson's ratio. Moreover, the front shape and the computed values of the stress intensity factor along the crack front are related. The curvature of the crack front can be considered as a geometrical parameter and integrated in the analytical expression used to evaluate the stress intensity factor. The notion of effective stress intensity factor K_{eff} and effective dimensionless function F_{eff} are introduced in chapter 5.3. Thus, a fit of the curve da/dN - ΔK_{eff} returns coefficients (C_{eff}, m_{eff}) of the modified Paris law. Finally, a 3D model without plane strain conditions and with a curved crack front through the sample is created. Conventional and effective Paris law are applied as material fatigue behaviour. While the conventional fatigue behaviour returns an error of 50% on the lifetime, the effective Paris law enables an accurate estimation of the time to failure.

8 Discussion: "Fracture mechanics in conception"

Within the context of electronic packaging, interfaces are sources of severe discontinuities in thermal and mechanical properties [Har01, SuS01, Leb04]. Mismatches due to different coefficients of thermal expansion, Young's moduli or Poisson's ratios create stress concentrations at the assembly interface. If critical stress gradients are reached, delamination occurs. As well, crack propagation inside the encapsulating material may lead to the component failure. The current work focuses on this phenomenon: experimental and numerical methods are proposed to predict the crack propagation in epoxy resins. The use of these techniques during the development of automotive components will improve their resistance to fracture and their lifetime.

8.1 Crack growth under critical loading

Encapsulation materials have to ensure the protection of electronic parts. During the conception phase, material properties are examined to determine the optimal material. Epoxy resins present an appropriate behaviour for thermal and electrical isolation. Moreover, moulding processes enable a wide domain of applications. However, the capacity of epoxy resins to resist mechanical loading is limited. In fact, epoxy resins are brittle materials. A parameter to quantify the material resistance to critical loading is the fracture toughness.

8.1.1 Material properties

The method described in chapter 6.1 enables the evaluation of fracture toughness for polymer materials. This technique can be applied to characterise the influence of chemical substances like modifiers and filler particles on fracture resistance [Wal04]. As the fracture toughness is sensitive to the composition of the epoxy resin, this mechanical parameter is analysed during the formulation of new epoxy resins. The development of epoxy resins which support high temperature and high stress conditions is a central topic for the automotive industry. Actually, epoxy resins protect electronic components dedicated to the engine regulation and placed in the motor compartment.

Mechanical failure of a structure is caused by the modification of the constrained material. Epoxy resins are high brittle materials ($K_{Ic} \approx 1$ MPa.mm$^{1/2}$) in comparison with metallic materials ($K_{Ic} > 10$ MPa.mm$^{1/2}$). For this reason, the analysis of their mechanical properties is essential in the determination of the applied material. The measurement of fracture toughness for various epoxy resins creates a material database specific for fracture mechanics, as seen in Tab. 12. As the energy release rate integrates the stiffness and the fracture toughness under a unique parameter, the energy G may also be chosen to characterise the resistance to fracture, as shown in Tab. 14. Classifications obtained with the energy or fracture toughness are analogous, because the modulus of elasticity E is comparable from one epoxy resin to the other. Finally, the material which minimises the risk of fracture can be extracted from this classification. From a scientific point of view, only the material properties are considered. However, the choice of the material in industry is generally a compromise between price, manufacturing process and material properties.

8.1.2   Fracture prediction with numerical analysis

Numerical tools facilitate changes in the design of components. Not only the material properties may be easily modified, but also the component geometry or the loading conditions. This enables the development of reliable structures considering fracture criteria.

The introduction of a crack in a numerical model requires the definition of the crack orientation and crack length. First, a virgin model is numerically generated. A Finite Element (FE) analysis is run to determine zones of stress concentration. In most cases, cracks occur where stress gradients are maximal and perpendicular to the maximal principal stress [Wit04]. In fact, opening mode (mode I) is by far the most critical mode of fracture [Bro82]. Critical locations can also be identified from a damage mechanics analysis [Dep05]. Therefore, the length of the crack may be assumed equal to the characteristic size of flaws contained in the material. For example, delamination between filler particle and matrix can be considered as a precrack and the crack length is assumed equal to the particle size. Nevertheless, the exact location and orientation of a crack is only possible from pictures of real components containing a crack. Non-destructive techniques like acoustic or ultrasonic scanning microscopy enable the detection of cracks inside the structure [Leb04]. A precise representation of the crack in the FE model is then possible.

As defined in chapter 3, FE methods propose numerous techniques to mesh the structure. In order to improve the precision of the computed stress intensity factors or energy release rate, it is recommended to represent the stress singularity at the crack tip. Consequently, a fine mesh near the crack tip is required, while a coarse mesh is applied on the rest of the structure to limit the degrees of freedom in the model and so the calculation time. Specific software packages, like ADAPCRACK3D or Zencrack, make use of submodeling or special elements disposition techniques to generate the mesh.

Once the stress intensity factors (or energy release rate) are computed, they may be compared to the material critical values. If an opening mode of fracture is preponderant at the crack tip, the fracture criteria is based on the fracture toughness K_{Ic} (see Eq. 30). A crack propagation is assumed, if the computed stress intensity factor K_I reaches the fracture toughness K_{Ic}. An extension of this fracture criterion is made for cracks under mixed mode loading condition. Actually, shear stresses are not negligible in the case of complex loading. Fig. 109 is a graphical representation of this criterion, which divides the (K_I, K_{II})-plane in a *safe zone*, where no crack propagation occurs, and an *unsafe zone*, where the applied loads lead to fracture. Stress intensity factors K_I and K_{II} at the crack tip can be numerically evaluated. In the diagram, the position of the point with computed coordinates (K_I, K_{II}) determines if the crack will grow or not.

Based on fracture criteria, the combination of numerical and experimental methods enables:
- the determination of the critical loading acceptable for a given structure. This technique can be used to establish the service conditions of a structure.
- the estimation of the critical default size for a given loading condition. For this, the "worst case" of a crack perpendicular to the maximal principal stress is modelled. By varying the crack length, it is possible to estimate the critical crack size.
- the comparison between various component geometries for a given loading condition.

The application of such methods is for the moment limited to the analysis of failure in existing structures. The complete integration of these methods in the conception of new components is associated to the development of strategies to improve the design of the studied component. The combination of software packages dedicated to fracture mechanics with optimisation algorithms may be a complex but powerful numerical solution.

8.2 Fatigue crack growth

Products can be dimensioned to resist fracture under extreme static loading using the fracture toughness. Nevertheless, progressive crack propagation may occur under repeated loading. This phenomenon is named fatigue crack growth.

This study has the ambition to provide simulation methods able to accurately predict fatigue crack growth in epoxy resins. As depicted in chapter 7.2, a FE approach is used to incrementally evaluate the growth of a crack under fatigue loading. To update the position of the crack front, two parameters have to be estimated at each step:
- the direction of crack growth
- the crack growth amplitude between two steps

The capability of numerical software to predict the direction of crack propagation using theoretical models (MTS, MERR, MSED) is shown in sections 6.2.3 and 6.2.6. The crack advance is evaluated from the fatigue material behaviour.

8.2.1 Fatigue material behaviour

Material data are required to run fatigue crack growth simulations. The complete procedure to characterise epoxy resins is described in section 7.1. Tests are performed in accordance with the ASTM standard [A-647]. A Paris law is used to express the fatigue crack growth rate da/dN as a function of the stress intensity factor range ΔK. As epoxy resins are brittle materials, the domain used to fit the curve da/dN-ΔK to a Paris law is restrained. In fact, the crack growth rate da/dN is included between 10^{-7} and 5.10^{-6} m/cycles. Above and below these rates, the interpolation is not more appropriate, as seen in Fig. 119. For the tested material, the couple $(C; m) = (1.62 \text{ E-6}; 8.99)$ describes the fatigue crack growth for a load ratio $R = 0.1$.

For the evaluation of ΔK, the ASTM standard assumes a constant crack front and a plane strain state through the sample. It means that this conventional method does not take into account the thickness effect. Particularly, the curved nature of the crack front is not considered. Section 5.3 presents a numerical study which integrates the through-thickness effect in the formulation $\Delta K = f(a)$. It leads to the definition of effective material parameters (C_{eff}, m_{eff}) to describe the fatigue behaviour. This effective formulation finds its application in problems where 3D effects are not negligible. For 2D cases, the ASTM standard has to be applied. Actually, the use of a standardised method enables a comparison of the extracted fatigue parameters with other works based on the ASTM standard. Moreover, the ASTM formulation is not dependent of the material Poisson's ratio.

8.2.2 Numerical simulation based on 2D or 3D models

Particular geometries and loading conditions allow the representation of structures with 2D models. The implemented fatigue behaviour of the material has to be appropriate to the numerical model. For 2D cases, the conventional material parameters from the ASTM standard have to be applied as input data. This method is validated in the case of a CT specimen in section 7.2. As a result, the lifetime in structure containing a crack is accurately estimated with 2D numerical models.

The case of non-symmetric components with complex loading requires the investigation of 3D models. Using the same procedure, a fatigue crack growth can be simulated. Concerning the material data, two approaches are possible: either the conventional or the effective material may be implemented. The use of conventional material parameters (from the ASTM)

provides an approximation of the lifetime. Though a huge difference about 50% with experiments is observed in the present study, the prediction is conservative. On the other hand, simulations performed with effective material parameters are in good agreement with experiments, as seen in Fig. 128. In 3D models, the use of effective material parameters improves the prediction quality by providing an accurate evaluation of the lifetime.

8.3 Perspectives

Nowadays, fracture analysis is essentially applied to the understanding of crack propagation after failure. The increasing influence of simulation in the conception phase leads to an integration of numerical fracture analysis during the development of components. Nevertheless, the application of such techniques has to be validated. The current work demonstrates the accuracy of numerical fracture analysis to predict crack propagation under critical loading for pure mode I or mixed mode conditions. As well, fatigue behaviour is described with precision for cracks under pure mode I. A particular attention is required for the material data applied in 2D or 3D models.

8.3.1 Fatigue crack growth under mixed mode loading

Mixed mode loading implies that mode II of fracture is not negligible and that the crack deviates from its original plane. As stated in chapter 6.2.3, the crack propagation direction may be accurately estimated with the help of numerical models. In addition, tests with perforated SEN specimens show that the profile of a curved crack path can be numerically predicted with precision.

To characterise the material fatigue behaviour, the fatigue crack growth rate da/dN is expressed as a function of the applied loading ΔK. Formulations are extracted from tests performed on cracks under pure mode I of loading [A-647, Zen06, Bro82]. As these expressions do not integrate effects due to shear stress, their application to fatigue crack growth under mixed mode conditions is not optimal. Concepts integrating effects of mode II and mode I seem to be more appropriate. The definition of a global stress intensity factor combining mode I and II has the drawback to introduce a new factor. In contrast, the energy release rate G is a global fracture mechanics parameter, whose formulation is valid for pure mode and also for mixed mode loading (see Eq. 95). A relation $da/dN = f(\Delta G)$ may enable the prediction of lifetime based on an energetic criterion.

8.3.2 Thermo-mechanical loading

The present work focuses on crack propagation under mechanical loading. However, mechanical properties of epoxy resins depend on temperature. As seen in Fig. 97, the Young's modulus decreases with increasing temperature, especially with an abrupt drop near the glass transition temperature T_g. As well, important effects of temperature are observed on Poisson's ratio or on fracture toughness (see Fig. 99). Thermal variation should be avoided on epoxy resins due to their low toughness, low thermal conductivity and high CTE.

For thermo-mechanical analyses, transient and steady states have to be distinguished. Tests to measure the fracture toughness, which are performed on CT specimens at different fixed temperatures, correspond to a steady state. In fact, a temperature equilibrium is maintained during the test and the temperature stays uniform in the sample. Let consider a structure containing a crack and under service conditions which implies a fixed temperature T_0. The deformation response to a mechanical loading is controlled by the mechanical properties of

the material at T_o. If the crack is subjected to a pure mode I of loading, the fracture toughness may be used as fracture criteria. Consequently the stress intensity factor K_I at the crack tip has to be compared with the value of the fracture toughness at T_o. The temperature dependence of the fracture toughness K_{Ic} is shown in Fig. 99. As well, the temperature may have significant effects on K_{IIc} which is the critical stress intensity factor for pure mode II of loading. Consequently, the fracture criterion for mixed mode loading probably has to be specified as a function of the temperature.

As well, cooling down or heating period, during which a uniform temperature is hold in the sample, can be treated as steady state problems. In epoxy materials, the gelification temperature can be assumed as a state free of stresses in the material. After the curing, the material is cooling down to the room temperature. In the case of electronic packaging, shrinkage of the epoxy resin causes the apparition of residual stresses in the structure. In fact, internal stresses are induced by the mismatch of thermal expansion coefficients (CTE) between the different materials in the structure. This phenomenon can lead to crack propagation. A numerical analysis provides the evolution of stress intensity factor during the temperature change. A comparison between the computed SIF and the experimental fracture toughness $K_{Ic}(T)$ predicts if the structure will fail and if it fails at which temperature [Wit04].

In the case of a fast temperature variation, the assumption of a steady state is not more valid. This transient state leads to a thermal gradient in the structure. Consequently, the material properties are inhomogeneously distributed and additional stresses are generated. For example, thermal shock experiments enable to characterise the behaviour of cracks in the case of rapid temperature change [Pom93]. Based on a power law, a thermal fatigue crack growth $da/dN = f(\Delta G)$ is formulated in [Tan05]. However, the expression is only valid for a given temperature amplitude ΔT, as the term ΔT is not integrated in the formulation. This shows the difficulty to establish a global concept for crack growth under thermo-mechanical loading.

8.3.3 Crack at interface or in bulk material

As mentioned earlier, crack propagation in electronic packaging occurs at interfaces and in bulk material. In most cases, cracks at interfaces propagate as long as a complete debonding of the two materials is reached. However, kinking of cracks out of the interface is sometimes observed [Leb04]. As the concept of stress intensity factor is not appropriate for interfacial cracks, the energy release rate is applied to characterise the crack growth [Leb04, Rog05]. Kinking out can be interpreted using a thermodynamical approach: the energy released to create the surface in one of the bulk materials is lower than the energy required for the delamination [HeH89].

Cracks propagating in bulk materials may come close to interfaces. A crack arrest is possible if the interface has a strong toughness and the second material is ductile or has a high resistance to fracture. However, two others scenarii are possible. Either the crack deviates from the bulk material to the interface, or the crack propagates in the second material. At the interface, effects of shear and tensile stresses cannot be dissociated due to the presence of two materials with different material properties. Consequently, the angle between the crack and the interface planes may have an influence on the propagation [HeH88].

In most cases, two distinct numerical analyses are performed to examine cracks in homogeneous material or at interfaces. However, concepts of LEFM are valid for both situations. Moreover, simulation techniques are similar. The implementation of kinking out criteria in software packages may improve the possibilities of numerical crack analyses.

9 Conclusion

In this works, several goals are reached for the characterisation of crack propagation under critical loading, as well as for fatigue crack growth in epoxy resins. For this, the combination of experimental and numerical methods is investigated.

In order to characterise the brittle behaviour of epoxy resins, principles of the linear elastic fracture mechanics (LEFM) are introduced in the first chapter. Within the context of LEFM, four equivalent parameters are available to describe the behaviour of a system containing a crack. Since the energy release rate G and the J-integral quantify the global energy released to create a cracked surface, the stress intensity factors K and the crack tip opening displacement are defined from local stress and respectively strain fields at the crack tip. These parameters are particularly useful to express fracture criteria. For example, the fracture toughness K_{Ic} is introduced to characterise the material resistance to fracture. If the stress intensity at the crack tip of a crack under mode I loading reaches the critical value K_{Ic}, the crack propagates. Equivalent fracture criteria may be formulated based on energy concepts. *"Material flaw or pre-cracks, which may have been introduced unintentionally during the manufacturing process, can have an arbitrary orientation with respect to the loading applied to the component."* This remark of Dhondt [Dho01] points out the necessity to investigate mixed mode loading configurations. Consequently, fracture criteria for cracks under mixed mode loading are presented. Moreover if mode II and III of loading are not negligible, the crack deviates from its original crack plane as it propagates. Theoretical models based on energy release rate, maximum principal stress or strain energy density enable the prediction of the propagation direction.

No simple models are available to predict the risk of material failure in complex structures. Nevertheless, simulation methods offer an efficient way to study cracks in real geometries. The implementation of LEFM concepts in Finite Element Method (FEM) enables actually the evaluation of fracture mechanics parameters, as explained in chapter 3. Stress intensity factors are generally evaluated from nodal displacements, while the energy release rate is estimated using Virtual Crack Extension (VCE) or Virtual Crack Closure Techniques (VCCT). Yet, the application of these techniques requires special mesh geometries around the crack tip. The VCCT justifies a regular mesh composed with hexahedron elements (see Fig. 43). As well, the use of quarter-point noded elements at the crack tip ensures the representation of the stress singularity (see Fig. 37). More than fracture mechanics parameters, numerical simulations are able to estimate the direction of crack propagation using LEFM models. Furthermore, a sequential approach is implemented in software packages Zencrack or ADAPCRACK3D in order to predict the path along which a crack propagates. At each increment, the magnitude and direction of crack propagation are computed to update the position of the crack. As well, the mesh has to be updated between each crack extension. Special methods implemented in Zencrack (crack block advancement) and in Zencrack (insertion of nodes in the existing mesh) are detailed in chapter 3.

Experimental methods applied to characterise the material behaviour are presented in chapter 4. The evaluation of fracture toughness is described by standard procedures which recommend the use of specific geometries, like Compact Tension (CT) specimens. So, analytical solutions provide the expression of fracture toughness as a function of specimen dimensions, crack length and critical force applied during the test. Fatigue crack growth is investigated with similar specimens. Instead of a crack under quasi-static loading, a cyclic tensile loading is applied. The relation between the crack growth rate da/dN and the applied

stress intensity factor range ΔK allows the description of sub-critical crack propagation. Cracks are not only subjected to tensile, but also to shear loadings. Amongst others, Center Cracked Tension (CCT) specimens enable the study of crack propagation under mixed mode conditions. This covers the observation of the crack propagation direction and the establishment of a fracture criterion for mixed mode loadings. As well, a modified single-edge-notched (SEN) specimen is described, in which holes are machined to perturb the stress field in the centre of the sample. A resulting curved crack propagation path is observed.

Chapter 5 presents a numerical study of specimens used in the current work. Results computed with specimen models are compared to analytical solutions in order to verify the accuracy of FE methods. First, a model of CT specimen under static loading conditions is generated for various crack lengths. To be consistent with ASTM standards, a plane strain state is enforced through the sample and the crack is represented by a straight front [A-399]. As a result, the model is simplified to a 2D representation. Computed stress intensity factors are in good agreement with the analytical solutions [A-399]. This validates the capability of FE methods to accurately compute the stress intensity factor K_I. The accuracy of simulation techniques have also to be investigated with 3D models. In 3D, the assumption of a straight crack front is not more valid as depicted in Fig. 122 or Fig. 124. The curvature of the crack front in CT specimens can be numerically extracted, as it is controlled by the material Poisson's ratio [Yam78]. A 3D model of CT specimen with a curved crack front shows that the stress intensity factor is distributed uniformly along the crack front, as suggested from Broek [Bro82]. However, the extracted stress intensity factor differs from the ASTM solution K_{ASTM}. For this reason, the concept of effective stress intensity factor K_{eff} is introduced. Effective functions F_{eff} are specified to integrate the 3D effect in the evaluation of the effective stress intensity factor K_{eff} with CT specimens. Besides, the case of mixed mode loading is investigated with a model of CCT specimen. The computed stress intensity factors K_I and K_{II} are in accordance with the reference solution [Mur87]. Finally, the perforated SEN specimen is considered in order to verify the capability of FE software packages to predict curved crack paths. Simulations are completed with software packages Zencrack and ADAPCRACK3D. The prediction of similar crack paths implies that both implemented remeshing techniques provide reliable results. Further parameters, like commercial availability, computation time or efforts required to create a model are compared.

The experimental characterisation of cracks under critical loading conditions in epoxy resins is presented in chapter 6. First, tests are performed on CT specimens at ambient temperature to measure the fracture toughness of epoxy resins. The test dispersion is estimated with a statistical method based on a Weibull distribution. A minimum of 10 samples is recommended to characterise the fracture toughness with a good precision. The campaign is realised on filled and unfilled materials and shows the difficulty to prepare reproducible crack fronts for filled epoxy resins. Therefore, the presence of filler particles has the effect to increase the fracture toughness. The fracture toughness K_{Ic} measured on different filled epoxy resins is included between 1 and 2 $MPa.m^{1/2}$. Tests on the unfilled epoxy resin return a fracture toughness smaller than 1 $MPa.m^{1/2}$. Finally, the influence of the temperature on the fracture toughness is determined, as seen in Fig. 99. Mixed mode configurations of loading are then investigated with CCT specimens. The direction of crack propagation is measured with the help of an optical system. The expression of the crack propagation angle as a function of the parameters K_I and K_{II} is in accordance with the analytical models presented in chapter 2. This validates the use of these models for the numerical prediction of the propagation direction. Moreover, a fracture criterion for cracks under mixed mode loading conditions is extracted for one material. The theoretical model MSED is the most appropriate to represent the mixed mode fracture behaviour. Finally, the capability to compute a curved a curved crack path is verified with tests on perforated SEN specimens. Actually, experimental and numerical crack paths are similar.

Chapter 7 analyses the fatigue crack growth in epoxy resins. First, the material is characterised with experiments in accordance with the ASTM procedure [A-647]. Tests with CT specimens allow to express the crack growth rate da/dN as a function of the applied stress intensity factor range ΔK. Data are fitted to a Paris law with a good agreement. Only a moderate scatter is observed due to inherent material inhomogeneities. For the tested epoxy resin, the extracted Paris exponent m is evaluated as about 9, which is higher than for metallic materials. Experimental coefficients are then used as input data for FE analysis. During the simulation, the crack is updated step by step. To be consistent with ASTM standards [A-647], the 2D model investigated in chapter 5.2 is considered. A comparison between simulation and experiments enables to verify the accuracy of lifetime prediction with 2D models. However, the case of non-symmetric components with complex loading requires the investigation of fatigue crack growth with 3D models. First, the shape of the crack front through the thickness is experimentally characterised with filled and unfilled epoxy resins. A good correlation is observed with the computed crack front geometries. The notion of effective stress intensity factor K_{eff} and effective dimensionless function F_{eff} are introduced in chapter 5.3. On that purpose, an effective Paris law is proposed. A fit of the curve da/dN - ΔK_{eff} returns the effective material coefficients (C_{eff}, m_{eff}). Finally, simulations are computed with the 3D model presented in chapter 5.3. Conventional and effective Paris law are applied as material fatigue behaviour. While the conventional fatigue behaviour returns an error of 50% on the lifetime, the effective Paris law enables an accurate estimation of the time-to-failure. This establishes a numerical tool adequate to predict material rupture

This work proposes experimental and numerical methods to predict crack propagation in epoxy resins. The integration of these methods in the development of electronic components is discussed in chapter 8. In fact, this approach enables to improve the design of structures and to increase their lifetime with respect to crack propagation. Amongst others, the resistance to fracture can be optimised by modifying the applied material or the geometry of the component. First, experimental methods are essential to determine the material with the best resistance to fracture. The generation of a database specific to fracture mechanics enables an effective comparison of the materials. In addition, the combination of simulations and experiments may be used to dimension structures. For example, the critical loading acceptable for a given structure can be determined or the critical default size may be estimated. As well, various geometries can be compared for a given loading condition. With similar numerical techniques, the lifetime of components can be estimated for cracks under mode I loading. Although the generation of 2D or 3D finite element models is complex, the time-to-failure can be accurately predicted. The extension of lifetime prediction to the case of mixed mode loading requires the introduction of a fatigue law, which integrates the effects of shear loading. Concepts of fatigue crack growth have also to be completed to take into account the temperature influence. Finally, crack propagation in electronic assembly occurs not only in bulk material, but also at interfaces. The competition between propagation at the interface or in a bulk material can lead to kinking out of cracks. The understanding of this phenomenon needs to be enhanced by further investigations.

Appendix:
Infinite plate containing an inclined crack

Infinite plate

The relative proportion of mode I and mode II can be analytically described in the case of an infinite plate, containing a crack inclined of an angle φ to the applied tensile loading σ_∞ (see Fig. 129). The tensile-shear loading repartition at the crack tip is directly related to the crack orientation. The stress intensity factors at the crack tip are given by [Erd63]:

$$\begin{cases} K_I = \sigma_\infty \sqrt{\pi a} \cos^2\varphi \\ K_{II} = \sigma_\infty \sqrt{\pi a} \sin\varphi \cos\varphi \end{cases} \quad \text{and} \quad \frac{K_{II}}{K_I} = \tan\varphi \qquad \textbf{Eq. 158}$$

The ratio K_{II} / K_I is independent of the applied loading. Consequently, it is taken as reference value for the comparison between analytical and numerical results.
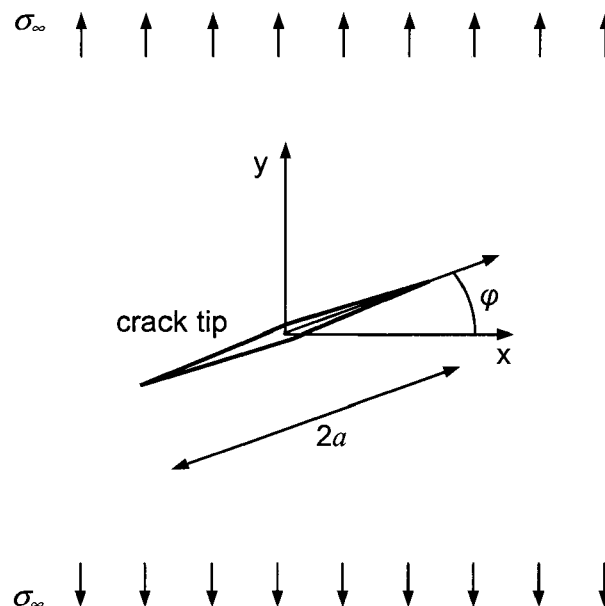
Fig. 129: Infinite plate with a slant crack under a uniform uniaxial tensile stress

FE model

A plate with a notch of length $2a$ = 25 mm, with dimensions $2H = 2W = 30a$ and B = 3 mm is modelled. A distance of $15a$ between the crack tip and the plate borders ensures that the singularity is far from the applied load. Nodal displacements in the thickness are fixed, so that the 3D model of the infinite plate is equivalent to the 2D reference solutions. The crack is introduced with the software Zencrack. FE models are generated for angles φ = 0° to 75° with steps of 15°. By varying the angle φ, distinct mixed mode loadings are generated.

Fig. 130: FE model of the infinite plate (a) dimensions; (b) mesh

Stress intensity factors are extracted with the crack tip opening displacement method available in Zencrack (see chapter 3.1.2). Finally, the ratio K_{II} / K_I is evaluated. Numerical results are compared with the analytical solution in Tab. 17.

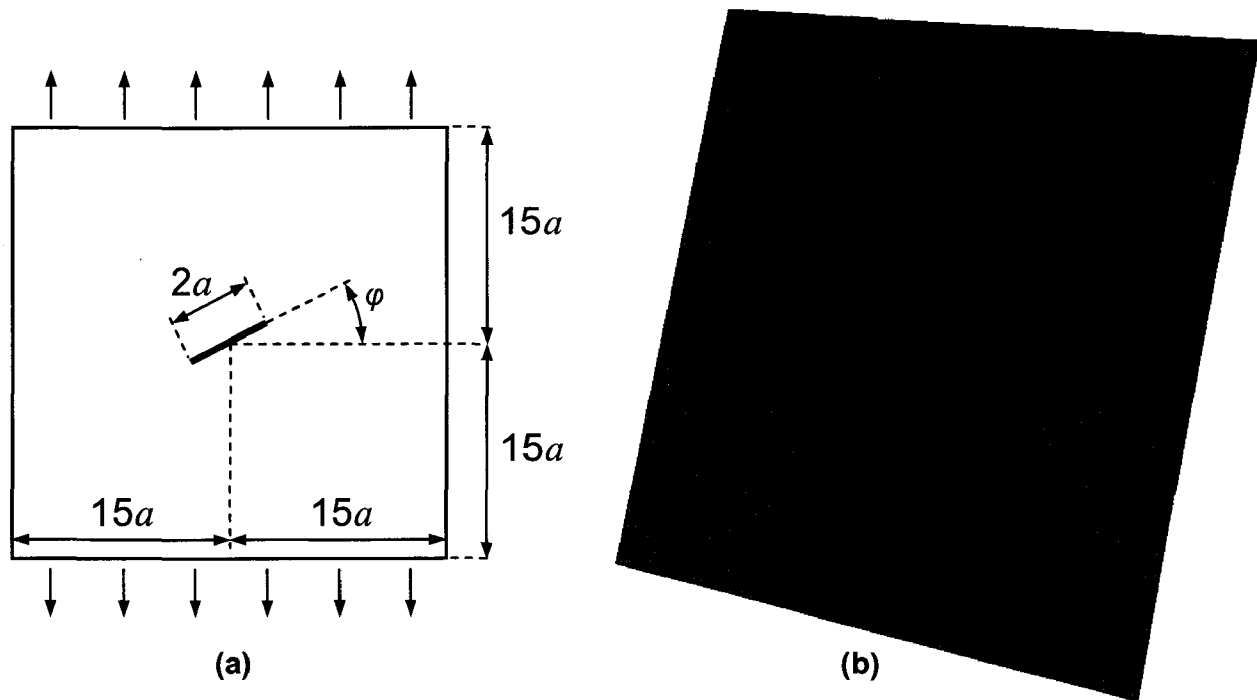| Crack orientation φ	Analytical solution (tan φ)	FE result (K_{II} / K_I)	Error
0°	0.000	0.000	0.0%
15°	0.268	0.265	1.2%
30°	0.577	0.574	0.6%
45°	1.000	0.993	0.6%
60°	1.732	1.744	0.7%
75°	3.732	3.669	1.7%

Tab. 17: Infinite plate - Comparison between FEM results and analytic solution

Numerical results are very close to the theoretical solutions. In fact, the relative error between analytical solution and numerical estimation remains less than 2% for φ included between 0° and 75°. The error on K_I and K_{II} is also less than 3%. The crack tip opening displacement method provides an accurate computation of the stress intensity factors in the context of mixed mode.

The accuracy of the J-integral method is investigated with the same model. The combination of Eq. 158 and Eq. 45 gives the possibility to estimate the energy release rate from the stress intensity factors. This analytical solution is taken as reference value. A relative error on the energy release rate less than 6% is reasonable, considering that the modelled plate is an approximation of an infinite plate.

References

[Aba05]   Abaqus Documentation, version 6.5, 2005

[A-399]   ASTM Standard E 399-90, *Standard Test Method for Plane-Strain Fracture Toughness of Metallic Materials*, 1997

[A-5045] ASTM Standard D 5045-99, *Standard Test Methods for Plane-Strain Fracture Toughness and Strain Energy Release Rate of Plastics Materials*, 1999

[A-647]   ASTM Standard E 647-95, *Standard test method for measurement of fatigue crack growth rates*, Annual Book of ASTM Standards, vol. 03.01, pp. 578-614, 1995

[And95]   T. L. Anderson, *Fracture mechanics: fundamentals and applications*, 2nd Ed. CRC Press, 1995

[Azi96]   H. R. Azimi, R. A. Pearson, R. W. Hertzberg, *Fatigue of rubber-modified epoxies: effect of particle size and volume fraction*, Journal of Materials Science, vol. 31, pp. 3777-3789, 1996

[Bar74]   R. S. Barsoum, *Application of quadratic isoparametric finite elements in linear fracture mechanics,* International Journal of Fracture, vol. 10, pp. 603-605, 1974

[Bar76]   R. S. Barsoum, *Application of triangular quarter-point elements as elements of power law hardening material,* International Journal of Fracture, vol. 12, pp. 463-466, 1976

[Bil86]   R. Billardon, C. Adam, J. Lemaitre, *Study of the non-uniform growth of a plane crack in a three-dimensional body subjected to non-proportional loadings*, Int. J. Solids Structures, vol. 22, pp. 677-692, 1986

[Bit96]   T. N. Bittencourt, P. A Wawrzynek, A. R. Ingraffea, J. L .A. Sousa, *Quasi-automatic simulation of crack propagation for 2D LEFM problems*, Engineering Fracture Mechanics, vol. 55, pp. 321-34, 1996

[Bit00]   T. D. de Araujo T. N. Bittencourt, D. Roehl, L. F. Martha, *Numerical estimation of fracture parameters in elastic and plastic-elastic analysis*, ECCOMAS, Barcelona, 11-14 Sept. 2000

[Bro76]   D. Broek, R. C. Rice, *Fatigue crack growth properties of rail steels*, Battelle report to DOT/TC, 1976

[Bro82]   D. Broek, *Elementary engineering fracture mechanics*, 3rd revised edition: Kluwer academic publishers, 1982

[Buc04]   F. G. Buchholz, A. Chergui, H. A. Richard, *Fracture analysis and experimental results of crack growth under general mixed mode loading conditions*, Engineering Fracture Mechanics, vol. 71, pp. 455-468, 2004

[Daw92]   D. S. Dawidcke, K. N. Shivakumar, K. N. Newman, A. F. Grandt, *An inverse method for the calculation of through thickness fatigue crack closure behaviour*, Fracture mechanics: 22nd Symposium, ASTM STP 1131, pp. 46-57, 1992

[Dep05]   N. Depoorter, *Development of simulation methods for the damage behavior and the reliability of epoxy resin*, PhD Thesis, University of Valenciennes, 2005

[Dho01]   G. Dhondt, A. Chergui, F.-G. Buchholz, *Computational fracture analysis of different specimens regarding 3D and mode coupling effects*, Engineering Fracture Mechanics, vol. 68, pp. 383-401, 2001

[Dom98]   J. Dompierre, P. Labbé,F. Guibault and R. Camaro, *Proposal of benchmarks for 3D unstructured tetrahedral mesh optimization,* Proceedings 7th international meshing roundtable, Dearborn, pp. 525-537, 1998

[Dug60]   D. S. Dugdale, *Yielding of steel sheets containing slits*, Journal of the Mechanics and Physics of Solids, vol. 8, pp. 100-108, 1960

[Erd63]   F. Erdogan, G.C. Sih, *On the crack extension in plates under plane loading and transverse shear,* Journal Basic Engineering 85, pp. 519-527, 1963

[ESI01]   *Fracture mechanics testing methods for polymers adhesives*, ESIS Publication 28, Edited by D. R. Moore, A. Pavan, J. G. Williams, Elsevier, 2001

[Fis81]   K. F. Fischer, H. Göldner, *On the formulation of a principal strain criterion in crack fracture mechanics*, International Journal of Fracture, vol. 17, pp. R3-R6, 1981

[Fis82]   K. F. Fischer, *Zum Verhalten der Mehrachsigkeitszahl in Rissspitzenumgebung*, Techn. Mathematik 3, pp. 31-36, 1982

[Ful02]   M. Fulland, Rißsimulationen in dreidimensionalen Strukturen mit automatischer adaptiver Finite-Elemente-Netzgenerierung, Fortschritt-Bericht VDI, Reihe 18, Nr. 280, VDI Verlag, Düsseldorf, 2002

[Gil86]   J. W. Gillespie, Jr, L. A. Carlsson, R. B. Pipes, *Finite element analysis of the end notched flexure specimen for measuring mode II fracture toughness*, Composites Science and Technology, vol. 27, pp. 177-197, 1986

[Gri21]   A. A. Griffith, *The phenomena of rupture and flow in solids*, Phil. Trans. Royal Society London, A 221, pp.163-197, 1921

[Gri24]   A. A. Griffith, *The theory of rupture*, Proceedings of the 1st international congress for applied mechanics, Delft, pp. 55-63, 1924

[Gro96]   D. Gross, *Bruchmechanik*, Springer Verlag, 1996

[Har01]   R. J. Harries and S. K. Sitaraman, *Numerical modeling of interfacial delamination propagation in a novel peripheral array package,* IEEE Transactions on components and packaging technologies, vol. 24, no. 2, pp. 256-264, 2001

[HeH88]   M-Y He, J. W. Hutchinson, *Crack deflection at an interface between dissimilar elastic materials*, International Journal of Solids and Structures, vol. 25, no. 9, pp. 1053-1067, 1988

[HeH89]   M-Y He, J. W. Hutchinson, *Kinking of a crack out of an interface*, Journal of Applied Mechanics, Trans. ASME, vol. 56, pp. 270-278, 1989

[Hel75]   T. K. Hellen, *On the method of virtual crack extensions*, International Journal for Numerical methods in Engineering, vol. 9, pp. 187-207, 1975

[Hen75]   R. D. Henshell; K. G. Shaw, *Crack tip finite elements are unnecessary*, International Journal for Numerical Methods in Engineering, vol. 9, no. 3, pp. 495-507, 1975

[Her80]   R. W. Hertzberg, J. A. Manson, *Fatigue of Engineering Plastics*, Academic Press, 1980

[Hus74]   M.A. Hussain, S.L. Pu, J. Underwood, *Strain energy release rate for a crack under combined mode I and mode II*, Fracture analysis ASTM STP 560, pp 2-28, 1974

[Ing13]   C. E. Inglis, *Stresses in a plate due to the presence of cracks and sharp corners*, Trans. Inst. Naval Arch., London, vol. 40, pp. 219-230, 1913

[Irw54]   G. R. Irwin, J. A. Kies, *Critical energy release rate analysis of fracture strength*, Welding research supplement, pp. 193-198, 1954

[Irw57]   G. R. Irwin, *Analysis of stresses and strains near the end of a crack traversing a plate*, Journal of Applied Mechanics, Trans. ASME, vol. 79, pp. 361-364, 1957

[Irw58]   G. R. Irwin, *Fracture*, in Handbuch der Physik, Springer Verlag, Berlin, vol. 6, pp. 551-590, 1958

[JiM03]   M. A. Jimènez and A. Miravete, *Data reduction of interlaminar fracture tests for laminated composites combining Finite Element Analysis and Linear Elastic Fracture Mechanics*, 2003 Abaqus user's conference, 2003

[Kit77]   H. Kitagawa, R. Yuuki, *Analysis of arbitrarily shaped crack in a finite plate using conformal mapping*, 1st report - Construction of analysis procedure and its applicability, Trans. JSME, vol. 43, no. 376, pp. 4354-4362, 1977

[KnS72]   J. K. Knowles, E. Sternberg, *On a class of conservation laws in linearized and finite elastostatics*, Archive for Rational Mechanics and Analysis, vol. 44-3, 1972

[Kru02]   R. Krueger, *The virtual crack closure technique: history, approach and applications*, NASA/CR-2002-211628, ICASE Report No. 2002-10, 2002

[Kru03]   R. Krueger, P. J. Minguet and T. K. O'brien, *Implementation of interlaminar fracture mechanics in design: an overview*, 14th international conference on composite materials (ICCM-14), San Diego, 2003

[Kus04]   H. D. Kuske, M. Bastian, *Bruchzähigkeitsverhalten und Ermüdungsrisswachstum als Dimensionierungskriterium für Polyolefinkonstruktionswerkstoffe*, 3R International, vol. 43, pp. 497-507, 2004

[Law93]   B. R. Lawn, *Fracture of brittle solids*, 2nd edition, Cambridge University Press, 1993

[Leb04]   F. Leblanc, *Contribution to a methodology for the analysis of fracture phenomena in encapsulated components*, PhD Thesis, University of Valenciennes, 2004

[Mir03]   A. C. O. Miranda, M. A. Meggiolaro, J. T. P. Castro, L. F. Martha, T. N. Bittencourt, *Fatigue life and crack path predictions in generic 2D structural components*, Engineering Fracture Mechanics, vol. 70, pp. 1259-1279, 2003

[Mur87]   Y. Murakami, *Stress intensity factors handbook*, Vol. 1-2, Pergamon Press, 1987

[Oso83]   A. M. B. A. Osorio, J. G. Williams, *Some results on fatigue crack growth in polymers*, Intern. conf. "Fatigue in polymers", pp. 7.1-7.10, 29-30 June 1983

[Par61]   P. C. Paris, R. E. Gomez, W. E. Anderson, *A rational analytic theory of fatigue*, The Trend in Engineering, vol. 13-1, pp. 9-14, 1961

[Par63]   P. C. Paris, F. Erdogan, *A critical analysis of crack propagation laws*, Journal of Basic Engineering, Trans. ASME, vol. 85, pp. 528-534, 1963

[Pak74]   D. M. Parks, *A stiffness derivative finite element technique for determination of crack tip stress intensity factors*, International Journal of Fracture, vol. 10, pp. 487-502, 1974

[Pom93]   W. E. Pompe, *Thermal shock behaviour of ceramic materials-modelling and measurement*, Proceedings of the NATO advanced research workshop on thermal shock and thermal fatigue behaviour of advanced ceramics, Kluwer Academic Publishers, pp. 3-14, 1993

[Ric68]   J. R. Rice, *A path dependent integral and the approximate analysis of strain concentration by notches and cracks*, Journal of Applied Mechanics, Trans. ASME, pp. 379-386, 1968

[Rich81]   H. A. Richard, *A new compact shear specimen*, International Journal of Fracture, vol. 17, pp. 105-108, 1981

[Rich85]   H. A. Richard, *Bruchvorhersage bei überlagerter Normal- und Schub-Beanspruchung von Rissen*, VDI-Forschungsheft 631, VDI-Verlag, Düsseldorf, Habilitationsheft, ISBN 3-18-850631-7, 1985

[Rid83]   R. A. Riddle, R. D. Streit, I. Finnie, *An evaluation of the compact shear specimen for mixed mode fracture studies*, Journal of Engineering Materials and Technology, vol. 105, pp. 268-272, 1983

[Rit83]   R. O. Ritchie, *Why ductile fracture mechanics ?*, Journal of Engineering Materials and Technology, Trans. ASME, vol. 105, pp. 1-7, 1983

[Rog05]   F. Leblanc, J. Roger, A. Zimmermann, D. Coutellier, *Détermination de la courbe de résistance interfaciale par corrélation expérimentale/numérique*, 14èmes Journées Nationales sur les Composites JNC14, Compiègne, France, 22-24 mars 2005

[Rog07a]   J. Roger, J. Mergheim, A. Zimmermann, D. Coutellier, *Three-dimensional simulation of fatigue crack growth*, DVM-Bericht 239, 39. Tagung des DVM-Arbeitkreises Bruchvorgänge, pp. 197-206, 2007

[Rog07b]   J. Roger, A. Zimmermann, D. Coutellier, *Determination of fatigue crack growth in epoxy resins using experiments and simulation*, 15èmes Journées Nationales sur les Composites JNC15, Marseille, France, 6-8 Juin 2007

[RyK77]   E. F. Rybicki, M. F. Kanninen, *A finite element calculation of stress intensity factors by a modified crack closure integral*, Engineering Fracture mechanics, vol. 9, pp. 931-938, 1977

[Sch01] M. Schöllmann, *Vorhersage des Risswachstums in ebenen und räumlichen Strukturen mittels numerischer Simulation,* Fortschritt-Bericht VDI, Reihe 18, Nr. 269, VDI Verlag, Düsseldorf, 2001

[SFR00] M. Schöllmann, M. Fulland, H.A. Richard, *Three-dimensional fatigue crack growth simulation under complex loading with ADAPCRACK3D,* in M. Fuentes, M. Elices, A. Martín-Meizoso, J.-M. Martínez-Esnaola (Eds.), "Fracture Mechanics: Applications and challenges", ESIS Publication 26, Elsevier, CD-ROM-Proceedings, section 9 (numerical methods), paper 5, pp. 1-8, 2000

[SFR01] M. Fulland, M. Schöllmann, H.A. Richard, *Simulation of fatigue crack propagation processes in arbitrary three-dimensional structures with the program system ADAPCRACK3D,* in Ravi-Chandar et al. (Eds.), "Advances in fracture research", Fatigue and fracture, Honolulu, USA, CD-Rom proceedings of the 10th international conference on fracture, 2001

[SFR03] M. Schöllmann, M. Fulland, H.A. Richard, *Development of a new software for adaptive crack growth simulations in 3D structures,* Engineering Fracture mechanics, vol. 70, pp. 249-268, 2003

[She99] J. R. Shewchuk, *Lecture notes on Delaunay mesh generation,* Departement of electrical engineering and computer science, University of California at Berkeley, 1999

[Shi86] C. F. Shih, B. Moran, T. Nakamura, *Energy release rate along 3D crack front in a thermally stressed body,* International Journal of Fracture, vol. 30, pp. 79-102, 1986

[Sih74] G. C. Sih, *Strain-energy-density factor applied to mixed mode crack problems,* Int. Fracture Mech., vol. 10, pp. 305-321,1974

[Sih80] G. C. Sih, B. Barthelemy, *Mixed mode fatigue crack growth predictions,* Engineering Fracture Mech., vol. 13, pp. 439-451, 1980

[Sra76] J. E. Srawley, *wide range stress intensity factor expressions for ASTM E 399 standard fracture toughness specimens,* International Journal of Fracture, vol.12, pp. 475-476, 1976

[Sun89] C. T. Sun, M. G. Mahonaran, *strain energy release rates of an interfacial crack between two orthotropic solids,* Journal of composite materials, vol. 23, pp. 460-478, 1989

[SuS01] V. Sundararaman, S. Sitaraman, *interfacial fracture toughness for delamination growth prediction in a novel peripheral array package,* IEEE Transactions on Components and Packaging Technologies, vol. 24, pp. 265-270, 2001

[Swe88] J. L. Swedlow, *Three dimensions versus two dimensions in fracture mechanics,* Fracture mechanics: 19th Symposium, ASTM STP 969, pp. 88-98, 1988

[Tan04] T. Tang, C. Y. Hui, H. G. Retsos, E. J. Kramer, *Characterization of a fracture specimen for crack growth in epoxy due to thermal fatigue,* Engineering Fracture mechanics, 2005

[Tim00] C. Timbrell, G. Cook, R. Chandwani, *3D crack analysis using MSC.Marc,* 1st northern european technology conference, Manchester, England, June 7-8, 2000

[Tim04]   C. Timbrell, R. Chandwani, G. Cook, *State Of The Art In Crack Propagation*, Journée Scientifique 2004: Les méthodes de dimensionnement en fatigue, Centre de Compétences Matériaux & Conception (CCM&C), Fribourg, Switzerland, Oct. 27 2004

[Tim05]   R. Chandwani, C. Timbrell, M. Wiehahn, *An FE Simulation Tool For Fracture Mechanics*, International Seminar on "Fatigue, Reliability & Performance Considerations In Design", Indian Institute of Science, Bangalore, India, July 14-15 2005

[Wal03]   H. Walter, *Morphologie-Zähigkeits-Korrelationen von modifizierten Epoxidharz-systemen mittels bruchmechanischer Prüfmethoden an Miniaturkörpern*, Dissertation genehmigt durch die Martin-Luther-Universität, Halle, 2003

[Wel65]   A. A. Wells, *The application of fracture mechanics to yielding materials*, Proceedings of the Royal Society of London, vol. 285, no. 1400, pp. 34-45, 1965

[Wes39]   H. M. Westergaard, *Bearing pressures and cracks*, Journal of Applied Mechanics, Trans. ASME, vol. 6, pp. A49-A53, 1939

[Wil52]   M. L. Williams, *Stress singularities from various boundary conditions in angular corners of plates in extension*, Journal of Applied Mechanics, Trans. ASME, vol. 19, pp. 526-528, 1952

[Wil57]   M. L. Williams, *On the stress distribution at the base of a stationary crack*, Journal of Applied Mechanics, Trans. ASME, vol. 24, pp. 109-114, 1957

[Wil84]   J. G. Williams, *Fracture mechanics of polymers*, Ellis Horwood Ltd, 1984

[Wil71]   J. K. Wilson, *Numerical method for determining stress intensity factors of an interior crack in a finite plate*, Journal of Basic Engineering, Trans. ASME, pp. 685-690, 1971

[Wit04]   O. Wittler, *Bruchmechanische Analyse von viskoelastischen Werkstoffen in elektronischen Bauteilen*, Dissertation genehmigt durch die Technische Universität Berlin, 2004

[Yam78]   Y. Yamamoto, Y. Sumi, *Stress intensity factors for three dimensional cracks*, International Journal of Fracture, vol. 14, pp. 17-38, 1978

[Yu82]   B. Y. Yu, *A discussion on mixed mode J-integral fracture criterion*, Engineering Fracture mechanics, vol. 16, pp. 156, 1982

[Zen06]   Zencrack User Manual, issue 7.4, 2006
            Zentech International Limited, Web Site: http://www.zentech.co.uk/